Structural and optical properties of short period superlattices for rational (In,Ga)N

D I S S E R T A T I O N

zur Erlangung des akademischen Grades

doctor rerum naturalium
(Dr. rer. nat.)

im Fach Physik
Spezialisierung: Experimentalphysik

eingereicht an der
Mathematisch-Naturwissenschaftlichen Fakultät
der Humboldt-Universität zu Berlin

von

Mariia Anikeeva

Präsident der Humboldt-Universität zu Berlin:
Prof. Dr.-Ing. Dr. Sabine Kunst

Dekan der Mathematisch-Naturwissenschaftlichen Fakultät:
Prof. Dr. Elmar Kulke

Gutachter/innen:
1. Prof. Dr. Thomas Schröder
2. Prof. Dr. Axel Hoffmann
3. Dr. Philippe Vennéguès

Tag der mündlichen Prüfung: 11 Dezember 2019

Kurzzusammenfassung

In dieser Arbeit untersuchen wir ultradünne (In,Ga)N Quantentöpfe, die mittels Molekularstrahlepitaxie in Form von kurzperiodischen Übergittern auf (0001) GaN abgeschieden wurden. Wir charakterisieren dieser Heterostrukturen mit verschiedenen strukturellen und optischen Methoden: Dazu gehören die hochauflösende Transmissionselektronenmikroskopie (HRTEM), die Rastertransmissionselektronenmikroskopie (STEM), Röntgenbeugung (XRD) und die hochenergetischer Refeflexionselektronenbeugung an Oberflächen (RHEED) sowie die Photolumineszenz (PL) und die Kathodolumineszenz. Wir fokussieren uns dabei auf die Quantifizierung des Indiumgehaltes solcher ultradünner Schichten, sowie auf die Thermodynamik und Kinetik des Indiumeinbaus. Auf Grundlage dieser Daten diskutieren wir grundlegende optische Eigenschaften dieser Übergitter. Die wichtigsten Ergebnisse unserer Untersuchungen sind:

1. Die quantitative Kompositionsanalyse von kurzperiodischen Übergittern mit ultradünnem (In,Ga)N Quantentöpfen ist am genauesten auf der Grundlage der Verzerrungsanalyse mittels "Peakfinding" von Abbildungen aus der aberrationskorrigierten hochauflösende Transmissionselektronenmikroskopie (HRTEM). Hochauflösenden Röntgenbeugung und STEM Z-Kontrast, die in der Regel für solche Analysen einegsetzt werden haben jeweils ihre eigenen Begrenzungen und reichen nicht an die Genauigkeit der HRTEM basierten Methoden heran.

2. Der Indiumeinbau in GaN unter Exposition von In und N-Fluss ist selbst-begrenzend auf eine Zusammensetzung von 25% und eine Schichtdicke von einer Monolage. Die Variation der Wachstumsbedingungen über einen weiten Bereich von III-V-Verhältnissen, Wachstumstemperaturen und Depositionszeiten führen weder zu iener Höhuing des Indiumgehalt noch zu einer Erhöhung derSchichtdicke über diese Werte hinaus.

3. Diese Selbstbegrenzung ist im Ergebnis einer seits auf die Unterschiede in der Bildungsenthalpie von InN und GaN und andererseits auf die hohe Gitterfehlanpassung des Systems zurückzuführen. Das Wachstum von (In,Ga)N mit hohem In-Gehalt erfordert ein hohes chemisches Potential des Stickstoffs. Unter diesen Bedingungen bildet sich eine 2×2-Stickstoff-Ad-Atomrekonstruktion auf der Oberfläche aus. Die an das N-Adatom gebundenen Ga-Atome sind 4-fach koordiniert. Basierend auf DFT-Berechnungen schlagen wir ein Modell vor, In dem In Atome einen Teil dier 4-fach koordinierten Ga-Oberflächenatome ersetzen . Durch die verzerrungsbedingte Abstoßung wird nur jeweils eines der 4 -fach koordinierten Plätzebesetzt. Gleichzeitig bevorzugen Ga-Atome 3-fach koordinierte Stellen, da sie dort re-hybridisieren und Bindungsnergie gewinnen. Die resultierende $(2\sqrt{3}\times2\sqrt{3})R30^\circ$ Oberflächenrekonstruktion ist die niedrigste Energiekonfiguration. Die maximale Indiumkonzentration von 25% ist durch die N-Adatombedeckung von 25% gegeben.

4. Aufgrund dass, in unseren polaren $In_{0.25}Ga_{0.75}N$ Übergitter, Polarisationsfelder, Dickenfluktuationen oder Kompositionsschwankungen keine wesentliche Rolle spielen, stellen

sie ein ideales Modellsystem für optische Rekombinationsprozesse in (In,Ga)N Legierungen und Quantentöpfen da. Durch die Änderung der Barrierendicke kann die Lokalisation der Lochwellenfunktion in diesen Strukturen gezielt manipuliert werden. Dadurch erhalten wir einen Einblick in die Rolle des Einschlusses der Lochwellenfunktion (In,Ga)N-Legierungen und von Quantentöpfe allgemein. Unsere optischen Studien in Kombination mit DFT-Berechnungen zeigen, dass der Rekombinationsprozess durch den Einschluss der Lochwellenfunktion in den Monoschichten gesteuert wird, während die Elektronenwellenfunktion delokalisiert ist. Mit abnehmender Barrieredicke kommt es zur Delokalisierung der Lochwellenfunktion und zu nichtstrahlende Rekombinationsprozesse in den Barrieren. Wir zeigen, dass unsere Übergitter Phänomene zeigen, wie sie in konventionellen QWs oder Bulk-Legierungen beobachtet werden, z.B. einen nicht-exponentiellen Abfall der PL-Intensität, die spektrale Abhängigkeit der PL Lebensdauer und eine S-förmige Temperaturabhängigkeit des Emissionspeaks: Diese lassen sich durch das Zusammenspiel von Ladunsgträgerlokalisation und nicht-strahliger Rekombination erklären. Wir zeigen auch, dass wir bei der Abscheidung fraktionaler Monolagen lateral begrenzte Quantenscheiben beobachten, deren Emissionen eine Linienbreite geringer als im 1 meV haben. Durch die Erhöhung ders Bedeckungsgardes verschmelzen diese Linien zu einem breiten Spektrum, das dem von konventionellen Legierungen gleicht.

Abstract

In this work we investigate ultra-thin (In,Ga)N quantum wells (QWs) grown on (0001) GaN by molecular beam epitaxy in the form of short-period superlattices. We perform a comprehensive study of these heterostructures by means of various structural and optical methods: high resolution transmission electron microscopy (HRTEM), scanning transmission electron microscopy (STEM), x-ray diffraction (XRD) and reflection high-energy electron diffraction, as well as photoluminescence (PL) and cathodoluminescence. We focus on the quantification of indium incorporation and by employing these data study basic optical properties of these superlattices. The main results of our investigations are:

1. Quantitative compositional analysis of short period superlattices with ultra-thin (In,Ga)N QWs is most accurate based on strain analysis from unit cell maps obtained by aberration corrected HRTEM. XRD and STEM, usually employed for quantitative analysis, each have their own short comings.

2. The indium incorporation into GaN under exposure of In and N flux is self-limited to a composition of 25% and a layer thickness of one monolayer. Varying growth conditions over a wide range of III-V ratios, growth temperatures and deposition times, do not increase the indium content or the layer thickness beyond these values.

3. This self-limitation is a result of the differences in formation enthalpy of InN and GaN and the high lattice mismatch of the system. Growth of InGaN with high In content requires a high N-chemical potential. Under these conditions, starting from a GaN barrier a 2×2 nitrogen adatom reconstruction forms. Ga atoms bound to the N adatom are 4-fold coordinated. Based on DFT calculations we propose a model that implies a substitution of the 4-fold coordinated Ga surface atoms by incoming indium during the deposition of the nominally InN QW. Indium atoms favor to occupy 4-fold sites with nitrogen involving finite amount of N adatoms and undergo nearest-neighbor repulsion. At the same time, Ga atoms prefer 3-fold coordinated sites as they can re-hybridize and thereby gaining the energy. The resulting $(2\sqrt{3}\times2\sqrt{3})R30^{\circ}$ surface reconstruction is the lowest energy configuration that sets maximum indium concentration to a fundamental limit of 25% and is stable under various growth regimes.

4. Our polar $In_{0.25}Ga_{0.75}N$ superlattices serve as model system for recombination process in (In,Ga)N since their recombination is not suffering from polarization fields, well-width or high compositional fluctuations. By changing the barrier width we can intentionally change the localization of the hole wavefunction in these structures and thus get insight into the role of hole confinement in (In,Ga)N alloys and of QWs in general. Our optical studies combined with DFT calculations show that the recombination process is governed by the confinement of the hole wavefunction in the monolayers, while the electron wave function is delocalized. With decreasing barrier thickness the hole wavefunction gets

eventually delocalized and non-radiative recombination in the barriers becomes crucial. We reveal that our superlattices show common phenomena observed in conventional QWs or bulk alloys like a non-exponential decay of the PL intensity, spectral dependence of the decay time and S-shape temperature dependence of the emission peaks which can be explained by the interplay of carrier localization and non-radiative recombination. We show also that in case of deposition of fractional monolayers we observe laterally confined quantum discs that exhibit sub meV emission line widths. By increasing the coverage, these lines merge into broad spectra observed in conventional alloys.

Contents

1 Introduction and motivation 1

2 Theoretical background and methods 6

2.1 Basic structural properties of the hexagonal (In,Ga)N compound . . . 6
2.2 Growth by molecular beam epitaxy . . . 7
2.2.1 Growth technique . . . 7
2.2.2 Growth regimes . . . 9
2.2.3 Growth scheme of the experimental structures . . . 10
2.3 Methods of structural investigation . . . 11
2.3.1 Transmission electron microscopy . . . 11
2.3.1.1 Scattering of the electron beam . . . 11
2.3.1.2 Main principle and set up . . . 13
2.3.1.3 Phase contrast. High resolution transmission electron microscopy . . . 16
2.3.1.4 Aberration correction in HRTEM . . . 18
2.3.1.5 Scanning transmission electron microscopy . . . 20
2.3.1.6 Experimental details . . . 23
2.3.1.7 Scanning TEM-CL technique . . . 23
2.3.2 Reflection high-energy electron diffraction . . . 24
2.3.3 X-ray diffraction . . . 26
2.3.4 Atomic Force microscopy . . . 27
2.4 General optical properties and methods of optical investigation: . . . 28
2.4.1 Basic optical properties . . . 28
2.4.2 Cathodoluminescence measurements . . . 31
2.4.3 Photoluminescence investigations . . . 33
2.5 Overview of the (In,Ga)N material properties . . . 35
2.5.1 Growth of (In,Ga)N alloys . . . 35
2.5.1.1 (In,Ga)N alloy formation . . . 35
2.5.1.2 Phase diagram (In,Ga)N . . . 37
2.5.2 Optical phenomena in (In,Ga)N . . . 38
2.5.2.1 Polarization fields . . . 38
2.5.2.2 Localization phenomena in (In,Ga)N structures . . . 40

2.6 Theoretical calculations . . . 41
2.6.1 Density Functional Theory . . . 41
2.6.2 K*p model calculations . . . 42

3 Quantitative methods of the indium content analysis 44
3.1 Aim of the chapter . . . 44
3.2 Multislice image simulations . . . 44
3.3 Quantitative HRTEM analysis . . . 46
3.3.1 HRTEM analysis of the as-grown (In,Ga)N QW . . . 51
3.4 Quantification analysis in STEM. . . . 52
3.4.1 Simulations based on frozen phonon approximation . . . 52
3.4.2 Composition quantification via Z-contrast . . . 53
3.5 X-Ray diffraction as a quantitative method for ultra-thin quantum wells . . . 54

4 Study of the indium incorporation in ultra-thin (In,Ga)N quantum wells 57
4.1 Aim of the chapter . . . 57
4.2 Investigation of the indium content as dependent on growth conditions . . . 57
4.2.1 Influence of the III/V ratio . . . 57
4.2.2 Influence of the growth temperature . . . 61
4.2.3 Influence of the QW growth time . . . 67
4.2.4 Short summary . . . 69
4.3 Surface reconstructions of the $In_{0.25}Ga_{0.75}N$ monolayer grown on GaN . . . 71
4.3.1 Ordering in $In_{0.25}Ga_{0.75}N$ monolayers . . . 71
4.3.2 Experimental surface reconstructions. RHEED . . . 72
4.3.3 Identification of the surface reconstruction . . . 73
4.4 Model of the indium incorporation. . . . 76
4.4.1 DFT calculations . . . 76
4.4.2 Discussion of the model . . . 80
4.5 Summary . . . 82

5 Optical properties of $In_{0.25}Ga_{0.75}N$ superlattices: 84
5.1 Aim of the chapter . . . 84
5.2 Polarization fields in the ML-thick QWs . . . 84
5.3 Vertical confinement of charge carriers in SLs: . . . 85
5.3.1 SLs with different barrier thickness. Structural investigations. . . . 85
5.3.2 Continuous wave PL measurements . . . 88
5.3.3 Time-resolved PL measurements . . . 90
5.3.4 Temperature dependence . . . 93
5.3.5 DFT calculations. . . . 96
5.3.6 Discussion . . . 100
5.3.7 Conclusions . . . 107
5.4 Lateral confinement. Scanning TEM-CL measurements. . . . 109
5.4.1 Localization of the charge carriers . . . 109
5.4.2 Change in coverage. STEM-CL measurements . . . 110
5.4.3 Continuum k*p calculations . . . 113
5.4.4 Discussion of the lateral confinement . . . 114

6 Summary and conclusions 117

A Image simulations for different specimen thicknesses of the ordered $In_{0.25}Ga_{0.75}N$ MLs 120

B XRD measurements 123

C Estimation of the amount of non-equilibrium charge carriers 124

Bibliography 139

Acknowledgments 140

Publications and contributions 142

Selbständigkeitserklärung 144

List of Tables

1.1 Overview of the experimental data on the emission of the nominally grown InN MLs found in literature. 2

2.1 Material constants of GaN and InN. 6

2.2 Main parameters set for the HRTEM ans STEM investigations. 23

2.3 Material parameters of InN and GaN collected from literature: length of the bonds, bond strength, experimental values of formation enthalpy. 36

3.1 Elastic parameters for InN and GaN used in the multislice simulations. 48

3.2 Parameters utilized for the XRD simulations of both SLs, the best fitting is marked with bold letters. 55

4.1 III-V ratios set for the growth of the QWs and the corresponding In-fluxes. 58

4.2 Growth flux of both temperature gradient superlattice structures shown in at/cm^{2}s and translated into ML/s. 64

4.3 Indium content derived from the linear interpolation between the results obtained from HRTEM and STEM analysis. 67

4.4 Growth times and the corresponding thicknesses of the QW_3-QW_8 deposited with indium and nitrogen fluxes. 68

5.1 Parameters of the SL peaks obtained from the cw-PL experiment. 89

5.2 Decay times of SLs with different barriers estimated for high ($10 \times P_{low}$) and low excitation conditions. 92

5.3 *Calculated electron and hole effective masses for different barriers thicknesses.* 97

C.1 Results the calculation of the non-equilibrium carrier populations for the two extreme conditions. 125

List of Figures

2.1 Wurtzite atomic structure of polar GaN. 6

2.2 (a) A principle scheme of the MBE setup. (b) Main transport processes occurring during the MBE growth: adsorption, desorption and diffusion of atoms. 8

2.3 Standard growth scheme of the nominal InN/GaN superlattice. 10

2.4 Bragg scattering shown in real and reciprocal space. 12

2.5 Main parts of the transmission electron microscopy setup. 13

2.6 CTF, chromatic and spatial aberration envelope functions, and final transfer function computed for an uncorrected TEM and for the imaging conditions used for our HRTEM experiments. 18

2.7 Simulations of the HRTEM images of a single monolayer (In,Ga)N/GaN quantum well in the <1-100> projection direction for the positive and small negative spherical aberrations. 20

2.8 Electron beam (light blue) passing through the STEM setup. 21

2.9 (a) Atomic planes used for our TEM analysis for the corresponding <1-100> and <11-20> projection directions. (b) A cross-section specimen glued on the titanium ring for the TEM investigations. 23

2.10 Scheme of the RHEED set up, the resulting RHEED pattern and top view of the GaN surface with two surface reconstructions. 25

2.11 (a) Standardized scheme of the XRD equipment representing the main parts of the set up. (b) Analysis of the lattice planes by scanning around the 0002 and 0006 lattice spots shown in the reciprocal space. 27

2.12 Band to band recombination of the charge carriers in semiconductor induced by the photon excitation. 29

2.13 (a) The main parts of the standard cathodoluminescence setup. (b) Simulation of the generation volume obtained in CL experiments for the standard SLs under discussion. . 32

2.14 (a) A principle scheme of the TRPL setup mounted in the Max Born Institute, Berlin, utilized for our experiments. (b) Color-coded image of the intensity distribution obtained on the CCD screen. 34

2.15 Schematic representation of the temperature-composition phase diagram of ternary (In,Ga)N alloy for: (a) relaxed and (b) strained layers. 37

2.16 Directions of the spontaneous polarization in GaN (a) and spontaneous and piezoelectric polarization in the (In,Ga)N ternary alloy (b). (c) Band bending and wave functions in conventional QW and ML thick quantum well. 39

3.1 Multislice simulations of the thickness series performed in the <1-100> and <11-20> projection directions. 45

3.2 Simulated supercells with InN monolayer thick quantum well in GaN shown in (a) [11-20] and (b) [1-100]. HRTEM-based strain analysis of the InN QW. 48

3.3 (a) C-lattice parameters as function of the In content in the monolayer and bilayer thick InGaN QW obtained from simulated supercells. (b) C-lattice parameter profiles obtained from the simulated supercells containing single ML InGaN QW under biaxial and uniaxial strain. 50

3.4 Strain analysis based on the HRTEM imaging for the experimentally grown standard (In,Ga)N ML. 51

3.5 Simulated STEM images along the <11-20> projection obtained for the InGaN quantum wells one and two monolayers thick. HAADF-STEM intensity ratio of 1 ML (In,Ga)N with 25% and InN to GaN depending on specimen thickness. 53

3.6 2ϑ-XRD scan around the (0002) reflection of the nominally InN/GaN SL structures grown at (a) 640 °C (a) and 600 °C (b) shown together with the XRD simulations. . . . 55

4.1 (a) Growth scheme of the superlattice with different III-V ratio. (b) Nominal structure of the sample. 58

4.2 (a) An original (unfiltered) overview STEM image of the III-V ratio structure. (b) STEM profile extracted from the image on the left. 59

4.3 High resolution HAADF-STEM images and their respective profiles from the individual layers grown under: (a) In-rich; (b) slightly N-rich; (c) In-poor conditions. 60

4.4 (a) Summation of 30 images taken under identical focus conditions. (b) Color-coded c-lattice parameter map derived as the measurement of the interatomic distances in (a). (c) Compositional profile of the experimental QW. 61

4.5 (a) Temperature gradient structure grown under 480-650 °C taken in <11-20> at specimen thickness approx 130 nm. (b) HAADF-STEM intensity profile of the SL extracted from (a). 63

4.6 AFM images of the (a) first temperature gradient structure grown in the 480-650 °C temperature range and (b) the second structure grown at 580-650 °C. 63

4.7 Growth scheme of the QW+barrier sequences deposited at varied temperatures shown together with the underlying buffer layers. 64

4.8 (a) Unprocessed HAADF-STEM image of the specimen area of the SL stack solely taken in <1-120> projection. (b) STEM-HAADF profile extracted from (a). 65

4.9 (a) Summation of 30 HRTEM images of the 610°C-grown QW taken under identical focus conditions in <1-100> projection. (b) C-lattice parameter map of the same QW proceeded from (a). (c) Experimental and simulated lattice parameters of the single (In,Ga)N ML. . . . 66

4.10 Growth scheme of the nominal InN QWs grown at (a) 4 and 8 s without N supply and (b) 4 - 60 s with both In and N fluxes. . . . 67

4.11 (a) STEM overview image of the gradient time superlattice taken in <11-20> projection. (b) HAADF-STEM profile extracted from (a). (c) High-resolution STEM image of the two QWs from the stack. . . . 68

4.12 (a) HRTEM image of the QW taken in <1-100> projection used for the compositional analysis. (b) C-lattice parameter map proceeded from (a). (c) Experimental c-lattice profile and simulated supercells with monolayer thick QWs and bilayer (In,Ga)N. . . . 69

4.13 HRTEM images of the 1 ML thick InGaN QW on GaN taken in <1-100> and <11-20> projections directions depicting a pronounced ordering of the indium and gallium atomic columns in <1-100>. . . . 71

4.14 In situ RHEED pattern after the deposition of GaN barrier and InN QW along the <1-100> and the <11-20> azimuths. . . . 72

4.15 RHEED patterns of the coherently grown (In,Ga)N ML extracted along the <1-100> azimuth at various temperatures during the annealing experiment. . . . 73

4.16 Appearance of the (√3×√ 3)R30○ surface reconstruction in different viewing projections. 73

4.17 Results of the RHEED pattern simulations performed for the (2√3×2√3)R30° and (√3×√3)R30° surface reconstructions. . . . 74

4.18 2 x 2 GaN surface reconstruction with nitrogen adatom observed after the barrier deposition. . . . 76

4.19 (a) The most energetically favorable (2√3×2√3)R30○ surface reconstruction for the InGaN shown in <0001>. (b) Relative increase of the chemical potential due to the implementation of each following In atom depending on indium content. . . . 77

4.20 Atomic geometry of the InGaN as a surface layer terminating the (0001) GaN barrier with 2×2 N adatom configuration with the (a)-(c) triply coordinated In atom and (d)-(h) four-fold coordinated indium. . . . 79

5.1 Excitation power dependencies measured for the 0.25-nm thick QW with 25 % In and 2 nm-thick QW with 17% In. . . . 85

5.2 (a) Samples structure, AFM images of the SLs with 50 MLs (b) and 6 MLs (c) for 1x1 $\mu m^2$and 2x2 μm^2area sizes. . . . 86

5.3 STEM images taken in <11-20> projection for the 50 MLs (a) and 6 MLs (b) structures.(c) High resolution STEM images of the samples with 50 MLs, 12 MLs and 6 MLs measured under higher magnifications. . . . 87

5.4 (a) Color coded c-lattice parameter map showing a single (In,Ga)N ML. (b) Laterally averaged c-lattice parameters and standard deviations for the measured sample. . . . 87

5.5 Spectra of the samples taken under 325-nm excitation. 88

5.6 (a) Above and below GaN band gap excitation PL of the samples with 50, 25, 12 and MLs barrier SL. (b) Emission spectra of the SL with 1.5 nm and 40 nm GaN-cap layers. 90

5.7 (a) TRPL transients measured under different excitation powers. (b) Power dependence of the initial decay for 6 MLs and 50 MLs barrier samples extracted in the 0-200 ps time window. 91

5.8 Spectral dependencies of the the SL with (a) 50 MLs (b) 6 MLs shown along with the regular PL spectra extracted from the same TRPL experiment. 92

5.9 Temperature dependencies of the SLs with 50 MLs (a) and 6 MLs (b). Peak positions extracted via the Gaussian fitting shown in (c) for the 50 MLs and (d) 6 MLs samples. (e) Temperature dependence of the FWHMs of the 50 MLs SL. 94

5.10 Comparison of the calculated and experimental transition energies for the samples with different barriers. 96

5.11 Partial charge densities of holes and electrons and their respective planar averaged profiles for (a) 1/1 (b) 1/5 and (c) 1/15 SLs. 98

5.12 Partial volume of the 80% of the electron and hole charge densities depending on the inverse barrier thickness. 99

5.13 Models explaining the spectral dependence of the decay time: involving carrier redistribution and the effect of extension the hole wavefunctions. 103

5.14 Experimental spectral dependencies and the ones calculated with different rate of non-radiative recombination. 105

5.15 CL spectral maps of the (a) thick (In,Ga)N film (b) (In,Ga)N ML with 25%. 109

5.16 STEM-CL maps of the time gradient sample under lower and higher magnification. Individual spectra extracted from different QWs. 111

5.17 STEM-CL intensity image of the temperature gradient sample. Local CL spectra from different parts of the structure. 112

5.18 Energetic distance between electron and hole ground states as a function of the lateral size of the (In,Ga)N ML for different contents. Top-view representative schemes of the ML coverage when the growth time is increased and growth temperature is lowered. . . 114

A.1 HRTEM images of the <11-20> projection direction obtained from the multislice image simulation for different thicknesses. 120

A.2 HRTEM images of the <1-100> projection direction obtained from the multislice image simulation for different thicknesses. 121

B.1 The 2ϑ experimental and simulated scans around the (a) (0002) and (b) (0006) GaN reflections. 123

1. Introduction and motivation

Light emitting diodes (LED) in the blue spectral range today are almost exclusively based on (In,Ga)N heterostructures grown on foreign substrates such as sapphire, silicon carbide or silicon. [1–4]. Despite an enormous amount of threading dislocations found in GaN heterostructures (for instance, $\sim 10^{10}$ cm^{-2} presented in [5]), these devices are characterized by a high thermal stability, long lifetime and impressive efficiency, e.g. external quantum efficiency (EQE)[1] up to ˜84% was reported [6, 7]. This is in strong contrast to classical III-V based light emitters, for instance, GaAs, were dislocation densities that are several orders in magnitude lower ($\sim 10^3$ cm^{-2} [8]) make the device ineffective. While the exact reason for the high efficiency of the (In,Ga)N structures despite high dislocation densities is still under debate, most researchers today agree that carrier localization in the alloy may explain this phenomenon. The success in realization of (In,Ga)N-based blue emitters encouraged researchers to push (In,Ga)N emission towards the green and red part of the spectrum, the ultimate goal being to substitute the common, but highly thermal sensitive [9], AlInGaP light sources used for red emission [3, 10, 11].

While the big difference in band gaps between InN ($\sim$ 0.7 eV [12]) and GaN (3.51 eV [13]) in principle provides the opportunity to tune the wavelength of $In_xGa_{1-x}N$ ternary alloys over a wide range from the ultraviolet (350 nm) to the infrared (1.8 µm) by growing structures with appropriate In mole fraction is challenging to cover the theoretically predicted band in practice. A so-called green gap problem of the (In,Ga)N-based LEDs, i.e. a severe decrease of the internal quantum efficiency (IQE) [2] from 95% at 400 nm to 45% at 550 nm emission wavelength [14], still cannot be solved. Several reason have been discussed to explain this experimental finding [15–17]. Polar (0001) (In,Ga)N QWs widely used as an active zone for LEDs suffer from strong polarization fields that are in part responsible for the low quantum efficiencies [18, 19]. Structural properties are expected to degrade with increasing In composition due to the low growth temperature required for incorporation of high amounts of In. Due to the high lattice mismatch ($\sim$11%) between InN and GaN plastic relaxation, i.e. a transition to three dimensional growth and strong alloy fluctuations were reported [14, 20] that at higher In contents may be followed by plastic relaxation, i.e formation of misfit dislocations [21]. In addition, a large miscibility gap for the growth of (In,Ga)N compounds at the growth temperatures [22] suggests phase separation of the constituents [23–25] instead of formation a homogeneous alloy.

To overcome the aforementioned obstacles, (In,Ga)N digital alloys with thicknesses as small as 1 monolayer (ML) can be employed. Digital alloying as an effective tool for band gap engineering that allows to adapt optical and electrical properties of the final structure. Previously, a periodical stacking of thin layers in the form of a superlattice structure have been extensively studied for arsenides, e.g. (In,Ga)As/GaAs heterostructures [26–28]. It was found that incorporation of $\sim$1ML InAs into the GaAs matrix considerably changes the properties of the host

[1]EQE of an LED is defined as the ratio of the emitted photons to the amount of electrons passing through the device.

[2]IQE of an LED is the ratio of all electron-hole radiative recombinations in the active region.

material, for instance, higher luminescence efficiencies [28] were reported.

Fabrication of such fine structures became possible with the development of the molecular beam epitaxy (MBE) that allows to control precisely composition and thickness of ternary (or quaternary) compounds at the atomic level. Although, several research groups are focusing on the improvement of the GaN and (In,Ga)N QWs, especially due to their technological importance [29–32], less effort has been spent on the investigation of (In,Ga)N/GaN digital alloys. After the first publication on realization of InN/GaN superlattices by Yoshikawa et al [33], this topic gained more attention in the III-nitride community. Indeed, ultra-thin (In,Ga)N alloys coherently grown on GaN are not suffering from dislocation formation [34, 35] and, at the same time, weaker polarization fields are expected [36]. Theoretical calculations have shown that variation of the periodicity of digital alloys should allow to change the band gap up to its transition to the metallic state [37] or to reach 99% overlap of electron-hole wavefunctions that should rise the radiative efficiency [38]. First-principle calculations of Miao et al. demonstrated that by variation of indium content in the coherent (In,Ga)N ML on GaN the available values of band gaps vary from 3.4 eV to 1.97 eV for pure InN monolayer [39]. This is higher in energy than the band gap of bulk InN (due to quantum confinement in the monolayer) but is still low enough to cover the red part of the spectrum. Despite such promising predictions by theory, the experimental data on the emission peak energies of the ML-thick (In,Ga)N alloys grown under different regimes were found only 300-500 meV below the band-to-band transition of GaN ([40–46]). In Table 1.1 we summarize the data on optical emission of the nominally InN MLs grown under different conditions published in literature.

Growth method	Growth conditions	Quantification method	In content	Emission	Reference
MBE	650 °C	XRD, non-quantitative TEM	100 %	2.99-3.10 eV	Yoshikawa et al. [33], Hwang et al. [44]
MBE	685 °C	non-quantitative TEM	100 %	3.26 eV	Dimakis et al. [42]
MOVPE	730 °C	XRD	100 %	3.14-3.18 eV	Lin et al. [47]
MBE	685 °C, In-rich	non-quantitative STEM	100 %	3.15-3.29 eV	Zhou et al. [41]
MBE	700 °C, In-rich	non-quantitative TEM	100 %	3.10 eV	Pan et al. [45]
MBE	680 °C	none	100%	3.30-3.35 eV	Li et al. [43]
MBE	550 °C, slightly In-rich	quantitative HRTEM	$\sim$ 33%	3.25 eV	Suski et al. [48]

Table 1.1.: Overview of the experimental data on the emission of the nominally grown InN MLs shown with the corresponding quantification methods used for the estimation of In concentration found in literature. NA denotes that the growth regime (Me or N-rich) was not specified.

As can be seen, the emission peaks from the 1 ML-thick QWs have the energies in range $\sim$ 3.0-3.3 eV that corresponds to the indium content of 20-30% in the alloy according to the theoretical estimation [39]. Several explanations have been proposed for such a discrepancy,

e.g.: (i) recombination of the carriers (either holes or electrons) from the QW taking place in the GaN band gap region [39]; (ii) emission of the GaN excitons placed in the QW region [44, 46, 49]; (iii) strong confinement of the energy states high in the QW [42, 45]; (iv) formation of the ternary alloys, e.g. intermixing of In with Ga in the ML [46, 48]. Although, most of the authors state that 100% of indium in the MLs was achieved, the precision of various methods used for structural characterization in these works is rather questionable. The first quantitative analysis of the ML-thick alloys was presented in the work of Suski et al. [48] that suggested indium content around 33%. To solve these discrepancies in literature, in the current work we will (i) compare the various methods used to measure In concentration in ultra-thin (In,Ga)N layers, (ii) analyze the indium incorporation in the polar ultra-thin (In,Ga)N QWs pseudomorphically grown on GaN and (iii) study basic optical properties of digital alloys based on these structural data.

Outline of the thesis

In the next section we give an overview of the (In,Ga)N properties, growth and characterization techniques. Starting from the brief introduction on basic structural properties of III-nitrides in 2.1, we continue by describing our main experimental tools used in the work. We start with MBE employed for the deposition of digital alloys (2.2). Our structural characterization methods, i.e. TEM, HRTEM and STEM are described in more details in 2.3, as well as reflection high-energy electron diffraction (RHEED), X-ray diffraction (XRD) and atomic force microscopy (AFM). Since, this work aims to present a complete study of digital (In,Ga)N alloys, in 2.4 we summarize the background knowledge on recombination in semiconductors, and present cathodoluminescence (CL) and photoluminescence (PL) measuring techniques for optical investigations. To link directly optical emission and composition, we applied a dedicated STEM-CL system introduced in 2.3.1.7. Further, in 2.5 we discuss the particularities related to (In,Ga)N, such as challenges found during the growth by MBE, as well as some optical issues, i.e. piezoelectric polarization fields and localization phenomena. Theoretical calculations provided for this work were done by density functional theory (DFT) and continuum k*p method (2.6.1, 2.6.2).

In 3 we systematically study the In concentration in the monolayers by HRTEM, STEM and XRD. By comparing these techniques we show that strain analysis based on an aberration corrected HRTEM imaging yields the most reliable data on Indium composition and the highest accuracy of all the employed methods (3.3). While absolute quantification by STEM is hampered by the strong effects of electron channeling that makes the measured composition highly dependent on the sample thickness 3.4. XRD quantification method falls short because of the comparatively low In content in the alloy, ambiguities in the thickness of the thin wells and possible compositional gradients in the barriers 3.5.

Our experimental HRTEM compositional analysis of the standard (In,Ga)N ML coherently grown on GaN reveals an In composition of 25% (see in 3.3.1), which however, corresponds to the optical emission obtained for these structures. In 4.2 we investigate if this low In concentration in (In,Ga)N ultra-thin QWs is a fundamental limit for In incorporation into coherently strained layers on GaN or merely due to inappropriate growth conditions. In series of systematic growth experiments we varied ratio between the In and N flux, temperature and deposition time.Our HRTEM analyses of these series clearly evidences that the found content of 25% is a fundamental limit and that at such composition the alloy is ordered with a specific $(2\sqrt{3}\times2\sqrt{3})R30^{\circ}$ surface reconstruction. Combining these results and DFT calculations, we discuss in 4.4 a model for indium incorporation in the layers grown coherently on GaN(0001) that successfully explains the observed compositional limit.

The second experimental part is dedicated to the study of optical properties of the the short period superlattices. We discuss both, vertical and lateral confinement of the ML-thick alloys. The former is investigated based on a series of samples with GaN barriers changing from 50 to 6 MLs (5.3). Our PL, time-resolved PL and results from the DFT calculations enable us to identify the hole confinement as a decisive factor influencing optical recombination in (In,Ga)N alloys of

any thickness. We find that holes are strongly localized and their degree of confinement can be strongly reduced by changing the SL periodicity, whereas electrons always behave like quasi-free particles. The delocalization of holes substantially changes optical phenomena typically observed for standard (In,Ga)N QWs, i.e. temperature dependence of the peak emission and spectral dependence of the decay time. In the last paragraph 5.4.2 by means of STEM-CL experiments we show that lateral confinement in the (In,Ga)N MLs can be also effectively manipulated by employing the proper growth conditions.

2. Theoretical background and methods

2.1. Basic structural properties of the hexagonal (In,Ga)N compound

Group III-nitrides crystallize at ambient pressure in two different phases, wurtzite and zincblende, where the wurtzite phase is the thermodynamical stable one. In this work we study wurtzite (In,Ga)N alloys. Wurtzites belong to the hexagonal crystal family and the P63mc space group. Each metal (Me) atom (In or Ga) is bonded to four nitrogen atoms. As a result, a tetrahedron formed by four equivalent orbitals (see red area in Fig. 2.1) corresponds to the sp^3 hybridization.

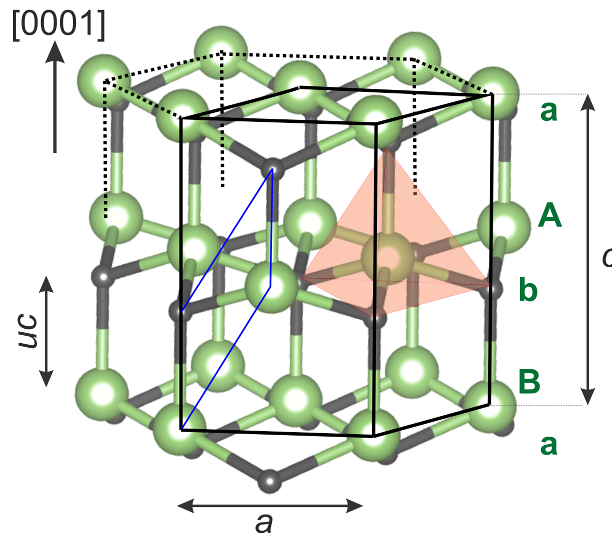

Fig. 2.1: Wurtzite atomic structure of polar GaN, for InN it would be the same but with larger lattice parameters listed in Table 2.1. Large green balls denote Ga atoms and small gray - N. Thin blue rhombus depicts the primitive hexagonal unit cell.

Material	*a*, Å	*c*, Å	*c/a*	*u*
GaN	3.190	5.189	1.627	0.377
InN	3.540	5.706	1.612	0.380

Table 2.1.: Material constants of GaN and InN taken from [50].

The wurtzite unit cell is formed of the vectors a_1 and a_2 in the basal plane, where $|\overline{a_1}| = |\overline{a_2}|$, $a_1 \wedge a_2 = 120°$, and the c vector that is orthogonal to the former ones. In the ideal wurtzite structure $c/a = \sqrt{8/3} = 1.633$ and the internal lattice parameter: $u = 3/8 = 0.375$. The internal

parameter defines the nearest neighbor distance given by *uc*. The stacking sequence of wurtzite sublattices are marked as ...AaBbAaBb... , where each sublattice formed by a Me-N pair is is shifted towards each other by $< \frac{1}{3}, \frac{1}{3}, \frac{1}{2} >$. The primitive hexagonal unit cell contains 4 atoms - two cations and two anions placed on the atomic positions: $(0,0,0)$ and $(\frac{2}{3}, \frac{1}{3}, \frac{1}{2})$ for nitrogen, $(0,0,\frac{3}{8})$ and $(\frac{2}{3}, \frac{1}{3}, \frac{7}{8})$ for Me atoms [51]. In real crystals, c/a and u/c differ from these ideal values and depend on the peculiarities of the bonding (see Table 2.1). In the wurtzite lattice the bonding is asymmetric, i.e.the length of the bond oriented in the [0001] direction is higher than the other ones. Therefore the center of the electron charge is displaced along the [0001] direction, which gives rise to spontaneous polarization (see 2.5.2.1). The c-axis is a polar axis, i.e. directions that correspond to the Me-N bonds (nitrogen atom on top of metal), i.e. [0001], and N-Me, i.e. $[000\bar{1}]$, are not equivalent. In this work we are focusing only on metal polar structures, i.e. structures grown along the [0001] direction.

According to Table 2.1, the lattice parameters of GaN and InN exhibit a considerably high lattice mismatch of 11% along *a* and of 10 % along the *c*-axis. The lattice parameters of the $In_xGa_{1-x}N$ compound follow to a good approximation a linear dependence according to Vegard's law [52]:

$$a_{(In,Ga)N}(x) = a_{InN}(x)x + a_{GaN}(x)(1-x), \; c_{(In,Ga)N}(x) = c_{InN}(x)x + c_{GaN}(x)(1-x) \qquad (2.1)$$

where a_{GaN}, a_{InN} and c_{GaN} and Cc_{InN} are the *a* and *c* equilibrium lattice constants of GaN and InN respectively, *x* is the In content of the alloy and $a_{(In,Ga)N}$ and $c_{(In,Ga)N}$ are the equilibrium lattice constants of the (In,Ga)N alloy with an In content *x*. Experimental data found literature reveal the validity of the Vegard's law for (In,Ga)N alloys and epilayers (see for instance, [6, 53, 54]).

2.2. Growth by molecular beam epitaxy

2.2.1. Growth technique

Molecular beam epitaxy (MBE) is the deposition method of a crystalline layer on a substrate from molecular beams under ultra high vacuum conditions ($\sim 10^{-9}$ Torr).

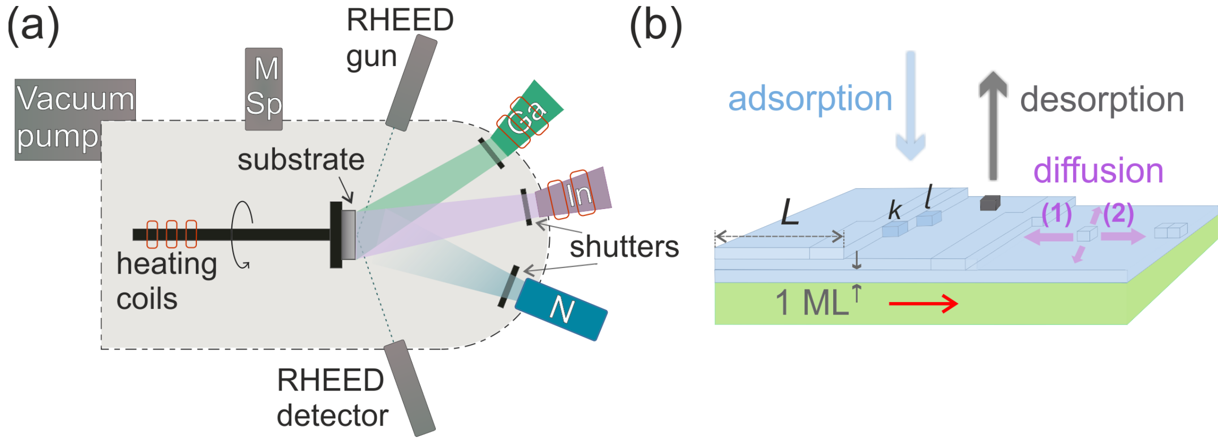

Fig. 2.2: (a) A principle scheme of the MBE setup. "M Sp" denotes a mass spectrometer and red squares - heating coils of the effusion cells. (b) Main transport processes occurring during the MBE growth are: adsorption, desorption (dark gray atom) and diffusion of atoms that may lead to the (1) 1D step flow and (2) 2D island growth. Small squares represent the atomic species, i.e. "k" kink atom and "l"ledge atom, green area denotes substrate and blue - the first successfully deposited monolayer. L is a terrace width for the given miscut. Red arrow indicates the direction of step flow growth.

Molecular or atomic beams are formed by evaporation of solid or liquid (e.g. Al, Ga, In..) source materials from an effusion cell by heating (see in Fig. 2.2(a)). An effusion cell is a crucible with a hole of a diameter much smaller than the mean free path of the evaporated molecules to prevent collision of the species when leaving the crucible. The flux is controlled by opening or closing of a shutter. The substrate is mounted on a stage that can be rotated to improve the uniformity in thickness and composition of the growing layer. At ultra high vacuum the mean free path of the particles is much larger than the dimensions of the growth chamber. The incoming molecules impinge, diffuse and interact on the heated substrate surface. The growth rate in MBE is controlled by the source parameters, i.e. the incoming flux pressure as controlled by temperature of the cells, and also by the temperature of the substrate. In a closed system an equilibrium between the solid and gas phases builds up given by the dependence of the vapor pressure on temperature, T, via:

$$p_{eq}(T) \sim \exp(-\frac{\triangle H}{k_B T}) \tag{2.2}$$

where ΔH - is the evaporation enthalpy, k_B- is the Boltzmann constant. Under equilibrium conditions, the number of molecules that are evaporated from the crucible into the gas phase and that leave the gas phase and are deposited on the heated substrate is equal [55]. In a Knudsen effusion cell a thermodynamic equilibrium of the precursor with the gas phase is obtained with an evaporate pressure p_{eq}.

The sticking coefficient of an atom reaching the substrate surface is defined as the ratio between the adsorbed species to the impinging ones. The Hertz–Knudsen equation describes the sticking of gas molecules, i.e. particles with mass m, on a surface as:

$$F_e = \frac{p_{eq}}{\sqrt{2\pi m k_B T}} \tag{2.3}$$

Once the atom arrives to the surface it may:

1. be *physically adsorbed*, i.e. bonded through weak van der Waals forces or chemically via

an electron exchange bonded to the surface;

2. *migrate* on the surface with a *diffusion length* $\lambda = \sqrt{D\tau}$,where D - is a diffusion coefficient and τ is the residence time [56];

3. *incorporate* into the crystal lattice of the substrate, here atoms can stick to a kink site of a surface step, i.e. follow the step flow growth, or form 2D nucleations on the surface;

4. *desorb* thermally leaving the substrate surface, i.e. via *re-evaporation* into the gas phase.

The actual growth of the crystallographically oriented material occurs when impinging atoms directly arrive or diffuse at the epitaxial sites and are chemically absorbed there.

The growth kinetics is governed by the surface diffusion constant, by adatom incorporation into the surface and by the molecular dissociation rate. The surface diffusion length is the distance which an impinging atom travels before it incorporates into an atomic kink site or forms a stable nucleus with another atoms at the surface. It is given by the diffusion coefficient of the adatom on the free surface and the density of adatoms on the surface, which is controlled by the incoming flux of atoms and the desorption rate.

The growth rate in MBE depends on the deposited material and growth conditions but is at maximum around 1 μm/h, or 1 ML/s. During the deposition, the growth surface and growth rate can be monitored *in situ* by reflection high-energy electron diffraction (RHEED) (see more in (2.3.2)). A mass spectrometer installed in the chamber as shown in Fig. 2.2(a) measures the desorbed species and thus permits a detailed analysis of the growth kinetics. to perform the residual gas analysis.

For a more detailed description we refer the reader to text books, e.g [57–59].

2.2.2. Growth regimes

In epitaxial growth three main growth modes are distinguished. If the layer growth is two-dimensional, monolayer by monolayer, this is called *Frank-van der Merwe* type of growth. Here, the free energy of the system[1] is reduced after a closed monolayer has formed, i.e. $\Delta\varphi \leq 0$. Frank-van-der-Merwe growth may proceed either by nucleation and lateral growth of stable 2D nuclei until the layer is closed or by attachment of adatoms to atomic ledges or atomic kinks at surface atomic steps (see l and k atom in Fig. 2.2 (b), correspondingly). The latter atoms are more stable due to the lower amount of dangling bonds involved in the monolayer formation, this type of growth is also called *step flow*. This process is facilitated by the presence of surface steps induced by a well-defined miscut angle of the substrate. If the surface diffusion length is smaller than the terrace width (L in Fig. 2.2(b)) adatoms may form two dimensional islands (2D growth) at the terraces. If the surface diffusion length is larger the step distance, monolayer steps may interact and form steps that are several monolayer high (step bunching) and, thus, destabilize the growth surface. Therefore, it is important to adjust the miscut angle, the flux of the incoming atoms and the substrate temperature appropriately to achieve step-flow growth. In some cases step-up and step-down diffusion is asymmetric, which may cause step bunching or meandering giving a potential energy barrier, i.e. *Ehrlich-Schwöbel barrier.*

In case of heteroepitaxial growth the difference in surface energy between layer and substrate and the strain induced by the lattice mismatch may cause formation of 3D islands. If the surface

[1] By free energy of the system we assume the difference between the layer (φ^{layer}) and substrate (φ^{subs}) free surface energies and the energy of the layer-substrate interface (φ^{int}): $\Delta\varphi = \varphi^{layer} + \varphi^{subs} - \varphi^{int}$ [60].

energy of the substrate is lower than that of the deposited layer 3D islands form, which is called *Volmer-Weber* regime. Here, the system has no gain in free energy, but increases with the formation of the closed layer, i.e. $\Delta\varphi \geq 0$. In case the surface energy of the layer is lower than that of the substrate a thin wetting layer forms and growth after a critical thickness undergoes a transition to 3D growth (Stranski-Krastanov growth) to relax strain elastically. Which of these growth modes takes place depends on a subtle balance of surface energy and strain. More on the growth regimes can be found in the pioneering works by Stranski and Krastanov [61], Bauer [60][2] and textbooks dedicated to the epitaxial growth, e.g. [58, 59].

2.2.3. Growth scheme of the experimental structures

The samples discussed in this work were grown by C. Cheze in the group of Dr. R. Calarco at the Paul Drude Insitute (PDI), Berlin, and by P. Wolny, M. Siekacz and M. Sawicka in the group of Dr. C. Skierbiszewski at the Institute of High Pressure Physics (Unipress), Warsaw. The samples from PDI were grown in a DCA P600 plasma-assisted MBE system. Solid Ga- and In effusion cells and a radio frequency plasma source (SVT Associates and Addon) for the supply of active nitrogen were employed. The growth control was performed *in situ* via quadrupole mass spectroscopy and RHEED that enabled to monitor the balance between desorbed and incorporated Ga and In species and the formation of surface adlayers, respectively. The temperature of the substrate was measured by a pyrometer. Samples grown in the Institute of High Pressure Physics were realized in a Gen20A reactor or a Riber-VG90 system with a RFX600 plasma source. The backside of the substrates were coated with molybdenum to improve the substrate heating. The substrate temperature is monitored by a thermocouple. The values of Ga and N fluxes were calibrated by *in situ* laser reflectometry and the growth rate by measuring the desorption time after the growth of GaN or (In,Ga)N compound.

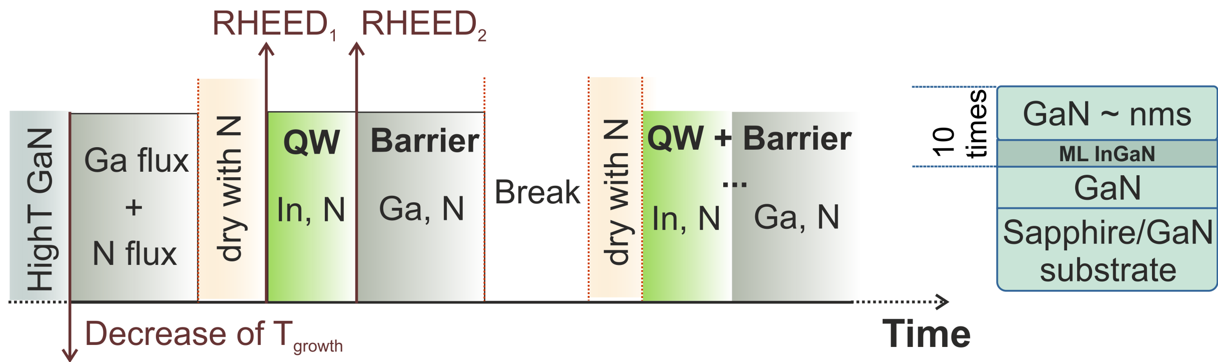

Fig. 2.3: Standard growth scheme of the nominal InN/GaN superlattice. “HighT” GaN denotes the growth step of the GaN buffer layer deposited at 800 °C. $RHEED_1$ and $RHEED_2$ mark the time periods when the RHEED data were obtained and shown later in 4.3.2.

All structures discussed in this work were grown either on commercial Me-polar (0001) GaN/AlN/Al_2O_3templates from Kyma technologies, Raleigh, USA or on bulk GaN from Saint Gobain-Lumilog, Valbonne, France grown by hydride vapor phase epitaxy with a dislocation density of approximately 2×10^7cm^{-2}. In the case of templates grown on sapphire, the dislocation density lies in the range of $\sim 10^8$-10^9cm^{-2} [62]. The substrates had a miscut towards [1-100] direction to obtain parallel atomic steps [63] with miscut angles not exceeding 1°.

[2] *published in German

A thick, ∼100 nm, GaN buffer is deposited at approximately 800 °C on these templates. In the next step a nominal InN/GaN superlattice is grown consisting of 1 monolayer InN and a GaN barrier of N monolayers (1<N<50). For the superlattice deposition the growth temperature is decreased to values suitable for (In,Ga)N growth, i.e. $550 < T_{growth} < 650$ °C (see Fig. 2.3). GaN barriers are grown at the same temperature as the nominal InN monolayer but under slightly Me-rich conditions to prevent dissociation of that layer. After growth of the GaN barrier the gallium flux was switched off and the nitrogen flux was kept to remove residual metallic species from the surface, i.e. to "dry the surface". Then, the InN monolayer is deposited by switching the indium flux on without Ga exposure. To improve the indium incorporation usually nitrogen-rich conditions are utilized (see Refs. [63, 64] and explanation in the following). After deposition of "InN", the structure is immediately overgrown with the GaN barrier, similar as done by Yoshikawa et al. [65], to avoid desorption of nitrogen. Again a Ga-rich regime is chosen to obtain sharp QW/barrier interfaces and suppress the incorporation of residual In into the barrier [66]. The indium excess is desorbed during growth interruption followed by the next "drying" step with nitrogen. Then, the QW+GaN barrier sequence was repeated as much periods as intended. The deposition of each period was adopted to the respective growth rate and III/V ratio discussed in details further.

Previously, it was disputed if indium predisposition is necessary to prevent the fast desorption of the indium species from the surface at relatively high growth temperatures used for InN (typically ∼ 450 °C [67]). However, it was found that this procedure did not lead to an increase of the indium content and as presented in the work of Cheze et al. was measured below 10% [66].

2.3. Methods of structural investigation

2.3.1. Transmission electron microscopy

2.3.1.1. Scattering of the electron beam

According to the *de Broglie's* equation, the wavelength of electrons accelerated by a voltage V is given by:

$$\lambda = \frac{h}{\sqrt{2meV}} = \frac{h}{\sqrt{2m_0eV\left(1+\frac{eV}{2m_0c^2}\right)}} \tag{2.4}$$

taking into account the relativistic correction, where h is the Planck constant, m is the electron rest mass, e is the elementary charge of the electron and c is the speed of light.

The electron interacts with matter causing elastic and inelastic scattering. Elastic scattering may be coherent or incoherent. Coherent elastic scattering is used to resolve the atomic structure in case of phase contrast imaging; incoherent elastic scattering is used to resolve the atomic structure in scanning transmission electron microscopy, bypassing phase relations between neighboring atomic columns [68]. In case of inelastic scattering, electrons loose their energy by excitation the electronic transitions, e.g. inner shell transitions or transitions from the valence to the conduction band. This can be measured from the specific loss in energies of the transmitted electrons (electron energy loss spectroscopy (EELS)), or by the detection of X-rays (energy dispersive X-ray spectroscopy) or light (cathodoluminescence, see more in (2.4.2))

using appropriate detectors.

When the incident plane electron wave passes through the periodic potential of a crystalline solid, the atoms can be considered as a source of spherical waves that superimpose according to Huygens principle (see Fig. 2.4 (a)). The diffracted spherical waves are in phase if the path length between them is an integer number of the wavelength, λ. In the latter case the resulting signal is reinforced in the far field. This condition is well known as Bragg´s law :

$$2d_{hkl}sin\theta_B = n\lambda \quad (2.5)$$

where d_{hkl} is the spacing between the diffracting lattice planes and the angle ϑ, the Bragg angle.

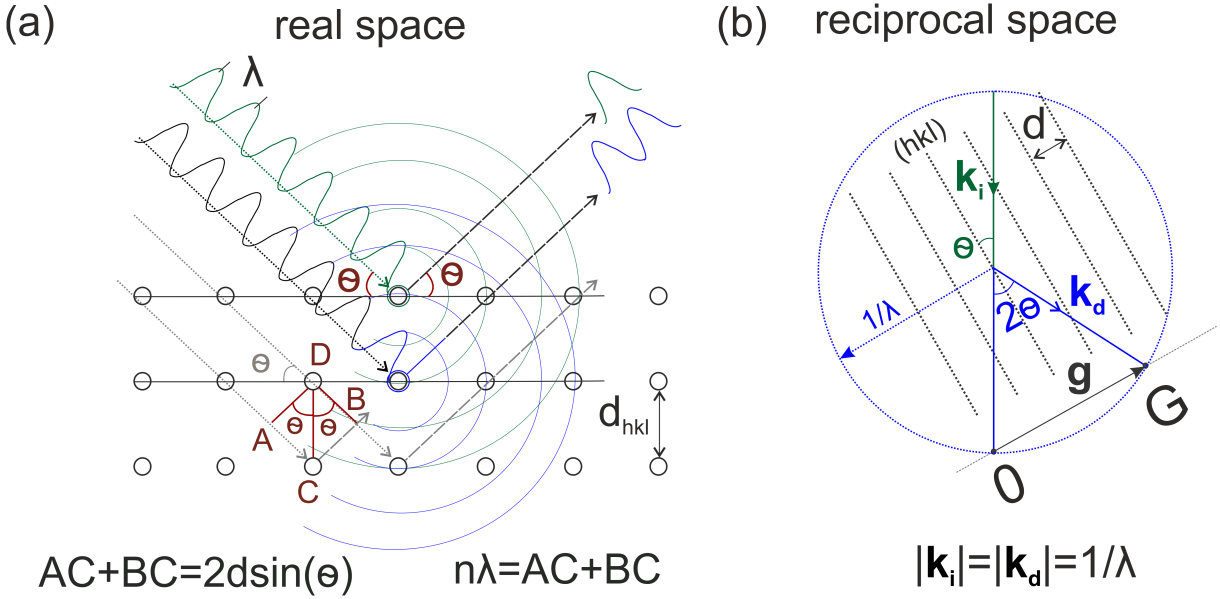

Fig. 2.4: (a) Bragg scattering shown in real space. Small black circles represent the arrangement of atoms in the lattice planes in some crystal. Green and black waves are the incident beams and large circles - the scattered wavefront. In red we depict geometry of the path-length difference between two waves. (b) Bragg's law shown in reciprocal space. O is an origin of the incident vector and G - is the first diffraction spot. Each of the reciprocal points G correspond to the particular hkl planes in real space. Blue dotted circle belongs to the Ewald sphere shown in 2D.

The diffraction condition for constructive interference in the reciprocal space is represented by the relation between the incident and diffracted wave vectors:

$$\bar{k}_d - \bar{k}_i = \bar{g} \quad (2.6)$$

This is the Laue diffraction condition which can be written in real space via the Miller indices (i.e. integer numbers):

$$(\bar{k}_d - \bar{k}_i) \cdot \bar{a} = h; (\bar{k}_d - \bar{k}_i) \cdot \bar{b} = k; (\bar{k}_d - \bar{k}_i) \cdot \bar{c} = l \quad (2.7)$$

All the scattered vectors that belong to the surface of the sphere of constant energy, i.e. the Ewald sphere constructed with the radius *1/λ* from the origin *O* (see Fig. 2.4 (b)), automatically fulfill the diffraction condition. When the sphere intersects both - the origin and the reciprocal lattice spot, G, separated by the reciprocal vector *g* diffraction occurs. For the resulting vector

we have: $\overline{g} \perp (hkl)$ and $|\overline{g}| = \frac{1}{d_{hkl}}$. Thus, the diffraction pattern with the ... -2G, -G, O, G, 2G ... spots would be observed only at particular angles ϑ related to the lattice planes distances.

2.3.1.2. Main principle and set up

A transmission electron microscope essentially consists of (i) an electron source, (ii) a condenser that shapes the beam (iii) an objective lens and (iv) a projection system. In our FEI Titan 80-300 microscope a field emission source is used as an electron source, the emitted electrons are accelerated by high voltage (300 kV for our experiments) and the beam is controlled by the deflection coils (labeled as DC in Fig. 2.5). The corresponding electron wavelength is 1.97 pm (Eq. 2.4).

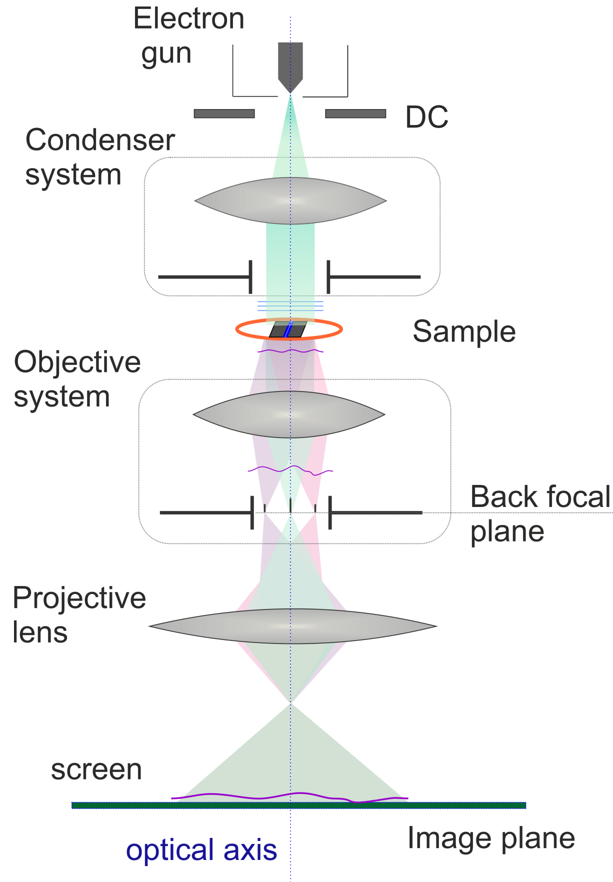

Fig. 2.5: Main parts of the transmission electron microscopy setup. The incident electron plane wave is depicted by the blue parallel lines that are transformed into the exit object wave (purple curve) that is modulated by the object lens and magnified at the image plane.

The electrons pass through the condenser consisting in our case of three electromagnetic lenses forming the spot, i.e. the spot size, brightness and convergence of the beam controlled by a condenser aperture. The formed parallel beam can be described by the wavefunction of the plane wave in one direction (z-axis):

$$\psi_i = A_0 \exp[2\pi i(\overline{k}_i \cdot \overline{r})] \tag{2.8}$$

Here, $A_0$is the amplitude, the wave vector k_i captures the direction with the modulus *1/λ*. After interaction with the atomic potential of the sample the electron wave can be presented in

the form of spherical symmetric wave that for a single scattering event is:

$$\psi_d = \frac{\psi_i f(\theta)}{|\bar{r}-\bar{r}_1|}\exp[2\pi i(\bar{k}_d \cdot (\bar{r}-\bar{r}_1)] \tag{2.9}$$

The vector r_1 is measured from the atomic nucleus, and k_d fulfills the diffraction condition Eq. 2.6; $f(\vartheta)$ is *the atomic form factor*. It is strongly angular dependent and represents the scattering strength. The resulting scattering wave on the array of atoms, n, exciting the specimen thickness is a sum of the single scattering events:

$$\psi_{ex}(\bar{r}) = \psi_i(\bar{r}) + \sum_n \frac{\psi_{i_n} f_n(\theta)}{|\bar{r}-\bar{r}_n|}\exp[2\pi i(\bar{k}_{d_n} \cdot (\bar{r}-\bar{r}_n) + \varphi_n] \tag{2.10}$$

where ψ_i- is the transmitted beam through the sample and $\varphi_n$is a phase shift. Eq. 2.10 follows a kinematic approach, i. e. we consider only single scattering per atom and it is purely elastic. These scattered wavelets interfere with each other and pass through the electromagnetic objective lens and an objective aperture. Following Bragg's law Eq. (2.6) the diffraction pattern (containing no phase information) is formed in the back focal plane of the objective system. Here the diffracted waves that contribute to the image formation can be selected by an appropriate objective aperture. The intensity of the diffraction spot is derived as:

$$I_d = |\psi|^2 = (\frac{\pi h}{2\xi})^2,\ \xi = \frac{\pi V_c \cos\theta_B}{\lambda f(\theta)} \tag{2.11}$$

where h is thickness of the specimen. Eq. 2.11 describes an ideal completion of the diffraction condition Eq. 2.6, i.e. the intensity of the diffraction spot is given only by the reciprocal spots crossing the Ewald sphere. The extinction length parameter, ξ, is derived via the structure factor, $f(\vartheta)$, and volume of the unit cell V_c. It is a material constant for the given Bragg angle and excitation voltage, i.e. wavelength of the beam. The extinction length is inverse proportional to the atomic weight [69]. Physically, it describes the attenuation of the electron wavefunction by *1/e* inside the crystal with depth - similar to optical absorption.

In general, the residual intensity from the reciprocal spots not perfectly lying on the intersection with the Ewald sphere can be taken into account. A shift from the equilibrium positions on the sphere is given by the deviation parameter, s:

$$I_d(\bar{s},h) = |\psi|^2 = (\frac{\pi}{\xi})^2 \frac{\sin^2(\pi h|\bar{s}|)}{(\pi|\bar{s}|)^2} \tag{2.12}$$

The dynamic approach assumes multiple scattering of the electron wave passing through the periodic potential of the crystal. Description of the wavefunctions in this case is more complex, i.e. introducing the transmitted and diffracted beams as coupled. Here, the amplitude of the beam is modulated and attenuated by the absorption during their travel through the specimen which affects the Bragg condition [70]. Interaction between the transmitted and diffracted beams that interfere with each other can be described via the so-called Pendellösung oscillations depending on the specimen thickness. These two beams would obtain a phase shift of 180° that implies their wave amplitudes to oscillate between the transmitted and diffracted beams depending on the traveled thickness of the crystal [71]. For the thicknesses defined via: $h = (n+\frac{1}{2})\xi$ - the intensity is maximum for the scattered beams only; maximum intensity of the forward propagated beam is obtained at: $h = n\xi$ [69]. The extinction distance defines the period of this oscillations, that is, however, not constant but reduces with thickness due to the complex

multiple interactions of the scattered beams.

The wavelets at the exit of the sample are collected in the back focal plane of the objective lens. Their amplitude and phase are then modulated by the imaging system, i.e the objective lens of the microscope:

$$\psi'_{ex}(q) = \Psi(\bar{r}) \cdot T(q) \tag{2.13}$$

Ψ(r) is a Fourier transform of the $\psi_{ex}(r)$ that contains the full information on the atomic potential of the specimen. The spatial frequency, q, is the reciprocal parameter depended on the scattering angle: $q = \theta/\lambda$. *T(q)* describes the modulation of the exit wave by the electromagnetic lens, the contrast transfer function (CTF) and is given by:

$$T(q) = A(q) \cdot B(q) \cdot E(q) \tag{2.14}$$

where:

- *A(q)* - is the aperture function of the objective lens that blocks the spatial frequencies higher than some specific value of q_{ap}given by the aperture radius;
- *B(q)* - is the aberration function defined by two factors - the defocus (Δf) of the objective lens and its spherical aberration (Cs):

$$B(q) = \exp(i\chi(q)) = \pi\Delta f\lambda q^2 + \frac{1}{2}\pi C_s\lambda^3 q^4 \tag{2.15}$$

From Eq. 2.10 one can see that the electron wavefunction undergoes a phase shift when passing through the objective lens that depends on the diffraction angle (spatial frequency), defocus and spherical aberration (in the maximum range from -π to +π). The defocus shifts the crossover of the beams along the optical axis and can be controlled by changing the excitation of the magnetic lens. The spherical aberration directly affects the resolution since beams that are transmitted far from the optical axis are transmitted at larger angles (for a positive spherical aberration) moving the focus along the optical axis and, thus, spreading out the point-like object.

- *E(q)* - the envelope function that describes the attenuation of the electron wave due to the limited spatial and temporal coherence of the source and the chromatic aberration. Higher spatial frequencies may be attenuated, i.e. it acts like an additional virtual aperture cutting off higher spatial frequencies. This particular function sets the information limit - the spatial frequency at which the contrast is reduced to the value of $1/e^2$ - and is described by:

$$E(q) = E_t(q) \cdot E_s(q) \cdot E_d(q) \cdot E_v(q) \cdot E_D(q) \tag{2.16}$$

Here, $E_t(q)$ is the envelope function that represents the temporal coherence, $E_s(q)$ - the spatial coherence of the source, $E_d(q)$ and $E_v(q)$ - the specimen drift and vibration, $E_D(q)$ - the signal-to-noise ratio of the detection system. These envelope functions set the information limit of the microscope. Even if we have ideal conditions, i.e. no sample move and a highly coherent parallel beam, the information limit still depends on the detector and the temporal coherence of the source:

$$E_t(q) = \exp\left(-\frac{1}{2}(\pi\lambda C_c)^2 q^4 \left[4(\frac{\Delta I_{obj}}{I_{obj}})^2 + (\frac{\Delta E}{V_{acc}})^2 + (\frac{\Delta V_{acc}}{V_{acc}})^2\right]\right) \tag{2.17}$$

This function represents the instability of the objective lens current (ΔI_{obj}), voltage supply of the source (ΔV) and the energy spread of the electron source (ΔE). The latter is reduced for field emission sources when compared to thermionic sources. In general, the contrast transfer function (CTF) tends to give a linear relation between the initial and resulting signals, since the electron wave function arriving to the image plane is not preserved.

Then, the beam passes through the projection system that consists of intermediate (controlling the projection of the diffraction and imaging regimes) and projection lenses forming the final image in the image plane. Mathematically this can be expressed by the inverse Fourier transformation:

$$\psi_{image}(x,y) = F^{-1}(\Psi(\bar{r}) \cdot T(q)) \tag{2.18}$$

The final signal is recorded by the charge coupled device (CCD) camera and intensity is measured:

$$I(x,y) = \left|\psi_{image}(x,y)\right|^2 \tag{2.19}$$

2.3.1.3. Phase contrast. High resolution transmission electron microscopy

We have shown that the exit wavefunction of the specimen contains information about both - of the amplitude and phase, where the latter one is missing for the case of the diffraction imaging. A general form of the object exit wave function (that is basically the Eq. 2.10 in real space) can be written as:

$$f(x,y) = A(x,y)\exp(-i\varphi_h(x,y)) \tag{2.20}$$

Assuming $A(x,y) = 1$, all information about the specimen is contained in the phase shift of the electron wave $\Delta\varphi_h$. For thin samples it only slightly changes going through the specimen with thickness h. If the projected potential of the atomic lattice is expressed, then, as:

$$U_h(x,y) = \int^{h} U(x,y,z)dz \tag{2.21}$$

the phase change is given by the interaction constant, σ, and $U_h(x,y)$ according to:

$$\Delta\varphi_h = \sigma U_h(x,y) \tag{2.22}$$

For an extremely thin specimen (~ 5-10 nm) utilized for High-Resolution TEM, $U(x,y) << 1$, so Eq. 2.20 can be transformed into:

$$f(x,y) = 1 - i\sigma U_h(x,y) \tag{2.23}$$

Eq. 2.23 represents the weak phase object approximation (WPOA) that assumes the transmitted wave function to be linearly proportional to the potential of the specimen in the projection direction. The highest signal is expected at the atomic nucleus, where $U(x,y)$ is maximum. The limit for this approach is given by the extinction distance, ξ, introduced above (see Eq. 2.11). The thickness of the investigated specimen should be at least half of the extinction distance [72]. All the structural information about the specimens is contained in the phase. However, for an

ideal lens no contrast is expected keeping in mind the 2.19, i.e. the final intensity is just a modulus of the exit wavefunction. In a non-corrected microscope we, nevertheless, obtain phase contrast images due to the fact that the spherical aberration of the objective lens induces a phase shift dependent on the diffraction angle. The information on the deviation of the phase is stored in the transfer function, *T(q)*, that for the WPOA is:

$$T(q) = A(q) \cdot E(q) \cdot 2\sin(\chi(q)) \tag{2.24}$$

Here only the imaginary part of the aberration function (see Eq. 2.15) expressed via the phase distortion function, $\chi(q)$, contributes to the intensity modulation. The objective aperture described via the aperture function, A(q), should be chosen the largest possible to avoid the cutting off the high spatial frequencies. The final image is strongly influenced by the aberrations of the objective lens and the $\chi(q)$ function shows how the phase shift is affected by lens. Moreover, it has been shown that this phase shift is not linear, but strongly depends on q and may result in oscillatory behavior (see an example below in Fig. 2.6(a)) [68]. If the CTF approaches 0 at a given spacial frequency the intensity is zero for this q and, at larger spacial frequency the function changes its sign. Positive or negative CTF indicate the phase shift of the electron waves by $+\pi/2$ or $-\pi/2$, correspondingly, leading to the atoms appearing at bright or dark contrast in respect to the background, respectively. For an ideal lens the CTF should be independent on the spacial frequency with no phase oscillations. Due to spherical aberration this is not the case. The focus at which a maximum of spatial frequencies is transmitted with the same phase until the CTF crosses 0 is the Scherzer defocus. It depends on spherical aberration, C_s, and wavelength as demonstrated by Scherzer [73]:

$$\Delta f_{Sch} = -1.2\sqrt{C_s\lambda} \tag{2.25}$$

The resolution of the microscope at Scherzer defocus is given by [68]:

$$r_{min} = 0.66\left(C_s\lambda^3\right)^{1/4} \tag{2.26}$$

In Fig. 2.6(a), we present an example of the contrast transfer function, i.e. $2sin(\chi(q))$, for an acceleration voltage of 300kV and a spherical aberration of 640 μm[1] (see light blue curve) at a Scherzer defocus of -37 nm according to Eq. 2.25.

As can be seen, for spatial frequencies $q > 5.9\ nm^{-1}$ (i.e. below the resolution limit) the CTF reveals dense oscillations making structural details in this range of spatial frequencies hardly interpretable. The second parameter that can be obtained, is the information limit set by the attenuation of the transfer function to $1/e^2$ and defined by the envelope functions of the microscope (see Eq. 2.16 and light and dark green curves in Fig. 2.6 (a)).

[1]This value was chosen as one of the lowest spherical aberration coefficients for standard uncorrected objective lenses.

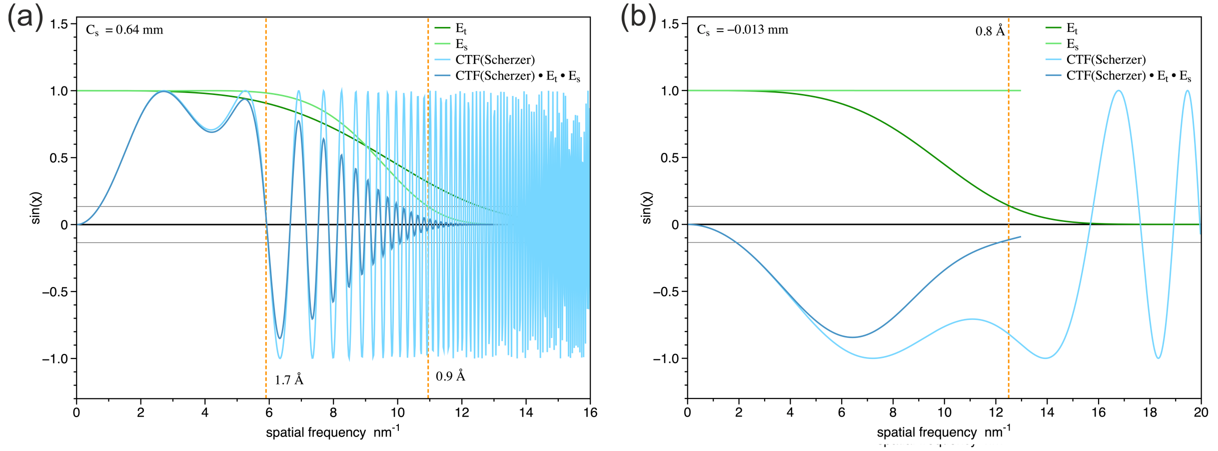

Fig. 2.6: CTF (light blue), chromatic aberration, E_s, (light green) and spatial aberration, E_s, (dark green) envelope functions, and final transfer function (dark blue) computed for: (a) an uncorrected TEM with C_s=640 μm and the corresponding Scherzer defocus -37 nm. Two orange dot lines mark (i) the resolution limit of approx 0.17 nm according to the Eq. 2.26 and (ii) the information limit set to 0.09 nm by the first crossing of the envelope function with y=1/e^2 (thin gray line). (b) the imaging conditions used for our HRTEM experiments: Cs=-13 μm and Δf=+5.8 nm. The focus spread that is defined by chromatic aberration and stability of the electron beam was set to 2.9 nm.

Another factor that affects the resolution is the contrast delocalization common for the microscopes with high spatial coherence of the source [74]. Induced by spherical aberration, an original exit object wavefunction would be spread out on the image plane with the radius related to the information limit:

$$r = \max\left|\frac{\partial\chi}{\partial q}\right|, q \in [0, q_{max}] \tag{2.27}$$

where q_{max} is the highest spacial frequency accepted by the objective aperture. It leads to the smearing out of the HRTEM image details and, thus, to a false localization of the objects in the image. A special defocus condition, Δf_{Lich}, was proposed by Lichte et al. [75] to reduce the "contrast confusion" that reduces the radius of contrast delocalization according to:

$$\Delta f_{Lich} = -0.75 C_s \lambda^2 q_{max}^2,\ r_{Lich} = 0.75 C_s \lambda^3 q_{max}^3 \tag{2.28}$$

2.3.1.4. Aberration correction in HRTEM

According to Eq. 2.26 the resolution limit strongly depends on the spherical aberration, therefore, one could improve the resolution of the microscope by changing the C_s. Rose et al. [76] have developed a double-hexapole corrector that placed after the objective lens can correct the main lens aberrations, i.e. the spherical aberration, the axial coma, the star aberration and the 3- and 4-fold astigmatism. However, due to the correction of the spherical aberration the phase shift between transmitted and diffracted beams, thus the contrast, is minimum. Lentzen et al. suggested optimum imaging conditions by adjusting the C_s and defocus to optimal values, so that phase contrast is maximum (Scherzer condition) and contrast delocalization is minimum (Lichte condition) at the same time [77]:

$$\Delta f_{opt} = -1.8 \lambda^{-1} q_{max}^{-2},\ C_s^{opt} = 2.4 \lambda^3 q_{max}^4,\ r_{opt} = 0.6 q_{max}^{-1} \tag{2.29}$$

Under these conditions resolution up to the information limit of the microscope can be obtained as we show in Fig. 2.6(b) for the corrected Cs=-13 μm (and Δf=+5.8 nm correspondingly), as utilized in in this work. In case of an aberration correction we thus obtain resolution down to the information limit of the microscope (that is ~15nm^{-1}). In details, less amount of contrast oscillations are observed so the CTF is more stable in a larger range of the spatial frequencies. While the envelope function of the temporal coherence (E_t) is constant, thus, not affecting the information limit, the spatial coherence function (E_s) results in a point resolution of 0.8 Å. Scattering angles up to 24.6 mrad will contribute to the HRTEM image contrast. Thus, maximum resolvable spatial frequencies are up to 12.5 nm^{-1}, contrast confusion (Eq. 2.29) is 47 pm.

Importantly, in this work we use NCSI conditions as proposed by Lenzen et al. and Jia et al. [77, 78], i.e a small negative aberration coefficient and a positive defocus. Under these conditions: (1) atoms appear bright and at higher contrast than at negative defocus and (2) the intensity of weakly scattering atoms, i.e. nitrogen atoms in our case, is enhanced.[2] Jia et al. [79] have explained the higher contrast in this regime via: (i) adding the non-linear terms to the intensity function due to the contribution from the interference of diffracted beams with each other; and (ii) a phase shift of $-\pi/2$ due to the positive overall distortion function $\chi(q)$ that changes a sign of the linear term. The final image intensity for the WPOA is represented by:

$$I(x,y) = 1 + 2\pi\lambda hU(x,y) + (\pi\lambda hU(x,y))^2 \tag{2.30}$$

In Fig. 2.7 we show a comparison between the imaging conditions with contrast transfer functions presented in Fig. 2.6 (a) and (b). The simulations of the HRTEM images were performed by our home-developed software based on the EMS program package by Stadelmann with the multislice approach (see description below) [80]. In order to demonstrate the influence of the imaging conditions on the image formation we simulate a supercell that contains an ordered $In_{0.33}Ga_{0.67}N$ monolayer in a Me-polar GaN matrix. Fig. 2.7(a) shows the projected potential of the exit wavefunction before passing through the objective lens. A simulated HRTEM image at positive spherical aberration and negative defocus in Fig. 2.7(b). As can be seen, the atoms appear dark and image artifacts, i.e. false contrast between the Ga and In atomic columns, are present.

[2]Note that, the distance between heavy and light atomic columns should be larger than the information limit - otherwise the signal of the weakly scattering atoms may fall below the noise level.

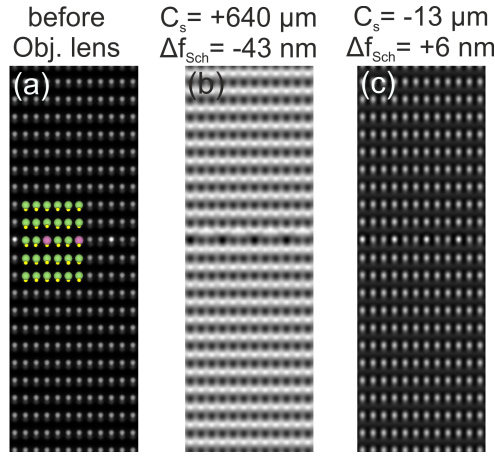

Fig. 2.7: Simulations of the HRTEM images of a single monolayer (In,Ga)N/GaN quantum well in the <1-100> projection direction. Simulations were performed for the sample thickness 1.6 nm. The ordered structure was designed as one pure indium columns (see violet balls in (a)) is followed by two purely Ga columns (green balls). (a) Projected potential of the supercell. The nitrogen atoms are visible below the Ga and In atomic columns (small yellow balls in the colored scheme). Images simulated for (b) the positive spherical aberration and Scherzer underfocus condition and (c) small negative C_s and Scherzer overfocus.

At negative spherical aberration (see Fig. 2.7(c)) well resolved bright atomic columns on the dark background with In atoms emerging brighter than Ga are observed. The latter imaging condition shows a better agreement with the projected potential from Fig. 2.7(a).

Results of the simulations of defocus series for a GaN supercell solely in two main projection directions <1-100> and <11-20> are shown in Ref. [81]. Simulations were performed for negative C_s and overfocus in the range of Δf=+2 to +11 nm with 3 nm focus step. The results showed that even slight variation of the defocus out of the optimum value (~5 nm) leads to the blurring of the simulated image or contrast reversal. This was most severe for the <11-20> projection, where maximum contrast changes between Ga and N with minor changes in thickness and focus.

We have shown that by adjusting the spherical aberration to a proper value we can significantly improve both, the point resolution and the image contrast.

2.3.1.5. Scanning transmission electron microscopy

Instead of using the interference between the diffracted and transmitted beams obtained after the interaction of the parallel beam with the specimen (as done in the TEM), in scanning transmission electron microscopy (STEM) the beam is focused to the smallest possible probe size. In microscopes operating between 100-300 kV the beam spot size is $\sim$ 0.5-3 Å. Then, the focused beam is scanned across the specimen, which is ideally oriented along a low index direction of the crystal. When the probe is focused on an atomic column.Electrons are scattered - electrons that are scattered into large angles are detected by a high angular annular dark-field detector. On the image the atomic column thus can be seen as a self-luminous object. Field emission gun (FEG) sources are preferential for the STEM analysis due to the high coherence of the electron beam which permits to get small probes. The STEM signal is registered by an annular detector collecting the electrons scattered into high angles and forming the image step-by-step during the scanning of each point of the specimen. The resolution in our STEM investigations is 1.3 Å

(note, that we employ an uncorrected STEM). Employing an aberration corrector for the probe forming condenser lens the spatial resolution can be improved to 0.5Å [82].

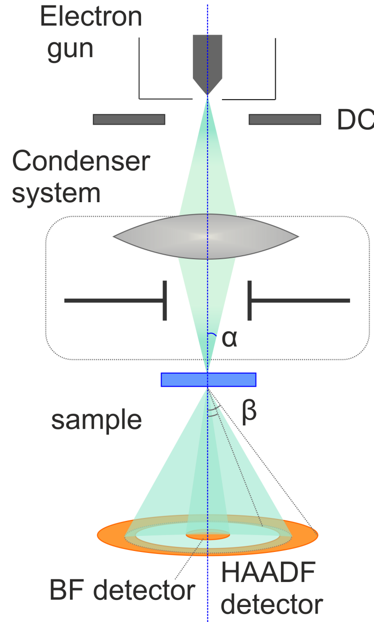

Fig. 2.8: Electron beam (light blue) passing through the STEM setup, DF and BF denote the dark and bright field detectors, respectively. Dotted blue line is the zone axis, where α is a convergence semi-angle of the incident beam and β - an acceptance semi-angle of the annular detector.

A standard STEM setup can be combined with electron energy loss spectrometer (EELS) , which provides information on the chemical composition, details of the bonding and the pseudo dielectric function via the measurement of the energy losses of the transmitted beam; energy dispersive X-ray spectrometer can be used for measuring the chemical composition and a cathodoluminescence spectrometer registers optical transitions in the material.

In STEM imaging we circumvent the phase relation between the individual columns: thus the images can be directly interpreted and do not depend strongly on thickness as phase contrast images do. The transmitted beam and beams scattered on low angles (<10 mrad) can be registered by a bright field detector (see Fig. 2.8). Here, we record both - coherent (following the Laue diffraction conditions Eqs. 2.6,2.7) and incoherent elastically scattered beams. The high annular dark field detector (HAADF) collects beams scattered on larger angles (> 50 mrad) in respect to the zone axis and which is used for Z-contrast imaging, revealing atomic number contrast [68]. In this case, the Bragg diffraction is negligible. Our HAADF-detector has acceptance semi-angles, β, in the range of 35-350 mrad.

Scattering strength, i.e. the intensity of the signal, is defined predominantly by the atomic number of the species that according to the Rutherford scattering is $\sim Z^2$ [83]. This principle is used for the so-called *Z-contrast* imaging. Scattering on the atomic lattice undergoes interaction with phonons - the so-called thermal diffuse scattering (TDS). The corresponding intensity of the scattered beam with the vector, s ($|s| = \frac{sin\theta}{\lambda}$), is described as:

$$I(s) = f(\theta)^2[1 - \exp(-2M(s))] \tag{2.31}$$

, where *M(s)* - is a Debye-Weller factor: $M(s) = 2(\pi s\bar{u})^2$ [84]. It is temperature dependent via the $\bar{u}$ - mean displacement of atoms from their static positions.

The atomic form factor $f(\vartheta)$ (see Eq. 2.10) defines the dependence of intensity on atomic number, i.e.:

$$f(\theta) = 2m_e(\frac{e}{h})^2\frac{Z}{s^2} \tag{2.32}$$

However, experimentally it was found that TDS is not strictly quadratic proportional to the atomic number, but $\sim Z^{1.7}$ [85, 86]. Another factor that affects scattering, specifically in alloys, is related to the deviation of atomic positions in real crystal from the equilibrium configuration, i.e. static atomic displacements that may sufficiently affect the HAADF intensity for instance, decreasing the overall contrast [87]. Nevertheless, Eq. 2.32 gives a general rule for the contrast evaluation on the HAADF-STEM images, i.e. atoms with larger atomic weight would appear brighter, e.g. In compared to Ga in our investigations.

The ascribed scattering processes acquired by the annular detector to form the intensity signal are incoherent. The final intensity registered by a HAADF detector is a convolution between the object function, $O(\bar{r})$, related to the each scanning point on the specimen (dependent on the atomic number) and point spread function $P(\bar{r})$ that is a response of the imaging system to a point object [88]:

$$I_{HAADF} = O(\bar{r}) \otimes |P(\bar{r})|^2 \tag{2.33}$$

The probe function, $P(\bar{r})$ determines the resolution in STEM imaging. It depends on the aberrations of the condenser system only and focusing of the probe. The STEM images are less affected by high order aberrations since the objective and intermediate lens systems are not involved in the imaging process. In our experiments images were mostly disturbed by spherical aberration (1.2 mm) and astigmatism. A focusing angle of the incident electron probe, α, (see Fig. 2.8) is controlled by the condenser aperture and in our STEM experiments is 9 mrad.

The Eq. 2.33 describes the incoherent image formation. We see, that image is an object blurred by intensity of the illuminating probe. Changing the focus and specimen thicknesses will not lead to the periodic phase reversals. The thicker investigated specimen area is, the more scattered beams we collect and the image intensity would increase. Nevertheless, for a direct chemical analysis thermal lattice vibrations and channeling effects should be considered. Generally, the incident electron passing through the sample is accelerated by the lattice potential, $U(x,y)$. When the electron beam self-focuses on an atomic column being attracted by electrostatic potential it can pass very close to the atomic nuclei. This results in a strong scattering probability and higher intensity is recorded, this process is called an electron channeling. If the scattering angle is too high the electron may deviate from its channel and not contribute to the signal formation, this is the dechanneling effect that decreases the intensity [89]. A probe channeling phenomenon is related to the transition of the signal from one atomic column to the neighboring one due to the spreading of the probe during the propagation through the thickness of a crystal [90]. To account for channeling and dechanneling effects, as well as TDS and static atomic displacements occurring inside the crystal during probe propagation on the image contrast, multislice image simulations based on frozen phonon approximation are performed as discussed further in 3.4.

2.3.1.6. Experimental details

In order to to reduce the multiple scattering and enable the elastic forward scattering, very thin specimens are required for the HRTEM and STEM imaging. Samples are thinned down first by mechanical polishing to the ∼ 10 µm thickness. The procedure is followed by the Ar-ion milling with a precision ion polishing system (PIPS) from Gatan using acceleration voltages from 4 kV to 0.1 kV. Final thicknesses of the specimens are as small as 5-10 nm. We have investigated the cross-sectional specimens prepared in the <1-100> and <11-20> projections (see Fig. 2.9 (a)) glued together.

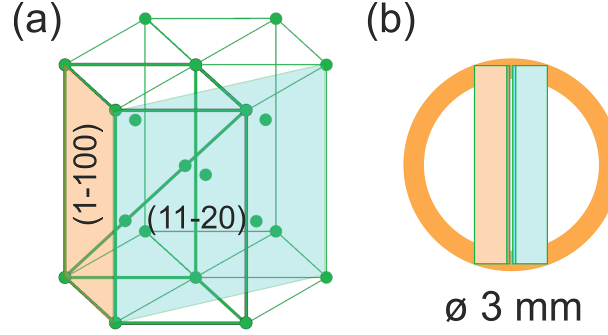

Fig. 2.9: (a) Atomic planes used for our TEM analysis highlighted in the wurtzite atomic structure with the corresponding <1-100> and <11-20> projection directions. (b) A cross-section specimen glued on the titanium ring for the TEM investigations.

At the end, in Table 2.2 we summarize the parameters and experimental conditions utilized for the TEM and STEM investigations.

Used settings	**HRTEM**	**STEM**
operation voltage	300 kV	
beam current	0.1-1 nA	1-2 pA
beam convergence semi-angle	<0.4 mrad (‖ beam condition)	9 mrad
convergence semi-angle	-	35-350 mrad
spherical aberration	-0.012 mm (Scherzer defocus +5.8nm)	1.2 mm
resolution	0.8 A	1.3 A
recording time	∼ 4 sec (120 sec for image series including exposure and readout time)	50 µs per scanning point, ∼ 30s in total
camera	Eagle 2k HR CCD camera, 2048×2048 pixels, 17.1 pm/pixel sampling	Fishione model 3000 annular detector (16 bit dynamical range)
highest magnification	1.4 Mx	10 Mx

Table 2.2.: Main parameters set for the HRTEM ans STEM investigations.

2.3.1.7. Scanning TEM-CL technique

High-energy electrons excite also carriers from the valence band to the conduction band. This process is followed by radiative recombination of electron-hole pairs. By scanning the electron probe across the sample and collecting the photons emitted by the sample and analyzing them

in an optical spectrometer we can get spatially resolved information on the optical properties of the material. The advantage of performing cathodoluminescence in a TEM is mainly the high achievable spatial resolution and the correlation between optical, spectroscopic and structural information at the same time. A more detailed account on CL in the STEM can be found, for instance, in Ref. [91]

An aluminum parabolic mirror inserted between the upper and lower pole piece of the objective lens collects the incandescent light (more on the CL method can be found in 2.4.2). The CL-signal is dispersed in a monochromator and then reordered parallel optical emission is registered either by a CCD-detector at each scanning point continuously with the forward-scattered electrons into high angles gathered by an HAADF-detector.

Our measurements were performed in the group of Prof. Dr. J.Christen in the Institute of Physics of Otto-von-Guericke-University, Magdeburg, on the FEI STEM Tecnai F20 electron microscope equipped with a Gatan MonoCL4 monochromator [92, 93]. Investigations were done at an acceleration voltage of 80 kV to reduce the beam damage of the sample as much as possible. Panchromatic CL imaging was done with the peltier-cooled GaAs(Cs) photo multiplier. The set up is equipped with a liquid helium stage that enables measurements down to 16 K. Cross-sectional specimens were 200 nm thick, i.e. thicker than in our standard TEM investigations to suppress surface recombination of the excited carriers that reduces the CL intensity. Complete set of data, I(x,y,λ), were obtained by the recording of local spectra at each scanning point on the specimen (pixel).

The spatial resolution in the CL is defined by the excitation volume, i.e. beam diameter and beam broadening, that was minimum 0.56 nm (for 80 kV) and the diffusion of excited carriers in the material. For GaN the final resolution was approximately 6 nm in GaN that is far below the resolution limit of the standard CL set up ($\sim$ 1 µm). This technique is very useful for the investigation of the emission in complex structures or structures with content variations [94].

2.3.2. Reflection high-energy electron diffraction

Reflection high-energy electron diffraction (RHEED) is a technique used for the *in situ* monitoring of surfaces in molecular beam epitaxy. It allows to estimate the growth rate and to analyze the as-grown surfaces. The RHEED set up, usually installed in the growth chamber (see Fig. 2.2), requires mainly an electron source and a detector. The electron beam is aligned by the deflection coils to hit the specimen surface at glancing angle, ϑ_g, almost parallel to the surface (Fig. 2.10). The focal lenses can be placed after the electron gun and before the CCD camera.

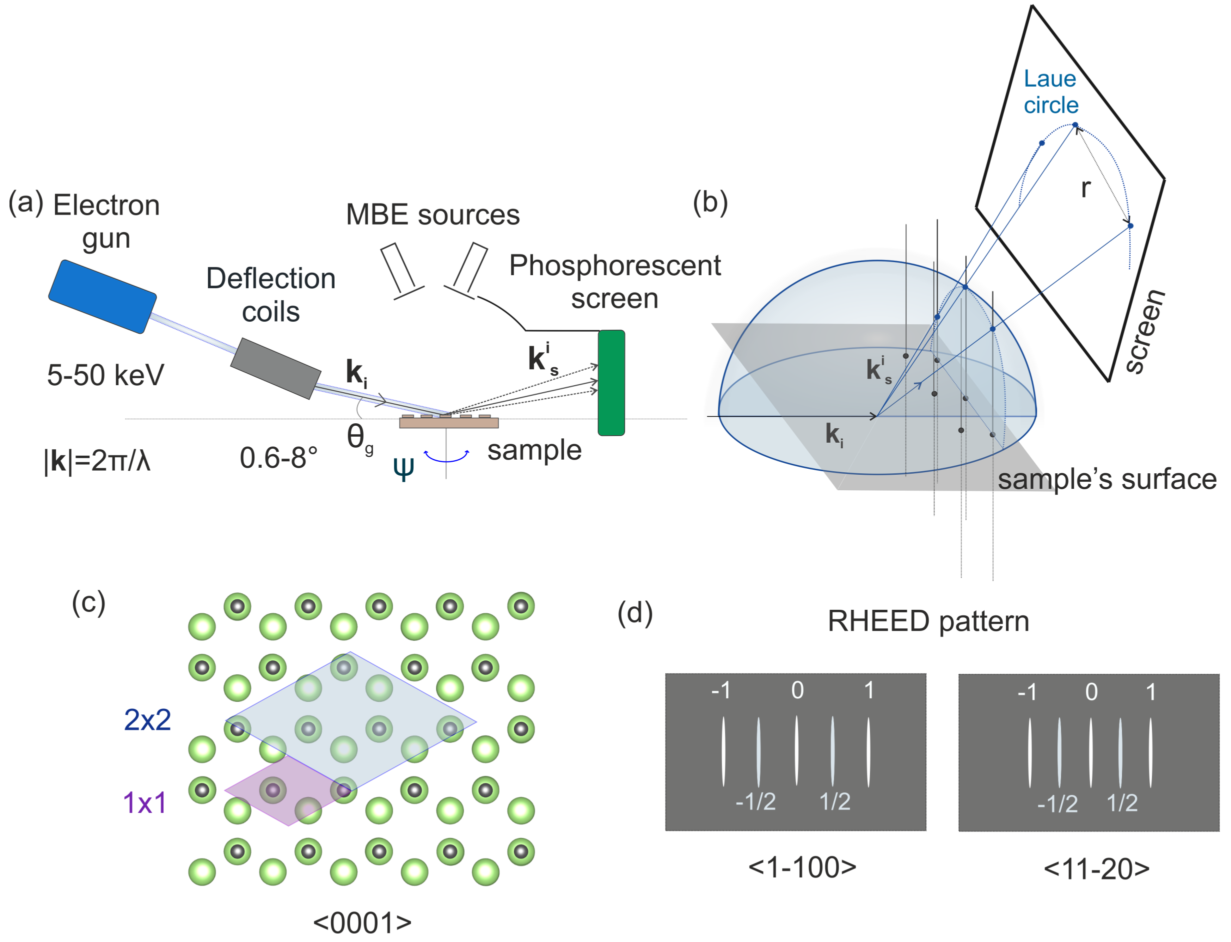

Fig. 2.10: (a) Scheme of the set up for the RHEED measurements implemented into the MBE chamber, here ϑ_g is the glancing angle of the incoming beam, ψ is the rotation angle of the specimen. (b) Part of the Ewald sphere formed by the incident, $\mathbf{k_i}$, and scattered, $\mathbf{k_s}$, wave-vectors and the corresponding RHEED pattern observed during the experiment. (c) Top view of the GaN surface, where green balls indicate the Ga atoms and N atoms are shown as small gray balls. The violet and blue rhomboids depict the 1×1 and 2×2 arrangements of the surface Ga atoms. (d) A schematic representation of the RHEED patterns corresponding to the surface reconstructions from (c). The white streaks represent the primary bulk-like diffraction rods and the light blue colored streaks are the half-order rods originating from the 2x2 reconstruction.

The resulting divergence angle, $\Delta\vartheta$, of the incident electron beam is usually ~0.1 mrad and the recorded spot size ~0.1 mm [95]. Diffracted electrons reaching the phosphor coating of the vacuum window inside the MBE chamber are registered by an outer high sensitivity CCD camera directly reveal the RHEED pattern [96]. It depicts the reciprocal lattice of the subsurface layers with atomic precision up to 0.1–0.01 pm [97]. Rotation of the sample allows to obtain the full symmetry of the surface reconstruction. The spatial resolution of the method is defined by the monochromatism and collimation of the beam, i.e. its coherency. The coherence length is usually in the range of 50-200 nm given by:

$$l = \frac{\lambda}{\sqrt{2(\Delta\theta)^2 \sin^2\alpha + (\frac{\Delta E}{E})^2 \cos^2\alpha}} \tag{2.34}$$

where ΔE - is the energy spread, E - the electron beam energy, $\alpha = 0°$ correspond to the longitudinal coherence length (up to 200 nm) and $\alpha = 90°$ - to the transverse coherence length (30-80

nm). The lateral size of the investigated area is of a few *cm* size.

The RHEED pattern is a result of the coherent elastic scattering described in 2.3.1.1. Nevertheless, the Laue diffraction condition is not fully obeyed - a Laue equation for the <0001> direction Eq. 2.7 is not satisfied. Therefore, instead of the standard diffraction pattern in reciprocal space, surface atoms are represented by vertical rods. When these rods intersect the Ewald sphere (like shown in Fig. 2.10 (b)), constructive interference occurs. The resulting scattered electrons will have a specific spots-like pattern lying on the Laue circles of different order starting from zero. The diffraction spot obtained at angle close to the one of the incident beam is called a specular spot, all other spots are obtained from the crossing of the rods with the Ewald sphere moving further from the surface. The kinematic approach of the RHEED pattern analysis is based on the assumption of elastic scattering. Considering very small angles ϑ of the glancing incident beam, the Bragg law Eq. 2.5) can be approximated by ($sin\theta \approx \theta$) and the in-plane lattice constants can be estimated from the distance between the streaks:

$$d_{hkl} = \frac{L\lambda}{r} \tag{2.35}$$

where L is measured between the incident point on the sample's surface and the screen, r is a distance between the spots [98]. Following this approach even the change of the strain state of the alloy can be measured *in situ* during the growth can be obtained. The analysis of the specular spot intensity during growth enables to estimate the growth rate and the coverage of the layer. Here, the maximum signal corresponds to the atomically flat ideal surface.

If the morphology of the surface is very rough the incident beam can be transmitted through the island-type structures and the third Laue condition implies. This results in a spot-like regular diffraction pattern, see example in Ref. [29]. When the surface atoms are specifically arranged forming surface reconstructions spots transform into various forms of elongated streaks. To obtain complete information of the surface reconstructions and lattice periodicity in different directions the sample is rotated by ψ angle (90°). In Fig. 2.10 (c) and (d) we show an example of the modification of the RHEED pattern from the bulk-like 1×1 to 2×2 surface reconstruction. For the latter case the surface will be constructed of atomic arrangements with double spacings that leads to the decrease of the distances between the streaks in the reciprocal space. These new streaks appear a half way from the primary order reflections. Due to the symmetry of the 2×2 reconstruction, additional streaks are observed for the RHEED patterns in both directions. Combination of the *in situ* RHEED data with the (scanning) transmission electron microscopy techniques enables to understands the formation of surface reconstructions [99, 100]. For the III-N surfaces mostly 1×1, 2×2 and (√3×√3)R30 reconstructions have been found depending on the fluxes and growth temperature [101–103].

2.3.3. X-ray diffraction

X-ray diffraction (XRD) is a quantitative non-destructive method used to determine the crystalline structure, strain state and crystal orientation of materials. The wavelengths of X-rays in X-ray diffractometer used in the lab are of the of the interplanar distances, i.e. ~ 1 Å. The analysis of X-ray data is mainly based on Bragg's law. The resulting diffraction pattern obtained under the excitation by the X-rays of a known wavelength encloses data on the crystalline structure. Note, due to the small wavelength of the X-Rays (as compared to the high-energy electron beam) the Ewald sphere is limited and fewer diffraction spots are available.

Our XRD measurements were performed in the Paul Drude Institute on the Panalytical X'Pert system and in Unipress with using the similar PANalytical Empyrean equipment. Generally, structural data of a single crystal can be gathered by radiation of the X-ray beams in some limited range of wavelength or by tilting the specimen and the X-ray source-detector couple. In Fig. 2.11 (a) we show the scheme of the ω-2ϴ geometry XRD setup. The maximum usable range for the source and detector rotation in our experimental setup was -111°<2ϴ<168°. An X-Ray Ceramic tube with a copper-based anode was used as a source. The incident beam then reaches the optical systems composed of a parabolic mirror for collimation, followed by a monochromator (in our case a Ge(220) hybrid monochromator was installed) that permits to select the Cu-K$\alpha_1$radiation with ∼1.5 Å wavelength. Additionally, filters can be used to suppress the detrimental radiations from the source and soller slits realized in the form of parallel plates - to narrow the beam hitting the sample. The specimen is placed into the goniometer stage that enables additional rotations for the sample itself in three directions (x, y, z) depicted in Fig. 2.11 (a) as angles ω, ψ, φ. The diffracted beam optics usually contains selection slits for reducing the scattering, soller slit and monochromator.

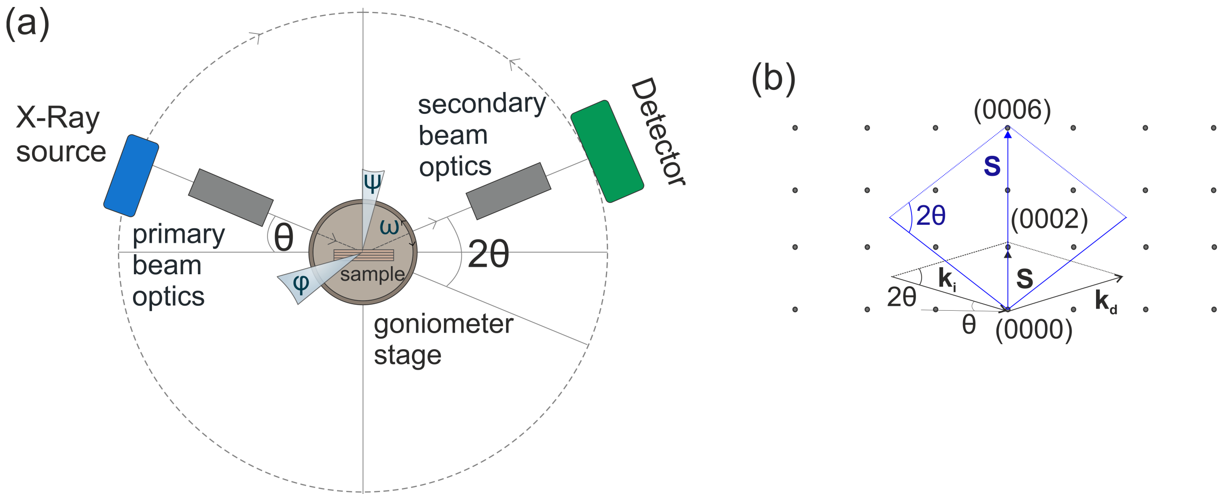

Fig. 2.11: (a) Standardized scheme of the XRD equipment representing the main parts of the set up; components of the incident and diffracted beam optics can be varied. (b) Analysis of the lattice planes by scanning around the 0002 and 0006 lattice spots shown in the reciprocal space. $\mathbf{k_i}$ and $\mathbf{k_d}$- are vectors corresponding to the incident and diffracted beams, where $\mathbf{k_d}$-$\mathbf{k_i}$=**S**. Black- and blue-colored scattering vectors are registered at two different 2ϑ scans and perpendicular to the (0002) and (0006) planes, respectively.

Reaching the Bragg condition at the Bragg angle, θ_B, the diffraction signal increases to maximum and the signal is registered. In our experiments we have recorded the ω–2ϑ scans around the (0002) and (0006) reflections shown in Fig. 2.11(b). In this geometry the orientation is constant but different spacings, represented by the scattering vector **S** inverse proportional to the interplanar distances in this direction, are measured.

2.3.4. Atomic Force microscopy

Atomic Force microscopy (AFM) is a non-destructive method widely used for examination of the as-grown surfaces up to atomic resolution. Information about the surface is collected during scanning of a sharp tip across the surface. The lateral resolution is usually in the range of a few

nm and depends on the shape and radius of the tip [104], out-of-plane resolution depends on the scanning mode and vertical movement of the tip and can be as low as 0.1 nm.

Scanning by the tip is performed via movement of the sample by piezoelectric elements in all three directions. A tip with a typical radius of 10-50 nm is connected to a cantilever that deflects or attracts to the surface during the scanning. The force arising from the surface-tip interaction and its deflection, is described by Hook's law according to: $F = -kh$, where k - is the stiffness coefficient and h - is the height . More explicitly: (i) when approaching the surface the tip deflects towards it via the attractive Van der Waals, capillary or electrostatic forces - this regime is called *non-contact*; (ii) when the tip almost touches the sample the Van der Waals force is at maximum and the repulsive forces deflect the cantilever deflection away from the specimen surface, i.e. the measurement occurs in *contact* regime. However, in this regime the resolution can be impaired by surface contamination. If the tip is too far from the sample, no feedback signal is obtained. The tapping mode regime is set for the intermediate distances between tip and sample. At this mode the tip oscillates close to the surface with amplitudes up to 100 nm depending on the surface roughness. The deflection of the cantilever is monitored by a laser beam pointing on the cantilever and reflected to the position sensitive detector [105]. The feedback control system always returns the oscillations to their initial amplitude values. Finally, a topographic image of the surface roughness derived from the variations of amplitude is constructed. Roughness is defined by the Root Mean Square (RMS) parameter that is a standard deviation of the height from the average value, h, within a scanned area:

$$RMS = \sqrt{\frac{\sum_{i=1}^{N} (h_i - h)}{N}} \tag{2.36}$$

Our AFM measurements were performed in the Institute of High Pressure Physics (Unipress), Warsaw using a Nanoscope Veeco Instruments setup, and in the Paul Drude Insitute (PDI), Berlin.

2.4. General optical properties and methods of optical investigation:

2.4.1. Basic optical properties

In this section we give a brief overview on recombination in semiconductors, for more information we refer to the textbooks [106, 107].

Electronic band structure of semiconductors is described via the energy dispersion:

$$E(\bar{k}) = \frac{\hbar^2 \left|\bar{k}\right|^2}{2m^*_{e/h}} \tag{2.37}$$

where $m^*_{e/h}$ is the electron or hole effective mass at the conduction band (CB) minimum or valance band (VB) maximum and $\bar{k}$ is the wavevector. In the most simple case they are considered to be parabolic, isotropic and non-degenerate. The effective mass in Eq. 2.37 accounts for the weak perturbations of the periodic potential of the lattice - this is so-called an effective mass approximation. Effective masses of electrons and holes of the crystals usually

differ from the values obtained for free particles. For instance, for electrons in GaN it was estimated theoretically and experimentally $\sim 0.2\ m_0$ [108, 109]) and holes usually obtain larger effective masses $>1.0\ m_0$ in GaN-based materials [110, 111]. The non-parabolicity of the energy dispersion close to the band minima, i.e. Γ point of the Brillouin zone, can be neglected. Moving towards larger k-vectors the energy dispersion of the real crystal can be steep and characterized by small effective mass or broad - more corresponding to heavy charge carriers. In heterostructures with a big difference between the QW and barrier potentials, the effective mass approximation is not applicable and the band structure is strongly non-parabollic. To define the energy band structure, the Schrödinger equation are usually solved by various calculation methods.

Moving further, the bands are anisotropic so two transverse and one longitudinal effective masses are distinguished. Moreover, the valence band of GaN and InN is split into sub-bands that are denoted as heavy holes, light holes and crystal field split-off bands [6, 13]. In the biaxially strained structures the crystal field band splitting non-linearly depends on strain [50]. This sub-band moves towards lower energies if it is compressively strained [6]. Separation between the light and heavy holes due to the spin-orbit interaction is smaller [109], but in the tensile-strained III-V semiconductors the light-holes state becomes the upper-most valence sub-band [112]. Band structure, i.e. the energetic positions of the highest occupied and lowest unoccupied states of the coherent (In,Ga)N MLs on GaN discussed here, i.e. were accessed by the DFT 2.6.1 and k*p model 2.6.2 calculations.

In the current work we will discuss direct band-to-band (see Fig. 2.12) transitions resulting in the emission of visible light. Overlap of the electron and hole wavefunctions defines the rate of the radiative recombination described by the transition matrix element. Electron-hole annihilation which is not accompanied by photon emission is a non-radiative recombination. Trapping levels in the band gap region formed by the point defects of the material (e.g. vacancies, interstitials, impurity and doping atoms) or larger defects (e.g. threading dislocations) are the most common sources of non-radiative recombination. Other non-radiative processes are Auger recombination [1] and heating of the lattice by creation of the phonons.

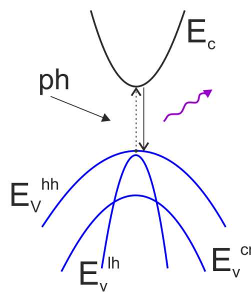

Fig. 2.12: Band to band recombination of the charge carriers in semiconductor induced by the photon excitation (ph). E_c, E_v^{hh}, E_v^{lh} and E_v^{cr} denote the conduction band minimum and valence band maxima of the heavy holes, light holes and crystal-filed sub-bands, respectively.

Another radiative mechanism is attributed to the recombination of excitons - bound electron-hole pairs attracted by the Coulomb force. Therefore, emission energy of the excitons is lower than the band gap of the corresponding semiconductor. Different types of excitons can be

[1] Here, the energy gained after the recombination of the initial electron-hole pair is transferred to the third particle.

obtained: small-radius (Frenkel), charge transfer (usually found in ionic crystals) and large-radius (Wannier-Mott) excitons. The latter ones are the most common in semiconductors. The exciton radius may extend over several lattice constants (for GaN the radius is $\sim$ 3.1 nm) and move inside the crystal transferring the excitation energy. The electron-hole pairs are stable if their binding energy ($\sim$ 23-30 meV for GaN [13, 113, 114]) is higher than k_BT (10 meV), therefore the excitonic emission is usually observed at low temperatures. The energy of this free-type excitons is defined as:

$$E_F(k) = E_g + \frac{(\hbar k)^2}{2(m_e^* + m_h^*)} - \frac{m_e^* m_h^*}{(m_e^* + m_h^*) m_0} \frac{Ry(H)}{\varepsilon^2} \tag{2.38}$$

In Eq. 2.38 effective masses of electrons and holes are referring to the motion of a free exciton in the periodic potential of the lattice with dielectric constant ε and *Ry(H)* - is a Rydberg energy of the ground state of the hydrogen atom (13.6 eV). When a free exciton is trapped by a lattice defect, impurity or dopant atom, it is confined by their potential and can recombine radiatively or non-radiatively. Emission lines of the bound excitons are shifted to lower energies on the spectra as of the free excitons because the latter ones give away small part of the energy to the surrounding lattice by phonon interaction. The difference between the energies of bound and free excitons is the localization energy that can be, for instance, a measure of the ionization energy of impurity. Excitonic peaks typically observed in GaN have narrow line width in the range of 1-7 meV depending on the type of the electron-hole pair and precision of the experiment [114–116].

After a radiative recombination of an exciton the created photon can be reabsorbed and generate a new bound electron-hole pair. As a result of such sequence the dispersion curve of such exciton-photon interaction would have the form of a bottleneck. Transition to lower energies within this new energy dispersion curve is accompanied by the emission of the high-energy optical phonons and moving downwards the bottleneck - by the emission of low-energy acoustic phonons. Phonons are lattice vibrations, however, described by a discrete set of eigenstates in the electronic configuration. The dispersion relation of the phonons connects frequency of the vibration and wavevector and describes two branches of the allowed frequencies - higher and lower frequency branches corresponding to optical and acoustic phonons, respectively. They are separated by an array of forbidden frequencies depending on the variation of the atomic masses in the unit cell, e.g. it is large for InN [6]. Optical phonons describe the motion of atoms in the opposite direction (out-of phase) and can be found only in the systems with at least two different atomic species in the cell. In the acoustic mode atoms are moved together in the same direction and amplitude. Longitudinal acoustic and optical phonons correspond to the movement along the direction of propagation and transverse - to the motion normal to the plane.

When an electron and hole are separated from each other there is a dipole moment between them that would locally deform the crystal lattice. After the recombination the potential energy excites the longitudinal optical (LO) phonon inducing a phonon replica on the lower energy side of the main emission peak (zero-phonon emission). The strength of the interaction between electron and polar phonon is described via the Huang-Rhys factor [117], S, that characterizes the intensity distribution of the nth phonon side-band via [118]:

$$\frac{I_n}{I_0} = \frac{S^n}{n!} \tag{2.39}$$

In GaN the energy of the LO phonon is $\sim$ 90 meV [6, 119]. Although, LO phonons are

the most examined in GaN the values of *S*-factors are spread for low dimensional GaN-based structures from 0.07-0.8 [120]. Coupling to LO phonons in (In,Ga)N quantum structures is mainly governed by the following factors: the localization of the charge carriers (or excitons), their spatial separation along the polar axis and strain state of the (In,Ga)N.

Another characteristic parameter analyzed in semiconductors is the temperature dependence of the band gap. In general, the band gap shrinks at elevated temperatures due to the thermal lattice expansion and interaction of the electrons with phonons [121, 122]. Several models that tend to describe the peak positions behavior under increased temperatures can be found in literature, for instance, a classical Varshnii's empirical equation with the temperature coefficients, α and β, constant for the corresponding bulk material [123]:

$$E_g(T) = E_g(0K) - \frac{\alpha T^2}{\beta + T} \tag{2.40}$$

However, Vina et al. have shown that change in occupation of the states by phonons at rising temperatures is predominant [124]. The work of O'Donnel et al. described the temperature dependence of the band gap through the amount of phonons available for the interaction with electrons [125]:

$$E_g(T) = E_g(0K) - S < \hbar\varpi > \left[\coth\left(\frac{< \hbar\varpi >}{2k_B T}\right) - 1\right] \tag{2.41}$$

where S - is the electron-phonon coupling, $< \hbar\varpi >$ - is the average phonon energy. A model that considers the dispersion of phonons is described in Ref. [126].

2.4.2. Cathodoluminescence measurements

Cathodoluminescence, i.e. emission of the photons as a product of the electron beam excitation, is a relatively non-destructive technique used for structural and optical characterization. This process may be accompanied with the formation of backscattered electron- (with energy conservation), secondary electron- (with energy loss) or characteristic X-rays signals.

The main part of a standard CL-setup are (see Fig. 2.13(a)): (i) electron beam source, in our case it was lanthanum hexaboride (LaB6) cathode, that emits electrons that are then accelerated to the voltage of 3-30 kV and focused by magnetic lens; (ii) a parabolic mirror with a hole for the incident beam that collects emitted photons and redirects them to the entrance slit of the spectrometer; (iii) a detection system. Two modes are possible: (1) *parallel*, where all the wavelengths dispersed after passing through the grating of the monochromator are collected and recorded by the CCD camera (the sensitivity range is ~120-1100 nm); (2) *monocl-mode*, i.e. a particular wavelength is selected by a monochromator, detected by a photomultiplier and monochromatic images are recorded. For our investigations we used a Gatan MonoCL3 system equipped with the Zeiss DSM scanning electron microscope (SEM). SEM is another type of electron microscopes but with lower energies of the incident electrons (less than 30 kV) than in the transmission electron microscope (~200-300kV). It is a surface sensitive method that registers signal of the secondary emitted electrons from the subsurface region, ~100 nm depth.

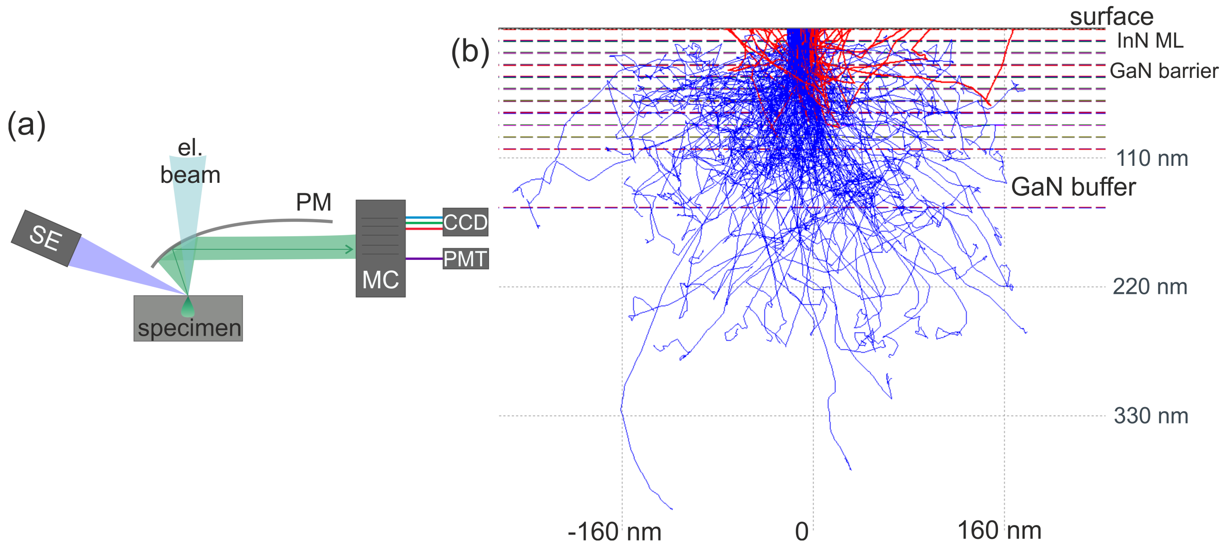

Fig. 2.13: (a) The main parts of the standard cathodoluminescence setup: SE - a secondary electron detector, PM - a parabollic mirror, MC - a monochromator, PMT - a photomultiplier tube. (b) Simulation of the generation volume obtained in CL experiments for the standard SLs under discussion: ten periods of ML-thick QWs separated by GaN barriers on the sapphire substrate. Blue and red lines are trajectories of the forward and inelastically backscattered electrons.

A fundamental difference of CL from the other optical measuring technique, PL (where luminescence occurs under the photon irradiation of the specimen), is that in the former, one ~10kV electron generates thousands of electron-hole pairs in a small excitation volume. This gives rise to multiple elastic and inelastic (leading to the electron-hole pair generation) scattering events. Therefore, the trajectories of the incident electrons are random, where, the significant part is dissipated in the area of the incident beam interaction [127]. To model the energy dissipation for the given material, the trajectories of the electrons penetrating into the sample are computed by means of Monte Carlo simulation. Structures under investigation in this work are short-range superlattices of various thickness. In Fig. 2.13 (b) we show an example of the generation volume obtained from the simulation for the typical SLs. The acceleration volume of 5 kV was chosen similar to the one used in our experiments (~3-10kV). The simulation was performed via the Casino ("monte CArlo SImulation of electroN trajectory in sOlids") software [128] suitable for the low energy beam interaction in solids. Electron trajectories are computed gradually as each electron travels a small distance in a straight line till it randomly scatters. The excitation volume has a specific droplet-shape with the penetration depth of ~250 nm for the given acceleration voltage of around 5 kV that passes through the whole thickness of the SL and lateral spreading diameter ~300 nm.

Spatial resolution in CL lies in the range 100 nm - ~10 nm [129] is better than be obtained in PL (defined by the Abbe limit, $\sim\lambda/2NA$, hundreds of nm). In CL it is given by the beam size (minimum few Å for the FEG guns), the generation volume and diffusion length of the carriers, i.e. investigated material [127]. Moreover, to avoid the saturation effects observed under higher injection densities, an optimum spatial resolution for a focused beam is reached under low acceleration voltage and low beam currents. Spectral resolution in CL depends on the dispersion grating that can be chosen as 150 l/mm or 2400 l/mm in our monochromator and slit width varied between 10 μm and 5 mm. The finest spectral resolution obtained for our setup is ~ 0.1 nm for the high resolution grating (2400 l/mm) and the smallest slit. Our experiments

were conducted at various temperatures down to 7 K using a He cooled stage with a Oxford ITC-503 temperature controller.

2.4.3. Photoluminescence investigations

In photoluminescence the incident photon beam is absorbed by the semiconductor resulting in the creation of electron-hole pairs that further recombine radiatively or non-radiatively. The main parts of our PL equipment are: a monochromatic laser source, a spectrometer and a detection system. We have conducted two types of photoluminescence measurements - under continuous wave (CW-) and pulsed laser excitation. The 325 nm line of a HeCd laser was used for excitation in the CW-PL experiments. An Acton spectrometer from Princeton instruments with 750 mm focal length combined with a CCD camera was employed as a detection system. A spectrometer is needed for dispersion of the incoming light. The operating range of our spectrometer was from 0 to 1400 nm. Spectral resolution of the system can be as low as 0.03 nm for the smallest 10 µm entrance slit of the spectrometer and a diffraction grating of 1200 l/mm [130]. The excitation power of the laser was $\sim$ 100 mW with a spot size $\sim$ 5 µm. Samples were placed into the closed-cycle cryostat which allowed cooling down to liquid He temperature (4.2 K). The excitation power of the laser was controlled by neutral density filters.

In time-resolved photoluminescence (TR-PL) the recombination process investigated by recording the dynamics of the intensity decay. Periodic laser pulses create electron-hole pairs that recombine following, in the most simple case, an exponential decay. The time needed for a decrease of the initial signal by *1/e* is called the lifetime of the carriers and is determined by the change in carrier concentration. The total amount of the generated carriers will reduce exponentially:

$$\frac{n(t)}{n_0} = e^{-\Gamma t} \tag{2.42}$$

resulting in:

$$I(t) = I_0 e^{-\Gamma_{tot} t} \tag{2.43}$$

where n_0 - is the initial carrier concentration under excitation, I_0 - is the intensity directly after the excitation. The total decay rate can be defined as: $\Gamma_{tot} = \Gamma_{rad} + \Gamma_{nrad}$, that for a single exponential decay is inverse proportional to the average decay time, τ: $\Gamma = \tau^{-1}$. As a result of TR-PL measurements one gets the temporal and spectral dependence of the intensity decays for a given time window.

In semiconductors decay times usually lie in the range from *ps* to *ns*. Luminescence gain is rather low, therefore, for the detection of the signal *streak* cameras are used providing better spectral resolution compared to standard spectrometers. A streak camera is a tube-shaped device used for the recording of ultra-fast signals. The portions of incident light emitted from the specimen gets through the entrance slit of the camera and generates electrons on the photocathode with the corresponding intensities. The signal is, then, accelerated by the electrodes and swept in the electric field to different distances in respect to their arrival time. The phase of the sweeping electrodes should be identical to the pulse repetition length. After that, the electron beam is intensified on the micro-channel plate [2] and hits the phosphor screen. As a

[2] Micro-channel plate is a type of an electron multiplier that generates ~10^4electrons from a single charge carrier.

result, on the screen one obtains a vertically elongated luminescence image that has an order corresponding to the arrival time of the electrons moving from top to bottom, i.e. fast electrons are deflected to lesser angles and would hit the upper part of the screen. In other words, streak cameras convert the temporal picture into a spatial distribution of the pulse. Horizontal dispersion of the "streak" pattern represents the wavelength and brightness of the picture - an intensity of the incoming light [131, 132].

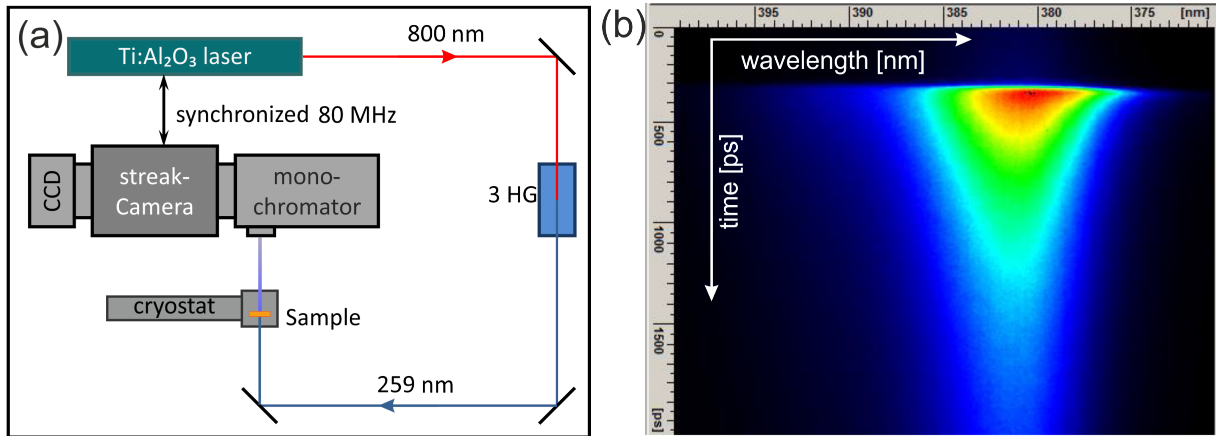

Fig. 2.14: (a) A principle scheme of the TRPL setup mounted in the Max Born Institute, Berlin, utilized for our experiments. Monochromatic light λ=800 nm passes through the third harmonic generator system (3 HG) to obtain 259 nm excitation utilized for the experiments. An additional unit for the focusing of the light emitted from the specimen is not shown. (b) Color-coded image of the intensity distribution obtained on the CCD screen: more intense signal in the upper part of the image represented in red corresponds to the fastest transitions.

Our TR-PL experiments were done in the Max Born Institute for Nonlinear Optics and Short Pulse Spectroscopy, Berlin, in the group of Dr. J. Tomm. A principle scheme of the setup is shown in Fig. 2.14 (a). For the excitation we have utilized the third harmonic of a frequency tripled Spectra-Physics Tsunami Ti:sapphire laser operating at 259 nm (4.79 eV) to obtain the emission from GaN (∼340 nm) and (In,Ga)N (∼380 nm). Moreover, the original excitation laser wavelength (780 nm) could be tuned in the range of approximately 50 nm and by overlapping it with the second harmonic. The resulting emission wavelength could be used to obtain a quasi-resonant excitation condition for (In,Ga)N solely. The laser was mode-locked[3] to have a repetition rate of 80 MHz (or 12.5 ns). The operation phase could be adjusted by a delay generator. The pulse length was around 100 fs, the focus spot diameter of the beam ∼ 100 μm and excitation power 30 mW. The laser was synchronized to the streak unit via a delay generator (Hamamatsu C6878) to acquire a syncro-scan measuring mode. The generated laser beam was passing through a spectrometer Acton SP 2300 with 300 mm focal length (several gratings were available) to obtain the dispersion, i.e. spectral resolution of the emission. A Hamamatsu Streak-Camera C5680 with a S20 cathode, sensitive to UV light, was used for detection giving a temporal resolution approximately 10 ps. The samples were mounted in an optical Helium closed-cycle cryostat that controlled the temperature allowing measurements up to 5 K. An example of the TRPL spectrum of the standard SL structure, i.e. 1 ML (In,Ga)N

It is constructed with multiple thin glass tubes covered with a secondary electron emitting material from inside.
[3] i.e. several laser pulses of the Gaussian shape overlap or cancel each other with a constant periodicity in a fixed cavity resonator of a laser.

QW with 10 nm GaN barrier repeated 10 times, discussed in this work, is presented in Fig. 2.14 (b). The spectrum is a 2 dimensional picture of the intensity distribution in time and emission wavelength.

2.5. Overview of the (In,Ga)N material properties

2.5.1. Growth of (In,Ga)N alloys

For the deposition of GaN-based alloys by molecular beam epitaxy two types of nitrogen gas sources are employed - molecular N_2 and ammonia NH_3sources. Due to the low incorporation rate of ammonia under the temperatures used in MBE, molecular nitrogen sources are mostly used for the III-nitride deposition [6]. Because of the high dissociation energy of nitrogen molecules [133] for the formation of nitride compounds, active nitrogen is needed that for the growth of our samples was generated by radio-frequency (RF) plasma [134]. As a result of RF plasma excitation, ground-state atomic N, ionized N_2^+ and molecular N_2 - either in neutral or metastable excited state, N_2* are present in the growth chamber. The binding energy of active N_2* is more than 6 eV lower than of the ground state N_2. Duff et al. have shown that in addition to the atomic nitrogen, excited molecular nitrogen species may significantly contribute to (In,Ga)N growth [135, 136].

The partial pressure of the nitrogen source lies in the range of 10^{-5}-10^{-6} Torr [136], for Ga and In the range is wider 10^{-4}-10^{-7} Torr depending on temperature of the effusion cell [137]. Growth rates of GaN-based alloys usually are in the range of 0.5-2 ML/s [138, 139].

2.5.1.1. (In,Ga)N alloy formation

The formation of (In,Ga)N alloys is generally governed by kinetics and thermodynamics. Kinetics can be described via the adsorption/desorption of the atomic species from the surface. Desorption of GaN sets in at considerably higher temperatures than of InN. For GaN thermal desorption emerges at 750 °C and above 800 °C the adsorption rate diminishes [140, 141]. Below these temperatures Ga incorporation and diffusion rates would prevail. The activation energy for Ga thermal desorption was estimated in the range of 2.8-2.88 eV [140, 142]. Considering InN, the desorption emerges at temperatures higher than 470 °C with an activation energy of ∼2.5 eV [67]. These conditions define the maximum sticking of the atomic species to the substrate introduced in 2.2.1, i.e. the difference between the absorbed and desorbed atoms, that for indium is at temperatures lower than 540 °C, while that of Ga, is essentially higher, at 700 °C [6].

The chemical reaction to form (In,Ga)N is described as follows:

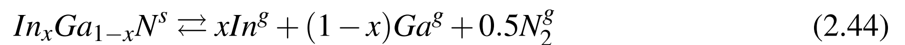

$$In_xGa_{1-x}N^s \rightleftarrows xIn^g + (1-x)Ga^g + 0.5N_2^g \tag{2.44}$$

where g and s denote the gas- and solid state of the components, respectively. According to the thermodynamics approach solid (In,Ga)N is stable for suggests negative values of the Gibbs free energy:

$$\Delta G_f[In_xGa_{1-x}N] = \mu^s_{In_xGa_{1-x}N} - x\mu^g_{In} - (1-x)\mu^g_{Ga} - 0.5\mu^g_N \leq 0 \tag{2.45}$$

Decomposition of the InN and GaN binaries is a thermodynamical factor, that strongly impacts the growth of the alloys and is governed by the growth temperature. Thermal decomposition of the GaN binary starts through nitrogen evaporation into gaseous phase and Ga vaporization straight from the solid phase [143]. For instance, Grandjean et al. have shown experimentally that evaporation of GaN strongly emerges at 800 °C with an activation energy of 3.6 eV [138]. InN decomposes into nitrogen gas and liquid indium [144] at temperatures higher than 470 °C, the activation energy for this process is ∼1.9 eV [67]. Note, that this activation energy is lower than the activation energy required for the thermal desorption. Therefore, after the binary decomposes, the In species floating on the surface tend to form liquid droplets. Decomposition of the (In,Ga)N ternary alloys is defined by the differences in the bond strengths of the constitutes [1] giving a rise to the different formation enthalpy [2] of InN and GaN.

Binary	Length of the bond [Å]	Bond strength [eV]	Formation enthalpy [eV]
GaN	1.95	2.20	-1.08
InN	2.15	1.93	-0.21

Table 2.3.: Material parameters of InN and GaN collected from literature: length of the bonds [145], bond strength [57, 67], experimental values of formation enthalpy [146]. Value of the In-N bond strength correlates well with the activation energy of the binary decomposition.

As can be seen from Table 2.3, the bond strength of InN is significantly lower than that of GaN, which results in a significantly lower formation enthalpy and makes the growth of ternary (In,Ga)N alloys challenging, and requires low growth temperatures, where, as we will see below the In solubility is low. At these low growth temperatures, where InN is still stable, the In composition in an (In,Ga)N alloy is given by the difference of Ga and N atoms at the growth surface, i.e. at a given flux of In and Ga atoms it is the the N flux controls the In incorporation.

At high growth temperatures dissociation of the weaker In-N bonds in respect to GaN of the grown alloy becomes crucial. This leads to loss of In from the alloy and has to be compensated for by an increased N flux to keep alloy stable [147]. The loss of N by dissociation of the InN bonds was described by Averbeck et al. [148] and Turski et al. [147] and actually defines the InN loss:

$$InN^{loss} = x \cdot const \cdot \exp(-\frac{E^{a}_{InGaN}(x)}{k_B T}) \tag{2.46}$$

where x - is the concentration of In in the alloy, k_B - Boltzmann constant, T - the growth temperature and $E^{a}{}_{InGaN}$ - the activation energy for decomposition. The activation energy of the compound can be estimated via a linear interpolation of GaN and InN activation energies [67, 138]:

$$E^{a}_{InGaN}(x) = (1-x)E^{a}_{GaN}[3.6eV] + xE^{a}_{InN}[1.9eV] \tag{2.47}$$

For (In,Ga)N alloys grown at temperatures close to the optimum for GaN only low In concentrations were examined [17].

[1] Bond strength represents the energy required to break the bond between atoms.

[2] Here, enthalpy describes the amount of energy released (when $\Delta H_{InN,GaN} < 0$) with the formation of the bond. Formation enthalpy is calculated as a difference between the total energy of the compound and energy of the bulk metal atoms and energy of the nitrogen atom: $\Delta H_{InN,GaN} = H^{Tot}_{InN,GaN} - H_N - H_{In,Ga}$.

In conclusion, to reach high In concentrations in (In,Ga)N it is essential to keep growth temperature low and the nitrogen flux high to prevent fast (In,Ga)N decomposition at a given temperature [30].

2.5.1.2. Phase diagram (In,Ga)N

Solubility in (In,Ga)N alloys in terms of thermodynamics has been discussed mainly by theory. Starting with the work of Ho and Stringfellow [149] it has been shown that a large miscibility gap exists at the low temperatures that are required to stabilize the In-N bond during the growth. As a result, phase separation is expected. This is mainly due huge discrepancy in the lattice constants between the GaN and InN of the binaries in the compound. While the aforementioned calculations based on empirical potentials studied were focused on relaxed bulk (In,Ga)N, work by Karpov [22] showed that strain as it is present in pseudomorphically grown (In,Ga)N on GaN stabilizes the alloy against phase separation (see Fig. 2.15 (a), (b)). More explicitly, for relaxed epilayers the spinodal curve[3] defines a large area across the whole compositional range. A single phase alloy is obtained only for the high temperatures not desirable for MBE growth of In-rich alloys (> 600 °C). Within this region, the compound, therefore, is expected to exhibit severe compositional fluctuations. Moreover, as was discussed by Stringfellow et al. [150], the solubility of InN into GaN should be $<5\%$ under the MBE growth temperatures, giving the spinodal decomposition of the (In,Ga)N compound into two coexisting phases, InN and GaN. Binodal phase separation (light green regions in Fig. 2.15(a)) requires some energy and occurs near lattice disruptions or impurities.

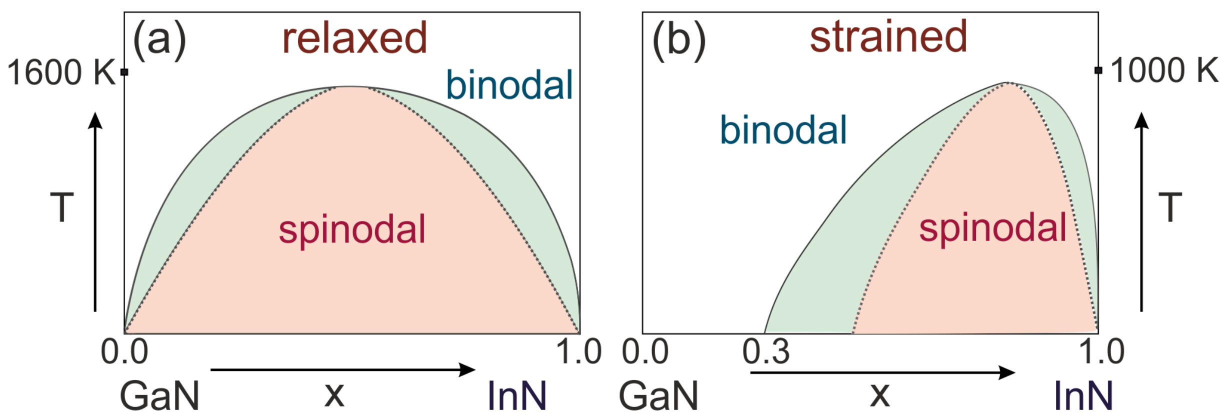

Fig. 2.15: Schematic representation of the temperature-composition phase diagram of ternary (In,Ga)N alloy for: (a) relaxed and (b) strained layers. The phase diagrams were adapted from the various works of [22,150,151]. Spinodal curve (dashed) and binodal (solid) separate the unstable, metastable and stable regions.

On the other hand, strong compressive strain of the In-containing layers grown on GaN suppresses the nucleation of In-rich clusters and, therefore, phase separation. As a result, the critical temperatures for phase separation decrease so the metastable and unstable regions move towards high indium concentrations (see Fig. 2.15 (b)). The calculations performed by Karpov, based on thermodynamics have been later confirmed by ab-initio calculations, based on cluster expansion by Zunger [152]. Experimentally there are few works that would evidence phase separation or spinodal decomposition (see, for instance, Doppalapudi et al. [23]). Partially relaxed layers still can be grown inside the binodal curve due to the residual strain stored in the

[3]Spinodal curve separates the metastable (binodal) region from the unstable (noted spinodal).

alloy and, e.g. thick epilayers from Rao et. al. with a graded compressive strain profile showed coherent and phase separated regions [153].

To sum up, growth of high In content (In,Ga)N ternary alloys requires lower growth temperatures and high nitrogen chemical potentials. Phase separation is effectively suppressed for the biaxially strained (In,Ga)N layers grown on GaN. Up to 30% indium composition is accessible at the growth temperatures low enough to avoid (In,Ga)N decomposition as shown by Karpov et al. [22]. Going towards higher growth temperatures is hampered due to the higher probability of the dissociation of the In-N bonds. At the same time, in literature there is a lack of works reporting on the (In,Ga)N alloys grown on GaN with high indium contents without relaxation followed by dislocation formation. In the experimental work of Singh et al. authors reported on the growth of the biaxially strained GaN/(In,Ga)N/GaN heterostructures with indium concentration up to 81% [154], however, without an information on the degree of relaxation in these structures.

According to the phase diagram, both In rich and Ga rich alloys are stable over a wide range of temperatures, while compositions from 30% to 80% are prone to phase separation and spinodal decomposition. Therefore, growth of digital alloys formed of InN and GaN becomes an obvious choice. Yoshikawa et al. were the first to present the ultra-thin InN quantum wells on GaN below the critical thickness for plastic relaxation[4] but deposited at high growth temperatures, 650 °C [33]. Although, Ga-N bonds are stable at this temperature, the possible dissociation of the In-N bond was prevented by the deposition of the capping layer of GaN. Thus, nitrogen bonds of the 1 monolayer thick InN QW is stabilized by the bonding with upper GaN-matrix. However, a quantitative analysis of the final composition was not presented. These types of structures, i.e. thin (In,Ga)N QWs ($\sim$ 1 ML thick) coherently grown on GaN are investigated and discussed in the current work.

2.5.2. Optical phenomena in (In,Ga)N

2.5.2.1. Polarization fields

In polar (In,Ga)N/GaN heterostructures polarization fields considerably impact the recombination properties. Along with the macroscopic spontaneous polarization present in wurtzite crystals, an additional piezoelectric component arises for the InN and GaN compounds. The spontaneous polarization is intrinsic to the hexagonal lattice symmetry and an effect that is caused by the nature of the chemical bonds. Ga and N differ in electronegativity, so every Ga-N bond is partly ionic and therefore has a certain dipole moment. This differs for the cubic GaN phase where dipole of the bonds cancel out due to the higher symmetry. In wurtzite GaN, the bonds along the c-axis have a different length than the bonds nearly perpendicular to the c-axis, so there is an effective electronic dipole induced along c-direction [51]. The piezoelectric polarization originates from the strain induced by the lattice mismatch of the constituents that shifts the atoms, thus, the charges along and cause the piezoelectric polarization. Likewise, significant difference in both in-plane and out-of plane lattice constants of InN and GaN ($\sim$ 11%) leads to the presence of the strain components along the c-direction. Although piezoelectric and spontaneous polarization were found to be of comparable magnitude, the latter one

[4] Various theoretical works have presented on the critical thickness of the (In,Ga)N grown on GaN for misfit dislocations depending on indium content. Critical thicknesses for pseudomorphic growth of InN/GaN were found in the range 1-2 MLs [21, 155, 156]

could be hardly estimated in bulk materials. Defects, impurities and surface charges obscure the measurements, thus the spontaneous one can be quantified only theoretically [51, 157].On the other hand, compositional variations in the heterostructures have both uncompensated spontaneous and piezoelectric polarization fields that induce charge densities influencing the optical properties of alloys.

The total polarization of the system will be defined as:

$$P_{tot} = P_{sp} + P_{pz} \tag{2.48}$$

Where P_{sp} is a constant value that is defined for the material and P_{pz} is defined by strain. The piezoelectric polarization can be expressed via either the strain tensor,ε_j, or the stress tensor, σ_j, and their corresponding piezoelectric coefficients, e_{ij} and d_{ij}.

$P_{pz} = e_{ij}\varepsilon_j = d_{ij}c_{jk}\varepsilon_j = d_{ij}\sigma_j$, where $c_{jk}$is an elastic tensor, $j,k = xx,yy,zz,xy,zx,yz$.

If we consider an alloy grown in (0001) orientation we obtain a z-component of P_{pz}:

$$P^z_{pz} = 2\left(e_{31} - \frac{c_{13}}{c_{33}}e_{33}\right)\varepsilon_x \tag{2.49}$$

, where $\varepsilon_x = \frac{a^{sub}-a}{a}$.

Here a and a^{sub} are the in-plane lattice parameters of the material grown on top of the substrate and the substrate itself, respectively. Elastic coefficients, c_{jk}, and piezoelectric components, e_{ij} were found for InN only theoretically and for GaN calculated and measured components have been obtained [157–159]. The spontaneous polarization of InN and GaN is found to be in the range of $\sim$ - 0.04 C/m^2 and -0.03 C/m^2, respectively [36, 51]; the piezoelectric polarization estimated for coherently grown InN on GaN is $\sim$ 0.15 C/m^2 [41]. The coefficients of (In,Ga)N compound are usually derived via Vegard's law, i.e. by linear interpolation. The resulting directions of the spontaneous polarization for GaN and both types of polarization of (In,Ga)N compound are displayed in Fig. 2.16.

The spontaneous polarization points towards [000-1], here the electric dipole is oriented from the nitrogen atom towards gallium. The direction of P_{pz} is determined by the strain. Likewise, tensely strained compounds suffer from [000-1] piezoelectric polarization and compressively strained - from [0001].

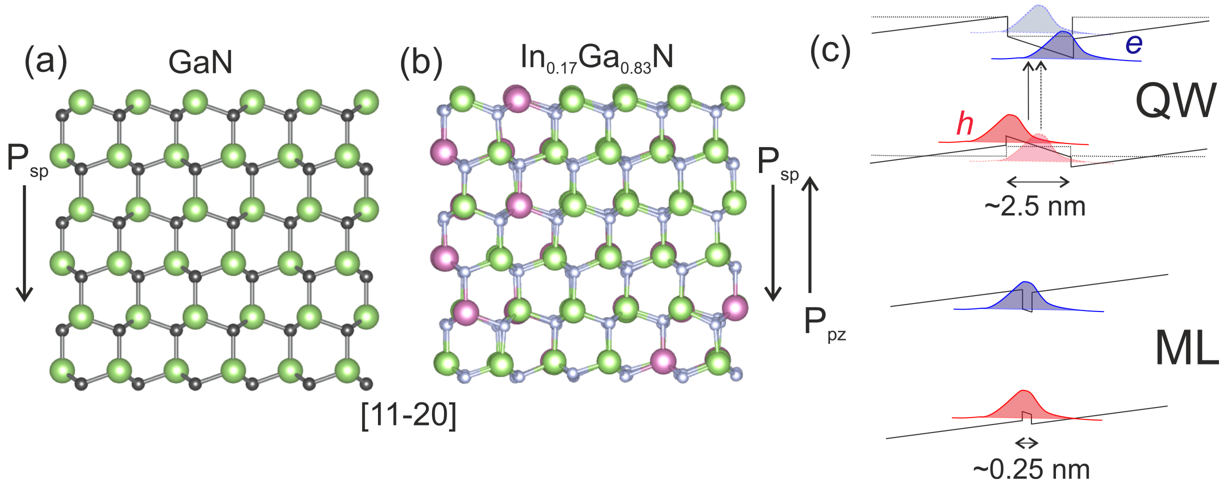

Fig. 2.16: Directions of the spontaneous polarization in GaN (a) and spontaneous and piezoelectric polarization in the (In,Ga)N ternary alloy (b). (c) Band bending and wave functions in conventional QW (upper) and ML thick quantum well (lower).

Thus, the (In,Ga)N/GaN interfaces are strongly charged. The polarization field crucially factor influences the optical properties of polar (In,Ga)N quantum wells. The electric field of the quantum well is defined via:

$$E_{QW} = \frac{h_B(P_B^{tot} - P_{QW}^{tot})}{h_{QW}\varepsilon_B + h_B\varepsilon_{QW}} \tag{2.50}$$

and

$$E_B = -\frac{h_{QW}E_{QW}}{h_B} \tag{2.51}$$

where $\varepsilon_{B/QW}$ are the static dielectric constants of the barrier and QW materials, $h_{B/QW}$ are thicknesses of the barrier and QW and $P_{B/QW}^{tot}$ - the total piezoelectric (spontaneous and piezoelectric) fields.

They significantly deform the electronic band structure and cause a separation between the electron and hole wavefunctions, thus reducing the probability of their recombination. The Coulomb interaction and recombination of the separated electrons and holes results in lower emission energies. This phenomenon is called quantum confined Stark effect (QCSE) [160]. In Fig. 2.16 (a) we show schematically the influence of the polarization fields on the band structure of a classical polar QW. Separation of the carrier wavefunctions due to the band tilting can be compensated via Coulomb screening of the polarization fields under additional electrical field (see dotted lines in Fig. 2.16 (a)). Then, a flat band condition is reached and one observes an increase of the emission energy of the band to band transitions under applied electric field [161]. Electric fields up to 6.5 MV/cm were estimated theoretically for the (In,Ga)N/GaN superlattices with thick ($\sim$ 2 nm) QWs [162]. The strength of the piezoelectric field causing the QCSE increases with the indium concentration in the (In,Ga)N alloys and with the thickness of the quantum wells [163, 164]. Due to the deformation of the bands the emission and absorption (that is near the flat band condition of the (In,Ga)N QW) edge energies are not the same, so the QCSE reflects the Stokes-like shift [165].

Increasing of the barrier thickness or decreasing of the QW width reduces the strength of the polarization fields [36,41,162]. Moreover, for the ML (0.26 nm-thick) a large separation of the wavefunctions is not expected simply due to the small thickness of the QW as we show in Fig. 2.16 (b).

2.5.2.2. Localization phenomena in (In,Ga)N structures

Strong localization of charge carriers due to the non-uniform distribution of the Indium atoms within the ternary alloy (e.g. ordering or clustering [166–169]) was suggested to explain the high internal quantum efficiencies of (In,Ga)N-based LEDs. At the same time, higher In contents induce larger In fluctuations that paired with the QCSE may induce stronger carrier separation within the QW and result in turn in lower probability of recombination [14, 19, 170]. Bellaiche et al. [171] were the first to show by theory that no In atomic clustering in the GaN lattice is needed for strong localization of the hole wavefunction. They revealed that even in a perfect random alloy a single In atom may cause resonant hole states that induce strong hole localization even below the valence band maximum of the alloy itself extending towards GaN valence band. The same trend was shown later for the In-rich quantum dots [172]. Random distribution of indium leading to the local variations of the potential minima was discussed in [173, 174]. Overall, localization of the charge carriers strongly influences recombination

properties of the alloys and leads to:

- broad emission peaks $\sim$ 100 meV measured at cryogenic temperatures [20, 175]. Schulz et al. have shown by atomistic calculations that electrons were localized at well-width fluctuations (giving a variation up to 45 meV of the ground state energies) and holes at In-rich regions (with variations in the ground state energies up to 150 meV) [176].
- a characteristic S-shape of the temperature dependence of the peak emission energy examined for the standard QWs [177–179] and discussed by means of the band-filling model. According to this model, the temperature dependence can be divided into three regions: (i) the first low temperature *redshift* occurs due to the thermally activated band filling of the states with lower energies; (ii) the following *blueshift* under higher temperatures has been argued in many works as induced by the carrier distribution between localized states in accordance with Boltzmann statistics [180]. Kazlauskas et al. has suggested that carrier transport between these local states is possible through phonon-assisted hopping of excitons [181]. (iii) The final redshift at high temperatures follows shrinkage of the band gap, as present for many semiconductors (see 2.4.1).
- stronger electron-phonon coupling, i.e. more intense phonon sidebands discussed in Refs [182, 183];
- non-exponential PL decays found for polar (In,Ga)N/GaN QWs at low temperatures [175]. For instance, Morel et al. has proposed a model, where recombination of the individually spatially separated electrons and holes on various distances slows down the recombination dynamics similar to the donor-acceptor pair-like recombination [184].

2.6. Theoretical calculations

2.6.1. Density Functional Theory

Very briefly we will introduce the methods used for theoretical calculations in this work. Density Functional Theory (DFT) enables to calculate the ground-state electronic structure of solid state materials, atoms and molecules. By means of DFT the energy band structures, thermodynamic and kinetic properties, defect energies, structural properties, e.g. elastic relaxation and phase stability, the prediction of the properties in novel structures can be addressed.

As a quantum mechanical method, in DFT the Schrödinger equation should be solved but via the functionals derived by the spatially dependent electron density. Properties of the many-electron system are derived through the external and internal, i.e. corresponding to the electron-electron interaction, potentials affecting the system. The Hamiltonian in the Schrödinger-like equation consists of three terms:

$$(U+T+V)\psi_n(\bar{r}_i) = E_n\psi_n(\bar{r}_i) \tag{2.52}$$

where $\boldsymbol{U}$ - operator of the interaction potential, i.e. exchange and correlation of the particles, $\boldsymbol{V}$ is an external potential operator that takes into account the external electric fields, $\boldsymbol{T}$ - the operator of the kinetic energy. For the full form of the Eq. 2.52, i.e. Kohn-Sham equation, that is very similar to Schrödinger equations, and potentials we refer to the [185].

Most important, in DFT the many-body problem can be simplified to a single particle by representing the kinetic and interaction potential operators via the particle density, $n(\bar{r})$. Hence, a set, N, of 1D (for each direction) electron equations should be solved for the supercell with N electrons. The Hohenberg-Kohn theorem states that the external potential, v_{ex}(that belongs to the $\boldsymbol{U}$ operator) is determined uniquely by the ground state density $n_0(\bar{r})$. This gives a solution to the Schrödinger equation, i.e. wavefunction ψ_n, that in turn defines ψ_0- the many-body ground-state wave function corresponding to the lowest energy of the system: $n_0(\bar{r}) \stackrel{d=3}{\rightarrow} v_{ex}(\bar{r}) \stackrel{d=3N}{\rightarrow} \psi_n(\bar{r}_i) \stackrel{d=3N}{\rightarrow} \psi_0(\bar{r})$.

Thus, the total ground state energy of a many electron system is a functional of the density, $\psi_0(n,\bar{r})$. Here the computational effort in the first iterations is reduced due to the low dimensionality, d, the overall costs for the system with N electrons are $N^{\alpha}$with $\alpha\sim$2-3. Nevertheless, DFT has some limitations in respect to the estimation of band gaps (typically underestimated) and since DFT gives a single particle picture, the electron-hole interactions, i.e. excitonic effects are not considered.

The interaction of the particles hidden in the operator $\boldsymbol{U}$ is described by the electron-electron Coulomb repulsion (following the Pauli principle) and exchange-correlation potential of the many particle system. The latter one is a matter of various approximations employed in DFT. The most used is a local-density approximation (LDA), also employed for the calculations performed for this work. In LDA the functional depends on the coordinates and density that is considered to be equally spread, its energy is derived via the summation of two terms - exchange and correlation part. Heyd, Scuseria, and Ernzerhof (HSE) [186] hybrid functional employs the exchange interaction based on a screened Coulomb operator. It was shown to give more accurate results of band gap energies [50] but with a higher computational effort, thus, cannot be employed for large supercells.

The DFT calculations presented in the main body of the text were performed by L. Lymperakis at Max-Planck-Institut für Eisenforschung by using the Vienna ab-initio simulation package.

2.6.2. K*p model calculations

$K \cdot p$ model calculations are used to determine of the energy band structure of semiconductors by employing a Hamiltonian that includes an interaction between the multiple bands. For instance, 2-band $k \cdot p$ model considers an interaction of the conduction band with one of the valence subbands. The 8-band $k \cdot p$ allows the coupling between the conduction band, where a spin of the electrons is taken into account, and all three upper valence subbands, i.e. the heavy-, the light-holes and the crystal field split-off bands. The corresponding Hamiltonian would have an 8x8 dimension [187]. However, this model considers only parabolic energy dispersion close to the center of the Brilluoine zone, i.e the single particle states in the proximity of Γ point. $k \cdot p$ is also a continuum model, i.e. the single particle Hamiltonian does not include an atomistic description of the ionic potential. Due to this macroscopic restriction, it may not be suitable for the complicated low-dimensional systems of small size. Therefore, the application of the continuum model might be questionable for ML-thick layers discussed in this work since they do not account for the atomistic nature of the alloy. However, the $k \cdot p$ method enables to calculate structure sizes that are not accessible to DFT calculations. In this work calculations were performed by O. Marquardt from the Weierstrass-Institut for Applied Analysis and Stochastics, Berlin, by means of an eight-band $k \cdot p$ theory in combination with linear elasticity theory [188]. Marquardt et. al [189] demonstrated a decent precision of the eight band k*p

method when compared to various microscopic approaches employed for the calculation of the energy levels in the GaN QD.

3. Quantitative methods of the indium content analysis

3.1. Aim of the chapter

In this part we discuss the methods to quantify the indium composition of ultra-thin (In,Ga)N quantum wells used in this work. In more details, we have employed strain analysis and Z-contrast analysis based on high resolution TEM and scanning TEM imaging, respectively. In the first method lattice parameters of the QW in respect to the surrounding GaN are measured that can be directly translated into the indium incorporation. The whole procedure described explicitly in 3.3.1 enables to estimate the indium incorporation in the (In,Ga)N alloys with a high precision, that for the HRTEM lattice parameter analysis results in the statistical error as low as 1.2 pm. On the other hand, *Z-contrast* analysis is a straightforward method not impaired by the phase contrast inversions present in HRTEM imaging. All our experimental data are compared to the results of the multislice image simulations and frozen phonon simulations performed on the *in house*-developed software. At the end we discuss XRD measurements as one of the methods widely used for the compositional quantification in QWs and its applicability for our ultra-thin (In,Ga)N alloys.

3.2. Multislice image simulations

Going back to the HRTEM imaging, the experimental results obtained under "proper" imaging conditions, i.e. negative spherical aberration and optimum overfocus, should be compared to computer simulations. They help us to ensure a direct interpretation of the HRTEM images and to consider the influence of the sample thicknesses of the investigated area in quantitative analysis. In this regard, we have done multislice simulations via a self-developed software, which uses the phase plates and Fresnel propagator calculated with the EMS program package [80].

In general, in the multislice method, suggested by Cowley [190] and developed by Goodman and Moodie [191], the specimen is divided into slices of thickness Δz separated by Δz vacuum space. The incident beam propagates normal to the sample surface through all the slices being. The slices are considered to be very thin, each of them inducing a phase shift to the scattered beam. The electron beam passes through the sequence of projected potentials of each slice, or phase gratings. The electron wavefunction on the exit of each slice would be represented via its small varied portion as:

$$\psi(x,y,z+\Delta z) = p(x,y,\Delta z) \otimes [t(x,y,z) \cdot \psi(x,y,z)] \quad (3.1)$$

– *p(x,y,z)* represents a propagator function of microscope (i.e. when the beam moves

between the two slices) that corresponds to the Fresnel propagator (note, that due to the small distances the near-field diffraction is considered) in the reciprocal space, i.e.:

$$p(x,y,\Delta z) = F^{-1}[P(k,\Delta z)],\ P(k,\Delta z) = \exp(-i\pi\lambda k^2\Delta z) \tag{3.2}$$

- *t(x,y,z)* is a phase grating function describing the transmission through the specimen defined by the inner atomic potential introduced in the WPOA Eq. 2.23, *U(x,y)*:

$$p(x,y,z) = \exp[\frac{2\pi ime\lambda}{h^2}U(x,y)\Delta z] \tag{3.3}$$

The multislice equation of two neighboring slices *n* and *n+1*, determined via the sample thickness *h,* where $h = n\Delta z$, would be:

$$\psi_{n+1}(x,y) = F^{-1}\{P_n(k_x,k_y,\Delta z_n)F[t_n(x,y)\cdot\psi_n(x,y)]\} \tag{3.4}$$

Eq. 3.4 has an FFT form that enables to reduce computational time of the multiple iterations to $Nlog(N)$ instead of N^2 [192]. In the next iteration the wave described by Eq. 3.4 propagates further to the following slice and the final exit wavefunction of the specimen is found as the wavefunction of the last slice. Now we have calculated interaction of the electron beam with the specimen, one should introduce aberrations of the objective lens (see the phase distortion function, $\chi(q)$ in 2.15). Above, in Fig. 2.7, we have presented the results of such simulations, although our software enables to add astigmatism induced by the condenser lens, chromatic, star aberration and axial coma.

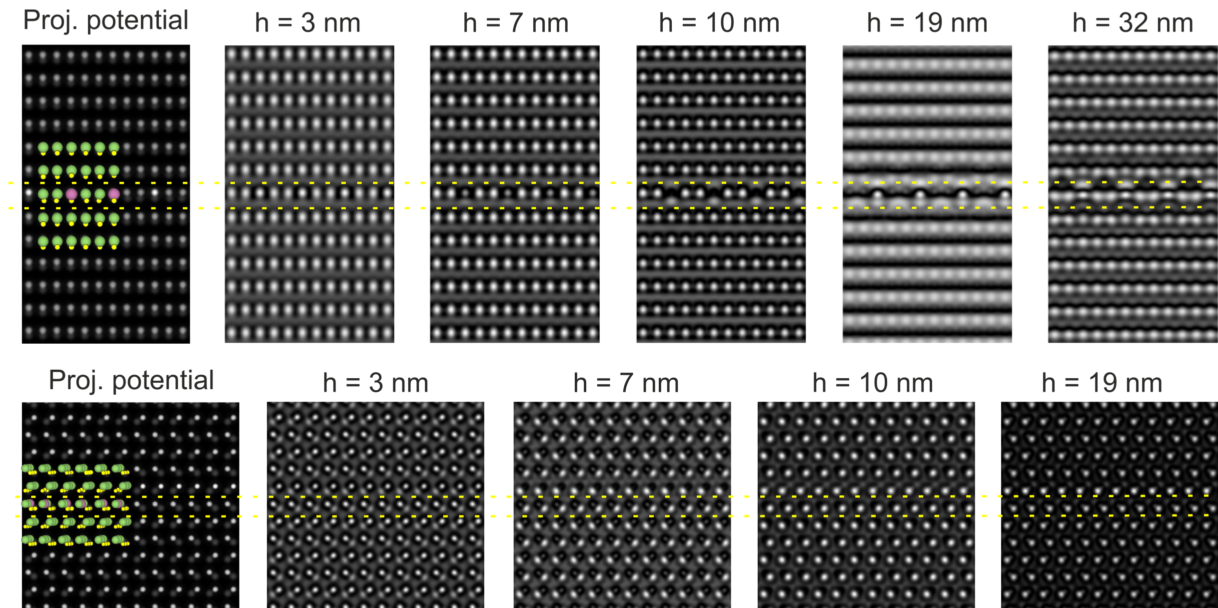

Fig. 3.1: Multislice simulations of the thickness series performed in the <1-100> (upper row) and <11-20> (lower row) projection directions. Relaxed supercell containing 1 ML $In_{0.33}Ga_{0.67}N$ QW is shown in color. Area of the monolayer is enclosed by two yellow dashed lines. Optimum imaging conditions, i.e. negative C_s and slight overfocus were applied.

In Fig. 3.1 we present results of the multislice simulations performed for the relaxed supercell with ordered one monolayer $In_{0.33}Ga_{0.67}N$ QW in thick GaN. The supercell was divided into slices of thicknesses $\frac{\sqrt{3}}{2}a$ normal to the simulated <1-100> (upper row) and <11-20> (lower

row) projection directions. For the <1-100> direction an increase of the thickness by ∼3-4 nm modifies significantly the image pattern - in the thinnest sample the In atomic columns are barely visible. At 7 nm thickness a well distinguished ordering of the indium atoms can be observed. At a thickness 10 nm the contrast from the indium atomic columns vanishes what indicates that the first extinction length for indium is reached. At this thickness an artificial intensity between atomic planes becomes more pronounced. At 19 nm the contrast inverts - no intensity from Ga atomic columns is seen, i.e. we have approached the first extinction distance for Ga. At the same time, intensity from half space fringes becomes predominant. Note that indium atoms appear bright, the second extinction length is not reached due to the non-uniform periodicity of the Pendellosung oscillations. Moving towards large thickness (32 nm) an atomic ordered pattern is again well-pronounced, however, multiple imaging artifacts emerge. As can be seen, the thickness at which the location of the atomic intensity maxima directly corresponds to the projected atom column structure shown on the left is very limited. An important effect that has to be considered when analyzing (In,Ga)N quantum wells in term of a projected atomic potential is the difference in the extinction lengths of In and Ga. An optimum thickness for quantitative analysis lies below the extinction distance of indium, i.e. < 10 nm.

Turning to the other projection direction, <11-20>, - contrast corresponding to the projected potential can be observed only for very thin areas (3 nm), here Ga is bright and dim nitrogen atoms are also visible. But the contrast of the Ga atomic columns reverses with N already at 7 nm, so nitrogen atoms are predominant. Moreover, indium atoms may be hidden between Ga (see the atomic supercell on the left of Fig. 3.1). Therefore, we perform our quantitative strain analysis of images taken mostly in <1-100> projection (see the description of the method in 3.3). In the work of Schulz et al. a thickness-defocus series but of the GaN layer showed a similar result, i.e. that image pattern is more stable in the <1-100> projection direction in the limited range of thicknesses 5-10 nm [81].

3.3. Quantitative HRTEM analysis

Once we know that our image pattern corresponds to the projected atomic potential we can measure lattice distortions induced by the implementation of the foreign, indium, atoms into the GaN matrix directly from the HRTEM images. Analysis of the atomic displacements due to strain does not take into account the contrast variations of the atomic species. The approach to measure compositions from image pattern was first introduced by Bierwolf et al. [193] for the measurement of the interatomic distortions of two strained lattices via the analysis of the Moiree patterns [1]. The distances are estimated independently and compared also with the computer simulations. Later, various works were dedicated to the strain measurement analysis of thick (In,Ga)N quantum wells in [194, 195], also by means of geometrical phase analysis in Ref. [168].

We perform the quantitative HRTEM investigations as follows:

1. In the thin part of a specimen (∼5-10 nm thick) 30 images are taken under 1.4Mx magnification and identical overfocus, approximately +6 nm. Schulz et al. [81] has shown that taking multiple images enables to reduce the statistical error, from 4.6 pm for a single

[1] Moiree fringes is an interference pattern of the beams diffracted from the layers with similar but not identical lattice plane parameters.

image to 1.2 pm. The main source of errors is an amorphous layer always present on top of the structure. Then, the whole series is cross-correlated in the *in house* software.

2. A peak finding algorithm assigns a gravity center of each bright spot, i.e. atom, on summation of the series with coordinates. Distances between the atoms are measured. This data set from the summation is then transferred to each image, averaged and merged into the lattice parameter map of the series. The c-lattice parameters are measured as double distance between the spots, S, and mean value is found as: $c_{ij} = \frac{1}{n}\sum_{k=1}^{30}(S_{ijk} - S_{i+2jk})$.

3. These data are compared to the ones obtained via multislice simulation of the atomic supercell of the structure corresponding to the experimental one. The supercells are relaxed by modified embedded atom method (MEAM) - potential [196] in order to access the lattice distortions of the alloys. This method was shown to be reliable, i.e. the bond length of the simulated InN (=1.07 GaN bond) was almost equal to the one obtained from the DFT calculations (=1.069 GaN bond) [197].

4. Indium content is calculated from the lattice plane parameters.

As mentioned in the beginning of the work, the content-strain dependence can be described by a simple Vegard's law relation (Eq. 2.1). However, for an accurate estimation, one should take into account the strain state of the (In,Ga)N alloy. In this work we have investigated thin (In,Ga)N quantum wells, ∼1 ML thick, coherently grown on GaN. The QW is under the biaxial strain, i.e. the stress is induced in two directions along the surface - <1-100> and <11-20>, the lattice relaxes along the <0001> plastically or elastically, i.e. with or without the formation of dislocations. For such type of structures the in-plane lattice constants can be considered identical to the a-plane parameters of the hosting layer, i.e. GaN. Thus, embedding of the InN monolayer leads to the expansion of the out-of plane lattice parameters solely. Thicker structures, for instance standard 2-3 nm-thick (In,Ga)N QWs, may suffer from the thin-foil effect originating from the outwards lattice distortion in <1-100> direction in the thin areas of the specimen comparable to the thickness of the quantum well itself [194]. This means that the QW is under uniaxial strain, i.e. the crystal is strained only in one direction but relaxes in two others. Rosenauer *et al.* has estimated the 5 nm thickness limit for the offset of the outward relaxation of the lattice for a conventional 4 nm QW, where thicker specimens would still undergo biaxial strain state [198]. In thicker QWs it was shown that analysis of the in-plane parameters improves the measurement precision impaired by local strain variation induced by alloy fluctuations [81, 197].

For the QWs discussed here a biaxial strain is applicable 2.1, thus, the in-plane strain components are identical:

$$\varepsilon_{xx}(x) = \varepsilon_{yy}(x) = \frac{a_{GaN} - a_{InGaN}(x)}{a_{InGaN}(x)} \tag{3.5}$$

where $a_{(In,Ga)N}$ is defined from the Vegards law Eq. 2.1. Out-of plane strain is defined via ε_{xx}:

$$\varepsilon_{zz}(x) = -2\frac{C_{13}(x)}{C_{33}(x)}\varepsilon_{xx}(x) \tag{3.6}$$

Elastic constants C_{13} and C_{33}similar to in-plane lattice parameters (see Eq. 2.1) can be found via the Vegard's law for the layer with In concentration, x:

$$C^{ij}_{InGaN}(x) = C^{ij}_{InN}(x)x + C^{ij}_{GaN}(x)(1-x) \tag{3.7}$$

The final out-of plane lattice parameter is found via the bulk c-lattice constant is found through Eq. 2.1:

$$c'(x) = c_{InGaN}(x)(1+\varepsilon_{zz}(x)) \tag{3.8}$$

Material	C_{13} [GPa]	C_{33}[GPa]
GaN	106	398
InN	92	224

Table 3.1.: Elastic parameters for InN [159] and GaN [51] used in the multislice simulations.

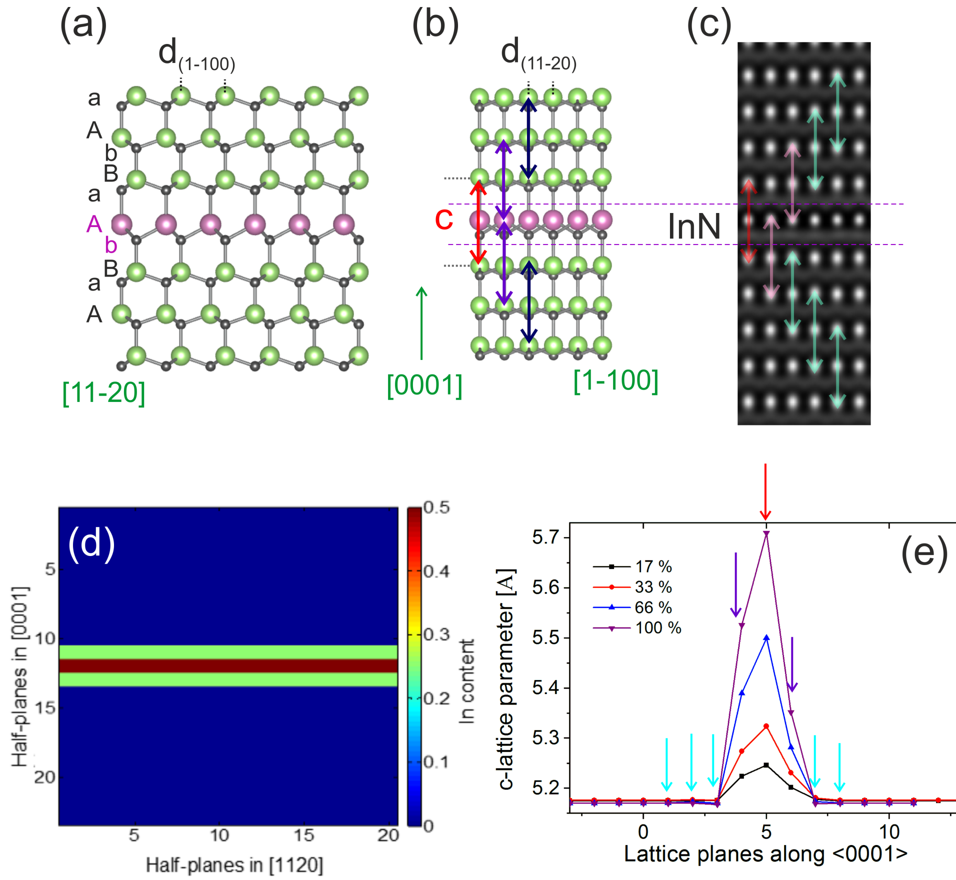

Fig. 3.2: Simulated InN (violet) monolayer thick quantum well in GaN (green atomic columns), nitrogen atoms shown as small gray balls shown in two imaging directions, i.e. (a) [11-20] and (b) [1-100]. "AaBbAa" letters mark the stacking sequence of wurtzite lattice, violet letters denote the atomic planes corresponding to the InN monolayer. (c) Simulated HRTEM image by means the multislice simulation method extracted from the thickness region of 4.4 nm. Colored arrows show the measured interplanar distances across the whole image. (d) Strain map converted to indium composition. C-lattice parameters are then averaged along the <11-20> direction. The resulting profile is presented in (e) for different simulated supercells with 17, 33, 66 and 100% of indium in the monolayer. The colored arrows correspond to the out-of-plane parameters measured in (c).

We have performed transmission electron microscopy imaging of (In,Ga)N/GaN superlattices in two principle projection directions <1-100> and <11-20> as shown in Fig. 3.2 (a),(b) where we present the simulated supercell containing ideal InN ML-thick quantum well and thick GaN barrier. The interplanar spacings can be derived via the in-plane lattice constants and are different in two projections: $d_{(11-20)} = 1/2 \cdot a$, $d_{(1-100)} = \sqrt{3/2} \cdot a$. The monolayer inserted into GaN is actually formed by two atomic planes: a plane of nitrogen and indium atoms, i.e. following the ... AaBbAaBb... notation of wurtzite sublattices, - bA (as shown in Fig. 3.2 (a)) or aB. The c-lattice parameter corresponding to the monolayer is measured as a spacing between the same sublattices, i.e. Bb-Bb or Aa-Aa.

In Fig. 3.2 (c)-(e) we show the procedure to measure the indium content of a *simulated* supercell containing a single InN monolayer. The quantum well in the corresponding simulated HRTEM image can be clearly identified by different contrast compared to the host GaN lattice, however, the out-of plane lattice distortions are too small as in Fig. 3.2 (c). The c-lattice parameters are measured as shown by colored arrows and the strain map, i.e. where the relative difference of the lattice parameters of the QW in respect to GaN c-lattice constants is constructed (see in Fig. 3.2(d)). The maximum indium content within one monolayer is 50% and the rest is distributed between the surrounding in <0001> direction lattice planes. As a result of the measurement, the averaged c-lattice constant profile has a triangular shape as shown in Fig. 3.2(e) with a maximum corresponding to that of bulk InN. This computer simulation shows that introducing a single monolayer InN leads to the expansion of 3 neighboring lattice planes. Note, that a similar triangular shaped strain profile but with lower maxima are obtained for the whole calculated range of indium contents - 17%, 33% and 66%.

It has been shown in [199] that beam damage during the TEM observation may induce false In fluctuations. Since we are measuring image series we can exclude such electron beam induced changes in the sample by analyzing the first and the last image in the series. No visible changes of the HRTEM images during the recording of series of 30 images have been observed. Moreover, the beam current density obtained in our experiments for the typical high-resolution TEM image (the investigated area of ˜ $50nm \times 50nm$) was approximately 25 A/cm^{-2}(for the maximum current of 1 nA). Such densities are non-destructive for GaN-based structures during the exposure times used in our experiments as reported in [200]. Schulz et. al. [81] have shown that the difference between the c-lattice parameters of the first and last image from the series is identical in the GaN and QW regions, although, the standard deviation (STD), i.e. the estimation error, of single images is larger.

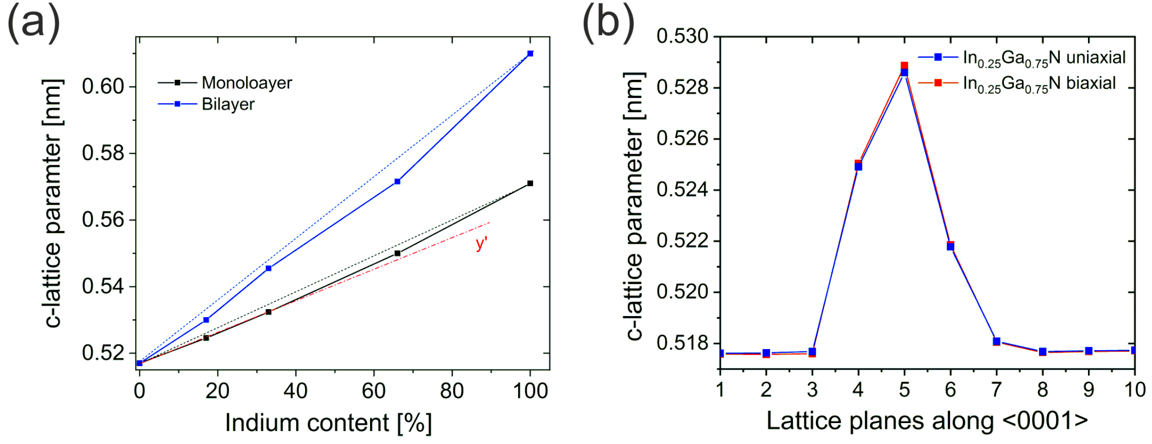

Fig. 3.3: (a) C-lattice parameters as function of the In content in the monolayer (black) and bilayer (blue) thick $In_xGa_{1-x}N$ QW obtained from simulated supercells. Blue and black solid lines are linear dependencies described via the Vegard's law: $c_{InGaN} = xc_{InN} + (1-x)c_{InGaN}$. The red line corresponds to the linear fit of the low indium content region till 33%. (b) A comparison of the c-lattice parameter profiles obtained from the simulated supercells containing single ML $In_{0.25}Ga_{0.75}N$ QW under biaxial (red) and uniaxial (blue) strain.

The resulting indium content is estimated from its linear dependence with the c-lattice parameter.

In Fig. 3.3 (a) we present the out-of-plane lattice parameters obtained from the simulated supercells (see Fig. 3.2(e)). The structures consist of a 1 ML thick quantum well, containing 17, 33, 66 and 100 % In. As can be seen from the plot, the relation between the out-of-plane lattice constant and In content is almost linear and only a slight bowing occurs for high concentrations. Considering a purely linear dependence of the c-lattice parameter and the In content results in a measuring error of around 2%. However, as we will demonstrate further, indium incorporation in our monolayers is less than 33%, therefore, our estimations are well described by the following linear dependence derived from the fitting (see red line in Fig. 3.3 (a)).

$$x = 2145.9[nm^{-1}]c'_{InGaN}[nm] - 1109.2 \tag{3.9}$$

, where $c'_{(In,Ga)N}$ is the out-of-plain lattice parameter measured in the experiment. A measuring distance of our method is in the range of 3 MLs, thus, trilayers can be treated already as the thick QWs, i.e. measuring of the in-plane lattice parameters is required.

For bilayer thick alloys (see Fig. 3.3 (a), blue curve) the dependence of the lattice parameter undergoes a larger deviation from the linear dependence. Since we consider a biaxial strain state of the sample and neglect thin foil relaxation this slight downward bowing occurs due to the configuration of the supercells that contained ordered (In,Ga)N. The first principle calculations from Cui et al. [201] demonstrated that ordered alloys obtain large discrepancy from the linear law than the supercells with random (In,Ga)N with small In fluctuations. Nevertheless, to account for the difference in the c-lattice parameters of the monolayers under uniaxial and biaxial strain, we have preformed multislice simulations of the uniaxially strained QW. According to Fig. 3.3 (b) although, the expansion of the out-of-plane lattice parameters under biaxial strain is slightly larger than under the uniaxial strain, the absolute difference between the lattice parameter profile is negligibly small.

3.3.1. HRTEM analysis of the as-grown (In,Ga)N QW

In Fig. 3.4 we present a quantitative analysis of one of the quantum wells from the SPSL stack grown following the recipe presented in 2.2.3 grown at 550°C. The experimental HRTEM image shown in Fig. 3.4(a) is a summation of the cross-correlated image series taken in <1-100> projection. The region containing a QW is hardly visible but can be inferred from faint contrast variation within the layer. In Fig. 3.4(b) a color-coded map shows the averaged relative distances between the atomic columns derived from the experimental images of the series following the procedure explained above (see 3.3). Larger distances correspond to the larger lattice distortions, i.e. higher Indium composition. The quantum well area is represented in red-orange color, the GaN barrier is almost uniform (blue-green) with small variations.

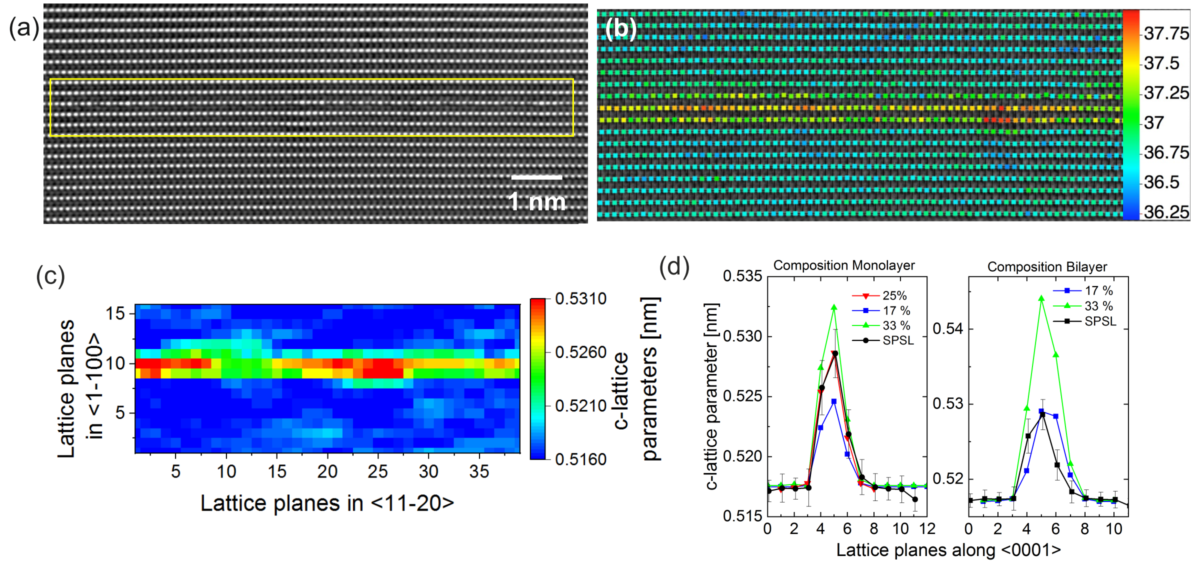

Fig. 3.4: (a) Summation of 30 cross-correlated images taken along <1-100> under identical focus conditions. QW-containing region is surrounded by the yellow box. A color-coded strain map represented in the pixel (b) and nm-scale (c). (d) The experimental (black) out-of-plain lattice parameters averaged in lateral direction shown with the STDs and compared to the profiles found from the simulated supercells containing a monolayer (left) with 17% (blue), 25% (red) and 33% (green) indium; and (right) bilayer (In,Ga)N with 17% (blue) and 33% (green).

A lattice parameter map with pixel scale converted to nanometers is presented in (Fig. 3.4(c)). Averaging along the <11-20> direction yields the mean c-lattice parameter of the layer, i.e. the mean composition Fig. 3.4(d). The resulting mean out-of-plane lattice constant is 0.5282±0.0011 nm. The experimental profile has a similar triangular shape as in the simulated supercells, but with a much lower composition than the nominal value, i.e. 100%. We also present a comparison with the bilayer simulation. For the double monolayers the profiles have larger width, because the incorporation of the two layers of (In,Ga)N leads to the expansion of 5 surrounding GaN atomic planes. However, the experimentally found profile is narrower and the best fitting is obtained with the simulated supercell containing single monolayer QW with 25% of In. More precisely, according to the empirical formula Eq. 3.9 the averaged indium composition is 24.2%. The measurement precision of each individual atomic column is given by STD in GaN region and is ± 1.6 pm, i.e. ± 3%. For the averaged value of c-lattice parameter

the precision is estimated from the mean c-lattice parameter deviation measured in the GaN that is slightly lower and for this particular example is 1.1 pm or 2%. The latter we define as the experimental error for the mean In content: 24.2±2.0%.

Compositional variations within the layer are present. Content fluctuations are estimated as an STD of the QW region with extracted error of the measurement, i.e. an STD of the barrier region giving 6%.

3.4. Quantification analysis in STEM.

3.4.1. Simulations based on frozen phonon approximation

For the multislice STEM image simulations we employ the so-called "frozen phonon" approach developed by Kirkland et al. [202]. Several configurations of the supercell divided into multiple slices (like was done for HRTEM simulations shown in 3.2) are simulated with the randomly varied atomic displacements corresponding to the lattice vibrations. The electron beam propagates through these slices. Since the incident electron has a higher velocity ($\sim 0.77c$), time for its travel through the crystal ($\sim$ fs) is much faster than one vibration period of an atom ($\sim$ ps) so the lattice would appear as "frozen". During the exposure time ($\sim ms$) of the real STEM experiment many interactions of the electrons and lattice are registered. In our simulations we have set 20-50 configurations that is found to be enough to account for thermal diffuse scattering and save computational time. The resulting STEM images are a superposition of all configurations.

In Fig. 3.5 (a) and (b) we present the STEM simulated images for the supercells containing thick GaN layers with 1ML and 2MLs (In,Ga)N with an In content of 33%, respectively. For this particular simulation, the maximum acceptance semi-angle range of the detector was set to 30-323 mrad, the semi-convergent angle of the incident beam - 9 mrad. Our simulations showed that the HAADF contrast of the (In,Ga)N layers along <11-20> projection is higher than the one obtained along <1-100>. The inter-atomic d-spacings in the <11-20> projection ($\sim$0.276 nm) are bigger than in <1-100> (0.159 nm) and twice time larger than the resolution limit of 0.13 nm obtained in STEM. Therefore atomic displacements contribute to a larger extent improving the electron channeling giving an additional contrast to the HAADF signal. The final (In,Ga)N layers appear brighter than GaN according to the Z-contrast principle of imaging.

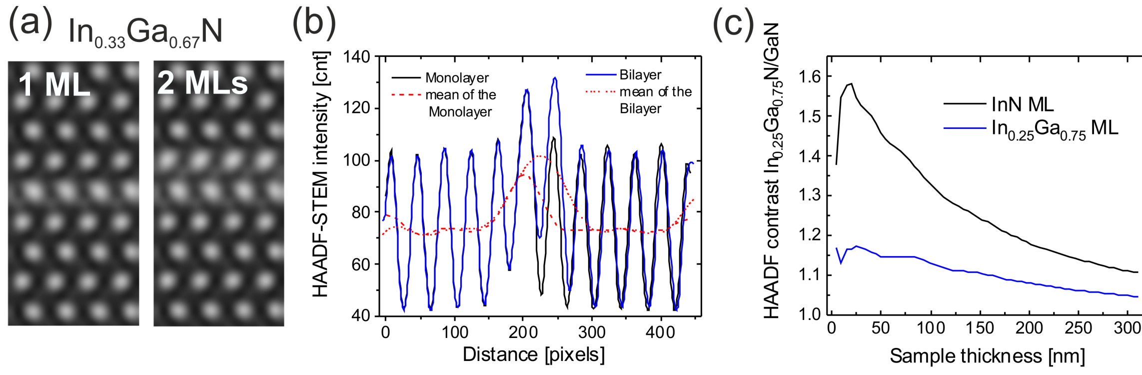

Fig. 3.5: (a) Simulated STEM images along the <11-20> projection obtained for the $In_{0.33}Ga_{0.67}N$ quantum wells one (left) and two (right) monolayers thick. Frozen phonon simulations were performed for the thickness range up to 37 nm (shown here). (b) STEM intensity profiles extracted for the 1 ML (black) and 2 MLs (blue) QWs by averaging along the growth (vertical) direction. Mean intensities of the profiles are shown as short-dashed (for a monolayer) and dotted (foe a bilayer) lines. (c) HAADF-STEM intensity ratio of 1 ML (In,Ga)N with 25% (blue curve) and InN (black curve) to GaN calculated for the specimen thickness range from 0 to 310 nm.

3.4.2. Composition quantification via Z-contrast

The *so-called* Z-contrast analysis is based on the assumption that the intensity of the beam scattered on the atomic columns is proportional to their atomic number (see Eqs. 2.31 2.32 in the description of the STEM investigation technique 2.3.1.5). Therefore, the difference in the intensities of the InN and GaN atomic columns is directly pronounced on the HAADF-images due to the higher atomic number of indium. For the quantification analysis in STEM, the measured HAADF intensities are normalized to the electron beam intensity, i.e. to the detector signal in every session. The fraction of electrons scattered from the incident beam and registered by the detector is given by:

$$I = \frac{I^{exp} - I^{vac}}{I^{det} - I^{vac}} \tag{3.10}$$

where I^{exp} - is the actual intensity measured from the experiment, I^{vac} - a background signal and I^{det} - intensity of the incident beam, the maximum signal registered by detector in current experiment.

The registered scattering intensity strongly depends on specimen thickness (increases for thicker specimens) and composition of the (In,Ga)N alloy (also increases for higher In content). Since, the composition of the (In,Ga)N layer is unknown and the investigated specimen has a wedge shape, the sample thickness is derived from the surrounding GaN, compared to the simulated HAADF intensities of the pure GaN. Then, it is extrapolated to the region with (In,Ga)N if the QW is relatively thick as most of the structures discussed in literature, i.e. 5-10 nm [87, 198]. The latter is not needed for our structures approximately 0.26 nm thick. Note, that the projection effect induced by the miscut of the substrate may give a false impression of the QW thickness especially of thin alloys. HR-STEM images taken from a thin specimen area, therefore, are required. For the known sample and QW thickness the final composition is estimated by comparison to simulated STEM images with various concentrations. More details on the method of compositional quantification by HAADF-STEM imaging can be found in the

works of Rosenauer et. al. [198, 203].

However, one should take into account that channeling and dechanneling effects are important factors that influence the contrast in STEM HAADF imaging in general and in ternary alloys in particular. The different bond length of In-N and Ga-N (due to the difference in the atomic radii of In and Ga) cause static displacements of the atoms from the position they would assume in the virtual crystal approximation and cause dechanneling, i.e. loss of the signal of the off-scattered electrons to the diffuse background (see more in [87]). This leads to a total intensity measured at high angles that is lower as compared to the case neglecting atomic static displacements. In Fig. 3.5 (c) we present a ratio of (In,Ga)N/GaN depending on thickness for the ML-thick quantum well with 25% and 100% of indium. The HAADF-STEM intensity was averaged from the small cells of the $\frac{1}{2}c \cdot 2.4nm$ - size containing 1 (In,Ga)N monolayer. For the sample thicknesses below 25 nm the contrast ratio of the $In_{0.25}Ga_{0.75}N$/GaN is oscillating reaching its maximum of 1.18 at approximately 30 nm. Then it slowly decreases to 1.05 at the largest calculated thickness 310 nm, except a limited region from 50 to 80 nm where the ratio remains constant. For a pure InN ML such dependence has a comparable dependence, though the absolute value of the ratio is considerably higher of 1.58. Nevertheless, for the samples thicker than 30 nm a steady intensity decay is observed. Similar results were found from the simulations of Dimitrakopulos et al. [204] for the 33% In-containing simulated supercell, the intensity reduction was even more pronounced for the supercells with 67% and 100% of In. Attraction of the scanning electron beam to the periodic atomic lattice induces the oscillation of the HAADF intensity with thicknesses in thinner area regions. In thicker specimen area the diminishing of the HAADF-intensity could be explained by the the electron probe spreading out through the sample thickness. Thus, the relation between the collected signal of ultra-thin (In,Ga)N and surrounding GaN reduces. Nevertheless, in the simulations of the $(In_xGa_{1-x})_2O_3$ compound from Wouters et al. [205] and simulation of the bulk InN [204] show the same trend, i.e. decrease of the intensity, opposite to the continuous rise of the HAADF-signal observed for GaN [198].

A circumstance to be particularly mentioned for single MLs is the projection effect induced by the miscut of the substrate that may give a false impression of the QW thickness. This occurs if the beam direction is at an oblique direction with respect to the step direction. For this reason HAADF-STEM image taken in thin specimen area is required to measure the alloy thickness. At the same time, the described channeling and suppression of the STEM intensity in thicker specimen regions examined in In-containing alloys specifies a narrow region available for quantification in STEM imaging.

3.5. X-Ray diffraction as a quantitative method for ultra-thin quantum wells

We have employed XRD to roughly estimate composition and periodicity of the superlattices. In detail, the diffraction peaks originating from the dynamic interference of the diffracted X-ray beams from the quantum wells in the multi QW structure, give a well pronounced intensity pattern. The satellite peaks of different orders are placed at some distinct relative positions so the respective periodicity of the superlattice structure is measured as distances between the peaks [40, 53]. Broadening of the XRD peaks and suppression of the high order satellites indicates the presence of compositional fluctuations and possible degradation of the structural

quality, respectively.

In Fig. 3.6 we present the XRD measurements of the two superlattice structures with nominally 4 MLs thick InN QWs separated by 10 nm (In,Ga)N barriers with indium content less than 2% deposited at 640 °C (a) and 600 °C (b). Measurements and simulations were preformed by Dr. M. Sawicka in Unipress, Warsaw. Stacking of the multiple quantum wells induces several satellite peaks from the -5th to the +3rd order on the XRD spectra. The 0th peak of the superlattice appears as a shoulder of the GaN (0002) reflection and is measure for the average In content in the stack. An increase of the In content in the monolayers leads to an increase in strain, i.e. an expansion of the out-of-plain lattice spacing. Thus, the satellite QW peak is shifted towards lower angles [66]. In our experimental X-Ray data the (0002) reflection is hardly separable from the GaN's which already indicates that the indium content is lower than 100%.

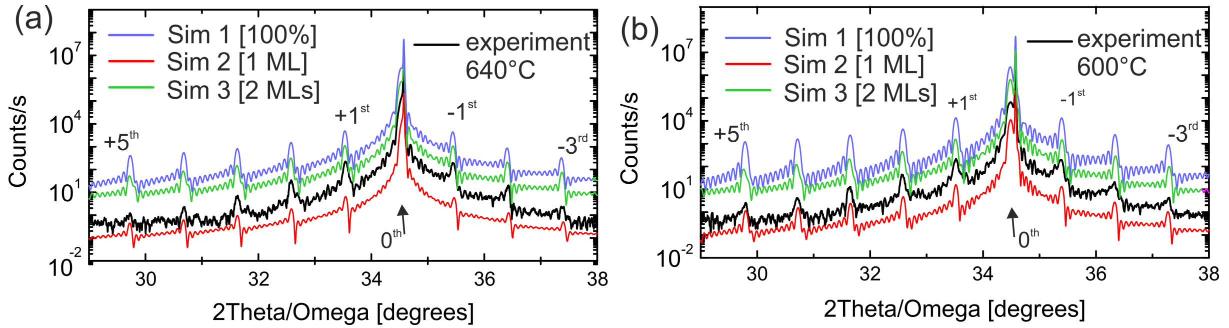

Fig. 3.6: 2ϑ-XRD scan around the (0002) reflection of the nominally InN/GaN SL structures (black) grown at (a) 640 °C (a) and 600 °C (b) shown together with the XRD simulations (shifted vertically) with various parameters: different thicknesses and indium contents.

Sample @640 °C

Nomenclature in Fig. 3.6 (a)	QW thickness [nm]	QW content [%]	QB thickness [nm]	QB content [%]	Correlation parameter
Sim 1 [100%]	0.07	100	9.58	0.5	7.21
Sim 2 [1 ML]	**0.26**	**11**	**9.4**	**0.7**	**6.22**
Sim 3 [2 MLs]	0.7	10	8.95	0.5	7.46

Sample @600 °C

Nomenclature in Fig. 3.6 (b)	QW thickness [nm]	QW content [%]	QB thickness [nm]	QB content [%]	Correlation parameter
Sim 1 [100%]	0.13	100	9.7	0.6	7.49
Sim 2 [1 ML]	**0.26**	**22**	**9.6**	**1.2**	**4.21**
Sim 3 [2 MLs]	0.7	13	9.1	1.0	5.18

Table 3.2.: Parameters utilized for the XRD simulations of both SLs, the best fitting is marked with bold letters.

Two factors - indium content and thickness of the QW define the superlattice peak positions. To simulate the data we have varied both parameters (see blue, green and red curves in Fig. 3.6). A change in fitting parameters (see Table 3.2) results only in barely small changes of the simulated spectra. The difference appears mainly for the 0th order peak - that shifts more for the QWs with 100% of indium, which, however, does not match with the experimental results.

Moreover, the InN/GaN SL simulation suggest a thickness of the layer of 0.07 nm and 0.13 nm for the 640 °C- and 600 °C-grown SLs what actually corresponds to 0.3 coverage . For comparison of the simulation and experimental data we have used the following parameter:

$$w = [log(I_{exp}) - log(I_{sim})]^2 \quad (3.11)$$

where I_{exp} and I_{sim} are the intensities at each point obtained from experiment and simulation. Maximum intensity of the experimental 0th order peak is $3.5 \cdot 10^6$ and $2.6 \cdot 10^6$cnts (Fig. 3.6 (a) and (b), respectively), the background signal is 0.1 cnts for both samples. The average correlation parameters for each simulation are listed in Table 3.2. The lowest parameter, i.e. best fitting for both SL is found for the 0.26 nm thick QW, i.e. 1 ML. The difference in the 0th peak positions between the SLs indicates higher average In content in the whole structure for the SL grown at 600 °C. The resulting compositions were estimated as 22% and 11% of indium (red curves in Fig. 3.6) for the samples grown at lower and higher temperatures, respectively. A slightly smaller spacing between the satellite peaks for the SL grown at 600 °C illustrate a larger (by 0.2nm) thickness and In content (by ∼0.5%) of the barrier.

Nevertheless, we can state that a quantitative measurement of the In content in ∼ ML-thick QWs by XRD is not accurate enough because of the small volume fraction of the QW in the measured structure and the degrees of freedom for the adjustable parameters (i.e. thickness and composition of the well and composition of the barriers). From the XRD simulations, Kusakabe et al. [206] have estimated ∼50 % of indium in single monolayer QWs of a superlattice structure with 4 MLs GaN barriers. In the work of Yoshikawa et al. nominally bilayer thick InN QWs obtained a good fitting for the QW of 0.17 nm thickness as input parameter corresponding to 25-30% of indium [35]. The authors also suggest an ambiguity of the XRD simulations for such fine (∼ ML thick) quantum wells. Cheze et al. [66] presented satisfactory good fittings of the nominally InN/GaN SPSLs with the parameters corresponding to an indium composition less than 10% in the QWs for XRD scans around the (0006) reflection.

Taking into account all these data from literature and our results on XRD simulations we can state that X-Ray diffraction does not give a satisfactory precision to quantify thickness and composition of very thin (In,Ga)N alloys coherently grown on GaN.

4. Study of the indium incorporation in ultra-thin (In,Ga)N quantum wells

4.1. Aim of the chapter

As we have shown above by means of the HRTEM quantification analysis, the indium content in the nominal InN quantum well grown pseudomorphically on GaN is less than 30% 3.3.1. Moreover, all our ultra-thin quantum wells grown according to the standard recipe (see 2.2.3) reveal indium concentrations around 25%. In this part, we will present the results of several growth experiments where thermodynamic and kinetic factors were varied. Indium flux, growth temperature and growth intervals of the (In,Ga)N thin quantum wells were changed in order to increase the In incorporation. We find a certain restriction on thickness and In content in the QWs coherently grown on GaN. Moreover, we will demonstrate an apparent ordering of the indium and gallium atomic columns recorded for the first time by means of HRTEM imaging. We find a direct connection between the examined ordering and a specific surface reconstruction observed by RHEED. At the end, we suggest a theoretical model that explains the compositional and thickness limitation and discuss it together with the other experimental data on nominal InN ML-thick quantum wells found in literature.

4.2. Investigation of the indium content as dependent on growth conditions

4.2.1. Influence of the III/V ratio

In this growth experiment a ratio between the indium and nitrogen flux pressures was gradually changed during the growth of the stack. Each QW was deposited under the progressively decreasing In flux with constant nitrogen flux. A sequence of eight QWs separated by 10 nm GaN barriers was deposited using the standard growth recipe described in 2.2.3. The growth scheme and nominal structure of the superlattice stack are presented in Fig. 4.1 (a) and (b), respectively.

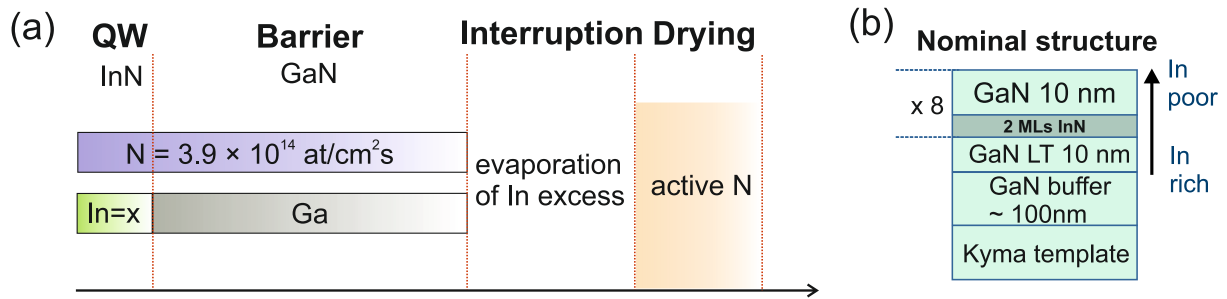

Fig. 4.1: (a) Growth scheme of the superlattice with different III-V ratio. Values of the varied indium flux pressures can be found below. (b) Nominal structure of the sample. Note that growth time was adapted to obtain 2 MLs-thick InN QWs. Indium flux was increasing towards the surface as shown by an arrow.

The growth temperature of the sample was 550 °C. Nominal InN layers were grown by applying indium and nitrogen fluxes, Ga-flux was switched off. Deposition of the barriers was followed by growth interruption and "drying" of the surface with active Nitrogen. The two first layers grown under In-rich conditions were limited by nitrogen flux and the growth time constant was chosen corresponding to 2 MLs deposition at the given N flux. The other six QWs were grown under N-rich regime and limited by the In flux and a growth time corresponding to nominal 2 MLs deposition at the given In flux. N-flux was φ_N=3.9×10^{14}at/s/cm^2in all QWs. The In/N ratios with the fluxes are listed in Table 4.1.

In/N rate	1.4	1.1	0.8	0.7	0.6	0.5	0.4	0.1
φ_{InN}, ×10^{14} atoms/cm^2s	5.39	4.08	3.26	2.71	2.31	1.9	1.37	0.54

Table 4.1.: III-V ratios set for the growth of the QWs and the corresponding In-fluxes. The sequence is shown as grown, i.e. the In flux pressure reduces in <0001> direction.

Composition and structural properties of the deposited QWs were analyzed by means of scanning TEM and high resolution TEM investigations in <11-20> and <1-100> projections, respectively. A STEM overview image of the whole stack taken in a specimen area where the transmitted sample thickness is approximately 80 nm is shown in Fig. 4.2(a). It reveals a high structural perfection of the QWs, represented by high HAADF intensity as compared to the surrounding GaN. The interfaces between the nominally InN QWs and the GaN barriers are abrupt and no obvious indications of In segregation[1] or interdiffusion are visible. The HAADF-STEM intensity from the GaN barriers was normalized by means of the polynomial fitting in *ImageJ* editor [208]. As discussed in (2.3.1.5), STEM intensity of the material, or Z-contrast, is proportional to the atomic number of its constitutes. Thus, by extracting the background signal linearly proportional to the sample thickness we estimate the evolution of indium content in the QWs grown under different conditions. Contrast of the QWs is progressively decreasing towards the surface, i.e. following the reduced indium flux. To ensure that these analysis is not corrupted by the aforementioned HAADF-STEM contrast-thickness dependence for (In,Ga)N (see in 3.4), the profile was extracted from the specimen area with small thickness variation

[1]Indium segregation arises due to the lower potential barrier for Indium driven to replace Ga close to the surface [207].

around 30 nm along the wedge and cross-checked with the other specimen regions giving the similar result.

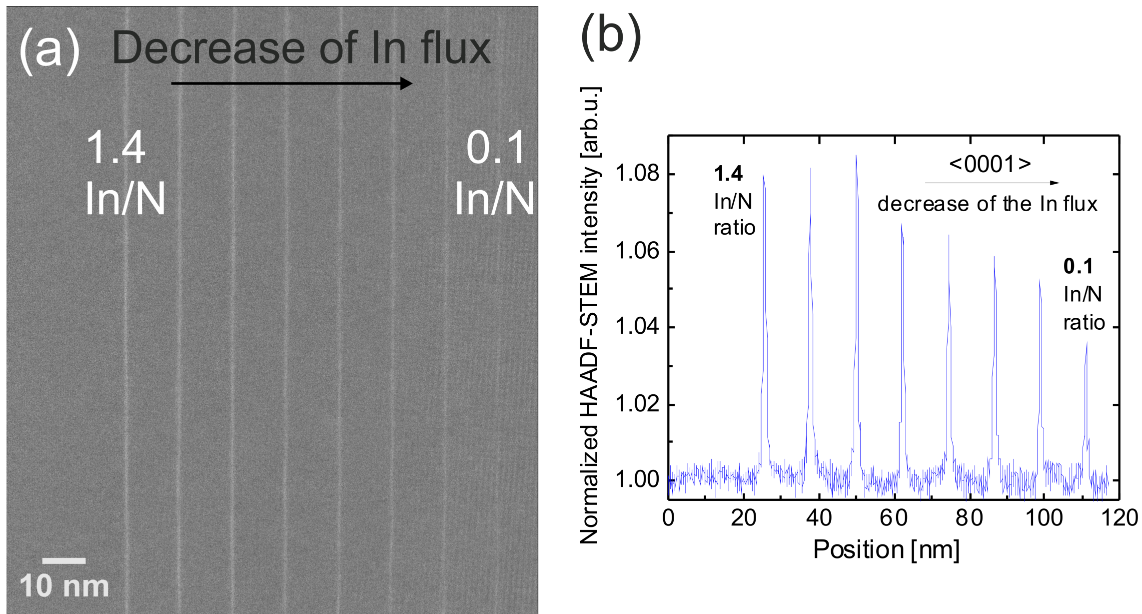

Fig. 4.2: (a) An original (unfiltered) overview STEM image of the III-V ratio structure. Scale is marked on the image. (b) STEM profile extracted from the image on the left.

From the STEM line profile shown in Fig. 4.2 (b)) extracted from Fig. 4.2 (a) the average In concentrations in the QWs can be quantified. Note, that for such thicknesses and magnification the inhomogeneities along the the projection and lateral fluctuations in the composition are averaged out. To account for the changing sample thickness the intensity of the QWs was normalized with respect to the GaN barrier intensity. The first QWs starting from the substrate deposited at In-rich and slightly N-rich conditions (In/N rate 0.8) exhibit an almost constant intensity. Then, keeping the N flux constant and reducing the In flux stepwise for the following QWs leads to a stepwise decrease of the HAADF-STEM intensities from the QWs, i.e. lower indium concentrations in the upper layers. For significantly low In/N fluxes ratio, i.e. 0.1 (see the last QW from the stack) an interrupted QW is formed with the In content of one third of the first QWs grown under the highest rate. The FWHM of the HAADF intensity peaks proportional to the thickness of the QW were symmetric Lorenzian shape and constant along the whole SL stack.

A detailed comparison of the STEM intensities of the selected three QWs extracted from different parts of the stack is shown in Fig. 4.3 (a)-(c), (bottom). The respective HAADF-STEM images (Fig. 4.3 (a)-(c), (top)) were done under higher magnification. To ensure a reliable comparison of the signals measured in the specimen areas with different thickness we have extracted the vacuum levels and the GaN background barrier intensities. According to these images the nominal bilayer QWs are one monolayer thick as can be obtained from the high-resolution STEM images. We compare these results to the frozen phonon STEM simulations of the 1 ML $In_{0.25}Ga_{0.75}$embedded into GaN matrix (see Fig. (3.5)(c)) done with the similar sampling as of the experimental images. The maximum intensity ratio between the $In_{0.25}Ga_{0.75}N$ single ML and GaN in the simulation was 1.18 that corresponds to the ratio observed for In-rich QW (see Fig. 4.3 (a), (bottom)). The contrast of the uppermost QW is 1.07 that implies approx 10% of indium via linear interpolation.

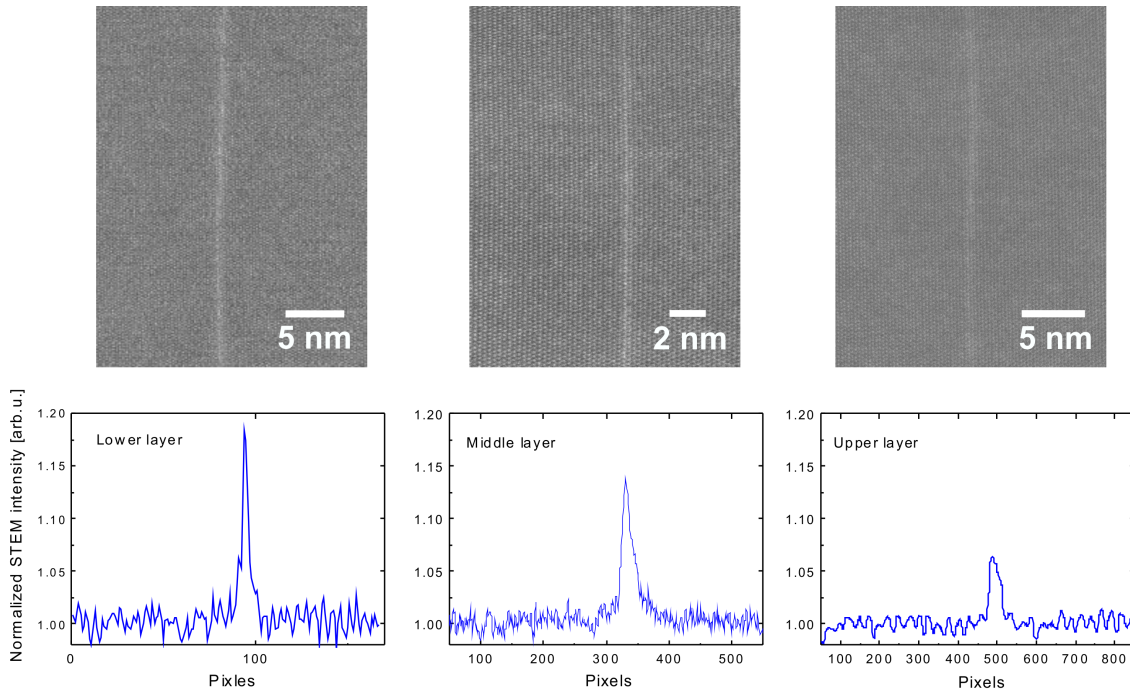

Fig. 4.3: High resolution HAADF-STEM images and their respective profiles from the individual layers grown under: (a) In-rich; (b) slightly N-rich; (c) In-poor conditions.

In Fig. 4.4 we present the results of the quantitative HRTEM analysis of the QW that had the highest HAADF intensity in our STEM investigations. This QW was grown under slightly In-poor condition with 0.8 In/N ratio (QW number 3) that is typically utilized for the standard monolayer deposition. For the out-of-plain parameter's analysis the whole presented field of view was employed. A resulting c-lattice parameter map is shown in Fig. 4.4 (b). Here, the expansion of the c-lattice constants is not homogeneous but a noticeable area of the local widening of the lattice planes can be obtained (see the red-colored region).

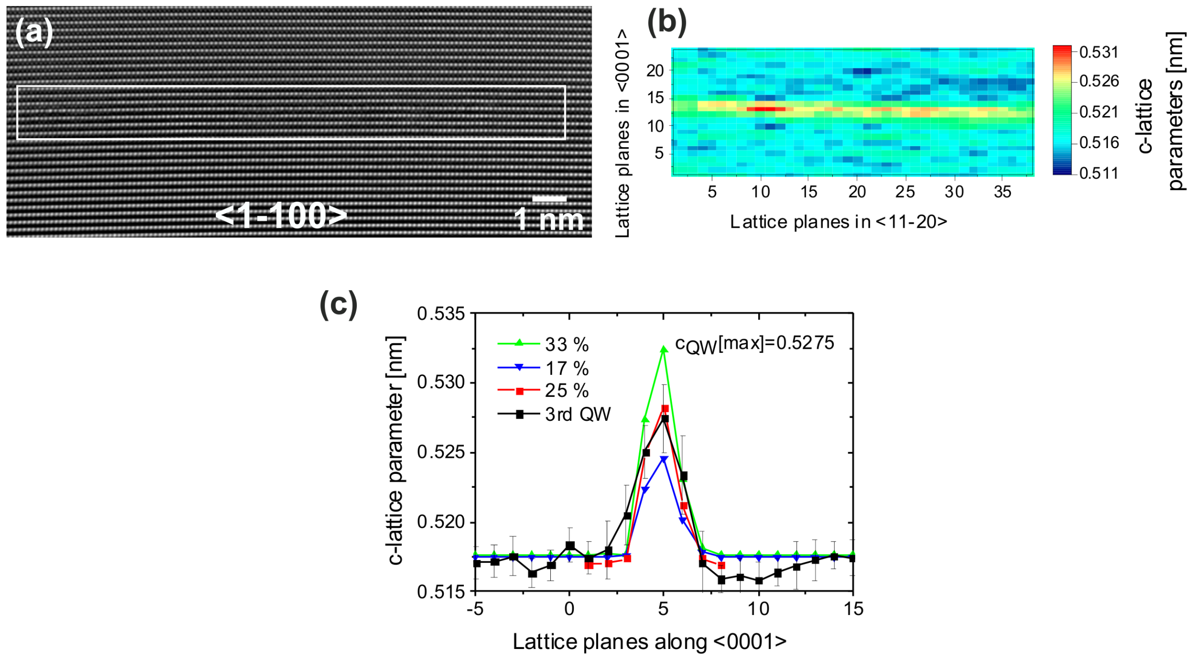

Fig. 4.4: (a) Summation of 30 images taken under identical focus conditions and the highest, 1.4 Mx, magnification. White box marks the area containing the QW. (b) Color-coded c-lattice parameter map derived as the measurement of the interatomic distances in (a). Blue color corresponds to the lower values of the c-lattice constants mostly found in the barrier region and yellow-red - to the expanded distances of the QW. (c) Comparison of the compositional profiles of the experimental QW (black) shown together with STDs and of the simulated supercells with 1 ML thick QW and 17% (blue), 25% (red) and 33% (green) indium concentrations.

The averaged c-lattice parameters along the <0001> direction is shown in Fig. 4.4 (c). This result is compared to the simulated supercells with 17, 25 and 33% of indium content. The profile exhibits a good accordance with the simulated supercell containing 1 ML-thick $In_{0.25}Ga_{0.75}N$ (red). However, the standard deviation of the c-lattice constants of the GaN and QW are relatively high (see thin black lines). The measuring precision was estimated in the barrier region that returns the final c-lattice parameter as 0.5275±0.0023 nm. This corresponds to the indium content in the experimental ML approximately 23%. The indium content variation within the ML was derived from the difference of the STDs in the GaN and (In,Ga)N areas as $\sim$ 3%.

From this growth experiment we conclude that: (i) the indium content at a given N flux increases with increasing indium flux; (ii) the concentration rises from 8% to 23%, until the In/N ratio reaches slightly nitrogen-rich conditions (In/N=0.8); (iii) shifting more towards In-rich conditions does not further increase the indium content.

4.2.2. Influence of the growth temperature

In the second series of experiments we study the influence of the growth temperature on In incorporation. A stack of (In,Ga)N/$In_{0.02}Ga_{0.98}N$ SPSL was grown in the temperature range between 480-650 °C. Each QW in the stack is deposited at a different temperature starting with the highest temperature close to the substrate and lowering the growth temperature in steps of 19°C for the following QWs. C-oriented bulk GaN substrates with 0.5° miscut angle towards <1-100> was utilized.

The structure consisted of 10 nominally InN QWs deposited for 4 sec each separated by 10 nm barriers. In this experiment we have added a small amount of indium to the barrier to obtain better structural and optical properties grown under unfavorable temperatures for pure GaN.[2] The fluxes were: $10.74 \cdot 10^{14}$ at/cm$^2\cdot$s (In), $13.02.10^{14}$ at/cm$^2\cdot$s (N) and $12.65.10^{14}$ at/cm$^2\cdot$s (Ga) thus resulting in $\sim 2.8\%$ of indium content in the barrier. This process was followed by the growth of the next pair sequence "QW+barrier" on the Me free surface. The AFM measurements performed by M.Sawicka (Institute of High Pressure Physics (Unipress), Warsaw) showing rough surface terminated with the 3D islands marked in Fig. 4.6(a), no surface steps were visible, the RMS was estimated as 1.8 nm.

STEM-HAADF image taken at 130 nm sample thickness of the superlattice stack is shown in Fig. 4.5 (a). As can be seen from the high magnification STEM image, the QW grown at 612°C is one ML thick (see inset of Fig. 4.5 (a)). Deposition at growth temperature as high as 650 °C does not to the formation of a continuous QW, i.e. the first layer is interrupted. Decreasing the growth temperature to 631 °C and 612 °C results in homogeneous QWs with no visible structural defects. However, plastic relaxation emerges already at the third QW visible as brighter areas due to the local bending of the specimen perpendicular to the SL. Substantial structural degradation starts from the QW grown at 575 °C. Here, multiple threading dislocations emerge and a severe structural deterioration of the last two layers grown at 499 and 480 °C can be observed.

[2] In details, as mentioned earlier the deposition of GaN in PAMBE under metal-excess is more preferable [63]. A drying step, i.e. the removal of the residual Ga from the surface may lead to the strong surface roughness. It was discussed, that indium may act as a surfactant during the deposition of the GaN barriers [209]. Here we use conditions, where the In flux is kept during the growth of the barriers and the Ga flux is slightly lower than N flux so that all Ga is incorporated. Some of portion of indium incorporates as well with the leftover of the Nitrogen flux and the residual In excess can be easily evaporated from the surface. As a result, the In content in the barriers was very low and controlled by the Nitrogen flux as:

$$x_{max}^{barrier} = \frac{\varphi_N - \varphi_{Ga}}{\varphi_N} \tag{4.1}$$

where φ_{N} and φ_{Ga} are fluxes.

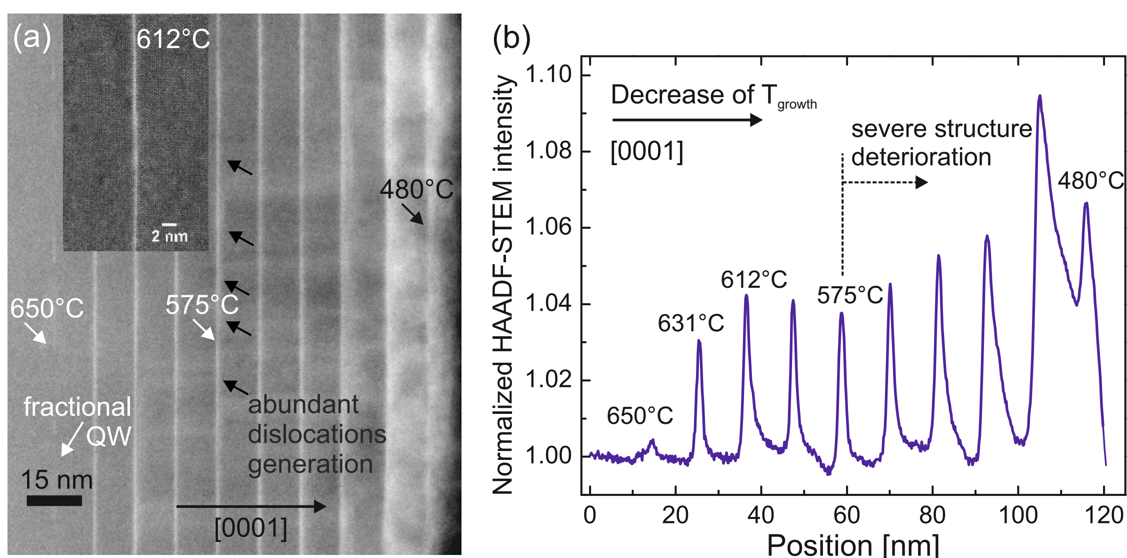

Fig. 4.5: (a) Temperature gradient structure grown under 480-650 °C taken in <11-20> at specimen thickness approx 130 nm. Arrows indicate the area of strong dislocation formation. High resolution STEM of the selected QW is shown in inset. (b) HAADF-STEM intensity profile of the SL extracted from (a).

The HAADF-STEM intensity profile extracted from Fig. 4.5 (a) is presented in Fig. 4.5 (b). Decreasing of the growth temperature from 650 to 612 °C leads to an increase of the indium content that is followed by a saturation of the HAADF-STEM signal for the next three QWs (593-556 °C). Nevertheless, due to the starting deterioration of the structure, the background level of the barrier is fluctuating, impairing a quantification of the Indium content of the QWs. Moving further to the surface, degradation of the crystalline quality becomes more severe also widening the FWHMs of the line profiles of the last four QWs. For the QWs grown below 612 °C analysis of the (In,Ga)N thickness and indium concentration is unreliable.

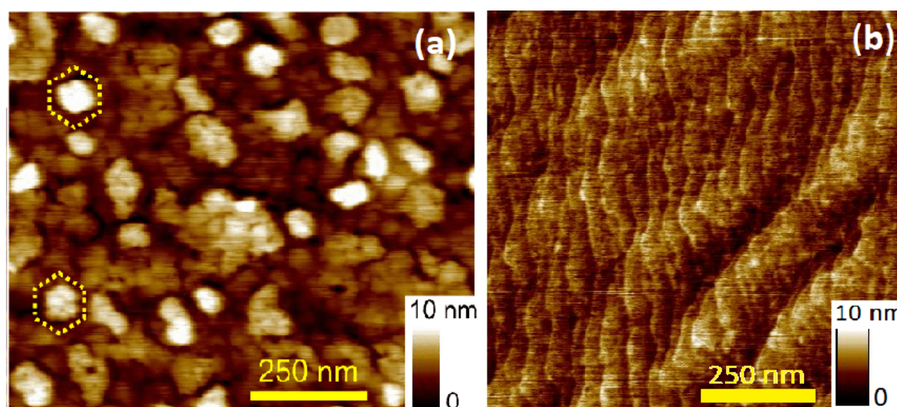

Fig. 4.6: AFM images of the (a) first temperature gradient structure grown in the 480-650 °C temperature range and (b) the second structure grown at 580-650 °C. The values of the RMS parameters are mentioned in the text.

4.7 (a) shows the growth scheme of a second superlattice grown in a narrow temperature range from 650 to 580°C. The analysis of this structure will be discussed in more details in the following. Before deposition of the SL stack surface roughness was estimated by AFM giving an RMS ~0.3-0.5 nm on 5x5 m^2 area.

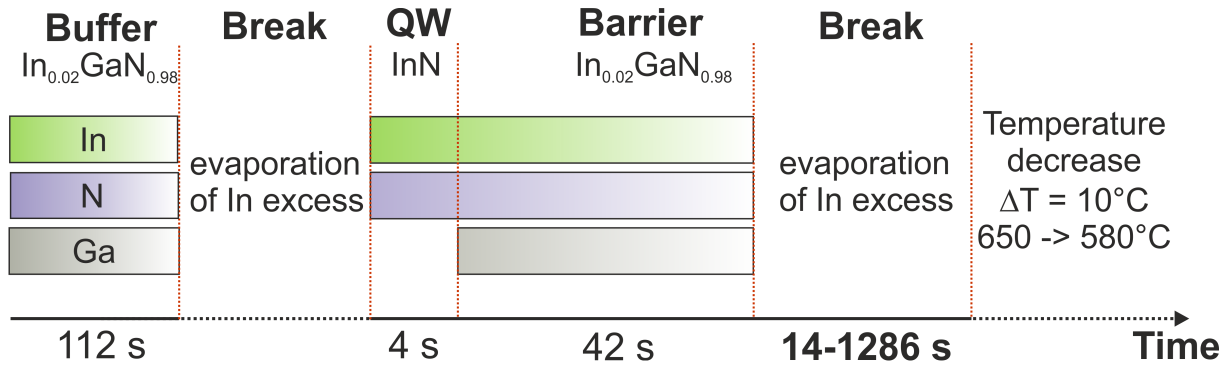

Fig. 4.7: Growth scheme of the QW+barrier sequences deposited at varied temperatures shown together with the underlying buffer layers.

T_{growth} range	Parameter	**In**	**N**	**Ga**
580-650 °C	flux [at/cm^{2}s]	$9.85 \cdot 10^{14}$	$10.95 \cdot 10^{14}$	$10.77 \cdot 10^{14}$
	growth rate [ML/s]	1.07 [InN]	1.19 [InN], 0.96 [GaN]	0.95 [GaN]
480-650 °C	flux [at/cm^{2}s]	$10.74 \cdot 10^{14}$	$13.02 \cdot 10^{14}$	$12.65 \cdot 10^{14}$
	growth rate [ML/s]	1.17 [InN]	1.42 [InN], 1.15 [GaN]	1.11 [GaN]

Table 4.2.: Growth parameters of both temperature gradient superlattice structures. Fluxes shown here in at/cm^{2}s are translated into ML/s. Note, that nitrogen rates for the QW and barriers are different when translated from the absolute value of nitrogen flux.

In this experiment In, Ga and N fluxes were kept constant throughout the the deposition of buffers, QWs and barriers controlled by the Ga flux. QWs were deposited under the turned off Ga supply. During growth of the buffer and barriers In flux pressure was kept on. At the same time, Ga flux was higher than In that led to the predominant GaN formation with small fraction of indium ($\sim$ 1.6%) according to the Eq. 4.1. The growth rates of the QWs and barriers (named as [InN] and [GaN], respectively) translated into ML/s (Table 4.2), were generally higher than those found in the works on (In,Ga)N ML deposition [65,66,210][3]. We have reduced the growth rates and fluxes as compared to the first temperature gradient structure discussed above (see the lower row in Table 4.2) but still kept a slightly nitrogen rich regime.

Two $In_{0.02}Ga_{0.98}$buffer layers approximately 30 nm thick were deposited during 112 s. They were followed by a growth interruption and by a deposition of nominally 4.3 MLs InN. Then, the QW was covered with a GaN barrier. For the following 7 QWs, the growth temperature range was reduced from 650°C to 580°C in steps of 10 °C. Growth interruptions were performed between the growth of each QW+barrier pair in order to evaporate the In excess on the surface. With lowering of the growth temperature the time needed to evaporate the remaining In had to be increased from 14 to 1286 sec. This indicates that higher amounts of In were accumulating on the surface that required longer times for thermal desorption. Finally, after completion of the full stack, the RMS has slightly increased to 0.3-0.65 nm on the 2x2 µm^2 area. Traces of metal droplets were obtained on the larger scans, i.e. not all the In that accumulated on the surface was absorbed and then completely removed. Nevertheless, pronounced surface steps were visible (see Fig. 4.6 (b)).

[3]The growth rates and fluxes are related to each other via the surface area density, i.e.: $[at/cm^2s] = [ML/s] \cdot \frac{at}{a_{XN}^2\sqrt{3}}$, where a_{XN} - is the in-plane lattice constant of InN or GaN.

The structure, shown in Fig. 4.8 (a), appears of high quality with no visible dislocation formation as in the temperature gradient SL discussed above. The image was taken in a rather thick specimen area of 150 nm where the effects of channeling that lead to oscillating intensities in the HAADF image die out but only a slow decrease of intensity is expected (see 3.4). Thickness gradient of this particular specimen was negligible in for the most of the QWs, except the last two alloys, where a steeper thinning was examined. To account for the accuracy of our measurement, we extracted the same HAADF-STEM profiles in different regions and found a similar outcome. The latter can be seen as a dimming of the contrast in the right part of the HAADF-STEM image. In some areas the QWs appear as bilayers due to the projection effect. The substrate with 0.5° miscut angle induces surface steps that may lay at an oblique angle in respect to the projection direction of the TEM sample and, thus, broaden the projected QW thickness if the sample includes a step. The first (In,Ga)N layers starting from the substrate appear with faint contrast of the QWs with respect to the barrier as the subsequent ones grown at lower temperatures. The second QW in sequence deposited at 640 °C (see inset 1 in Fig. 4.8) is partially interrupted. This image was taken in the thinner specimen region (60 nm) under higher magnification. Moving along the growth direction we observed the highest contrast for the QWs in the middle of the stack grown at 620 and 610 °C. The QW deposited at 610 °C is clearly 1 ML thick (see the inset 2 in Fig. 4.8). We note, that contrast in these insets was enhanced to bring up the In atoms and was not used for the quantitative analysis of the composition. The contrast of the last (In,Ga)N layers grown at lower temperatures is slightly reduced.

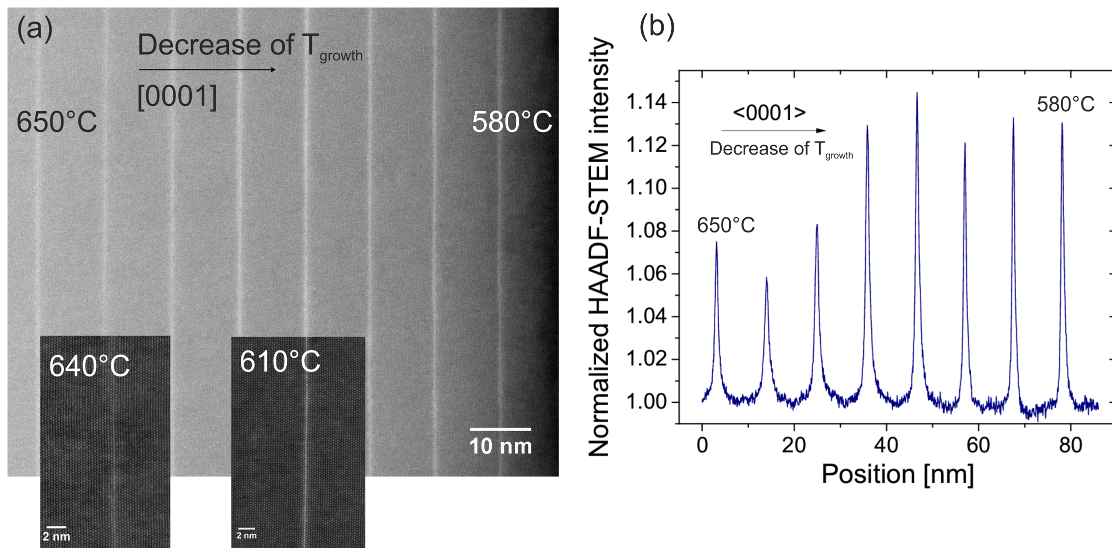

Fig. 4.8: (a) Unprocessed HAADF-STEM image of the specimen area of the SL stack solely taken in <1-120> projection, the <0001> direction is indicated by an arrow. Insets present the selected QWs grown at 640 °C and 610 °C under higher magnification from 60 nm and 30 nm specimen thicknesses. (b) STEM-HAADF profile extracted from (a). Growth direction corresponds to the one from the original STEM image.

HAADF-STEM intensities shown in Fig. 4.8 (b) were extracted from the Fig. 4.8 (a). Intensities of the pure GaN barriers from the simulation and experimental $In_{0.02}Ga_{0.98}N$ barriers can be assumed as equivalent. All the QW intensity line profiles have similar FWHMs. The lowest intensity is observed for the fractional QW grown at 640°C. Following the growth direction, i.e. decreasing the growth temperature, the HAADF-STEM contrast of the QWs increases and reaches a maximum value for the QW grown at 610°C. Further decrease of the growth tem-

perature does not lead to a continuous increase of the In incorporation but to saturation with a slight reduction of the In composition what can arise from the slight thinning of the specimen close to the surface.

The Indium content of the QW that showed the highest HAADF-STEM intensity was studied in addition by means of high-resolution TEM based strain analysis. An experimental HRTEM image of that QW taken in the <1-100> zone axis is shown in Fig. 4.9 (a). The (In,Ga)N QW exhibits a periodic intensity pattern representing an ordering of the Ga and In atomic columns (see Fig. 4.3.1 in the following). The c-lattice plane parameter of the QW and surrounding $In_{0.02}Ga_{0.98}N$ matrix were translated into the strain map presented in Fig. 4.9 (b). The lattice planes of the barrier appear as green colored, (In,Ga)N QW is represented by the increased interatomic distances shown in red. The mean c-lattice parameter is 0.5273±0.0011 nm. As can be seen, the strain in the QW layer is fluctuating, i.e. in the middle of the map there is a region with larger out-of-plain parameter ∼8 nm length (noted as region B), i.e. with higher with In content approximately 25.9%. The surrounding patches A and C both 3 nm long had slightly lower In concentration: A with ∼20.4% indium and patch C with ∼23.4%. Overall, averaging the indium content along <11-20> projection results in 23% with the measurement precision ∼2% and mean compositional fluctuations ∼3%. The QW thickness obtained by HR-STEM investigation (see inset in Fig. 4.8(a)) was one ML.

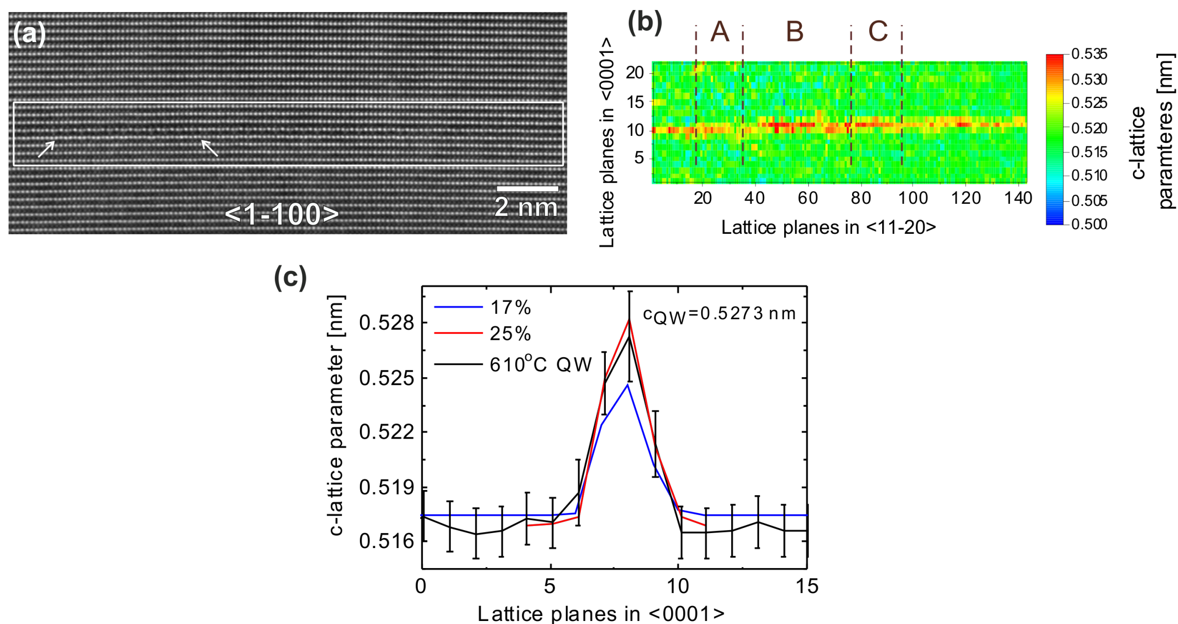

Fig. 4.9: (a) Summation of 30 HRTEM images of the 610°C-grown QW taken under identical focus conditions in <1-100> projection. The QW area is marked by a white box. The arrows indicate the interatomic ordering of the In and Ga atoms. (b) C-lattice parameter map of the same QW proceeded from (a). Colors depict the values of the c-lattice constants increasing from 0.500 (blue) to 0.537 (red). A, B, C denote the regions with fluctuating indium content, i.e. B - with higher and A, C - with lower indium composition. (c) Comparison of experimental (black) and simulated lattice parameters of single (In,Ga)N ML with 17% (blue) and 25% (red) compositions. STDs of the measured distortions are shown simultaneously.

Compositional evaluation of the QWs grown at the other temperatures was difficult due to the fact that: (i) the MLs grown at high temperatures (650-640 °C) were partially interrupted; (ii) a

high experimental error, i.e. big STD due to the low crystalline perfection of the barrier deposited at low temperatures (590-580 °C). Since the Z-contrast of the HAADF-STEM intensities has a direct and straightforward correlation to the composition, especially on the macroscopic scale [88], we utilize the concentration derived by means of the HRTEM and interpolate this value to the STEM intensity ratios found earlier. Assuming that width of the STEM line profiles was similar for all QWs in this gradient SL and that the (In,Ga)N layer deposited at 610 °C showed a thickness of one ML in both HRTEM and STEM analyzes, we conclude that all QWs were single MLs. The resulting values of mean In incorporation in each QW is summarized in Table 4.3. Compositional range lies between 11 and 23%, i.e. changing the growth temperature by just 40 °C results in the doubling of the In content.

T_{growth}[°C]	650	640	630	620	610	600	590	580
In content [%]	11	9	13	20	23	16	18	16

Table 4.3.: Indium content derived from the linear interpolation between the results obtained from HRTEM and STEM analysis. Layers are presented in the order as the SL was grown, i.e. from higher to lower temperatures.

4.2.3. Influence of the QW growth time

In the following section we study the incorporation kinetics, i.e. we grow QWs under identical conditions, but with different growth times. In Fig. 4.10 we present the growth scheme under fixed In and N fluxes the QWs were deposited for different times. Eight nominally InN layers were grown on a GaN template from Kyma. The first two QWs were deposited exclusively under In flux[4], with the N flux switched off followed by growth of a 10 nm GaN barrier. All other QWs were grown by applying of both - indium and nitrogen fluxes.

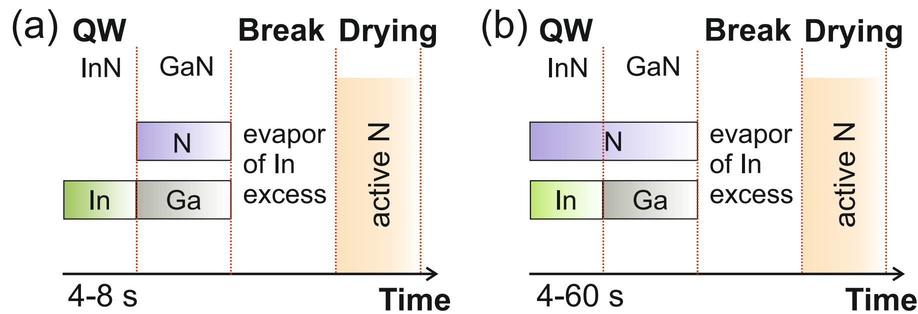

Fig. 4.10: Growth scheme of the nominal InN QWs grown at (a) 4 and 8 s without N supply and (b) 4 - 60 s with both In and N fluxes.

Growth intervals of the first two QWs (with only In flux) were 4 s and 8 s respectively, the next six layers were deposited at constantly increasing growth intervals from 4 s to 60 s. The growth rates were 1.1 ML/s for In and 0.9 ML/s for N which corresponds to 2 to 32 MLs nominal thicknesses of the QWs (see more details in 4.4). The growth temperature was set to 590 °C.

[4]Although, the nitrogen flux was nominally switched off, some nitrogen species may enter the growth chamber due to the MBE set up construction.

QW	QW_3	QW_4	QW_5	QW_6	QW_7	QW_8
growth intervals [s]	4 (In, N)	8 (In, N)	16 (In, N)	28 (In, N)	40 (In, N)	60 (In, N)
nominal thickness [MLs]	2.0	4.0	8.5	15.0	21.0	32.0

Table 4.4.: Growth times and the corresponding thicknesses of the QW_3-QW_8 deposited with indium and nitrogen fluxes.

An STEM-HAADF overview image extracted from the TEM specimen with a thickness of $\sim$ 120 nm is presented in Fig. 4.11 (a). The total change of the thickness along the superlattice was very small $\sim$ 20 nm. The QW_1 and QW_3 grown only with In flux show only a fractional coverage The QWs that were deposited with growth intervals of at least 8 s exhibit full coverage in the STEM image for the projected sample thickness of 120 nm. Fig. 4.11 also reveals that each QW has a similar thickness. The respective normalized HAADF-intensity line profile (Fig. 4.11(b)) shows that FWHMs of the QWs are equal and only the intensity ratio between (In,Ga)N and barrier, i.e. the mean composition of the QWs, changes. The weakest contrast, i.e the lowest mean indium content, can be observed for the first three layers, the two QWs grown at 4 s have the lowest but similar indium content. Increasing the growth time to 8 s results in a higher indium content (see QW_2, In flux only). Adding nitrogen flux leads to formation of QWs with substantially increased indium content (QW_4-QW_8). These QWs exhibit a very similar HAADF-STEM intensity. As can be seen from the HR-STEM images (see Fig. 4.11(c)) the QW_7 and QW_8 that are results of 21 and 32 MLs deposited layers still reveal 1 ML. This is confirmed by the HRTEM imaging performed for the last (In,Ga)N layer.

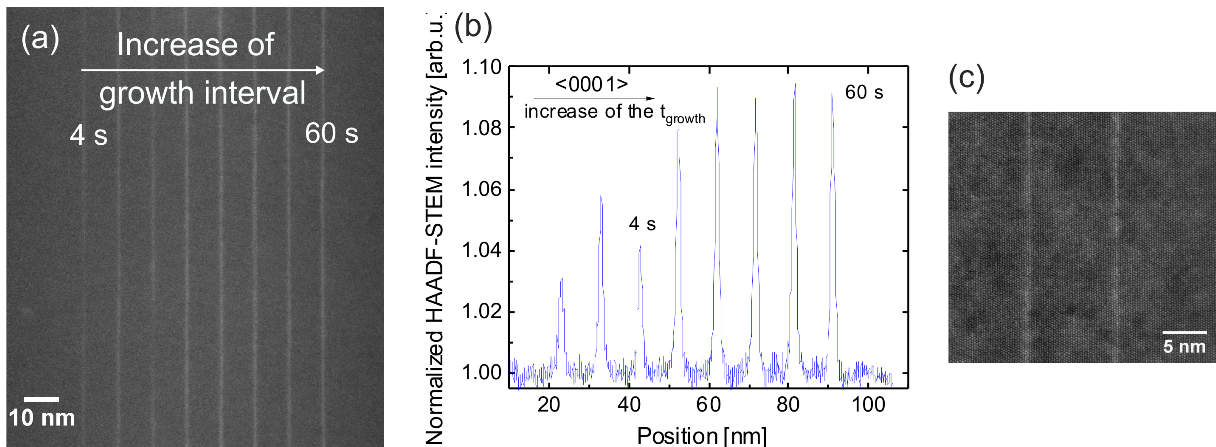

Fig. 4.11: (a) STEM overview image of the gradient time superlattice taken in <11-20> projection. Investigation thickness was approximately 120 nm. We note that for this sample we have performed our standard procedure of the normalization to the barrier signal followed by the correction of the gamma value to enhance the appearance of the QWs. (b) HAADF-STEM profile extracted from (a) before the adjustment of the gamma value. Growth time range is marked for the QW deposited with both In and N flux. (c) High-resolution STEM image of the last two QWs from the stack deposited at 40 and 60 s.

In Fig. 4.12 (a) and (b) we present a HRTEM image and a corresponding c-lattice parameter map. Again, similar to all our previous investigations we observe a pronounced expansion of the approx 2 lattice plains in the QW region (see the white box in (a)). On the left side of the

lattice parameter map a surface step can be observed. In the center a small area with the larger out-of plane parameters corresponding to a higher indium concentration is visible.

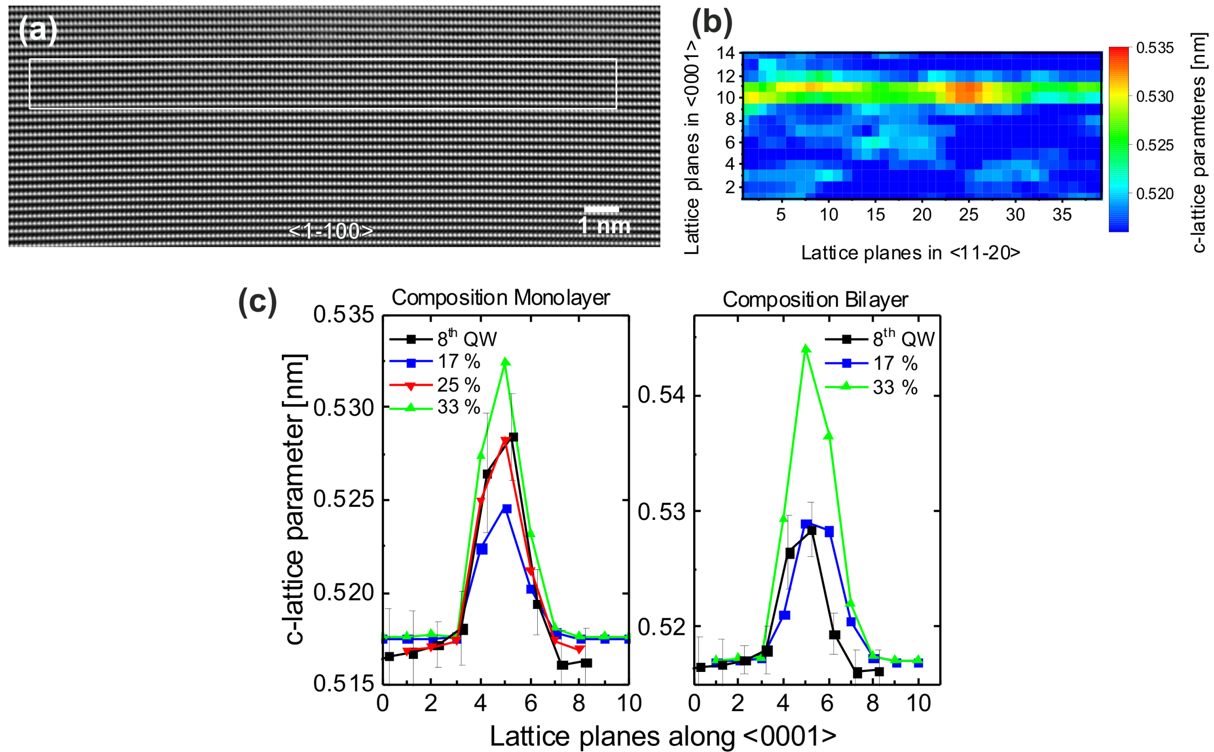

Fig. 4.12: (a) HRTEM image of the QW_8 taken in <1-100> projection used for the compositional analysis. The white box indicates the QW region. (b) C-lattice parameter map proceeded from (a). (c) Experimental c-lattice profile (black, thin black lines mark STDs) compared to the simulated supercells with (left) monolayer thick QWs and (right) bilayer (In,Ga)N.

In Fig. 4.12(c) we show the c-lattice profile derived from the strain map. The experimental result is compared to profiles obtained from image simulations of relaxed supercells containing a monolayer (left) and a bilayer (right) of (In,Ga)N. It can be seen from the simulation that supercells with bilayer QW would lead to a substantial expansion of the lattice parameters. For a composition of 33% the expected c-lattice parameter is 0.543 nm c-lattice constant, by far higher than what is experimentally found. Moreover, the width of the profile is larger than observed experimentally. (see black curve in Fig. 4.12(c), right). The best fit to our HRTEM data is obtained for supercells with one ML thick (In,Ga)N containing 25% (our c lattice parameter was $\sim$ 0.5284±0.0013 nm corresponding to 24.6%±2.7% of indium concentration). The indium fluctuations in the QW, estimated from the difference of the STD measured in the barrier and (In,Ga)N regions, were of about ± 4.3 %.

4.2.4. Short summary

Our compositional quantification was based on the strain analysis by means of HRTEM imaging and supported by HAADF-STEM imaging employed for a relative estimation and overview of the whole superlattice structures. Summarizing the results of the growth-condition experiments of the coherent nominal InN layers deposited on GaN, we find that:

- Despite the applying of only In and N fluxes with the growth rates higher than found in many experimental works, no pure InN QW was formed.
- Indium incorporation in the QW can be changed but only in a limited range. Lower growth temperatures and indium-rich conditions result in the mean indium content of maximum 25%.
- Thickness of the QW remains to be only one monolayer across all the experiments. At this point the study on the variation of growth intervals of the QWs give a surprising outcome. More explicitly, although, coverage of the layers rapidly improves with the increase of the growth time, yet, thickness of the alloys remained to be one monolayer. Deposition of the 32 MLs thick nominally InN quantum wells results in the single ML with 25% indium content.

4.3. Surface reconstructions of the $In_{0.25}Ga_{0.75}N$ monolayer grown on GaN

4.3.1. Ordering in $In_{0.25}Ga_{0.75}N$ monolayers

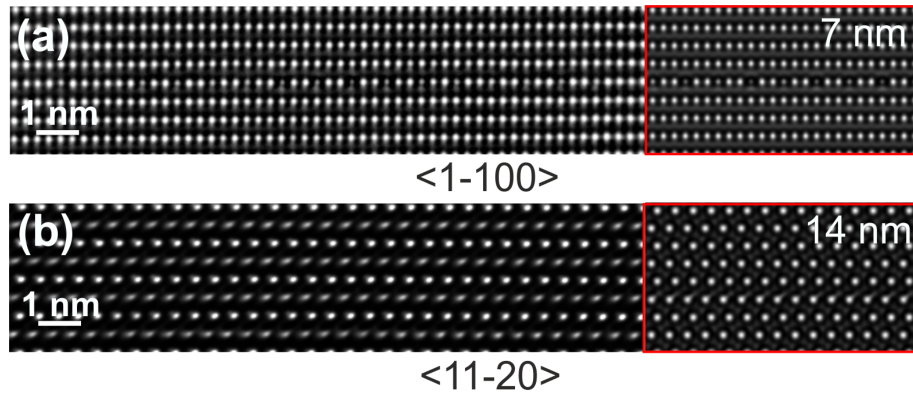

Fig. 4.13: HRTEM images of the 1 ML thick $In_{0.25}Ga_{0.75}N$ QW on GaN taken in (a) <1-100> and (b) <11-20> projections directions depicting a pronounced ordering of the indium and gallium atomic columns in <1-100>. In the red box the results of the multislice simulations are presented performed for the sample thicknesses 7 nm (for <1-100>) and 14 nm (for <11-20>).

For samples with the highest In concentration of 25% we have observed in-plane ordering. Fig. 4.13 shows a typical cross sectional HRTEM images of an $In_{0.25}Ga_{0.75}N$ monolayer along the <1-100> and <11-20> projection directions. This particular sample was grown in the group of X. Q. Wang at Peking University. The growth temperature of the monolayer was 550 °C. The image of the (In,Ga)N ML recorded in the <1-100 > zone axis is characterized by a periodic intensity variation of the atomic columns, with each third atomic column appearing darker than the surrounding GaN matrix. Under the used imaging conditions and at this particular thickness of the specimen that was identified as 7 nm for <1-100> projection and 14 nm for <11-20> from comparison with simulation, these darker spots indicate atomic columns with a high In content, while the bright spots refer to atomic columns composed of GaN as shown by the image simulation. In A we present image simulations performed for different thicknesses that demonstrate a very limited thickness range where the atomic ordering can be clearly distinguished. The ordering occurs in patches extending several nm within the ML plane as can bee seen in Fig. 4.13(a) and was shown earlier in Fig. 4.9(a) where the patch extended up to ∼15 nm. In the <1120> zone axis (see Fig. 4.13(b)), the ML is practically indistinguishable by means of contrast from the surrounding GaN matrix.

The observed atomic ordering, i.e. 3× periodicity of the In atomic columns has been examined earlier by RHEED as a transient phenomenon in Ref. [211]. Our TEM studies are the first to demonstrate the persistence of this surface reconstruction after overgrowth demonstrated. A simple model could be a $(\sqrt{3}\times\sqrt{3})$ R30° indium ordered ML with an In content of 33%. However, our quantitative TEM strain analysis shows consistently a maximum In content of 25%. To get more insight into the formation of this 3× ordering we performed RHEED measurements during the ML growth and as dependent on the growth temperature.

4.3.2. Experimental surface reconstructions. RHEED

Fig. 4.14 shows the RHEED pattern during growth of the superlattice along the <1-100> and the <11-20> azimuths after deposition of the GaN barrier ((a) and (b)) and after the growth of the nominal InN monolayer under N-rich regime ((c) and (d)). The measurements were performed in the group of X. Q. Wang at Peking University. After drying of the GaN barrier under slightly N-rich condition the surface exhibits a 2×2 reconstruction along the <1-100> azimuth (see two faint streaks in Fig. 4.14 (a)) and 1x periodicity of the GaN *a* lattice planes along <11-20> (see in Fig. 4.14 (b)).

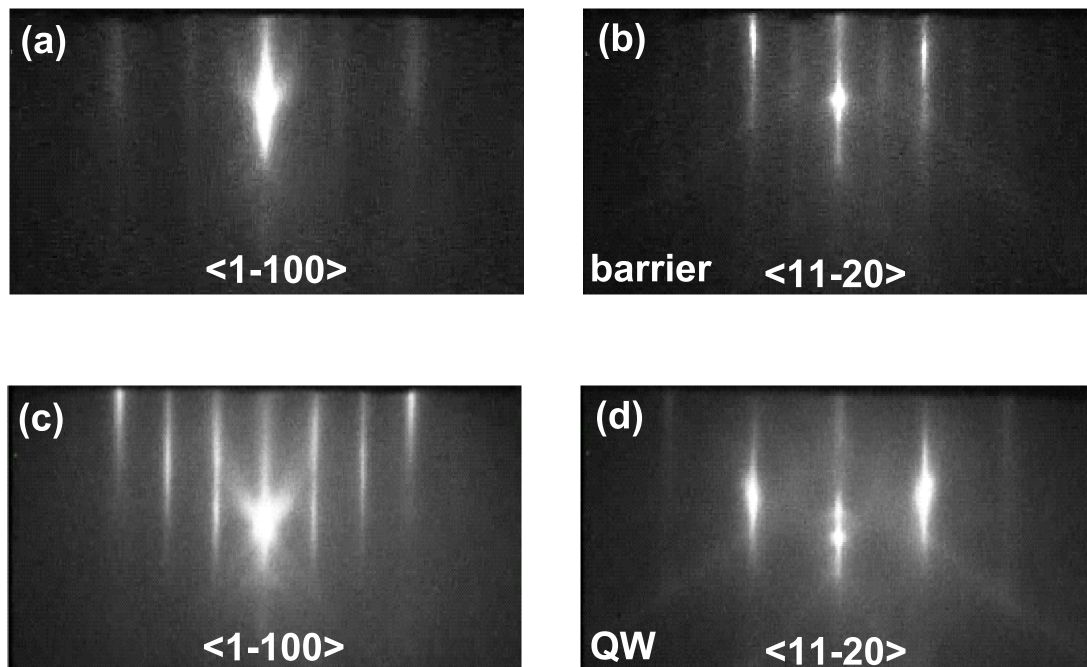

Fig. 4.14: In situ RHEED pattern after the deposition of (a) and (b) GaN barrier, (c) and (d) nominal InN QW along the <1-100> (left) and the <11-20> (right) azimuths.

After exposing this 2×2 reconstructed GaN barrier surface to In and N fluxes, streaks with 3× periodicity appear along <1-100> (Fig. 4.14(c)). Along the <11-20> azimuth the 1× periodicity is kept. If the In and N fluxes are kept for longer time during deposition of the QWs the RHEED pattern faints out and the 3× periodicity disappears, indicating metal accumulation at the growth surface. After overgrowth of the nominal InN monolayer by the GaN barrier under slightly N-rich conditions the 2×2 periodicity reappears in the RHEED pattern.

Next, we study a stability of the 3× periodicity in the RHEED pattern as dependent on growth temperature. A standard coherent (In,Ga)N ML is deposited at 530 °C keeping the In and N fluxes constant until the RHEED pattern faints out, i.e. the surface is covered by a metallic indium film. Subsequently, the QW is annealed up to 680 °C under nitrogen rich conditions, increasing the substrate temperature stepwise.

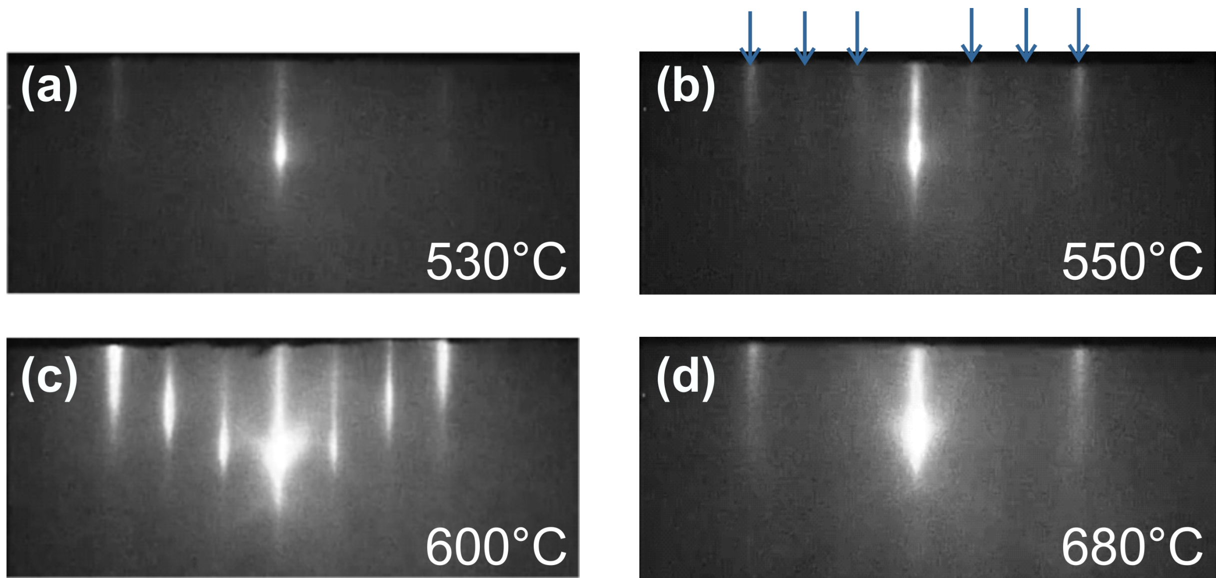

Fig. 4.15: RHEED patterns of the coherently grown (In,Ga)N ML extracted along the <1-100> azimuth at various temperatures during the annealing experiment. Blue arrows mark the appearing 3× periodicity.

In Fig. 4.15 we present the RHEED patterns taken along the <1-100> azimuth only, since no changes in the RHEED pattern along <11-20> were found. At low temperature, i.e. 530 °C, no surface reconstructions is observed by RHEED due to the presence of the metallic film on the surface, only the conventional 1×1 pattern is slightly visible. The first weak 3× patterns appear at 550 °C after In species are partially desorbed from the surface. The highest intensity of the 3× reflections are observed at 600 °C. Further increase of the temperature leads to a gradual decrease in intensity of the 3× pattern that becomes weak around 660 °C and then vanishes completely at 680 °C (see Fig. 4.15 (d)).

4.3.3. Identification of the surface reconstruction

Based on the RHEED studies and the HRTEM analysis presented in section 4.3.2 and Fig. 3.4, we will now develop a model that explains both the 3×1 RHEED pattern and the 3×1 ordering found along the same projection direction in our TEM studies and the measured composition of 25% in the buried ML-thick QW.

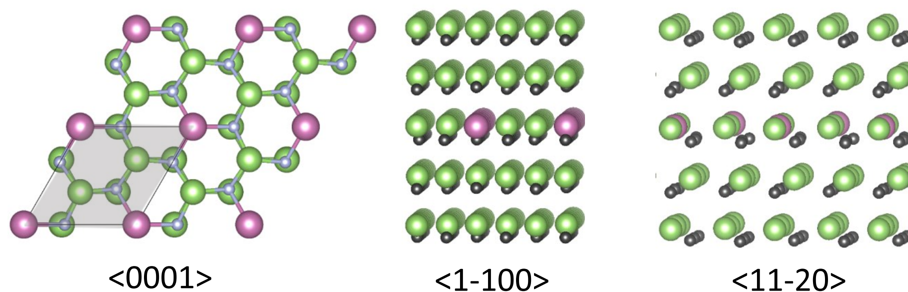

Fig. 4.16: Appearance of the (√3×√ 3)R30○ surface reconstruction (marked as shadowed area in <0001>) in different viewing projections. Green, purple and small gray atoms denote gallium, indium and nitrogen, respectively.

Chen et al. were the first to observe a 3×1 RHEED pattern during InN deposition on GaN(0001) [211]. These authors suggested a (√3×√ 3)R30° surface reconstruction but gave no explicit model of the structure. The (√3×√3)R30° characteristic pattern was discussed to be formed by In ad-atoms on top of the thick (0001) InN and (In,Ga)N layers [212,213]. Nevertheless, Chen et al. [211] have clearly shown that the deposition of In without presence of N does not result in the 3×1 RHEED pattern. Cheze et al. [210] found that the intensity of 3×1 RHEED pattern reaches its maximum at 0.32 ML coverage, which would correspond to the deposition of 1/3 ML.

All these findings are consistent with a (√3×√3)R30° arrangement of In atoms on the GaN surface shown in Fig. 4.16 and would fit with the finding of a similar order in the HRTEM images. Here, an ordered pattern, i.e. one In atom followed by two Ga atoms, is observed in <1-100>, while no specific arrangement can be seen in <11-20>, what is equivalent to the RHEED results, i.e. 3× and 1× periodicity observed in <1-100> and <11-20>, respectively. In this surface reconstruction the unit cell is constructed of a standard 1×1 unit cell expanded by √3 and rotated by 30°.

However, this type of ordering would result in an In content of 33% contrast to all our experiments that revealed a maximum In content of 25%. A surface reconstruction that fulfills both conditions, i.e. the 3×1 periodicity in the RHEED and HRTEM pattern and the maximum In content of 25% is (2√3×2√3)R30° that agrees well with the empirical compositional observations of 25%.

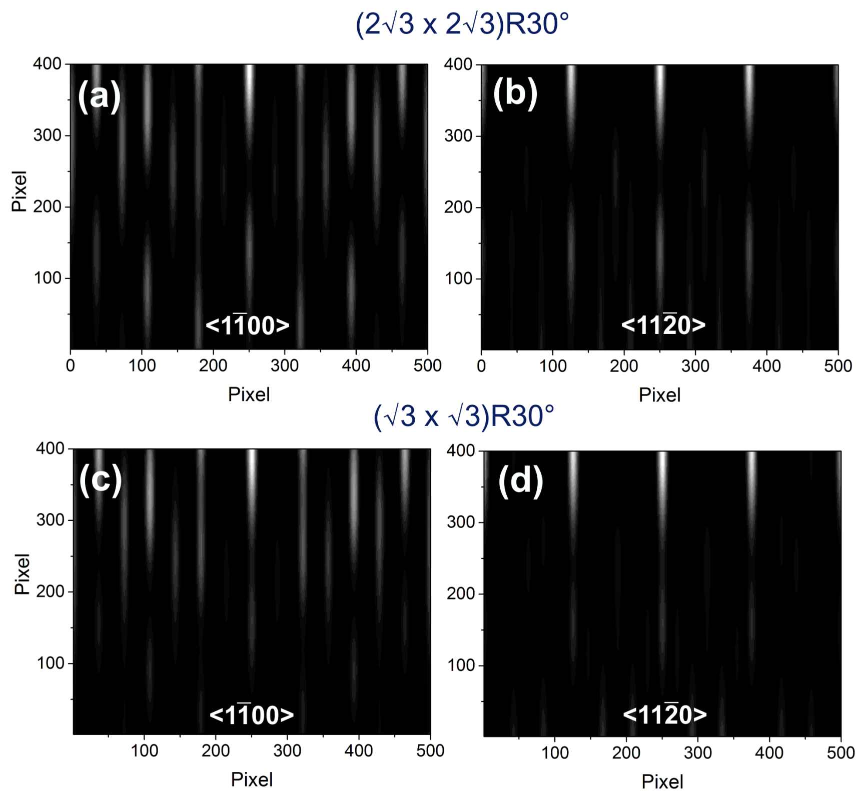

Fig. 4.17: Results of the RHEED pattern simulations performed for the (2√3×2√3)R30° (upper row, (a) and (b)) and (√3×√3)R30° (lower row, (c) and (d)) surface reconstructions in <1-100> and <11-20>.

In Fig. 4.17 we present the results of RHEED simulations comparing the diffraction streaks of the (In,Ga)N supercells with every third and fourth indium atoms corresponding to the

($\sqrt{3}\times\sqrt{3}$)R30° and ($2\sqrt{3}\times2\sqrt{3}$)R30° surface reconstructions. The simulations were done by T. Schulz from the Institut für Kristallzüchtung (IKZ) employing the code from [214]. Comparing the results, one can see an appearance of the additional streak for ($2\sqrt{3}\times2\sqrt{3}$)R30° between the a-planes along the <11-20> azimuth (see (b) and (d) in Fig. 4.17), that will be explained further. On the other hand, no measurable differences in the RHEED pattern along <1-100> can be observed. The same holds for HRTEM contrast simulations along the <1-100> projection (see for instance, Fig. 3.1 and Fig. 4.13 (a) for 7 nm thickness). Thus, the ($2\sqrt{3}\times2\sqrt{3}$)R30° and the ($\sqrt{3}\times\sqrt{3}$)R30° patterns are hardly distinguishable except for the difference in the strain state of both structures.

Moreover, we will see in the following discussion that the 2×2 reconstruction found in RHEED studies during "drying" of the GaN barrier under N-rich conditions is essential for the formation of the ($2\sqrt{3}\times2\sqrt{3}$)R30° surface structure.

4.4. Model of the indium incorporation.

4.4.1. DFT calculations

To understand the observed limit in indium concentration and the fact that the growth is self-limited to 1 monolayer, we have approached the process of the In incorporation into GaN matrix based on our experimental results by density functional theory with the local density approximation (LDA). The calculations were performed by L.Lymperakis from the Max-Planck-Institut für Eisenforschung. We started from the surface reconstruction of the underlying GaN barrier that serves as a substrate for the incoming indium and nitrogen atoms. By our RHEED studies we have shown that under N-rich conditions applied prior to In and N deposition a 2×2 surface reconstruction forms. According to Ref. [215] this reconstruction, which is energetically favorable under N-rich growth is constructed of a 2×2 N adatom arrangement shown in Fig. 4.18.

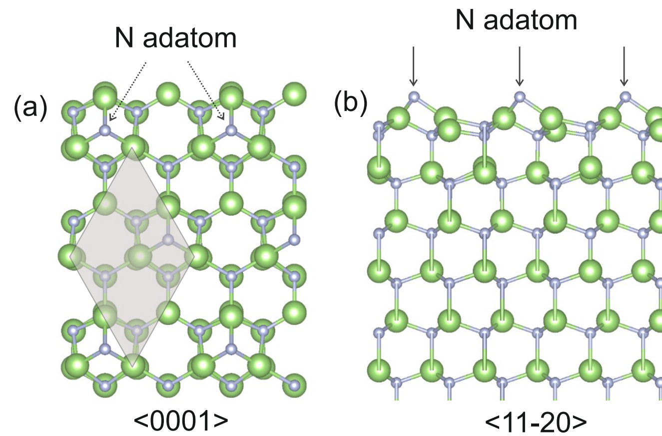

Fig. 4.18: 2 x 2 GaN surface reconstruction with nitrogen adatom observed after the barrier deposition.

Considering the suggested $(2\sqrt{3}\times2\sqrt{3})R30°$ reconstruction for the $In_{0.25}Ga_{0.75}N$ ML, we have constructed a model with the Me-polar surface terminated by triply coordinated N adatoms. Then, the Ga atoms were one by one replaced by In atoms, the energy needed for such exchange was calculated. Preserving the minimal energy configuration, the next Indium atom was inserted into the matrix. The resulting $(2\sqrt{3}\times2\sqrt{3})R30°$ surface reconstruction is represented in Fig. 4.19 (a) by light violet indium atoms, where both yellow- and violet-colored In are four-fold coordinated. Two colors were chosen to separate the nearest neighbors. Green balls denote the three-fold coordinated sites.

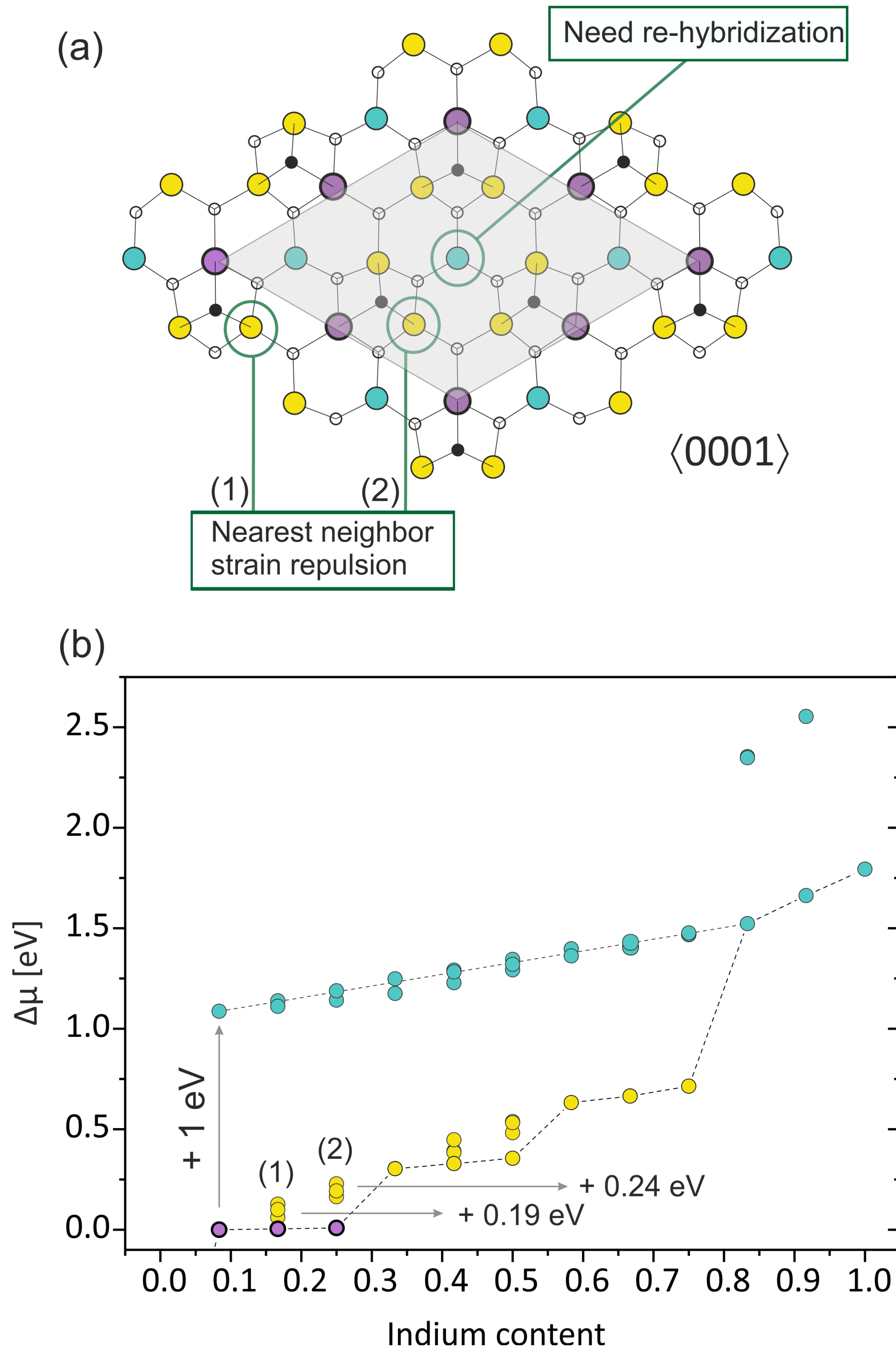

Fig. 4.19: (a) The most energetically favorable (2√3×2√3)R30○ surface reconstruction for the $In_{0.25}Ga_{0.75}N$ (indicated by the semi-transparent rhombus) shown in <0001>. Here the light violet balls are the In atoms forming the surface reconstruction, light green and yellow - three-fold and four-fold coordinated Ga atoms. Black small balls represent the nitrogen adatoms. (b) Relative increase of the chemical potential due to the implementation of each following In atom depending on indium content. Three-fold nitrogen coordinated atoms are marked in light green and four-fold - in yellow and light violet. Chemical potential corresponding to 33% is marked by a yellow arrow.

In Fig. 4.19 (b) we plot the relative chemical potential, $\Delta\mu = E_{n+1} - E_n$, necessary to insert an additional indium atom depending on the indium concentration. The E_n is a total energy of a

slab with (2√3×2√3)R30° reconstruction computed for each configuration with *n* indium atoms. The color coding of the atoms in Fig. 4.19 (a) corresponds directly to (b).

From the calculations we obtain:

1. Up to an Indium concentration of 25% (light violet In atoms in Fig. 4.19 (a) and (b)) the energy to add an indium into the four-fold coordinated site is constant and requires the lowest energy (∼0 eV). Due to the larger radius of In atoms (compared to Ga)[1], they tend to maximize their interatomic distance. Therefore, if an indium atom is added to a next four-fold coordinated site the nearest neighbor repulsion requires an additional energy between 190 and 250 meV (see the corresponding energies for the yellow circles marked as (1) and (2), respectively).

2. The composition of 25% filled at an equal energy cost, is simply given by the occupancy of the surface by nitrogen adatoms. To increase the In incorporation beyond 25%, e.g. to fill the nearest neighbor sites up to 33% (see an arrow in Fig. 4.19 (b)), would require an energy penalty of approx 300 meV. To accomplish this energy gain we would need to introduce the five times (5 ×) more In flux into the MBE growth chamber. This would lead to the indium droplet formation and rough growth interfaces.

3. If an In atom is placed in a three-fold surface site, this requires an energy cost of approximately 1 eV compared to the four-fold coordinated site. This is simply due to the fact that the In atom at this site lacks an In-N bond that is present at the fourfold coordinated site.

The ordering of In atoms on the four-fold coordinated sites, which finally results in the (2√3×2√3)R30° reconstruction can be explained via the second nearest neighbors interaction, minimizing the strain energy at the surface. Nevertheless, this result is puzzling since the proposed surface reconstruction suggests that despite the weaker In-N bonding, atoms tend to increase the amount of such bonds, instead of the stronger Ga-N ones. In general case, In atoms at the four-fold coordinated sites as energetically less favorable than Ga when are covered by the GaN barrier would exchange with Ga. This should lead to the In concentrations in the layer even lower than 25%. In opposite, our HRTEM and RHEED studies show, that the (2√3×2√3)R30° is preserved.

To explain this outcome, we have examined the bond configuration of In atoms placed either at the (i) three- or (ii) four-fold coordinated sites (note, that In atoms partially cover the four-fold sites according to the nearest neighbor repulsion principle) and compared the density of states in these two configurations.[2] Later, in the discussion we will denote the four-fold In configuration as the three-fold Ga. For the latter, the unoccupied states are moved upwards. This, however, does not affect thermodynamics and energy of the system. At the same time, dangling bonds of the N adatoms affect the doubly occupied surface band, what leads to its downwards shift in both of the cases. Although, this shift intersects with the valence-band states below the band gap. Nevertheless, the calculated simultaneous move of the unoccupied (to higher energies by 0.37 eV of the three-fold Ga atoms in respect to three-fold In atoms) and occupied (by 0.33 eV to lower energies between these to cases) orbitals in total decreases the energy of the

[1] r_{In}=156 pmand r_{Ga}=136 pm [6]

[2] The density of states is the number of different states at a particular energy level that are available for electrons.

system [216][3]. Therefore, for the four-fold In atom configuration we obtain a large energy gain.

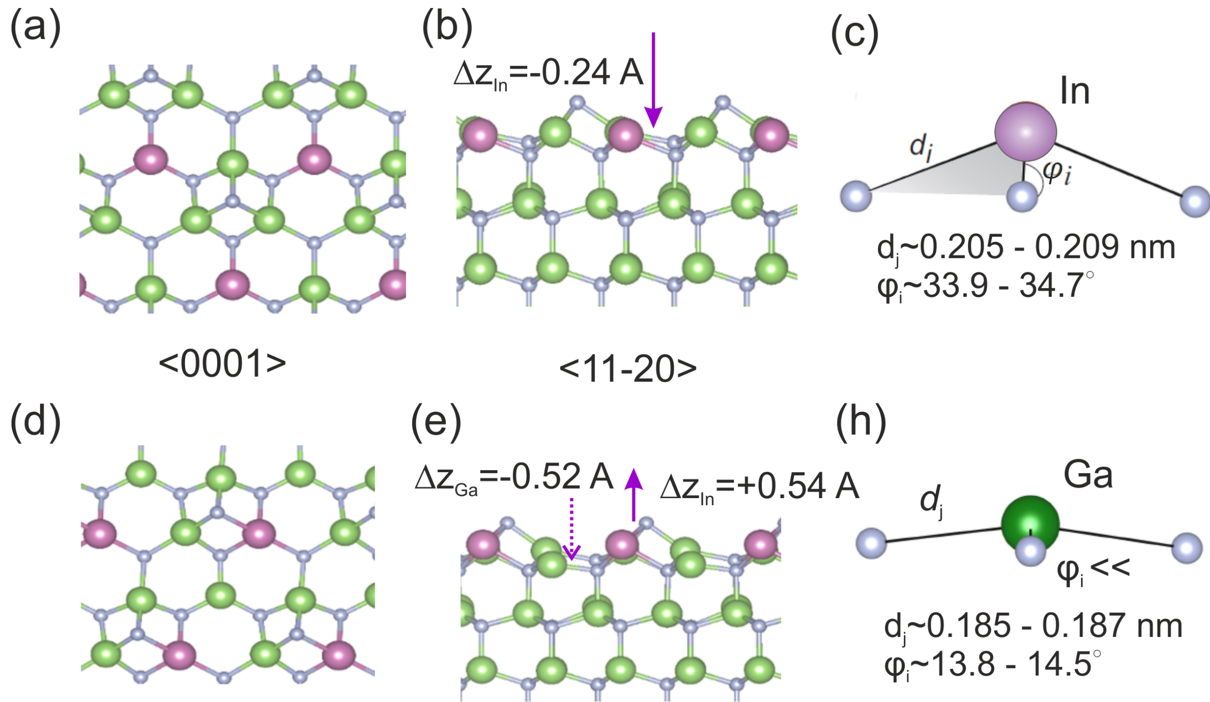

Fig. 4.20: Atomic geometry of the $In_{0.25}Ga_{0.75}N$ as a surface layer terminating the (0001) GaN barrier with 2×2 N adatom configuration with the (a)-(c) triply coordinated In atom and (d)-(h) four-fold coordinated indium. The viewing projections are: <0001> (a),(d) and <11-20> (b),(e). Here, Δz denotes the atomic displacement of the In and Ga atoms estimated in the respect to the bulk-like sites along the <0001>. (c) and (h) are the tetrahedra formed by the triply coordinated In and Ga atoms connected to the three neighboring N atoms. Numbers represent the bond length, d_j, and dihedral angles, φ_i, between the N and Me atoms brought to the surface. Violet, green and light gray balls correspond to the indium, gallium and nitrogen atoms.

Fig. 4.20 shows the atoms at the surface sites in the <0001> and <11-20> projection for both configurations, i.e. three- (upper row) and four-fold (lower row) coordinated In. In both of the cases, the triply coordinated Me atom (either In or Ga) can relax long the <0001> direction. In the case of triply coordinated In (Fig. 4.20 (c)), a tetrahedra constrained from the Me atom and the corresponding three N atoms slightly deforms as compared to the bulk-like state, i.e the relaxation is small. The difference in the dihedral angles, φ_i, between the surface- and sp^3-like atomic position is approximately ±1° and the In-N bonds are contracted by 2-4%.[4]For the triply-coordinated Ga atoms, i.e. four-fold In, (Fig. 4.20 (h)) the corresponding difference is larger - the Ga-N bond lengths reduced by $\sim$ 5.5%. More importantly, the dihedral angles decreased by $\sim$ 60%, resulting in the almost *planar* atomic disposition. Although, both, In and Ga as being brought from the bulk-like positions to the surface shift downwards, in the case of the four-fold coordinated indium (Fig. 4.20 (d)-(h)) the Ga bonds follow the *re-hybridization*

[3]In the terms of the bond orbital description, this process can be represented as an upward shift of the antibonding orbital, i.e. the conduction band, accompanied by a downshift of the occupied bonding orbital, i.e. the valence band.

[4]Bond length for In-N and Ga-N were listed in Table 2.3. The dihedral angles for In and Ga in the bulk InN and GaN were taken as 34.1° and 34.4° obtained from the DFT+LDA calculations of L.Lymperakis (Max-Planck-Institut für Eisenforschung).

mechanism from the bulk-like sp^3 to the *planar* sp^2configuration.[5] This mechanism reduces the bond energy with nitrogen atoms and results in an inward displacement of the triply coordinated Ga. The process saves up to 1 eV shown as a thin arrow in Fig. 4.19(b). Such remarkable energy gain would be not possible for the triply coordinated Indium atoms due to the large atomic size hampering the *inwards* relaxation of indium. Large amount of the strain energy would be needed to move the In atoms and prevail over the energetically favorable *re-hybridization*.

4.4.2. Discussion of the model

Summarizing our theoretical studies, In atoms favor the four-fold coordinated sites and following the nearest neighbor repulsion form the (2√3×2√3)R30° surface reconstruction. This result agrees perfectly with the experimentally found In concentration limitation of 25% by means of HRTEM and RHEED studies revealing a 3× periodicity along the <1-100> azimuth. Another surface reconstruction, that exhibits the same periodicity is (√3×√3)R30°.However, experimentally, the difference between (√3×√3)R30° and (2√3×2√3)R30° reconstructions would be negligible due the fact that the (In,Ga)N monolayer is not a perfectly ordered alloy but is partly random.

Compositional limitation

Our experiments reveal that despite the growth conditions utilized, i.e. only In and N supply during growth of the QWs deposited in a wide temperature range starting from 550°C to 650°C (see 3.3.1, 4.2.2), all nominally InN monolayers contain no more than 25% of indium. To increase the In content to 33% (also corresponding to the 3× periodicity observed in RHEED) requires a high energy penalty of 300 meV. The latter is demanding, as the thermodynamically allowed window for the In chemical potential to grow InN was calculated to be only 210 meV (see in [146]).

The model, presented here is in a perfect agreement with the experimental data. Moreover, multiple works on the standard QWs/GaN 2-3 nm thick investigated so far reported on the structures with indium concentrations around 30% (∼20% in [53, 147], ∼22% in [168], 25% in [198], ∼28% in [31], etc...). Only a few works reported on the higher Indium concentrations, however without the details on the growth conditions or methods of compositional quantification (see, for instance, $In_{0.43}Ga_{0.57}N$ QWs in Nakamura et al. [17]). The phase diagram of Duff et al. showed that a growth window of the coherent InN alloy had a positive formation enthalpy prohibiting the InN formation on GaN [217]. Therefore, a pioneer work of Yoshikawa et al. gained a lot of attention in the nitride community that reported on the realization of the ultra-thin pure InN/GaN quantum structures that can be used as an emission source for the optical devices [33]. The superlattice from the aforementioned work was grown at high growth temperature, i.e. 650 °C, what agrees well with our studies. However, the optical emission from the InN ML was very close to the one from GaN. Therefore, it has been brought into debate the real composition of the as-grown monolayers that later was revealed to be around 30% [48, 204]. Our several growth experiments supported by HRTEM analysis (an estimation precision is around 2%) resolves this confusion.

[5] Sp^2 can be formed on the surfaces, where Me atom may miss an electron leaving a dangling bond of nitrogen.

Thickness self-limitation

Now we will discuss the other limitation observed experimentally, i.e. the QW thickness was revealed to be 1 monolayer. Based on our RHEED and TEM data, we consider that exposure of the GaN surface with a 2×2 reconstruction to In and N leads to the 3x1 periodicity. Then, the surface is overgrown by GaN with again 2×2 reconstruction. This observation allows to explain how an $In_{0.25}Ga_{0.75}N$ alloy can form. We suggest an exchange process of an In atom impinging the surface with a four-fold coordinated Ga atom site. As have been shown above, this an energetically favorable process that leads to the downwards relaxation of the Ga atom. As we reach 25% by substituting Ga by In, adding more indium leads to its accumulation at the surface. In a next step, GaN is deposited under slightly Ga-rich conditions. Some In floating on the surface can be incorporated to small amounts, however, we have not observed any gradient profiles for the QWs deposited in the N-rich regime. Speculating, one could assume that drying the surface from Ga excess after growth of a single GaN monolayer and, then, offering In and N could result in a second $In_{0.25}Ga_{0.75}N$ monolayer and would form at the end an ordered bulk alloy. However, up to now no evidence for such an ordered bulk alloy can be found. Some works reported on the formation of (In,Ga)N bilayers grown under Me-rich conditions [204] or accumulation of the InN islands along the step edges [65]. Nevertheless, these data were accomplished by STEM imaging, very sensitive to the sample thickness as shown above.

Other models on surface reconstructions

Although, the (√3×√3)R30°-type reconstruction was examined before on the surface of (In,Ga)N alloys or (0001) InN and were assigned to indium adatoms [212], a preservation of this surface structure *inside* the bulk is not straightforward. In literature, several mechanisms were suggested. Li et al. [43] have performed growth experiments on the deposition of 100 MLs nominally InN under constant active N exposure. By monitoring the intensity of the specular spot in RHEED a stable coverage of 2 MLs with a characteristic 3× periodicity was observed at 680°C which under further exposure resulted in the formation of In-droplets. The first adlayer grown on top of this reconstruction stabilizes the underlying one from escaping. However, we have shown that there is no energy window for indium atoms to occupy additional surface sites when the energetically favorite sites are already filled up. Moreover, the authors deposit their QWs under constant N supply it is not clear whether Me or N-rich regime was established. In addition, their studies are not supported by any structural analysis of the as-grown alloys but based on methods working in the reciprocal space.

To this extent we refer to the other investigations performed by RHEED and HRTEM shown in Cheze et al. [210]. By measuring the intensity of the specular spot in RHEED a maximum coverage of 0.32 MLs for the nominally grown 2 InN MLs was found. Since the RHEED data can be affected by the desorption and decomposition processes, the actual coverage was cross-checked by the TEM studies showing lower In concentrations around 25%. The authors proposed an In adsorbate structure as a basis for the formation of the (√3×√3)R30° (In,Ga)N surface reconstruction embedded into GaN matrix. Here, an exchange process occurs between the pre-deposited 2.2 In MLs under N exposure and with the Ga atoms during the growth of the following GaN capping layer.

The main problem of the aforementioned works is that a (√3×√3)R30° indium adatom structure is supposed to be unstable at the surface. Moreover, as shown above, it can hardly be separated from In incorporated into subsurface sites by means of methods working in the reciprocal

space. Only the In species that cannot incorporate in the matrix floating on top are supposed to restrain the desorption of the underlying (In,Ga)N layer (see also [218]). According to our model, due to the energetic minimum established on the surface, these accumulated In atoms cannot be embedded inside the bulk without the supply of Ga and N. Our temperature dependent RHEED experiments revealed a high stability of the 3× periodicity. The $(2\sqrt{3}\times2\sqrt{3})$R30○ surface reconstruction is preserved up to the temperatures not expected for the regular MBE-grown ternary alloys that usually do not exceed 600 °C [31, 63]. Only annealing of the (In,Ga)N ML up to 680 °C results in a diminishing of the 3× reflexes in RHEED. Earlier, Lee et al. [219] have shown that top-most $In_xGa_{1-x}N$ layers with x˜0.3 tend to order forming a stable $\sqrt{3}\times\sqrt{3}$ phase at realistic growth temperatures ∼700-1000K.

Me-rich conditions

The $(2\sqrt{3}\times2\sqrt{3})$R30° surface reconstruction was shown to form only under N-rich conditions (current work and Ref. [211]). Although, our III/V ratio studies have revealed that going into the Me-rich regime does not change the indium content itself (see the saturation point in Fig. 4.2), one may wonder which surface structures are available under In-rich conditions. Northrup et al. reported that under moderate-rich Me conditions the III-nitrides tend to stabilize Me adlayers [215]. We have mentioned that continuous In supply leads to the In accumulation on the surface. Indium adlayers or bilayers may form as discussed in some theoretical works, for instance, in Refs [217, 219]. Neugebauer et al. have modeled different configurations involving the Me at the top surface, including the surface reconstruction with N adatoms bonded weakly to the upper In adlayers [209]. As mentioned earlier, the In adlayers can stabilize the underlying (In,Ga)N ternary alloys. However, when capped with GaN barrier, In may diffuse through the barrier. This results in the formation of droplets or in the intermixing with the overgrown capping layer smearing out the QW/barrier interfaces. The latter, i.e. gradient In profile on the QW-GaN interface due to the incorporation of the residual indium into following GaN barrier under N-rich regime was observed in our earlier experiments published in [210]. The authors also presented that the RHEED signal reveals a 3× periodicity for the (In,Ga)N MLs deposition, which attenuates under the continuous exposure of In flux. Although, the metallic species floating on top hampers the observation of the surface reconstruction, it could be possible that once formed $(2\sqrt{3}\times2\sqrt{3})$R30° arrangement stays even at Me-rich conditions, however no theoretical or experimental evidence has been reported so far. Nevertheless, to keep the interface abrupt, N-rich conditions and absence of In species on the surface before the capping by GaN should be employed.

4.5. Summary

In this chapter we have investigated various growth regimes employed in order to overcome the empirically found compositional and thickness limitations observed for thin coherently grown (In,Ga)N QWs on GaN. Growth experiments as dependent on In/N flux ratios, deposition temperatures and growth intervals of the QWs combined with the RHEED measurements led us to the development of the independent model of the specific surface reconstruction for In atoms on GaN. A stable $(2\sqrt{3}\times2\sqrt{3})$R30° configuration is stabilized when grown under the N-rich regime on top of GaN with a 2×2 surface reconstruction with N adatom. By substituting Ga atoms by In, the latter are incorporated into the crystal. Indium favors to bond with four N atoms, what

at first glance should be unfavorable since the InN bond is essentially weaker than GaN bond. We found that this is due to the difference in re-hybridization mechanism between the 3-fold Ga and In atoms that promotes indium to the 4-fold site. Here, Ga (as being on the 3-fold site) undergoes a re-hybridization from sp^3 to sp^2 lowering its energy what is not possible for the In atom due to the atomic size mismatch. In the ideal case the surface should consist of a perfectly ordered $In_{0.25}Ga_{0.75}N$ alloy self-limited to the 1 monolayer thickness. A higher energy penalty is needed for the further substitution of the Ga atoms by In at either the first nearest neighbors or triple coordinated sites what requires severe growth conditions involving extremely high In with even higher N flux to increase the chemical potential of the system.

We have tested the $(2\sqrt{3} \times 2\sqrt{3})R30\circ$ surface reconstruction as a stable arrangement for indium atoms and shown that it is preserved up to the growth temperatures as high as 650 °C. These deposition temperatures are preferential for the growth of GaN-based structures. Overall, although, we can extend the growth window of the biaxially strained (In,Ga)N MLs towards higher temperatures, we have not found a way of increasing the composition and thickness of the ultra-thin QWs.

5. Optical properties of $In_{0.25}Ga_{0.75}N$ superlattices:

5.1. Aim of the chapter

In this chapter, we will use monolayer thick quantum wells as model system to study the recombination dynamics in of (In,Ga)N quantum wells which are independent on piezoelectric fields and well thickness. We focus particularly on the lateral and vertical electron and hole confinement in short period superlattices which can be modified by changing the periodicity of the SL, as well as the alloy fluctuation within the monolayer, respectively. We discuss our results from continuous-wave and time-resolved photoluminescence studies involving the structural analysis by high resolution transmission electron microscopy. Our experimental studies are combined with state of the art density functional theory calculations. It will be shown that in sharp contrast to electrons, holes are strongly localized even in single monolayer thick quantum wells. Delocalization of the hole wave function starts for the SPSL structures with barrier thickness of 6 MLs and below. From our results general conclusions on carrier localization phenomena in (In,Ga)N alloys and quantum wells are drawn. With regard to the lateral confinement of carriers within the ML, we performed dedicated STEM-CL measurements that enable to resolve the quantum dot like spectra from (In,Ga)N discs with lateral extensions up to 20 nm.

5.2. Polarization fields in the ML-thick QWs

In Fig. 5.1 (a) we show typical spectra of SL structure consisting of 1 ML $In_{0.25}Ga_{0.75}N$ QW and 50 MLs GaN barrier under different excitation powers. Measurements were done under pulsed laser excitation at 256 nm with 12 ns pulse period and 0.1 ps pulse length. Using neutral density filters the excitation power power was reduced from 3 mW to 50 µW. Spectra were extracted from the 250 sec time window after the pulse. Power dependencies measured under similar excitation powers for the conventional 3 nm $In_{0.17}Ga_{0.83}N$ QW are presented in Fig. 5.1 (b). The QW peak emission exhibits a continuous blue shift with increasing excitation power.

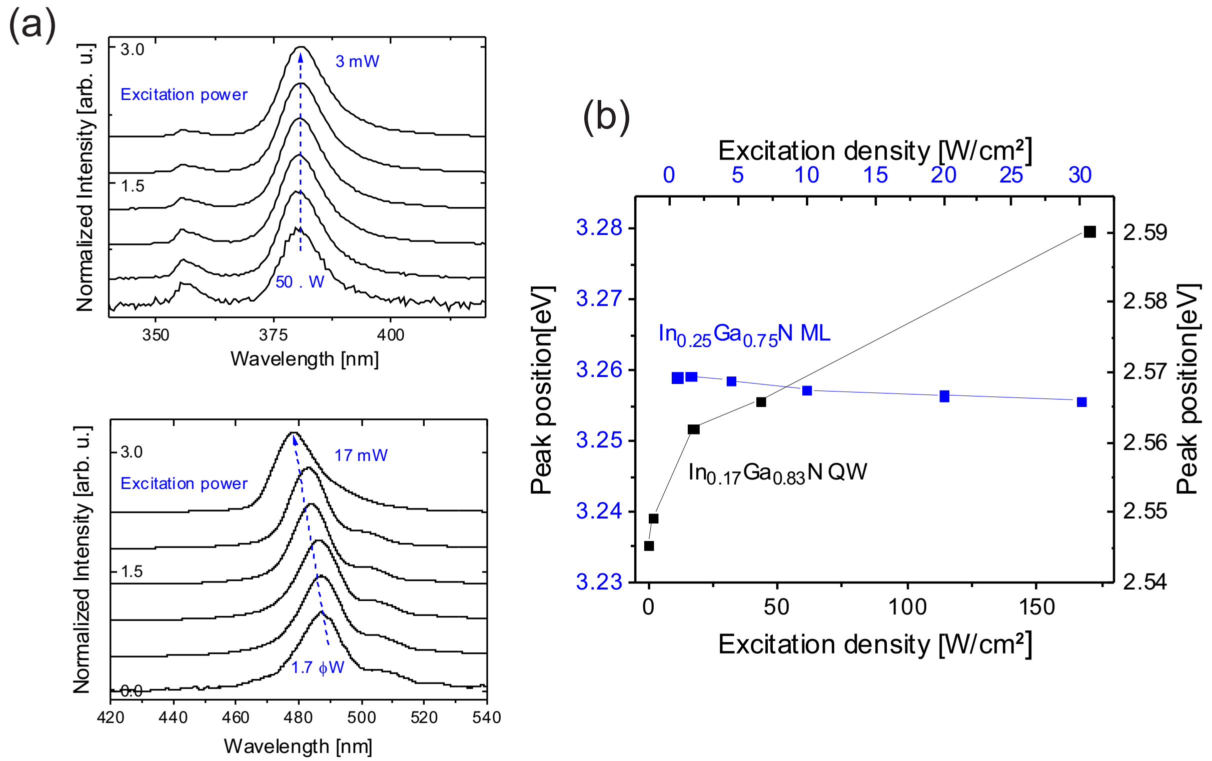

Fig. 5.1: Excitation power dependencies measured for the 0.25-nm thick QW with 25 % In (a) and 2 nm-thick QW with 17% In (b). Spectra are normalized to the QW emission. Both experiments were done at 5 K. (b) Peak positions of the ML (blue) and thick QW (black) on excitation density. The Y-axis are presented in the same range.

The peak positions of the experimental PL spectra as obtained from Gaussian fitting are displayed in Fig. 5.1 (c) for both samples. The total blueshift of the conventional QW emission within the excitation power range is 45 meV. In contrary, the peak position of the monolayer QWs is redshifted by the increase of excitation power. Such redshift of the PL spectra is usually attributed to the band gap renormalization observed in semiconductors [220, 221]. This effect is mostly hidden in the standard polar (In,Ga)N QWs, where the screening of the polarization fields is predominant under additional electrical field [160, 222]. A broadening of the ML QW emission spectrum is not observed, and the FHWM remains fixed at around 3.5±1.0 meV.

Similar power dependent measurements have been carried out other samples with ML-thick QWs revealing a similar outcome, i.e. no blueshift after the increased excitation. In the following chapters we will draw further conclusions on the charge carrier localization from this initial condition.

5.3. Vertical confinement of charge carriers in SLs:

5.3.1. SLs with different barrier thickness. Structural investigations.

We investigate a series of short period superlattices consisting of ten pairs of monolayer thick $In_{0.25}Ga_{0.75}N$ QWs and GaN barriers of 6 MLs (1.5 nm), 12 MLs (3 nm), 25 MLs (6 nm) and 50 MLs (12.5 nm) thicknesses. All samples were deposited on $GaN/AlN/Al_2O_3(0001)$ templates with a miscut angle of ± 1° towards <1-100> direction. The nominal InN QWs were grown under slightly N-rich conditions with the flux ratio In/N=0.82 and nominal coverage 2.2 MLs.

A scheme of the SL structure is shown in Fig. 5.2 (a). Details on the growth procedure can be found in [210]. A growth temperature of 550 °C was chosen to facilitate indium incorporation. Despite such comparatively low growth temperature, the layers grow in step flow mode and keeping the surface roughness at a low level. RMS parameters measured by atomic force microscopy on a 5x5 μm^2area increased from 0.5 to 1.3 nm for GaN barrier width changed from 6 MLs to 50 MLs. In Fig. 5.2 (b), (c) we show the AFM images taken under higher magnification for the thinnest and thickest barrier samples[1]. For the 50 MLs SL hillocks were observed originating from dislocations.

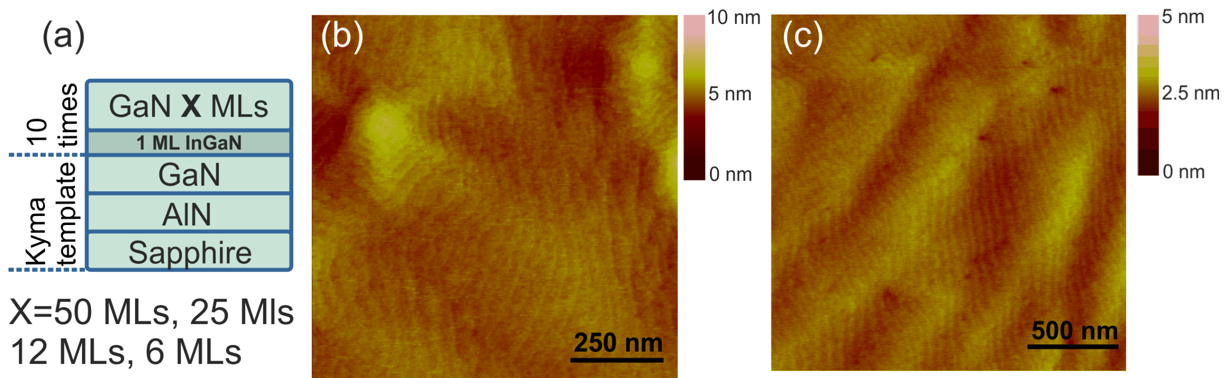

Fig. 5.2: (a) Samples structure, AFM images of the SLs with 50 MLs (b) and 6 MLs (c) for 1x1 $\mu m^2$and 2x2 μm^2area sizes.

Detailed structural investigations of the sample series were performed by means of STEM-HAADF and HRTEM under negative spherical aberration conditions. Results of selected STEM-HAADF images are presented in Fig. 5.3 for three samples from the series with 50, 12 and 6 MLs-thick barriers. Overview images of the SLs with the thickest and the thinnest barrier taken along the <11-20> projection reveal that the SL perfectly meet the intended structure size, and are well reproducible with atomically abrupt interfaces between QWs and barriers. No deterioration of the crystalline quality was observed throughout the sample series. High resolution STEM-HAADF images of the thickest and thinnest barrier SLs (see Fig. 5.3 (c) top-bottom) demonstrate that the QW thickness is clearly 1 ML for all samples of the series.Growth steps can be seen on the STEM images, for instance, see the arrows in Fig. 5.3 (b). An apparent increase of the QW thickness in the STEM images taken under high magnification is due to the projection of surface steps partially lying inclined with respect to the viewing direction. The barrier widths were within a +/-1 ML accuracy range from the nominal values demonstrating an excellent controllability of the growth procedure.

[1]The measurement were done by C.Cheze at the Paul Drude Insitute (PDI), Berlin.

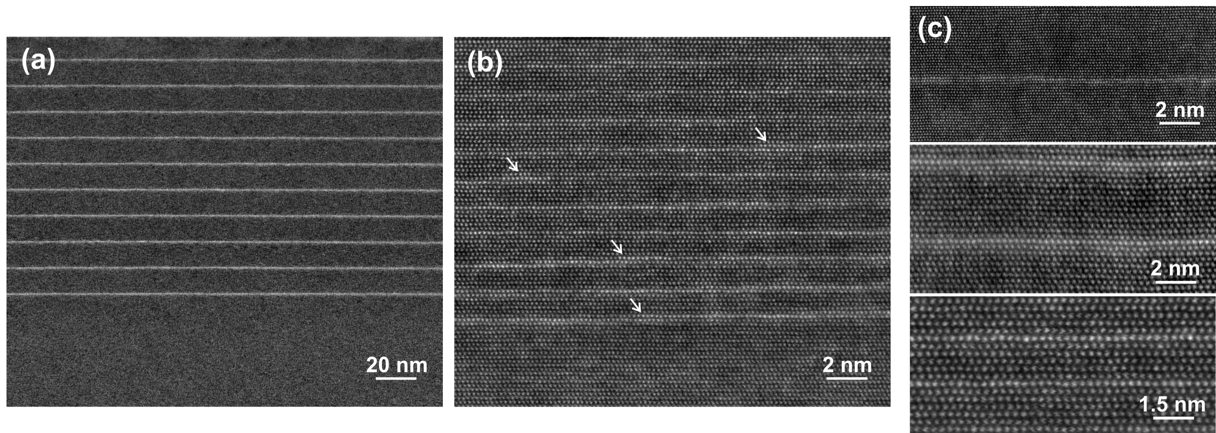

Fig. 5.3: STEM images taken in <11-20> projection for the 50 MLs (a) and 6 MLs (b) structures. Arrows mark the growth steps. (c) top to bottom: High resolution STEM images of the samples with 50 MLs, 12 MLs and 6 MLs measured under higher magnifications. Scales are indicated on the right bottom.

For quantifying the indium content in the (In,Ga)N MLs, we measured the c-lattice parameter in a series of HRTEM images according to our standard approach. The color-coded c-lattice parameter map of the (In,Ga)N ML region for the sample with 50 MLs GaN barrier is displayed in Fig. 5.4 (a). Single (In,Ga)N ML results in an increase of 2-3 neighboring c-lattice parameters along the <0001> directions as a consequence of the fact that the full c-lattice spacing is measured in the HRTEM images. The higher STD of the measured c-lattice parameters within the ML is a consequence of the inhomogeneous distribution of In. This can also be observed on the left side of the map revealing a larger c-lattice parameter and this a higher In content. To quantify the mean indium content of the layer, we averaged the measured c-lattice parameters laterally, as displayed in Fig. 5.4 (b) (dashed line). The average value of the c-lattice constant yields 0.5281±0.0015 nm.

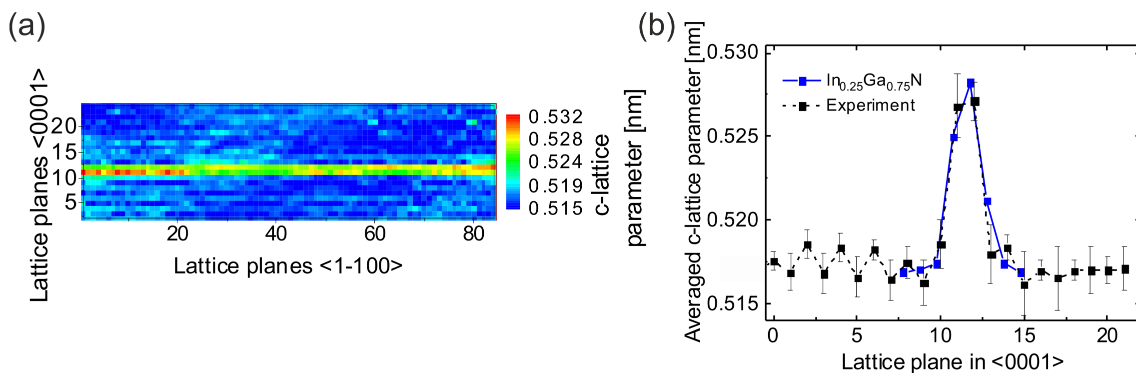

Fig. 5.4: (a) Color coded c-lattice parameter map showing a single (In,Ga)N ML. Red colored area indicates the region with higher indium content. (b) Laterally averaged c-lattice parameters and standard deviations for the measured sample and the calculated supercell (blue solid line) consisting of an (In,Ga)N ML with a mean In content of 25%.

A comparison of the experimentally measured profile of the laterally averaged c-lattice parameters (dashed curve), shows very good agreement with a simulated profile of an (In,Ga)N ML with an In content of 25 % (solid curve) as displayed in Fig. 5.4 (b). Very similar mean Indium compositions of around 25%, were observed for all QWs throughout the entire sample series.

Assuming a linear interpolation of the c-lattice parameter between GaN and (In,Ga)N ML with 25 % of In, this approximately yields a compositional fluctuation of ± 2 %. The out-of-plane lattice parameter of the monolayer quantum well of the superlattice with 12 ML barriers is 0.527±0.0021 nm corresponding to an In content of the well of 23% with a slightly higher 4 % STD.

In addition, XRD measurements and simulations were performed for the 50 MLs thick barrier SL suggest the formation of the 1 ML thick (In,Ga)N QW with 27% and 50 MLs thick GaN barriers in the stack (see B.1). Thus, XRD and TEM both yield similar results with regards to thickness and mean In content of the monolayers.

5.3.2. Continuous wave PL measurements

Optical properties of the series were measured at 20K under 325 nm (3.8 eV) excitation with a cw-HeCd laser. In Fig. 5.5 (a) all spectra are shown on a logarithmic scale. The band edge emission of the GaN substrate appears at 3.46 eV. The emission energy of the SLs with 50 MLs and 25 MLs barriers peaks at 3.25 eV. It decreases by ∼10 meV for structure with 12MLs barrier thickness and by 100 meV for the sample with 6 MLs barrier thickness.

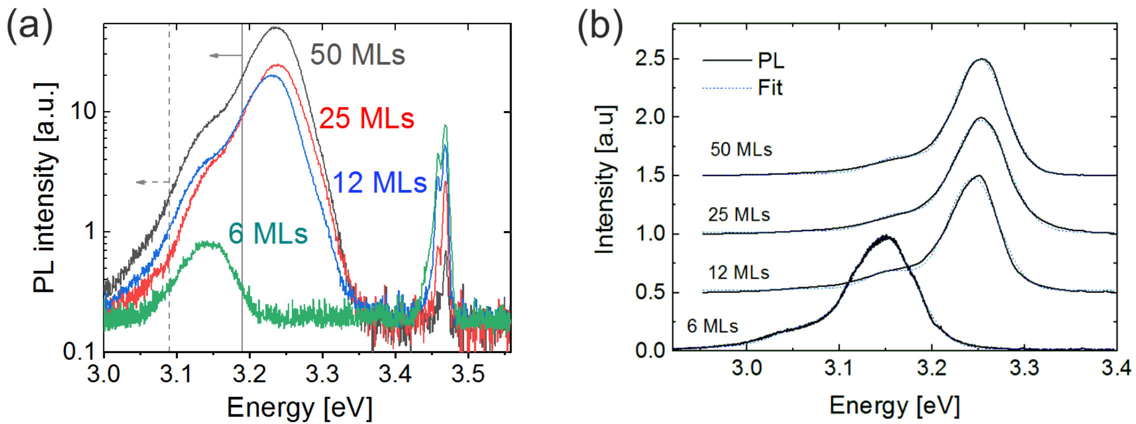

Fig. 5.5: Spectra of the samples taken under 325-nm excitation. (a) Original data from the experiment shown in logarithmic scale. Solid gray lines indicate the excitation laser energies used in TRPL quasi-resonant experiment, dashed line represents shifted spectral window for the 6 MLs SL. (b) Normalized peaks from the SLs fitted by Gaussian functions (blue dashed lines).

5.5(b) presents normalized spectra with respect to the SL emission peaks as well as Gaussian fit functions (shown as blue dashed lines). A distinct lower energy shoulder indicates the first longitudinal optical (LO) phonon replica separated by ∼90 meV as usually observed in wurtzite GaN [223]and (In,Ga)N [183, 224]. From the intensity ratio between zeroth - and the first phonon replica of the SL emission, we derive the electron-phonon coupling, expressed as the Huang-Rhys factor, S (Eq. (2.39)). We find a ratio of ∼0.16, which does not considerably change with barrier thickness. For the sample with the thinnest barrier it increases slightly by 0.02. Additional CW-PL investigations of the electron-phonon coupling of the 50 MLs sample performed under different temperatures in the range from 4 to 150 K revealed only a weak temperature dependence of the Huang-Rhys factor.

Barrier width [ML]	Peak energy [eV]	FWHM [meV]	Huang Rhys factor	Proportion of absorbed intensity [%]	A_{norm}[arb.u.]
50	3.25	76	0.17	76	5.6
25	3.25	70	0.14	52	4.0
12	3.24	67	0.16	31	5.8
6	3.15	69	0.18	18	0.3

Table 5.1.: Parameters of the SL peaks obtained from the cw-PL experiment.

In Table 5.1 we summarize the fitting parameters, i.e. peak positions, FWHM and Huang-Rhys factors for all samples of the series. The width of the emission peaks do not change considerably with decreasing barrier thicknesses, although, the sample with a barrier thickness of 6 MLs shows a slightly largest FWHM. To coarsely compare the SL emission yields of all samples against each other, we have normalized the experimental integrated intensities (A_{exp}) to the fraction of excitation light which is absorbed within the corresponding SL stack. This should eliminate the influence of the different total thickness of the structures. The absorbed intensity follows an exponential dependence with the sample thickness, h, according to the Beer Lambert law:

$$I = Io\exp(-\alpha h) \tag{5.1}$$

where α(3.8 eV laser excitation)=10^5cm^{-1}is the absorption coefficient which we assume to be equal for both (In,Ga)N and GaN for simplicity [225].

Thus the final absorption corrected gain of the SL will be defined as:

$$A_{norm} = \frac{A_{exp}}{1-\exp(-\alpha h)} \tag{5.2}$$

The fraction of light absorbed by the SLs yields the absorption-corrected integrated emission intensities, A_{norm}, are listed in Table 5.1. The three samples with barriers $\geqslant$ 12 MLs show a small variation of the A_{norm}parameter, whereas the thinnest barrier sample exhibits an integrated intensity which is about 17 times lower compared to the mean value of the other samples from the series.

The decrease of emission intensity of the SL with 6 ML thick barriers was crosschecked by means of a quasi-resonant PL experiment performed at the Paul Drude Institute. Here, we used an excitation energy of 3.41 eV (363 nm), i.e. below the band gap of GaN (3.46 eV), to ensure that electron-hole pairs are excited exclusively in the QWs. In Fig. 5.6 (a) we present the integrated intensities of the spectra of all 4 samples using the excitation above and below band gap of GaN. For the two excitation conditions, the luminescence yield of the sample with the

50 ML thick barrier under (3.54 eV) 350 nm excitation 2-3 times larger compared to the quasi-resonant one due to the contributions of the carriers transferred from the GaN barriers. With decrease of the barriers thickness this difference reduces. For the SL with 6 MLs barrier the yield is two orders of magnitude lower with respect to the other SLs under both types of excitation.

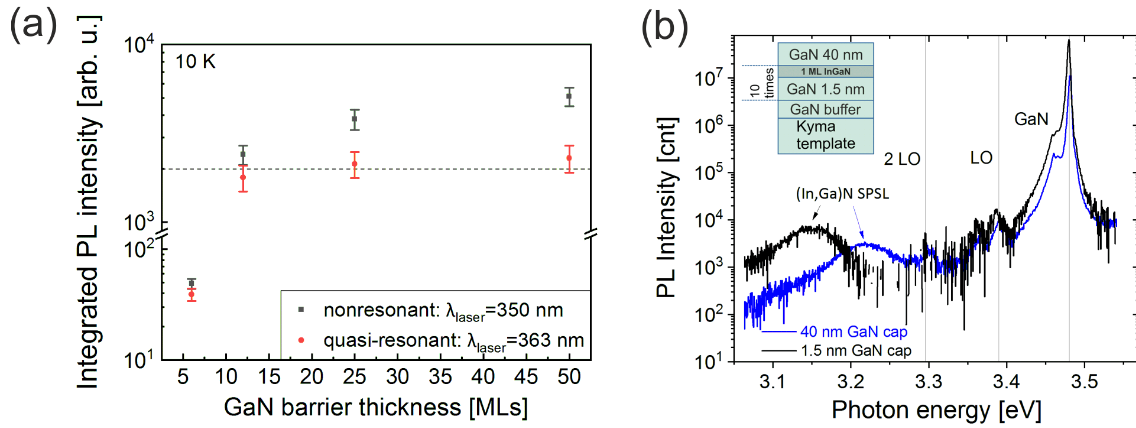

Fig. 5.6: (a) Above and below GaN band gap excitation PL of the samples with 50, 25, 12 and MLs barrier SL. (b) Emission spectra of the SL with 1.5 nm and 40 nm GaN-cap layers. The inset shows a scheme of the additional structure grown with a thick cap layer.

Furthermore, this effect does not depend on the thickness of a GaN cap layer. This was verified by PL measurements of an additional sample with an identical SL to that of the sample with a barrier thickness of 6 MLs, but capped with 40 nm of GaN. A comparison of the SL spectra of two structures - one from the barrier series and the one with the thicker cap layer is presented in Fig. 5.6 (b). PL spectra were taken under 3.8 eV (325-nm) line of a HeCd laser with an excitation power of 100 µW at 10 K. Two peaks are observed in the range typical for the GaN emission - one at 3.48 associated to the band gap emission and the second one redshifted by 30 meV. Barrier and cap-layer emission is also accompanied by two LO-phonon replicas separated by ∼90 meV. (In,Ga)N SLs from the sample with 40 nm GaN cap is blueshifted to the values almost corresponding to the samples from the series with thick barriers (∼3.22 eV). Luminescence yields of both of the samples are similar and significantly lower as compared to the GaN contributions.

5.3.3. Time-resolved PL measurements

TRPL experiments were performed using 259 nm-laser line (4.79 eV) for all samples from the series. Excitation powers were adapted for each SL individually to to account for the different total thicknesses of each SL stack and thus the the different proportion of absorbed excitation power This ensures a comparable non-equilibrium charge carrier generation in each sample.

According to the proportion of the absorbed light, excitation powers were 3.2 mW (50 MLs), 3.9 mW (25 MLs), 6.0 mW (12 MLs) and 10.3 mW (6 MLs). Furthermore, each sample was measured under two excitation power values altered by one order of magnitude. The calculation of the non-equilibrium carriers density created in all SLs with different barriers can be found in C. TRPL transients extracted from a ±40 meV window around the SL emission peak are presented in 5.7 (a) for each sample.

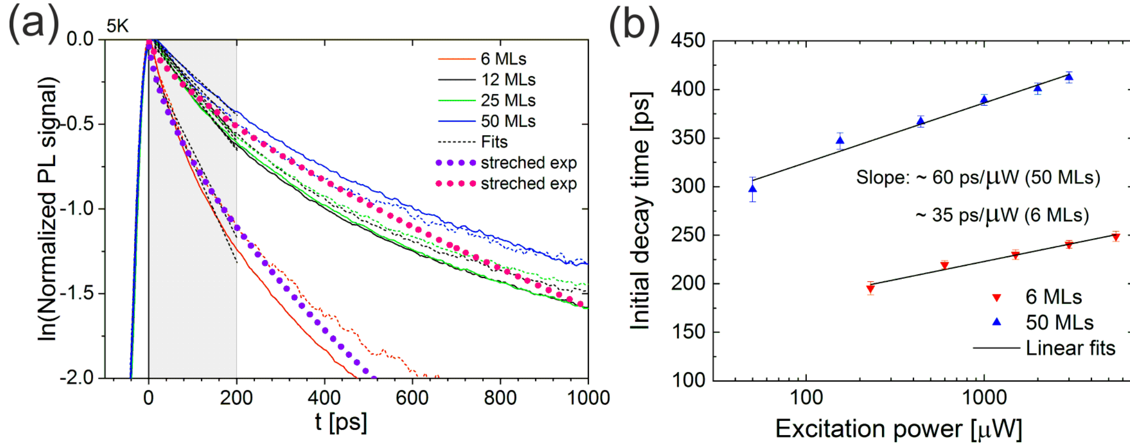

Fig. 5.7: (a) TRPL transients measured under 3.2-10.3 mW (solid lines) and 0.32 - 1.03 mW (dashed curves) shown in semi logarithmic scale. Black dashed lines are the single exponential fittings of the intensity decays made the gray shaded area. Magenta and purple circles are stretched exponential fittings. (b) Power dependence of the initial decay for 6 MLs and 50 MLs barrier samples extracted in the 0-200 ps time window. Experiment temperature was 5 K. Slopes of the lines are indicated.

The three samples with barrier thicknesses of 12 MLs, 25 MLs and 50 MLs exhibit a comparable decay behavior of the photoluminescence, while the sample with 6 MLs barrier thickness decays much faster. This behavior does not change under lower and higher excitation powers. All decay curves exhibit a non-exponential dependence, thus cannot be characterized by a single exponential function. Therefore, we employed two approaches to characterize the decay times. The first is done by fitting to a stretched exponential function, that describes long-tailed decays of many physical processes [226]:

$$I = I_0 \exp[-(\frac{t}{\tau})^{\beta}] \tag{5.3}$$

where τ is a stretched exponential lifetime and β - a stretching parameter. The latter one can be used as a qualitative criterion that expresses the system disorder, where the $\beta_{max} = 1$ returns a standard exponential function of the strongly isolated state (a single exponential case), and $\beta \leqq 1$ represents a diverse number of states (ensemble of different single exponential states). By fitting a stretched exponential we obtain (see Fig. 5.7 (a) (circles)) *life* times: $\tau = 170$ ps and $\tau = 520$ ps and stretching parameters$\beta = 0.63$ and β=0.7 for the 6 MLs-thick barrier SL and SLs with barriers $\geq$12 MLs, respectively. The decay of the sample with the thinnest barrier is fitted by a slightly lower stretching parameter, however, as can be seen from the fitting, it gives an acceptable agreement only in a limited range and fails already after approx 250 ps. Thus, a more accurate approach is based on bi-exponential fitting using two decay times. Generally, it is done to distinguish between different recombination processes - dynamics of the “fast” recombination shortly after the pulse, e.g. carrier trapping into defects (see, for instance, carrier relaxation in (Al,Ga)N SLs, Ref. [227]); and the long lasting decay indicating a “lifetime” of charge carriers.

We have evaluated the initial decay times in the 0 - 200 ps time window marked as gray shaded area in Fig. 5.7 (a). Results of the exponential fittings of each decay curves are shown in Table 5.2, the experimental errors are taken as double STDs of the fitting.

Excitation power	**6 MLs** [ps]	**12 MLs** [ps]	**25 MLs** [ps]	**50 MLs** [ps]
P_{low}	195 ± 10	326 ± 6	324 ± 8	377 ± 12
$10\times P_{low}$	171 ± 7	303 ± 7	314 ± 10	422 ± 9

Table 5.2.: Decay times of SLs with different barriers estimated for high ($10\times P_{low}$) and low excitation conditions.

According to Table 5.2, the initial decay times reduce with decreasing barrier thickness. This change is small or negligible when reducing the GaN barrier thickness from 50 over 25 to 12 MLs. Further decrease of the barrier to 6 MLs reduces the decay time by almost a factor of two. Since our setup allowed measuring of the decay in a limited time regime we may refer to the work of Feix et. al [228] who investigated the same sample series. There, the authors have recorded the PL decay up to 12 ns. The PL decay measured at 10 K was found to be rather slow and could be described by a power law ($T^{-2.4}$). The sample with the thinnest barrier showed a steeper decay than the thickest one.

Additional TRPL experiments were performed under an extended range of excitation power ranging from 50 µW to 3000 µW for the 50 MLs barrier SL and 230 – 5500 µW for the 6 MLs (see Fig. 5.7 (b)). The initial decay times extracted from the same time window of the SLs with the thinnest barrier showed a more gradual slope compared to the superlattice with a barrier thickness of 50 MLs (marked on Fig. 5.7 (b)).

We have also evaluated the dependence of the initial decay time (0 - 200 ps window) on the emission energy, the so-called spectral dependence of the decay time. In Fig. 5.8 we present the initial decay times for the thick barrier SL - with 50 MLs GaN - and 6 MLs. The decay time of the 50 MLs structure significantly increases towards the lower energy part of the emission spectrum , while the increase of the 6 ML sample is much less pronounced.

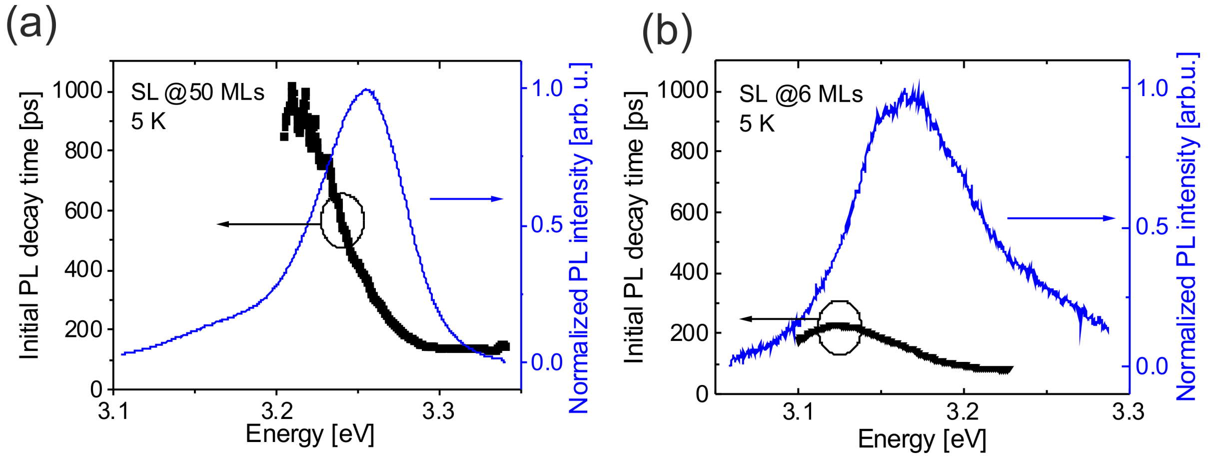

Fig. 5.8: Spectral dependencies of the the SL with (a) 50 MLs (b) 6 MLs shown along with the regular PL spectra extracted from the same TRPL experiment. The decay time scales used for the 6 and 50 MLs SLs were identical.

The initial decay time of the thin barrier structure monotonously raises starting from short wavelength, but saturates already at 230 ps then followed with a slight decrease in the low energy region. The PL spectrum extracted from the TRPL experiment appears noisy and slightly broadened. Noticeably, the decay times measured for the same SLs series in the longer time window till 12 ns were independent on the emission wavelength.

5.3.4. Temperature dependence

CW-PL temperature dependence measurements were done using the 325-nm line of a He-Cd laser at an excitation power density of 100 mW/cm^{-2}. Emission spectra were investigated in the temperature range from 4.2 to 300 K for the two samples with the thickest and thinnest barriers from the series. The original data from the experiment are shown in Fig. 5.9 (a) on a logarithmic scale. At low temperatures two LO phonon replicas can be resolved separated by ∼85 meV. Peak positions were extracted from the Gaussian fitting and presented in Fig. 5.9 (c); broadening of the spectra due to the phonon coupling was taken into account (i.e. FWHM was adjusted). The thickest barrier sample exhibits a characteristic *S*-shape dependence of the emission peak energy very similar to the ones observed for the conventional QWs [229]. Three regions marked in colors can be found: an initial redshift by ∼30 meV starting from 4.2 to 130 K; in the temperature range from 130 to 200 K, a remarkable blueshift of the PL peak position by ∼25 meV occurs accompanied by a strong quenching of the integrated intensity, followed by a redshift at temperatures higher than 200 K.

Another parameter that we have measured exclusively for the 50 MLs sample is the temperature dependence of the FWHMs as presented in Fig. 5.9 (e). The values were extracted from the same Gaussian fitting as done for the peak positions, i.e. broadening due to the phonon coupling was considered. Widths of the spectra monotonically increase with temperature and saturate at 114 meV at 150 K (marked as Γ_s and T_s). Further widening of the spectra continues at 240 K.

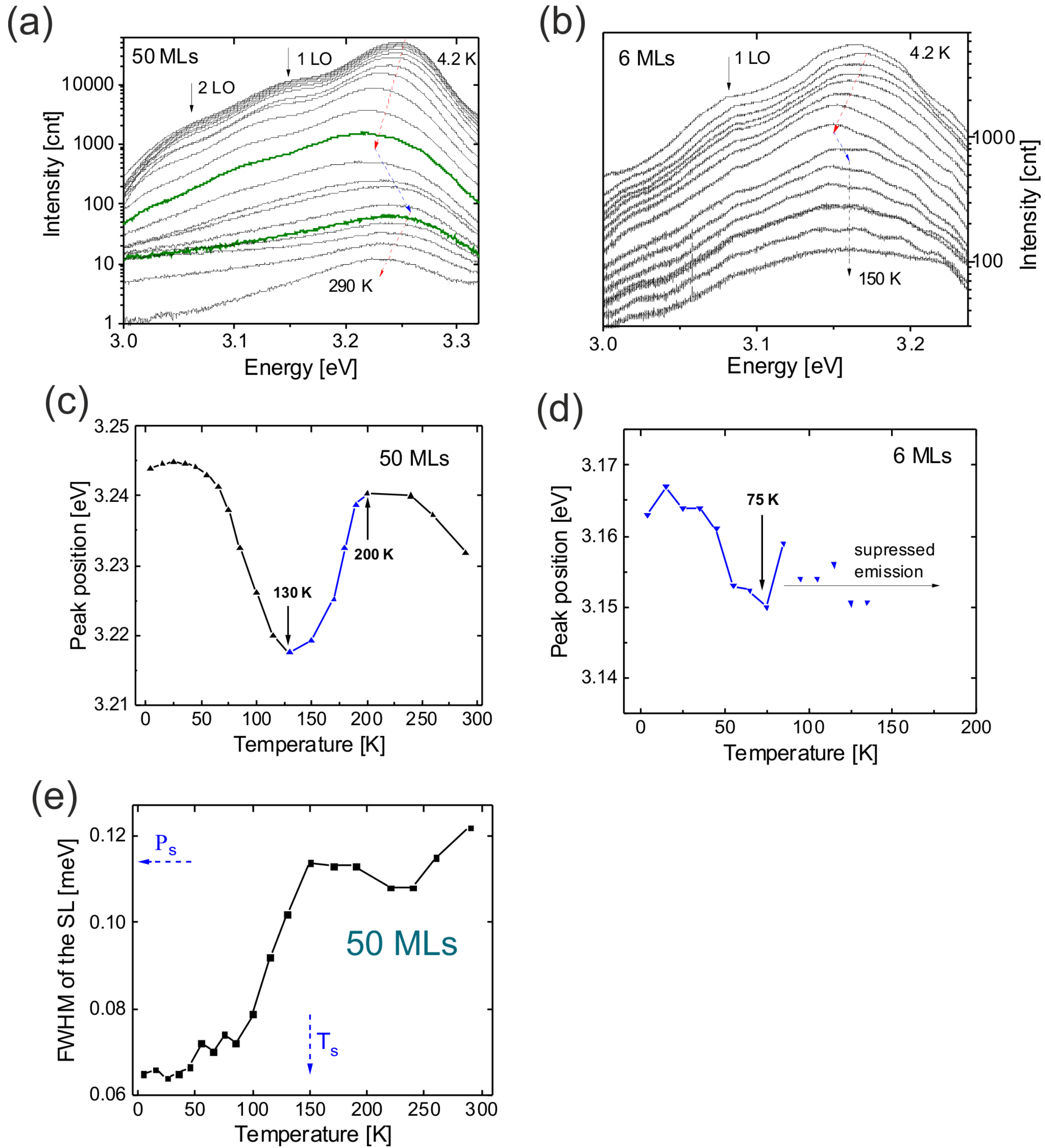

Fig. 5.9: Temperature dependencies of the SLs with 50 MLs (a) and 6 MLs (b) presented in the range from 4.2 to 290 K and 4.2 to 150 K, respectively. Dashed arrows follow the behavior of the peak positions that are extracted via the Gaussian fitting and shown in (c) for the 50 MLs and (d) 6 MLs samples. Here, the graphs are presented in the equal y-scale range (40 meV). Black arrows indicate the first and second (on the (a) solely) phonon replicas. The transition temperatures on the S-shape dependence of the thickest barrier sample are marked as green curves in (a). (e) Temperature dependence of the FWHMs of the 50 MLs SL extracted from the same Gaussian fitting done for (c). Arrows indicate the saturation point of the FWHM increase.

Fig. 5.9 (b) represents the experimental data of the thinnest barrier sample. Here, the first phonon replica can be observed, however the quantification of the results is complicated due to (i) broadening of the spectra already from 30 K and (ii) the presence of Fabry-Perot oscillations due to the difference in the refractive index of air/(In,Ga)N,GaN/and the sapphire substrate

[230, 231]. Gaussian fitting of the spectra was done for the whole temperature range. However, starting from 85 K the data are not reliable (see Fig. 5.9 (d)). The initial redshift by $\sim$17 meV stops already at 75 K and is followed by an increase of the emission energy. Peak positions at higher experimental temperatures are poorly resolvable, because of the weak luminescence of this sample.

5.3.5. DFT calculations.

To get deeper understanding of the charge carrier recombination DFT calculations by means of the Heyd, Scuseria, and Ernzerhof (HSE) hybrid functional and the projector augmented-wave method were performed by L. Lymperakis at Max-Planck-Institut für Eisenforschung. Computations were done for the SL structures similar to the ones investigated experimentally - 1 ML thick $In_{0.25}Ga_{0.75}N$ QW biaxially strained to GaN and separated by the barriers with varied thicknesses. The supercells boundaries were 2×2×(n+1), where n is the barrier thickness ranging from 1 to 19 MLs. The 2x2 size of the repeated cell in the basal plane fulfills the compositional criteria of 25% in the ML, i.e. 1 In atom and 3 Ga atoms.

First, the effective band gaps for the SL supercells with different barrier thicknesses were calculated. The calculated band gap GaN was 3.09 eV. The difference of the calculated absolute values of the SLs and experimental energies was ∼250 meV. Thus, in Fig. 5.10 we plot the difference between the GaN- and SL-peak emission obtained from the experiment and energy distance between the effective band gaps of GaN and (In,Ga)N-containing supercells from calculations.

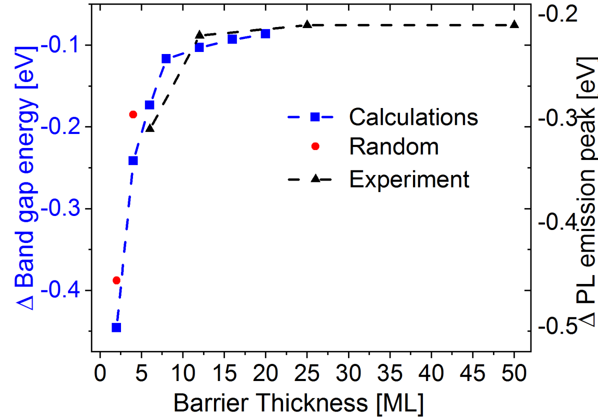

Fig. 5.10: Comparison of the calculated (blue symbols) and experimental (black triangles) transition energies for the samples with different barriers. Note the same energy range on the Y-axis.

The computed decrease of the effective SL band gap for thinner barriers reproduces the trends observed from optical investigations. The band gap shift shows three characteristic regions:

(i) “thick barriers” where the calculated energy difference is negligible (16 meV), when reducing the barrier thickness from 20 MLs to 12 MLs. Experimental data showed a very similar shift of 10 meV shift when barrier decreased from 25 MLs to 12 MLs.

(ii) for a barrier thickness of 7 MLs the band gap decrease becomes significant, i.e. the calculated and measured redshifts between the SLs with 12 and 6 MLs barrier thicknesses were 70 meV and 90 meV, respectively;

(iii) reduce of the barrier thicknesses from 5 MLs to 1 MLs (calculated only) results in a severe lowering of the band gap by 270 meV.

Next, charge carrier distribution and effective masses for both types of carriers were calculated along the <0001> direction. The effective masses of electrons and holes estimated from the fitting of the dispersion curves of the lowest unoccupied (VBM) and highest occupied (CBM) states around the Γ point are presented in Table 5.3. Here the carriers effective masses in

the SLs with barriers ranging from 1 to 15 MLs were normalized to the respective value found for the SL with 1 ML GaN. The effective masses of electrons show almost no change across the whole calculated range of the barrier thicknesses, fluctuating around the value found for a 1/1 SL. Results for the holes are opposite - a strong dependence on the barrier width can be seen for the SLs starting already from 5 MLs, where the barriers > 7 MLs exhibit a steep increment of the effective mass. We note that the calculations for holes showed a decent precision for the SLs with barrier thicknesses below 11 MLs due to the short length of the Brillouin zone of the thick SLs and the limited energy accuracy of the eigenstates (0.1 meV). The VBM is dispersionless already for the supercells with barriers thicker than 15 MLs.

m^*_n/m^*_1	**1 ML**	**3 MLs**	**5 MLs**	**7 MLs**	**11 MLs**	**15 MLs**
electrons	1	0.99	0.96	0.95	0.96	1.01
holes	1	1.17	1.59	2.61	**7.61**	*7.61*

Table 5.3.: Calculated electron and hole effective masses for different barriers thicknesses. Values are normalized to the corresponding effective masses of the SL with 1 ML thick GaN.

The charge density of the p- and s-states in the SLs with 1, 5 and 15 MLs GaN barriers are presented in Fig. 5.11. The charge is mostly located near the nitrogen atoms. The polarization fields are not taken into account due to the boundary conditions employed for the DFT, however, the discontinuity between (In,Ga)N and GaN induces elongation of the charge distribution mostly visible for holes towards <000-1>. Starting from the 1/1 SL both electron and hole charge densities are homogeneous throughout the supercell. States at the VBM are slightly more localized near the QW - their planar averaged density is twice larger than in the GaN region. An increase of the barrier thickness to 5 MLs leads to the consolidation of the hole's charge densities closer to (In,Ga)N ML, but approximately one *fifth* of the charge can still be found inside the barriers. With further increase of the barrier width to 15 MLs the hole wavefunction is localized exclusively near the (In,Ga)N ML and surrounding 3 MLs of GaN. The electron charge density appears homogeneously spread within the supercell even in the 1/15 SL: it is only two times lower in the middle of the barrier compared to the QW.

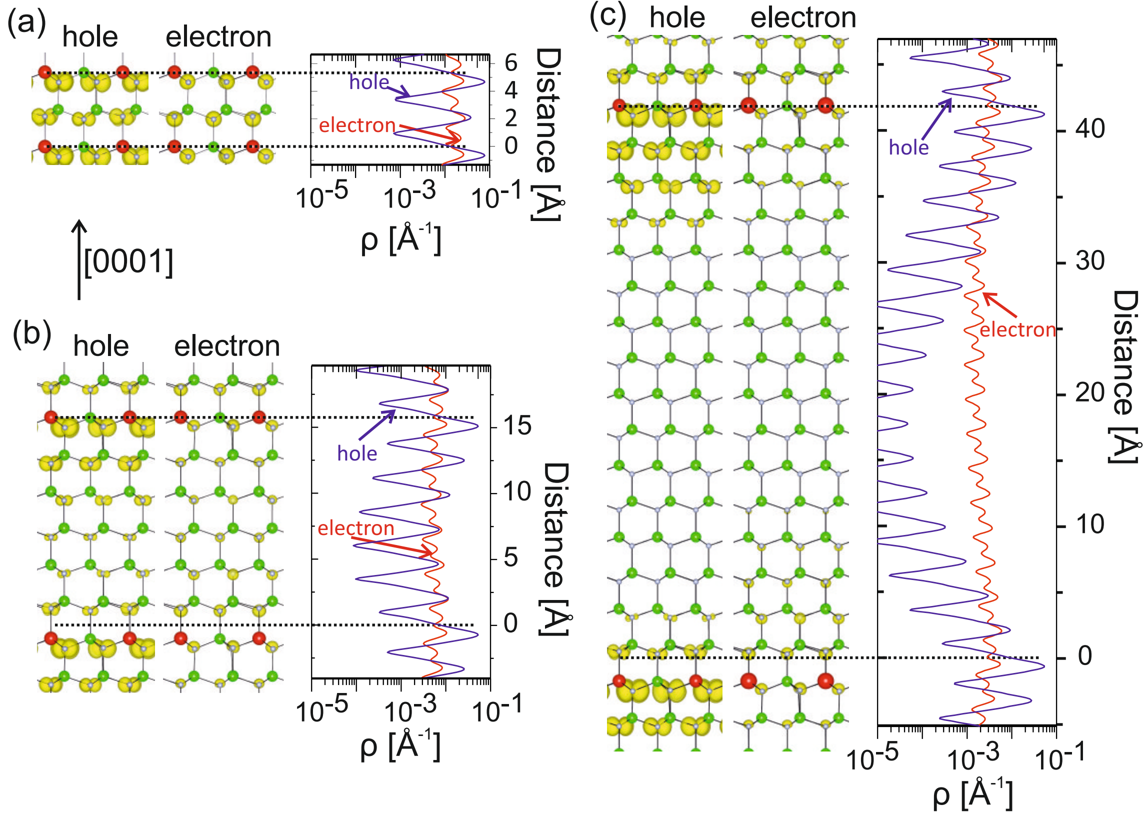

Fig. 5.11: Partial charge densities of holes and electrons and their respective planar averaged profiles (on the right) for (a) 1/1 (b) 1/5 and (c) 1/15 SLs. In, Ga and N atoms are shown as red, green and small gray circles, respectively. The short-dashed lines indicate the region with the $In_{0.25}Ga_{0.75}N$ ML.

Summing up the results of the DFT calculation from Fig. 5.11 the hole states exhibit stronger localization in the proximity of the QW region compared to the almost free electron distribution. To compare quantitatively the degree of confinement of both carriers in structures with varied barriers we have estimated the fraction of the prevailing part of carrier density volume, ΔV_i, from the total volume, V_i, of the corresponding supercell. Note, that the ratio $\Delta V_i/V_i \rightarrow 0$ indicates strong confinement of the carriers within some volume much smaller than the whole supercell, i.e. (In,Ga)N ML in our case. If $\Delta V_i/V_i \rightarrow 1$, the charge carriers are distributed all over the total volume V_i. The DFT calculations employing the HSE functional were done for the SLs with barriers ranging from 1 to 19 MLs. Partial volume, ΔV_i, was chosen as 80% [152], the supporting calculations for 95% revealed exactly the same tendencies for VBM and CBM states, thus not shown here.

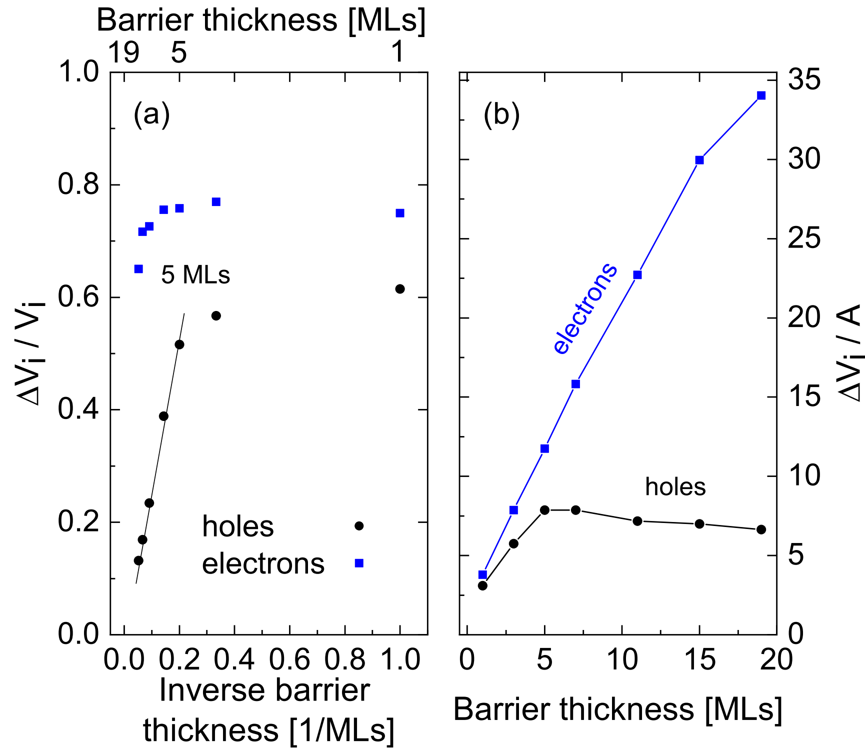

Fig. 5.12: (a) Partial volume of the 80% of the electron (blue squares) and hole (black circles) charge densities depending on the inverse barrier thickness. Black line is a linear fit of the VBM carrier densities for the SLs with barriers thicker than 5 MLs. (b) ΔV_i normalized to the cross section area of SL for both carriers.

The $\Delta V_i/V_i$ ratio of the CBM charge densities shown in Fig. 5.12 (a) is almost constant for the barrier thicknesses from 1 to approx 7 MLs, in detail, ~76% of the total SL volume confines 80% of electrons (ΔV_i). In Fig. 5.12 (b) the partial volume, ΔV_i, shown in respect to the cross section area of the SL (2×2×(n+1)), is proportional to the SL size. Explicitly, the faintly localized electron charge spreads with the extension of the supercell. Increase of the barrier to 19 MLs leads to the slight compression of the ΔV - here 65% of V_i is required to localize 80% of charge density at the CBM. However, this value is still larger than the volume needed for the confinement of the charge densities at VBM - the $\Delta V_i/V_i$ highest ratio (~0.6) is observed only for very thin barriers (1 and 3 MLs). Then, for the SLs with $>$ 5 MLs of GaN this ratio is inverse proportional to the barrier width. From Fig. 5.12 (b) it can be seen that the $\Delta V_i/A$ remains almost constant for the barriers from 5 to 19 MLs. Combining this observation with the data shown in Fig. 5.11, i.e. the confinement of the hole wavefunction close to QW, from the slope of the linear fit (Fig. 5.12 (a)) we have calculated the area size that contains 80% of the hole wavefunction - 2.6 MLs around the (In,Ga)N ML, or 1.65 nm. Thus, the partial volume ΔV_i needed to localize the major 80% of the VBM charge density is independent on the barrier thickness for large SLs andis located in the area of $A{*}c_{(In,Ga)N}$ size.

To check the influence of the Coulomb interactions we have introducing a hole into the MLs. Our calculations performed for the of the 1/7 and 1/11 structures revealed a negligibly small effect of the attractive electron-hole interactions on carrier confinement. In details, the ratio of the SL volume that localizes 80% of the electron charge density is decreased by only 2% and 5% for the 7 MLs and 11 MLs thick barrier SLs, correspondingly.

5.3.6. Discussion

Overview of the results

Summarizing the results obtained from the DFT calculations and optical experiments we find that our SLs can be divided into two groups depending on their thickness - with “thick” and “thin” barriers. PL investigations for the samples with “thick” barriers - 12, 25 and 50 MLs - revealed a similar peak positions at ∼3.25 eV and comparable decay dynamics of the PL emission. Moreover, we find an S-shape temperature dependence of the PL peak position and a spectral dependence of the PL decay time (i.e. an increase in the PL decay time with decreasing emission energy), comparable to that of conventional 2-3 nm thick quantum wells. Our theoretical calculations of the supercell with thick barriers, i.e.≥ 6 MLs, showed a strong confinement of the hole charge density near the (In,Ga)N ML region which results in large hole effective mass. In contrast, the electron wave function is only very weakly localized in the wells, making its effective mass mostly independent on the barrier thickness.

Next, the emission band of the “thin” 6 MLs barrier sample was redshifted by 100 meV, as compared to the thick barrier SLs. This redshift of the emission energy with the decrease of the barrier thickness is following the theoretically predicted band gap shrinking [37, 48]. Shifts of the peak positions with the reduced barrier thickness follow the similar trend calculated by DFT (Fig. 5.10). The differences in the absolute values of the effective band gaps is attributed to: (i) small content variations ∼25% of experimental MLs; (ii) charge carrier interaction, e.g. excitonic effects, are not taken into account in DFT.

In addition, for the thin barrier SL, the decay of the emission is significantly faster. Furthermore, the differences between thick and thin SL are observed with respect to the shift of the emission band with temperature (S-shape), as well as the spectral dependence of the PL decay time, which are both less pronounced for 6 MLs barrier thick SL.

Previous works on the electron and hole confinement were done for classical 2-3 nm thick QWs [20, 175, 232], and were focused on the influence of compositional and well-width fluctuations on the spread of the charge density. The quantum structures investigated in our work are 1 ML thick with moderate In content fluctuations, therefore we can study charge carrier localization independently on the aforementioned phenomena. More explicitly, from our DFT calculations we find that a decrease of the barrier thickness below 5 MLs abruptly changes the hole confinement and causes a reduce of the effective mass of holes. Even weaker localization is found for SLs with 3 and 1 ML thick barriers. Yet, electron charge density being spread in the supercell does not change its behavior for calculated barriers and their effective mass also remains stable.

One of the major effects influencing the recombination processes in classical polar (In,Ga)N QWs are the piezoelectric polarization fields. According to theoretical work by Gorczyca et al. [162]internal fields (piezoelectric and spontaneous) in the ML still contribute to the profile of the energy bands. The electron holography experiments in Zhou et al. [41] revealed an increase of the electrostatic fields for SLs with thinner GaN barriers. However, in later works, the influence of the internal electric fields on the transition energy was shown to be negligible in comparison to hybridization of the well-barrier wavefunctions or strain effects [36]. We have shown that no blueshift under the increased excitation power was observed for the ML-thick QWs, but either a renormalization effect. Therefore, although some residual piezoelectric or spontaneous polarization fields can be present in our monolayers, they do not affect the recombination in such extremely thin QWs. We note also, that the electron-phonon coupling is weaker in our

structures in respect to the conventional QWs with the same indium composition. For instance, a 2.5 nm thick (In,Ga)N QW with 25% indium content exhibited more intense phonon replica with S=0.35 [224] that is twice larger than observed in our experiment. The electron-phonon coupling is governed by: localization of charge carriers (or excitons) and polarization fields [233]. The latter factor is insignificant in our MLs, we suggest that the only contributing factor to the LO electron-phonon interaction originates from the strong localization of the hole states.

Coupling of the QWs via hole wavefunctions

Recombination dynamics in our SLs are governed by the hole confinement, which are strongly confined near the (In,Ga)N ML for SLs with thick barriers, i.e. $>$ 6 MLs. Our data agree with the results obtained by Bellaiche et al. [171] who demonstrated a strong hole localization near a single In atom in zinc-blende GaN. This picture was completely different from the hole distribution in GaAs.

We have shown that stronger carrier localization increases the hole effective mass, while delocalization of the carriers is accompanied by low effective masses. The latter phenomenon was observed for holes in the SLs with thin barriers ($<$ 5 MLs). In contrast, the electron wavefunction was distributed almost over the entire supercell for the whole calculated range of the barrier thicknesses (up to 19 MLs). However, the dependence of the effective mass vs. the barrier thickness is complicated by the limited k-space for larger barriers. . As can be seen, hole carrier confinement enhances more abruptly than the effective mass. Hole mass gradually increases for the SL with barriers $<$ 7 MLs and for larger barrier (11 MLs) raises steeply. We suggest the *critical barrier thickness* for the hole wavefunction interaction is in the range of 6 to 11 MLs. Thus, structures with 12, 25 and 50 MLs have decoupled QWs acting independently, whereas the SL with 6 MLs represents a quasi-ordered (In,Ga)N alloy along the $<$0001$>$ direction.

Kusakabe et al. [234] have shown by means of less sophisticated Schrodinger-Poisson calculations that both holes and electrons wavefunctions have stronger overlap in InN/GaN SLs when the barriers width decreases from 12 MLs to 3 MLs. Indeed, high indium concentration in the ML would better confine electrons inside the QW thus their localization may be also manipulated.

Non-exponential decay and spectral dependence

Turning to the TRPL results, the transients of all samples in the series showed a non-exponential behavior, also found in the standard 2-3 nm thick (In,Ga)N QWs [163, 175]. Such a decay behavior suggests a strong carrier confinement in the assemble of states [235] what is expected due to the severe hole localization, especially for the thick barrier SLs. Weakening of carrier localization results in an acceleration of the decay, as shown for 6 MLs barrier structure.

Note, that in polar conventional (In,Ga)N QWs a non-exponential decay was also discussed in the frame of piezoelectric polarization: high amount of the carrier densities generated after the pulse flatten out the energy levels, what temporary enhances the recombination and then diminishes gradually [236]. In our case,polarization fields cannot cause the slowing of the recombination dynamics, thus, this effect is not relevant to our system. Next, the decay curves measured for two samples from the series (with 6 MLs and 50 MLs barriers) in the longer time period (see Ref. [228]) the decay is characterized by a power law ($\sim$with a power $x^{-2.4}$). The

authors suggested a model where both of the carriers are strongly localized and the decay is proportional to the in-plane distance between the separated electron-hole pairs following the Donor-Acceptor-Pair (DAP) model as presented for the conventional thick (In,Ga)N QWs in Ref [184]. However, such models require individually localized electrons and holes , which in our case however does not account for electrons which practically act as quasi-free carriers according to our DFT studies

A significant contribution of the hole localization in the recombination dynamics can be observed via another optical phenomenon related to carrier confinement in semiconductors - the energy dependence of the decay time. The most pronounced spectral dependence was found in all thick barrier samples (spectral dependence for the 50 MLs-thick barrier SL was shown in Fig. 5.8). Such behavior, i.e longer decay times of the high energy shoulder of the emission spectra, was also found in various material systems and structures: $In_xGa_{1-x}As_{1-y}N_y$ [237] and $CdS_{1-x}S_x$ [238] epilayers, $In_xGa_{1-x}As_{1-y}N_y$/GaAs MQWs [239], porous Si [240]and etc... Models employed to explain the spectral dependence of the decay time in polar (In,Ga)N QWs [32, 184, 241] are mostly based on a decisive role of piezoelectric polarization. For instance, Langer et al. [242], suggested that there is an ensemble of recombination centers with various local magnitude of the QCSE induced by the compositional fluctuations in the conventional QW. For our samples, however, we have shown that the impact of the QCSE is negligible. Moreover, in our experiments the decay time window (0-200ps) covers a period right after the excitation pulse. Here, for the standard polar QW one would expect screening of the piezoelectric fields and, therefore, possibly very weak spectral dependence. But we show, that: (i) the spectral dependence is very pronounced for the 50 MLs SL and (ii) it cannot be explained by the QCSE. Thus, the model of Langer cannot account for the observers recombination properties in our samples.

An alternative scenario takes into account the charge carrier transfer of electron-hole pairs. Excitons can travel downwards the bottle neck of the density of localized states thus lower emission energies which are characterized by longer lifetimes [243]. Such exciton tunneling was proposed to be theoretically probable when accompanied by acoustic phonons and shown experimentally for bulk CdS_xSe_{1-x} (Ref. [244]), $CdS_{1-x}S_x$ [238] and proved to be valid in the (In,Ga)N QD ensemble in Ref. [245]. This type of charge transfer may be active even at cryogenic temperatures (our experimental conditions) and seems to be the most conceivable model for the recombination mechanism in our SLs. The potential landscape deformed by the inevitable In compositional fluctuations in the (In,Ga)N alloy [174] creates various local densities of states [173], also with lower energies that can be reached by carriers with time. Bellaiche et al. [171] have also discussed that severe hole confinement takes place even without the In clustering, i.e. the exciton localization is expected in every In-containing GaN alloy. Now, taking into account that electrons are quasi-free particles in our system, we develop a model where only the hole states are responsible for the shape of spectral dependence. A schematic representation of this hypothesis is shown in Fig. 5.13 (a). Here the potential profile for the electrons is considered to be almost flat even in the SLs with larger barrier. Whereas, the hole states are sensitive to the alloy fluctuations and disturb the exciton transport process. Heavy holes grabbed by electrons redistribute via the phonon assisted tunneling process. This should also induce a delay in the initial population of the lower energy states, thus extending their rise time. The preliminary estimation showed that, indeed, higher energy states have shorter rise times. Humphreys et al. have shown that random alloy fluctuations in the conventional thick QW strongly affect the localized holes wavefunction. Although, their works involved the dis-

cussion of the spread electron density that is mostly drifted by the well width that is avoided in our system.

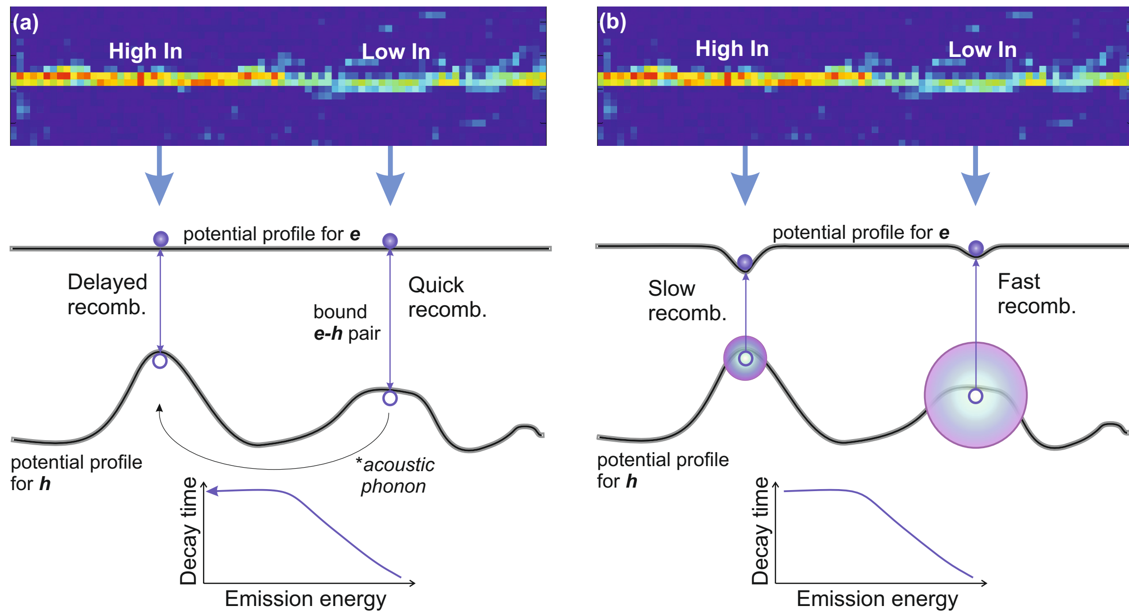

Fig. 5.13: Models explaining the spectral dependence of the decay time: (a) involving carrier redistribution; (b) employing solely the effect of extension the hole wavefunctions (shown as gradient colored circles). Open and filled circles represent holes electrons, respectively. The HRTEM color-coded experimental strain maps (top) depict the presence of the compositional fluctuations. (bottom) The final shape of the spectral dependence.

Moreover, slower recombination towards lower emission energies may be promoted by the smaller spatial spread more strongly confined holes in In rich regions of the ML. This might generally decrease the electron-hole overlap and, thus, the recombination efficiency. Holes in regions with lower In composition are expected to obtain wider extent of the wavefunction. Therefore, recombination of the high energy shoulder of the spectrum will be promoted as compared to the lower energy part (induced by higher In content)(see Fig. 5.13 (b)). This would result in the same outcome - longer decay times for higher recombination energy. Although such process may be possible in the inhomogeneous ML, larger indium contents are needed to notice such effect, i.e. to enable stronger localization of the carriers, especially electrons, in the $<0001>$ direction. In Fig. 5.13 (b) it is shown as the slight deformation of the electron potential profile. However, the experimental indium composition (less than 25%) and the in-plane content variations are too small ($\sim$3%) to achieve any considerable confinement for the electron states.

Note, that such fine feature of the recombination dynamics - carrier redistribution - was observed only in the very short time range (till 200 ps). On the longer time scales the spectral dependence was absent in the SLs with either thick and thin barriers (see Ref. [228]).

Non-radiative recombination

The presented spectral dependence of the decay time was mostly pronounced for the thickest barrier sample but was strongly diminished for the SL with 6 MLs barrier. Taking into account the intrinsic difference between the thick and thin barrier superlattice, with respect to the hole localization, we conclude that the delocalization of the holes for thin barrier SLs leads to the quenching of the PL intensity (see Fig. 5.5(a)). This is surprising, since a higher transition rate is expected for structures with thin barriers [36]. This would imply the shortening of the radiative decay times but also an enhanced luminescence yield, which is not observed for 6 MLs-thick barrier SL. Here we will discuss the origins of this phenomenon.

Results of the power dependent TRPL investigations (see Fig. 5.7 (b)) on the 6 MLs and 50 MLs barriers revealed a weaker dependence for the initial decay time for the thinnest barrier superlattice. Following the general assumption that a non-exponential decay may be caused by the initial carrier trapping into defects, a saturation of this process due to the limited number of defect centers should be observed. Yet, decay times of both samples continuously increase towards the increment of the excitation powers, one would expect longer decay times for the thinnest barrier SLs for the filled defect states. Likewise in Ref. [246], authors suggested that faster decay at the highest above-barrier pump intensity indicates the saturation of the non-radiative channels associated with defects. However, our 6 MLs barrier structure reveals only weak power dependence with still short decay times across the whole investigated power range. Thus, considering a strong decrease of the intensity, the non-radiative recombination rate is promoted for the thinnest SL. We will utilize spectral dependencies measured for the thinnest and thickest barrier samples (see Fig. 5.8 (a) and (b)) to illustrate this assumption.

The total rate can be estimated through the rates of energy dependent radiative, $\tau_{\mathrm{rad}}(\mathrm{E})$, and energy independent non-radiative, τ_{nonrad}, recombination times. For our estimation we take the spectral dependence of the initial decay times for the 50 MLs sample as input data since this sample demonstrated the highest luminescence intensity. Then we introduce the additional channel of non-radiative recombination by adding the τ_{nonrad}:

$$\frac{1}{\tau(E)} = \frac{1}{\tau_{rad}(E)[50MLs]} + \frac{1}{\tau_{nonrad}} \tag{5.4}$$

.

We gradually decrease the non-radiative decay time from 1000 ps to 100 ps in order to reproduce the shape of the weakest emitting 6 MLs SL (see Fig. 5.14). The best match between the initial decay times is observed when the non-radiative decay time decreases to 250 ps.

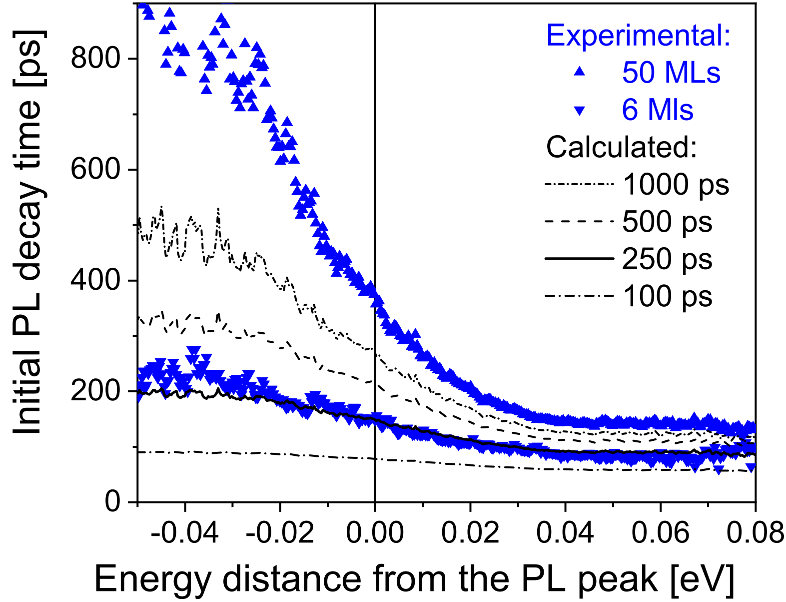

Fig. 5.14: Experimental (blue triangles) spectral dependencies and the ones calculated with different rate of non-radiative recombination (black curves).

This simple estimation shows that: (i) the radiative recombination mechanism is the same for the SL with the thick and thin barriers; (ii) the emission of the SL with 6 MLs barrier is strongly influenced by the non-radiative contributions. Therefore, only the degree of non-radiative recombination explains the difference in the PL decay between thin and thick barrier SLs.

Another barrier thickness series from Ref. [234] on the nominal InN/GaN SLs with 4-12 MLs GaN barriers showed the lowest intensity of the 4 MLs SL compared to the other samples. In the paper of [247] the authors have suggested that acceleration of the recombination dynamics with the reducing of the separating barrier in AlGaN/GaN MQW structures was also due to the enhanced ratio of the non-radiative recombination. The latter is induced by either spreading of the electron-hole wavefunctions to the barriers or by transport of the carriers to the misfit dislocations at the interfaces. We note that no plastic relaxation in our SL was observed as was shown by the structural investigations of the series. At the same time we have presented that reducing the barrier thickness between the two neighboring QWs indeed leads to the increased overlap of the charge carriers wavefunctions. We explain the enhancement of the non-radiative recombination by the high amount of point defects in barriers that consume the carriers. Indeed, the employed growth temperature (550°C) optimum for higher In concentrations may be not suitable to obtain good quality of the GaN barriers in MBE (typically more than 650°C [6,51]).

Temperature dependence

Regarding the temperature dependence of the peak position, we have observed a pronounced *S*-shape behavior for the sample with thick barrier (see Fig. 5.9 (c)) comparable to that of standard (In,Ga)N QWs. Three regions can be identified: initial redshift, blueshift and a final redshift towards higher temperatures as discussed in the scope of the band-filling model [178]. In detail, the low temperature redshift originates from the thermally activated filling of states with lower

energies. The following blueshift for elevated temperatures has been argued in many works as induced by the carrier distribution between localized states in accordance with Boltzmann statistics [180]. We will discuss this assumption later. The final redshift at high temperatures reflects the band gap shrinking effect as in many semiconductors [123, 125].

A blueshift in our MLs occurs at higher temperatures, i.e. from 130 to 200 K, as compared to the classical (In,Ga)N QWs, where an increase of the transition energy was typically observed from approx 60 to 150 K (see, for instance, [177, 179]). It is usually discussed as an indication of the stronger localization of the charge carriers. This assumption is supported by the characteristic temperature dependence of the half width shown in (Fig. 5.9(e)), where the saturation of the FWHM rise was observed at 150 K. Following the Ref. [181], we estimate the roughness of the potential landscape via the dispersion parameter of the small potential fluctuations, σ, that are implemented into the larger variations, Γ, induced by the indium clustering of different lateral size as:

$$\sigma = 2k_B T_S \tag{5.5}$$

and

$$\Gamma = \sqrt{\frac{\Gamma_S}{ln4} - \sigma^2} \tag{5.6}$$

From the experimental values on T_S= 150 K and Γ_S= 114 meV we get σ=26 meV and Γ=93 meV which is two times higher than the dispersion parameters of a 120-nm $In_{0.1}Ga_{0.9}N$ quasi-bulk film: σ=13 meV and Γ=45 meV. Such high values obtained in the single ML QWs supports our conclusions of a strong localization of charge carriers (i.e. holes) [179]. Transitions between the localized states within one indium cluster are enabled via the phonon-assisted hopping mechanism [181]. We suggest that there is an additional factor influencing the temperature dependence of the peak positions causing blueshift - increasing contribution of the non-radiative recombination. Assuming the energy dependence of the decay time discussed above, i.e. long living recombination occur in the low energy part of the spectrum. Thus under elevated temperatures when the non-radiative recombination enhances, such transitions are less probable than the fast high-energy recombination. This is always accompanied by the suppression of the intensity rate. Moreover, a saturation plateau of the temperature dependence of the FWHM may indicate not only the starting process of delocalization but also that the suppressed low-energy recombination what prevents the spectra from the broadening.

A connection between non-radiative transitions and the temperature dependence of the peak position is supported by the results of the 6 MLs barrier SL. Here, due to the higher contribution of non-radiative transitions, the blueshift starts at twice lower temperatures (Fig. 5.9(d)). Moreover, the blueshift is much smaller in the low temperature region. Multiple non-radiative recombination suppress the spectral dependence of the initial decay time (see above Fig. 5.14). Therefore, the blueshift of this sample is mostly caused by the decrease of the slower transitions towards lower emission energies. At the same time, for the thickest barrier sample, thermal charge carrier redistribution is less affected by non-radiative transitions and, thus, the blueshift starts at higher temperatures.

Employing our SLs with coupled and decoupled (In,Ga)N MLs we have shown that the intermediate-temperature blueshift on the S-shape originates from both - the delocalization of the charge carriers from their sites and an interplay of the radiative and non-radiative recombination. The latter hypothesis was discussed in the previous works of Cho et al. [177] and Langer

et al. [242]. Nevertheless, these works were done on the conventional polar QWs and involved the influence from the polarization fields into discussion [242].

Non-polar QWs

Flattening out of the spectral and S-shape dependence that were examined for the 6 MLs barrier sample have been also observed in non-polar (In,Ga)N QWs [232, 242]. This suggested that piezoelectric polarization is solely responsible for the energy dependence of the decay time. Phonon assisted carrier redistribution as the main mechanism for the longer decay in low energy region is efficient for the mobile carriers. Reduced effective mass of the holes for the thinnest barrier led to the arising rate of non-radiative recombination what occurs faster than the carriers can reach lower energy states. It was shown that effective mass of holes in GaN is strongly anisotropic, moreover, it is almost twice larger in polar direction than the one found for the basal plane [248]. Hence, in non-polar structures carriers distributing in lateral direction have larger effective masses than parallel to the c-axis. This implies less effective transfer of the heavy holes but fast recombination along $<0001>$ direction and reduces the spectral dependence. Such recombination dynamics for the non-polar QWs may also lead to the diminished S-shape dependence.

5.3.7. Conclusions

Summarizing our results, we have shown that solely localization of holes defines the recombination behavior in the (In,Ga)N MLs with concentrations below 25%. The discussed optical phenomena, i.e. non-exponential decay, spectral and S-shape temperature dependence discussed for the simplified structures - 1 ML QWs without thickness and low content fluctuations and thick barriers - were similar to the ones obtained in standard QWs. Moreover, all our structures are independent from influence of the polarization fields. Reducing the GaN barrier thickness between the (In,Ga)N MLs causes delocalization of the hole wavefunction. This results in the redshift of the emission and, also, in the increase of non-radiative recombination rate, which impairs the luminescence yield. This reduces the spectral dependence of the decay time and, hence, the temperature dependence in the low temperature region promoting the blueshift in the intermediate range. Thus, the change of the S-shape between thick and thin barrier SLs are reflecting the competition between radiative and non-radiative transitions. Analogous phenomena were exhibited for non-polar (In,Ga)N layers, thus rising doubts on the conventional explanations based on the impact of piezoelectric polarization found in literature.

The DFT calculations of the out-of plane confinement have shown that the hole wavefunctions interaction in the SLs with barriers below the critical thickness lies between 6 and 11 MLs. In thicker SLs decrease of the hole charge distribution affects directly the effective masses resulting in their presumably exponential increase. Electrons behave as quasi free particles and are almost indifferent on the barrier thicknesses. DFT computations including the lateral content variations in the supercells, not feasible due to the limited size of the supercell, could give the complete picture of the carrier localization in the basal plane and, thus, charge carrier transport. We suggest that carrier redistribution assisted by the acoustic phonons describe the energy dependence of the decay time that can be applicable for the both polar and non-polar (In,Ga)N layers. The probability of this tunneling depends on the charge carrier (hole) mass.

The important role of in-plane confinement explains another optical emission feature we

have not discussed in detail so far - the width of the SL peak. Measured FWHM were ~70 meV (see Table 5.1) what is in the range obtained for conventional 2-3 nm QWs [20, 249]. Thus, even small variations of the content strongly affect the localization of the holes that disturb their recombination with electrons and finally broaden the emission of the (In,Ga)N ML. To account for such lateral recombination centers we have performed the dedicated STEM-CL measurements and examined changes in lateral confinement in the gradient SLs.

5.4. Lateral confinement. Scanning TEM-CL measurements.

5.4.1. Localization of the charge carriers

Compositional fluctuations are often observed in several nm thick quantum wells, where statistical variations of the composition are expected [173, 197]. In 5.15 (a) we show the deconvolution of a CL spectral map of a quasi-bulk 120-nm $In_{0.06}Ga_{0.94}N$ film. The study was performed at 7 K in spot mode using 7kV acceleration voltage. The spectral plan view map of the peak positions is obtained from the Gaussian fittings of the emission spectra measured at each spot. Pronounced long range fluctuations of the In content lead to a variation of the emission energies by 182 meV. An average lateral size of these fluctuations is approximately 1-3 μm x 0.5 - 1.5 μm. In contrast similar CL studies of our ML-thick (In,Ga)N QWs exhibit an almost homogeneous luminescence as presented in Fig. 5.15 (b). The studied SL structure is formed of ten periods, consisting of a 10 nm GaN barrier and a $In_{0.25}Ga_{0.75}N$ ML-thick QW. The shift between the highest and lowest emission energy was 9 meV, i.e. much narrower, than the FWHM of the QW emission itself. Thus, the spectral map appears uniform without any significant spectral fluctuations. The halo-like feature in the Fig. 5.15 (b) (marked by arrows) is just a trace of the spherical collecting mirror.

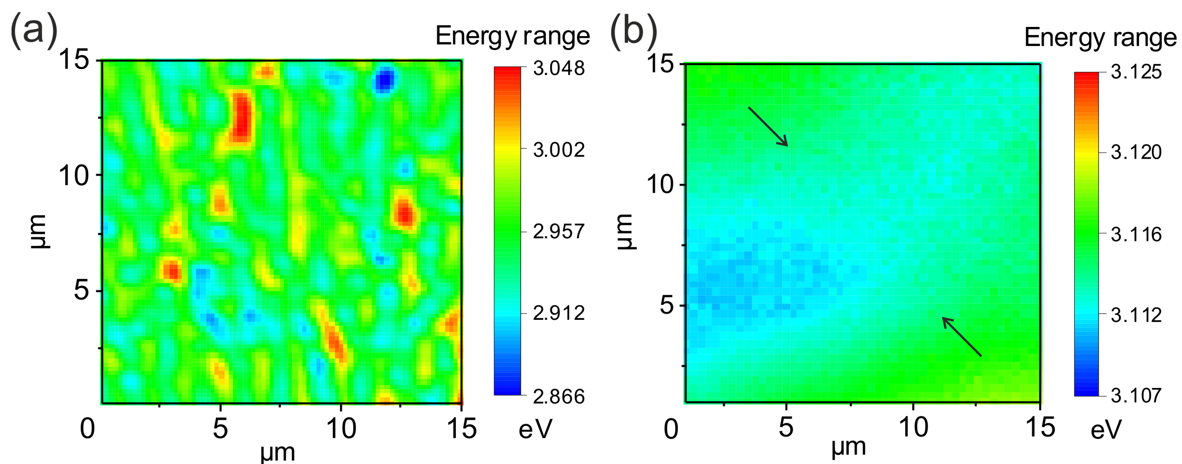

Fig. 5.15: CL spectral maps of the (a) thick (In,Ga)N film (b) (In,Ga)N ML with 25%. Excitation voltage was 7 kV and 7 K temperature was kept in both experiments. Size of the investigated area was 15 μm x 15 μm. A trace of the collecting mirror in (b) is pointed by the arrows. Note, the different scales used on the maps - 182 meV for the quasi-bulk and 20 meV for the SL.

To get more insights into the lateral carrier confinement within 1 ML thick QWs we investigated our QWs by means of cathodoluminescence in the STEM. Due to the small electron probe in a TEM and the small thickness of the specimen, the excitation volume is very small enabling a very high spatial resolution. We have already mentioned that MLs are not continuous with homogeneously distributed In composition but may obtain higher In content regions and intraplane ordered patches (see examples in Fig. 4.9). We estimate that the lateral extension of these areas with the $(2\sqrt{3}\times2\sqrt{3})R30\circ$ ordered pattern were found in the range from 3 to 35 nm. In the next section we will study films where the coverage of the (In,Ga)N MLs was intentionally

varied. This has been done by systematic change of the growth temperature and growth time within a superlattice stack. By means of STEM-CL we, then, study the influence of the ML coverage and mean composition on the optical spectra.

5.4.2. Change in coverage. STEM-CL measurements

The STEM-CL investigations that will be presented in the following are performed at an accelerating voltage of 80 kV at 16 K. For the evaluation of the results we extracted the color coded linescancs, i.e. spectral maps, along <0001> direction representing the position depended redistribution of emission intensity. Fig. 5.16 (a) shows a typical STEM-CL spectral map of the superlattice stack, where the growth time of the ML-thick quantum well was increased going from the first QW (4s) to the last one (60s) grown in a sequence. The structural data can be found in 4.2.3. The figure displays spectra gained from the line scan that extends 500 nm from the GaN substrate across the superlattice to the surface. The GaN buffer layer below the SL structure shows an intense emission peaking at ∼356 nm. This emission quenches towards the surface and is not visible in the GaN barriers. The superlattice emission shows two separate luminescence peaks that can be distinguished - one located in the lower part of the structure, at 3.34 eV (371 nm), and an intense major peak at 3.26 eV (380 nm). We assign this blueshift of the lower lying ML quantum wells to a reduced In incorporation into this particular layers. As was shown in the previous chapter, these lower lying MLs were grown at 4s and 8 s without N supply and where not fully closed but consisted of ML-thick discs well separated from each other.

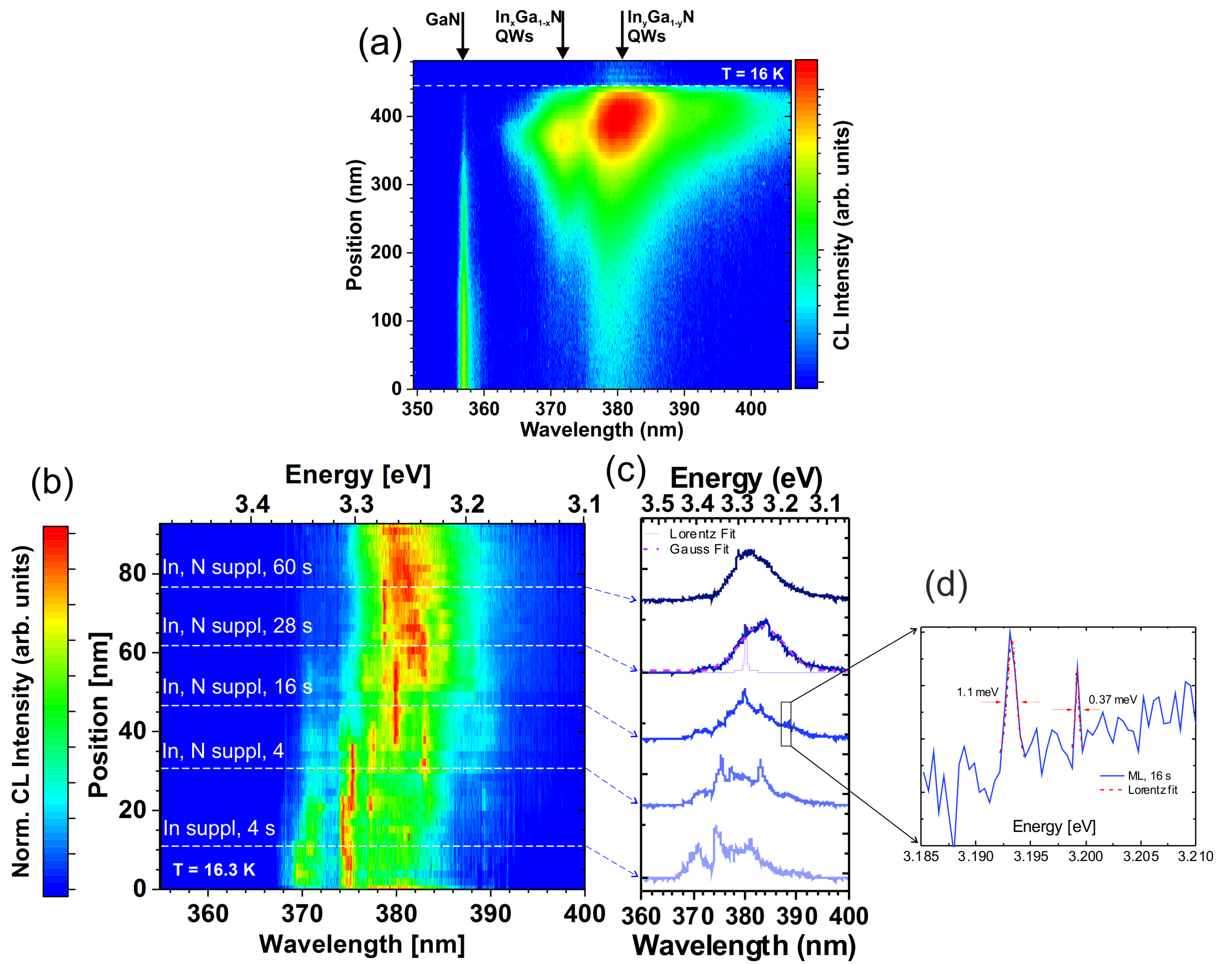

Fig. 5.16: (a) I(x,λ) spectral map derived as a linescan of the time gradient sample. Here the color code indicates strength of the emission, where the scale is normalized to the peak intensity maximum. Arrows point to the emissions from SLs with different In content and GaN buffers. Investigated area was 500 nm length. (b) I(x,λ) spectral map of the 90 nm structure thickness in <11-20> projection. Color code represents emission intensity normalized to the intensity maximum. (c) Individual spectra extracted from different QWs marked as dash white lines on the STEM-CL linescan (b). Gaussian fit of the broad emission of the ML grown for 28s is marked with thick magenta dash curve, Lorentz fit of one of the sharp lines is indicated by solid purple line. (d) Magnification of the selection of the “16 s” ML spectrum. Lorentz fits of QD-like sharp lines are shown as red dash-dot curves.

Fig. 5.16 (b)) shows a STEM-CL line scan from the same sample at higher magnification. Under these conditions distinct emission lines from the individual QWs can be revealed. Several local luminescence spectra extracted from different QWs are presented in Fig. 5.16 (c). The three QWs at the bottom of the stack, grown for 4s without and for 4s and 8s with N supply exhibit broad spectra that consist of series of sharp emission peaks. With increasing growth time of the QW, the density of these line increases and finally merges into a broad CL peak. The center of gravity of the band shifts toward higher wavelengths. By Lorentz fitting of the individual sharp lines of the QW grown for 16 s(see e.g. Fig. 5.16 (d)) we obtain a FWHM ranging from 0.37 meV to 1.2 meV. The spectrum of the following QW (grown for 28 s) becomes more smooth and the individual lines merge. The upper ML (grown for 60 s) exhibits a uniform spectrum with a narrow feature originating from the previous two QWs. FWHM of the upper

layers are ∼83-85 meV. Despite the remarkable evolution of the spectra shape, their center of mass shifts by 40 meV towards lower energies.

Similar STEM-CL investigations, i.e. at 80 kV accelerating voltage and at 16 K, were performed for the the superlattice where the subsequent monolayer quantum-wells were grown each at a different temperature. Structural data on this sample were presented in 4.2.2. We briefly summarize the main results here. The MLs were grown in the 580°C-650°C temperature range. Growth temperature of each ML-thick QW was decreasing stepwise towards the surface that resulted in the increase of the indium content from 11% to 23%. A panchromatic image of the superlattice stack done at low magnification shows the whole SL stack emitting though some intensity fluctuations along the investigated area of the specimen are present, very probably due to the presence of threading dislocations emerging in the upper layers close to the surface (in Fig. 5.17 (a)).

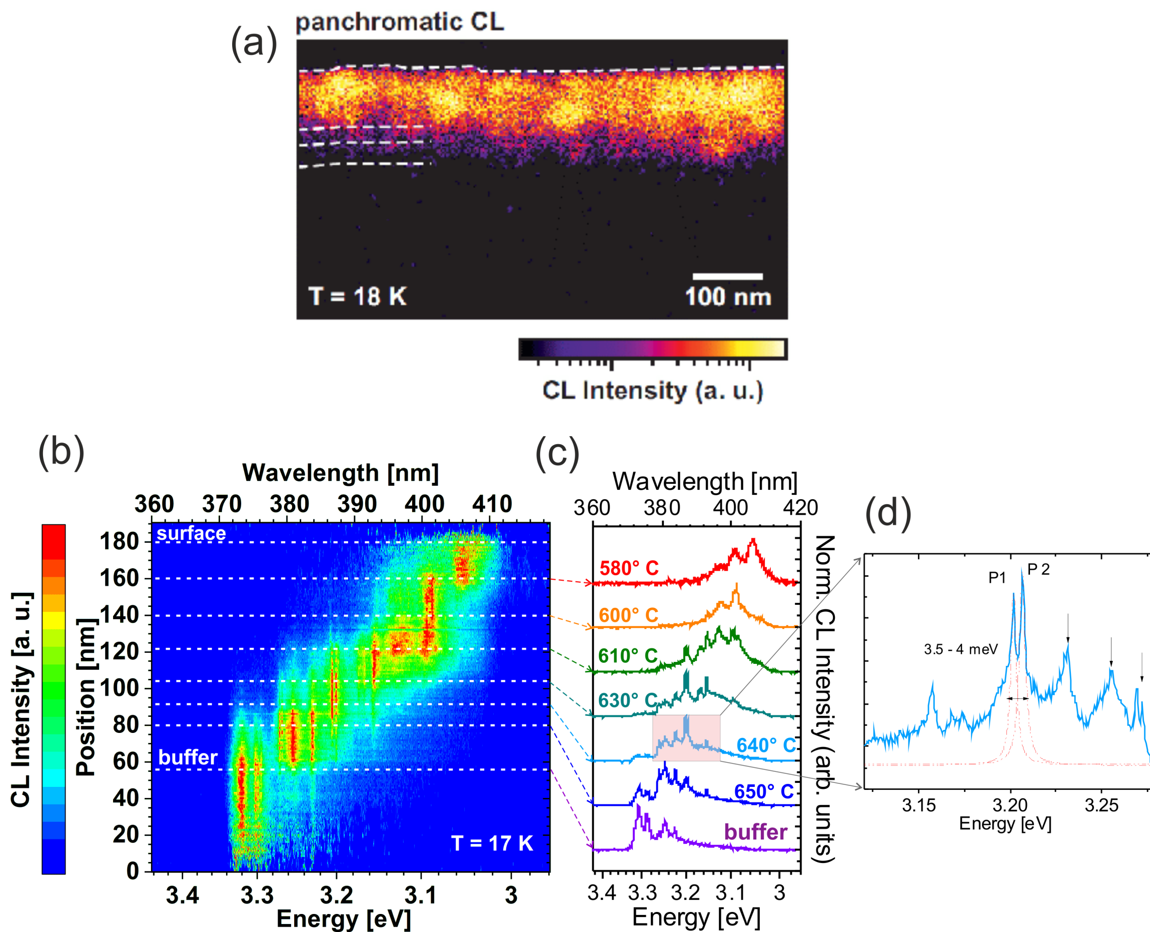

Fig. 5.17: (a) Panchromatic CL intensity image of the 2 buffer layer and 8 (In,Ga)N MLs. Dashed lines underline the borders between SL, buffers with 2 % In and GaN substrate; (b) STEM-CL linescan throughout the active region of the structure. The total investigated thickness was 180 nm. CL intensity was normalized to the maximum emission. Note that the energy axis is shown inversely to correspond directly to the wavelength scale on top; (c) Local CL spectra from different parts of the structure, marked by dashed lines. The approximate growth temperatures are indicated color-coded. Spectra are normalized for clarity; (d) A magnification of the part of the ML spectrum from (c) highlighted with pink. Red dash-dot curves are Lorentz fittings of the selected emission lines labeled Ex1 and Ex2.

A spectral line scan of the superlattice and the two underlying buffers is presented in Fig. 5.17 (c). The two emission lines at 3.31 eV (375 nm) and 3.26 eV (380 nm) present at the bottom of the structure correspond to the luminescence of two 20 nm thick buffer layers that contain approximately 2-3% In (according to the Vegards law with bowing parameter 2 eV). The individual spectra of the buffers and the six QWs are shown in Fig. 5.17 (c). We assigned the to each QW the respective growth temperature by considering its distance from the buffer layer and taking into account the barrier width of 10 nm. As can be seen the center of gravity of the spectra shifts continuously towards the red range, when moving from the bottom of the stack to the top, i.e. from MLs grown at high to those grown at low temperature. More precisely, the first ML grown at 650-640º C emits at ∼3.26 eV (380 nm) and the last ML deposited at 580 ºC at 3.06 eV (405 nm). Similar to the spectra shown before, they consist of series of narrow lines with a FWHM ranging from 1.5 meV up to 20 meV for the peaks forming the last QW's spectrum. The total shift of the centers of gravity between the spectra of the first and last QWs is 144 meV. In Fig. 5.17 (e) we present the magnified area of the spectrum of the ML grown at ∼640º C where a pair of distinct sharp lines separated by 4.5 meV can be resolved. Lorenz fitting returns the FWHM of the peaks P1 and P2 as 3.5 and 4 meV, respectively. These narrow lines are duplicated on the same spectrum each ∼25 meV (indicated by arrows). This characteristic pair of excitonic-type lines are also repeated on the spectra of the buffer layers and other MLs grown till 610º C.

Summarizing our STEM-CL results, we show that the broad PL lines found in conventional PL and CL spectra decompose into a set of narrow lines with FWHM in the meV range in STEM-CL measurements. These narrow lines resemble those of QDs found in classical semiconductors [250,251]. Our TEM studies show that the monolayer quantum wells in some cases do not consist of coherent layers but of patches or discs with identical composition but lateral extensions ranging from ∼ 3 to 25 nm. Since we find no thickness and compositional fluctuations within a ML grown under specific conditions but patches with different lateral extension, we may speculate that the individual sharp lines are due to emission of quantum discs with different lateral extension. In the following section we will present theoretical calculations by O. Marquardt from Weierstraß-Institut für Angewandte Analysis und Stochastik, Berlin for such objects based on continuum k*p calculations

5.4.3. Continuum k*p calculations

The k*p calculations 2.6.2 were performed for supercell structures that consist of a one ML thick (In,Ga)N discs with various base lengths embedded into a GaN matrix. In concentrations of 5%, 10%, 20% and 30% were considered. The material parameters were taken from Ref. [252]. VBM and CBM were calculated depending on the lateral size of the (In,Ga)N square form layers. Three types of transitions were computed: (i) basic band to band transition, (ii) transitions from the bands deformed by polarization fields and (iii) excitonic recombination in the energetic structure influenced by piezoelectric polarization. In the latter case the binding energy between electrons and holes by Coulomb interaction is taken into account.

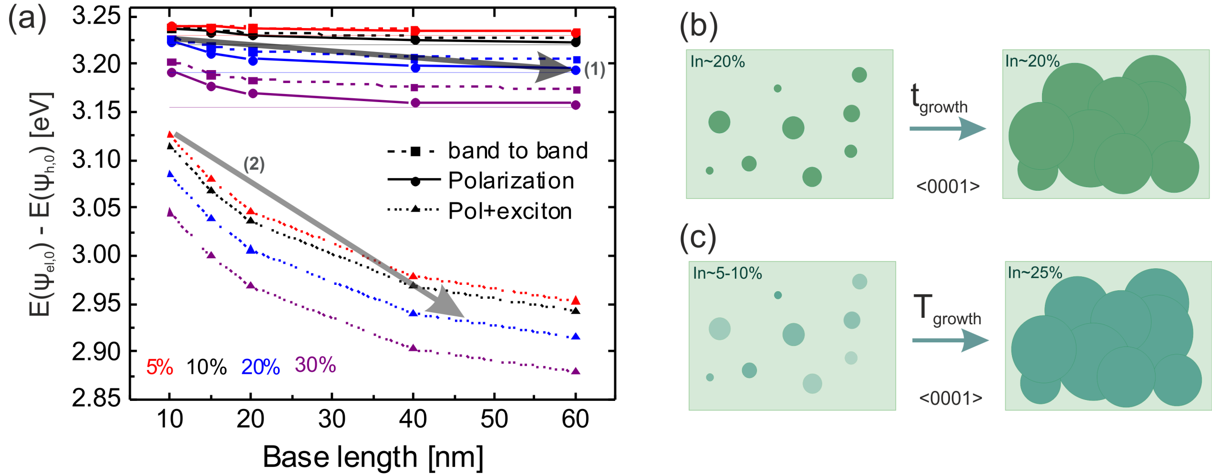

Fig. 5.18: Energetic distance between electron and hole ground states as a function of the lateral size of the $In_xGa_{1-x}N$ ML containing 5% (red), 10% (black), 20% (blue) or 30% (violet). Different cases are noted: (i) simple band to band transitions (dashed lines); (ii) transitions between the bands deformed by polarization fields (solid lines) and (iii) excitonic recombination between the bands modified by the piezoelectric fields (short dash lines). Thin dash lines indicate the asymptotes of the closed MLs energies for the cases (i),(ii). Upper and lower gray semi-transparent arrows represent the emission shifts associated with the growth time (1) and temperature gradient (2) structures, correspondingly. Top-view representative schemes of the ML coverage when the (b) growth time is increased and (c) growth temperature is lowered.

The results of these simulations are presented in Fig. 5.18 (a). In the cases (i) and (ii) MLs with low In contents, i.e. 5% (red) and 10% (black) show only a negligible change in the recombination energies, with lateral extension of the structure. Transitions in discs with higher In contents (20% and 30%) shift to higher energies once the ML is laterally confined to a base length of less than 20 nm. Reducing of the base length of the In containing region from 60 nm towards the small islands, minimum 10 nm, leads to the blueshifts of ∼34 meV and 44 meV for the 20% and 30% In concentrations (see case (ii), blue and purple solid lines), respectively. Polarization fields as still deforming the energy bands of the $In_xGa_{1-x}N$/GaN structures for a given indium content [36], however, induce a rather moderate additional shift of the band gap of ∼10 meV (20%) and ∼16 meV (30%). This is in a good agreement with our experimental data on the negligible impact of the piezoelectric fields on the recombination properties. Formation of excitons considerably decreases the overall ground state energy by 113 meV (5 %), 124 meV (10 %), 139 meV (20%) and 148 meV (30 %). It further redshifts the recombination energy by ∼170 meV for each concentration when the ML tends to close up.

5.4.4. Discussion of the lateral confinement

Reviewing our experimental and computational results, we have shown that ML-thick QWs are spectrally not uniform, i.e. the broad emission observed in the conventional PL experiments are a superposition of sharp peaks originating from In-containing patches with different lateral extension and composition. Our structural investigations also revealed pronounced areas with different In contents of the finite size, starting from 3 nm length. By means of the STEM-CL

technique with the spatial resolution ~ 6 nm we were enable to resolve the emission lines from these patches. Previous less complicated experiments, e.g. the standard CL and μ-PL studies, performed on the conventional (In,Ga)N QWs also allowed to observe sharp peaks emitting from the areas less than 60 nm lateral size [253] and narrow emission up to 0.8 meV [254] and 0.17 meV [255] width of the localization centers, respectively. But the employed techniques do not able to link the emission directly to the structure of the layers.

Experimental data of the time and temperature gradient structures follow the same trends in the change of the band gap as were obtained from the k*p calculations, i.e. the extension of the confined areas leads to the redshift of the spectra. Starting with the time gradient SL, MLs from the growth time experiment emitted at ~3.26 eV and shifted by ~40 meV with the increase of the deposition time. From structural investigations we have obtained similar In composition around 20% in the whole structure. Here, very narrow emission lines are related to the low ensemble density of the In-containing patches within the probe volume. But the Indium incorporation in these patches almost does not change but rather the lateral extension of these areas, like presented in the schematic model in Fig. 5.18 (b). K*p calculations involving the polarization fields revealed a shift by 33 meV for the $In_{0.2}Ga_{0.8}N$ patches extending from 10 to 60 nm (see semi-transparent thick line (1) in Fig. 5.18 (a)). The observed sharp lines were ~500 µeV - 1 meV width, that are usually examined in the fine structures, like QDs, or QD-like In-rich islands [250, 251, 256, 257]. Lateral size of such structures can vary in the range of several tenths nm and up to a few nm height. Notably, we observe very narrow emission peaks in the less sophisticated and straightforward system, i.e. 0.25 nm thick QW with lateral size approx 3-10 nm grown at limited time ~4s. Then, increasing coverage of the monolayers with time leads to the by laterally confined discs increases and the layers with broadening of the ML's spectra and the QWs deposited at 60 sec or 28 sec FWHM (~ 85 meV) is already comparable to that observed in the 3 nm-thick QWs of similar composition, i.e. ~70 - 100 meV, [20, 258].

The second superlattice structure grown under different temperatures revealed a large redshift across the structure by 144 meV across the SL, the absolute values of the emissions were in the range ~ 3.1-3.2 eV. Understanding of the origins of this remarkable shift is impeded via the interplay of the two parameters that change with temperature - indium content (~12%) and coverage, as can be obtained from the continuous broadening of the spectra (see Fig. 5.17 (c)). Moreover, under the employed experimental STEM-CL conditions we were able to examine the excitonic transitions. Our excitonic-like repeated peaks were ~3.5 meV width (see Fig. 5.17 (d)) which is comparable to the FWHM of the ones typically observed in GaN, i.e. 1-7 meV wide depending on the type of the electron-hole pair and precision of the experiment [114–116]. Comparing these results to the calculations, we find a decent agreement with the computations involving the electron-hole pair formation and increase of the In concentration throughout the structure accompanied with the extension of the In-containing patches (see the representation of this idea in Fig. 5.18(b)). The total shift obtained from calculation was 200 meV, although, the final size of the patch may be still less than 60 nm and the areas may co-interact with each other (see lower semi-transparent thick line (2) in Fig. 5.18(a)). Indeed, for this sample in the last MLs three emission peaks were still resolvable on the spectrum, therefore, perfect coverage was not achieved yet at 580ºC. Another peculiarity of these low-temperature grown MLs was an unexpected lowering of the In content, however, the spectra continuously shifted towards lower energies. This may originate from the unintentional increase of the In content in the upper barriers (more than 2%) that changes the strain between QW and barrier. Although the absolute values of the emissions of the two discussed structures are differing by almost 150 meV, the

main reason for the generally redshifted temperature gradient structure is the influence of the reduced strain between the barriers and QWs due to the presence of the indium in the barriers.

The observed QD-like patches cause a strong localization of charge carriers. Moreover, we have shown that even in the MLs with a high coverage the residual sharp peaks can be resolved (see, for instance, the intermediate QWs in the growth time gradient). These results explain the observed formation of the localized states in the previous section where the discussed MLs were deposited even during shorter time, 8 s. Holes that have large effective masses are strongly confined in the states that may be induced by even small indium fluctuations. This phenomenon was observed via a redistribution of carriers where the quasi-free electrons grab holes and move downwards the energy tail of states inducing a characteristic shape of spectral dependence, i.e. longer decay times of the high energy shoulder of the emission.

6. Summary and conclusions

In this thesis we studied ultra-thin (In,Ga)N QWs coherently grown on GaN in the form of a superlattice structure. Structural and optical properties have been addressed by means of various investigation methods: HRTEM, STEM, RHEED, XRD, as well as PL, TRPL, CL and STEM-CL.

These structures can be interesting for practical application as emitters for the whole visible and near-infrared range of spectrum. The band gap of superlattices can be tuned by changing the barrier width and by change of the indium composition of the thin wells. They have the advantage that a number of effects that influence the optical efficiency of several nm thick standard (0001) (In,Ga)N quantum wells negatively, such as piezoelectric fields, well-width or gross composition fluctuations can be avoided. Thus, these quantum structures are perfect for studying the fundamental properties of (In,Ga)N alloys. However, up to now, the promised flexible band gap tuning along the wide range of emission energies has not been fulfilled and there are a number of conflicting results in literature as regards the relation between emission and In composition. Therefore, we focus on three main aspects: (i) compositional quantification with highest possible accuracy; (ii) fundamental limits of In incorporation into polar (In,Ga)N structures and (iii) the basic understanding of localization phenomena in (In,Ga)N alloys. The first issue we have addressed by employing aberration corrected HRTEM. We revealed that among the other techniques available for concentration measurements of fine structures, e.g. XRD and STEM, only HRTEM allows the reliable compositional analysis with the pm precision.

Compositional and thickness limitation in (In,Ga)N ML-thick QW

We showed that deposition of pure InN MLs on a GaN barrier results in an indium composition of around 25% in the monolayer. To increase the In content beyond this limit we performed a systematic series of growth experiments in MBE by changing the III-V growth ratio from In-poor to In-rich regime, varying the growth temperature over a wide range and by increasing the deposition time of the alloys. As an outcome we observed a self-limitation process for both content and thickness of the QW independent on growth conditions that is concomitant with the formation of ordered alloy. These result supported by data on surface reconstructions obtained from RHEED measurements and DFT calculations allowed us to develop a model of In incorporation that explains all these findings. By examining the growth surfaces of GaN barriers and (In,Ga)N alloys we found under N-rich regime an omnipresent 2×2 N adatom surface structure that was previously described by Northrup et al. [215]. The N adatom binds three Ga atoms, which are the 4 fold coordinated on nominally metal polar surface. The (In,Ga)N quantum well forms by exchange of In present a the surface with the Ga at the surface. We showed that unexpectedly Ga atoms, which have the higher bond energy, prefer energetically the 3-coordinated sites while In favors the 4-fold coordinated (sub)surfaces sites. This can be explained by the energy gain of the Ga atom on the surface due to re-hybridization which is prevented for In due to its large size. Due to the nearest-neighbor repulsion between In atoms, it is energetically costly

to occupy the neighboring four-fold coordinated sites. This yields an upper limit of 25% of indium composition given by the number of N adatoms on the surface. To overcome this limit highly In-rich growth conditions are required, , which would lead to metal droplet formation and a degradation of the layer. Since further In incorporation is not possible the mechanism is at the same time self-limited, i.e. growth stops at a single monolayer.

Such apparent fundamental limitations suggest that other solutions are needed for the band gap modulation by means of increasing the In content. For instance, growth of the (In,Ga)N MLs on top of the lattice-matched (In,Ga)N buffers reduces the strain state. This idea has been developed in the theoretical work of Duff et al. [217], and some of experimental works [259–261]. However, by far it is still under debate, whether In content can be substantially increased over the found 25%-limit and requires further investigations.

Optical properties of the (In,Ga)N ML-thick QW. Carrier confinement

Our findings on indium incorporation correlate well with the data on optical emission of the MLs predicted by theory for such concentrations and that were found at ∼3.1-3.2 eV. Note that the same emission range was examined in literature but, as we can state now, falsely attributed to pure InN MLs.

By changing the barrier thickness in the superlattice we can shift the luminescence by 100 meV when reducing the GaN barrier thickness from 50 MLs to 6 MLs. Considering superlattices as a model system to study common optical phenomena in polar (In,Ga)N QWs,such as a non-exponential decay, the spectral dependence of the decay time and the S-shape in the temperature dependence of the PL peak emission. Very similar phenomena were found in our single ML QWs with thick barriers despite the reduced complexity of the system. Our results evidence that these recombination phenomena are governed by a strong hole localization in the (In,Ga)N monolayer that can be manipulated by changing the SL periodicity, and non-radiative recombination. Decrease of the barrier thickness below 12 MLs results in the interaction of the hole wavefunctions and, in consequence, in the hole delocalization in $<0001>$ direction. This triggers in turn non-radiative recombination in the GaN barriers. The higher rate of non-radiative recombination measured for the SL with thin barrier reduces the spectral dependence of the decay time, accelerates the intensity decay and affects the S-shape temperature dependence analogously as examined for non-polar QWs. At the same time, the out-of-plane electron confinement does not change and remains low for all calculated barriers. We propose a phonon-assisted transfer process of excitons formed by holes with large effective mass and quasi-free electrons to be responsible for the observed optical phenomena in SLs with thick barrier and, as well as, in standard (In,Ga)N QWs. The enhancement of non-radiative recombination hastens this exciton redistribution and results in the single exponential decay and negligible spectral dependence found for 6 MLs SL and non-polar QWs.

Lateral confinement is arising from the In content fluctuations common for (In,Ga)N compounds. However, as low as these fluctuations might be they still affect the ML emission due to the strong localization of holes. As a result, the FWHMs of the ML-thick (In,Ga)N luminescence peaks are comparable to the ones measured for regular 2-3 nm thick QWs. By combined HRTEM and STEM CL measurements we revealed that the optical properties are affected by the presence of two dimensional ordered (In,Ga)N patches within the monolayer. Experimental findings supported by k*p calculations showed that the density, size and composition of these

patches changes with growth time and growth temperature. We have presented that adjusting the growth conditions, MLs with very narrow luminescence peaks with the varied emission energy in a limited range can be deposited. This outcome can be useful for the fabrication of the (In,Ga)N-based quantum discs that exhibit sharp emission peaks with FWHM in the sub-meV range.

A. Image simulations for different specimen thicknesses of the ordered $In_{0.25}Ga_{0.75}N$ MLs

In the following we will show contrast simulations on ordered (In,Ga)N monolayers. We will show that the contrast by which ordering is detected in HRTEM images is strongly influenced by the used imaging conditions, i.e. thickness and defocus. The reason is the difference in extinction lengths of In and Ga atoms. Multislice simulations were similar to the ones presented in 3.2 but for (In,Ga)N ML with 25% of indium. Fig. A.1 and Fig. A.2 show the simulation results in two principle projections for the specimen thicknesses 3, 5, 7 and 10 nm with identical imaging conditions as for in the experiment, i.e. negative spherical aberration -13 μm and positive defocus 5.8 nm. We have put 10% of In atoms as randomly distributed within the ML, while 90% were arranged in a (2√3×2√3)R30○ ordering described earlier.

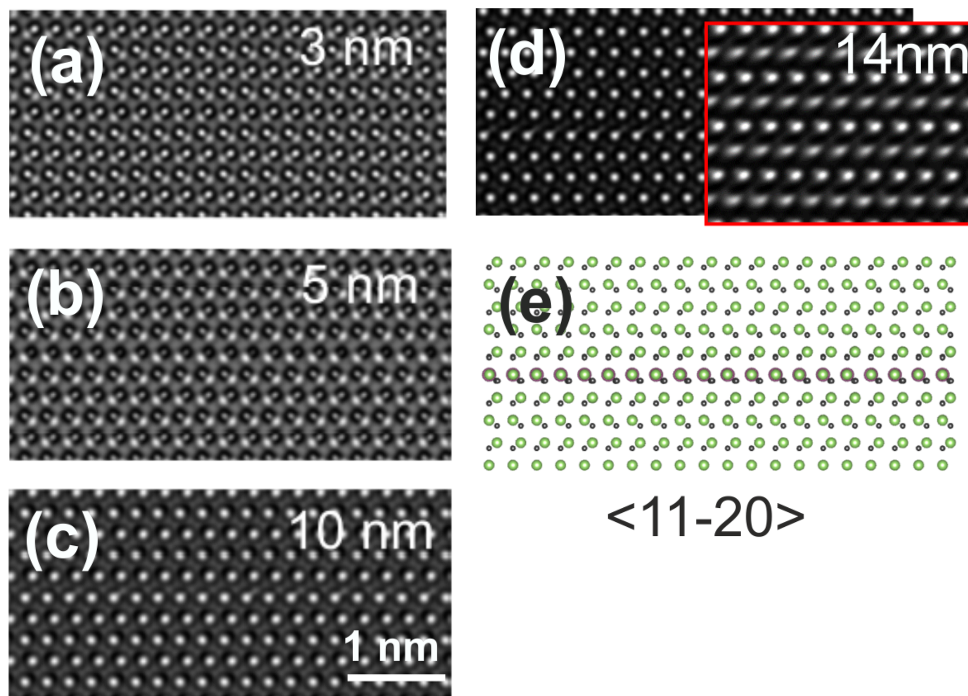

Fig. A.1: HRTEM images of the <11-20> projection direction obtained from the multislice image simulation for different thicknesses: (a) 3 nm; (b) 5 nm; (c) 10 nm and (d) 14 nm - shown together with the experimental image (enclosed in the red square) discussed above in 4.3.1. The supercell used for the simulation is presented in (e) in the same projection. Note, that here In atoms were also enlarged to accentuate the columns from the back rows. Green atoms denote Ga, violet - In and small gray - N.

In <11-20> projection the (In,Ga)N layer is hardly seen, as they can be barred by the Ga

atomic columns (Fig. A.2(e)), and no specific arrangements can be observed, we will focus on the differences arising in <1-100>.

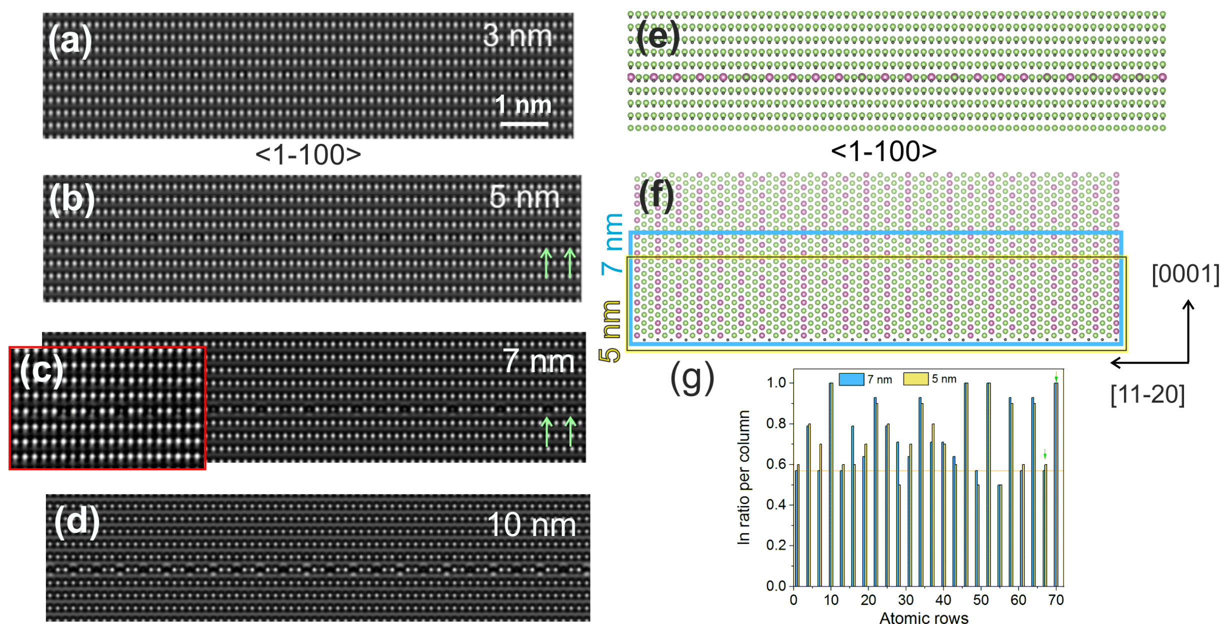

Fig. A.2: HRTEM images of the <1-100> projection direction obtained from the multislice image simulation for different thicknesses: (a) 3 nm; (b) 5 nm; (c) 7 nm - shown together with the experimental image (enclosed in the red square) discussed above in 4.3.1; (d) 10 nm. The supercell used for the simulation is presented in (e) in the same projection. Note, that In atoms were enlarged to accentuate the columns from the back rows. Green atoms denote Ga, violet - In and small gray - N. (f) The supercell with the cut out of the $In_{0.25}Ga_{0.75}N$ monolayer where light blue and yellow square encloses the 7 nm and 3 nm thickness specimen. (g) Histogram of the In ratio per column derived for each atomic row. The color code corresponds to the thickness shown in (f). The rows with pure Ga atomic columns are set to zero.

No intensity difference between the atomic columns can be observed for the very thin specimens, i.e. for 3 nm (A.2 (a)). In the thicker area, at 5 nm, one can distinguish five bright gallium-rich columns to one darker indium-rich column contrast periodicity (Fig. A.2 (b)). The best agreement for the experimental data can be found for a thickness of 7 nm simulation shown in Fig. A.2 (c). A clear intensity variation corresponding to the 1×3 ordering where two atomic columns with mostly gallium and one - with high indium concentration is obtained. For samples as thick as 10 nm Fig. A.2 (d) the indium-rich columns appear at reduced intensity, what correlates well with the first extinction distance of In atoms (approximately 10 nm).

Such sensitivity to the thickness and necessity of the high quality specimens may explain the lack of the TEM data on ordering and surface reconstruction in literature. Moreover, we showed experimentally that ordered patches are not continuous within the layer but may have a limited size. Random distribution of the ordered arrangements in the basal plane complicates their viewing in <1-100> by means of HRTEM. The effect of partial randomness on different thicknesses of the specimen was checked by a statistical calculations of the In atoms for each In-containing row, that for our particular cell was one of a third (see Fig. A.2 (f)). In Fig. A.2 (g) the ratios of In for the given row is shown for two thicknesses of 3 nm and 7 nm. In general, these ratios do not change considerably for the sample thickness. However, according to the simulated images, for 7 nm one can clearly distinguish In atomic ordering, even though in some

of the rows there is less than 60% of indium (marked by red line). For the thinner sample the ML is barely visible, thus the amount of In per row is not enough to view the In-containing columns. Our calculations clarify why ordering was not observed in every (In,Ga)N ML with indium concentrations close to 25%.

B. XRD measurements

In Fig. B.1 we show two XRD scans around (0002) and (0006) reflections of the standard SL structure deposited under the conditions corresponding to nominally 4 MLs thick InN QWs with 10 nm thick GaN barriers. The experimental scans are presented with the most satisfactory simulation curves. Here, for the (0002) GaN reflection no QW satellite peak was registered that was more pronounced and displaced from the GaN's one for scanning under higher angles (see Fig (b)). Satellite peaks up to the 9th order are visible indicating good structural quality of the SL.

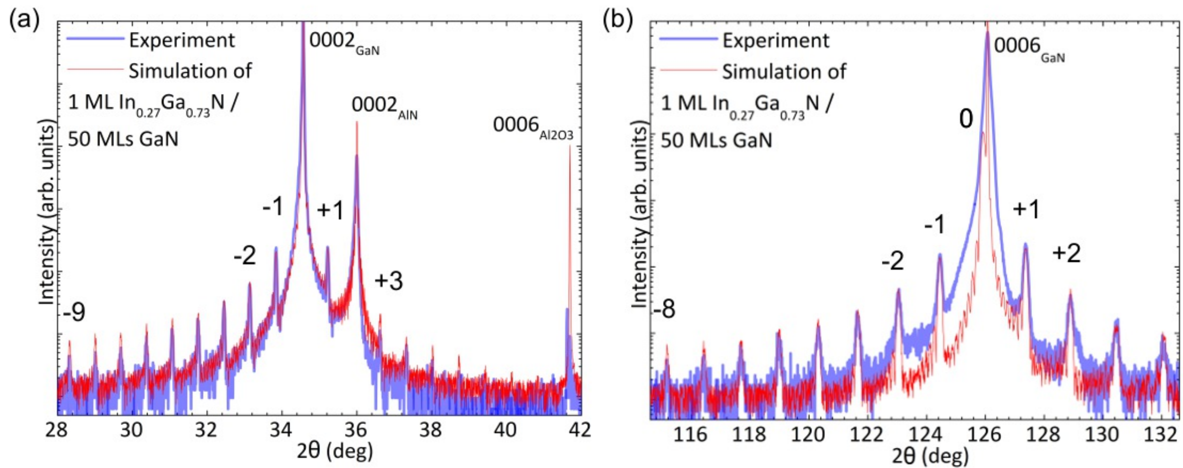

Fig. B.1: The 2ϑ experimental (semi-transparent blue) and simulated (red) scans around the (a) (0002) and (b) (0006) GaN reflections. Satellite peaks originating from the AlN and Al2O3 of the substrate are also observed.

Simulation curves of the SLs with 1 ML thick (In,Ga)N QWs of 27% indium concentration show a good agreement with the experimental data. Note, that for the ML-thick (0006) InN reflection of the QW should be highly pronounced and separated from the one of GaN (see XRD simulations for the InN/GaN superlattices from [210]).

C. Estimation of the amount of non-equilibrium charge carriers

Here we present a procedure of the calculation of the excitation powers used for the experiment. These values were chosen as depending on the involvement of the barriers into the creation of non-equilibrium carriers. Different absorption rates and the intensity gain in the structures were considered to hypothesize the following two scenarios: (i) all the carriers created in the barriers are transferred to the QWs and contribute to the emission; or (ii) all charge carriers from the barriers recombine non-radiatively.

The excitation energy can be converted to the power density via the measured spot diameter of the laser excitation (100 µm) and an excitation power of laser, for instance 1 mW according to:

$$\rho = \frac{P}{\pi d^2} = 3.2W/cm^2 \tag{C.1}$$

The duration of the pulse was only 100 fs, the measuring precision was estimated as 10 ps, therefore we consider that all carriers are immediately created.

The repetition rate of the laser pulse was 80 MHz, therefore pulse energy is:

$$i = \rho t_{pulse} = 38nJ/cm^{-2} \tag{C.2}$$

where t_{pulse} is the duration of the pulse.

The number of photons created at an excitation with an laser wavelength of 259 nm can be calculated as:

$$N_{ph} = i/(\frac{ph.energy}{\lambda}) = 4.95 \cdot 10^{10} photons \cdot cm^{-2} propulse \tag{C.3}$$

The total barrier thickness including the last cap layer is calculated as:

$$H_{tot} = 11 \frac{c_{GaN}(0.518nm)}{2} \cdot X_{MLs} \tag{C.4}$$

In the same manner the total thickness of all QWs results in 2.6 nm, where c_{QW}=0.526 as taken for approx 25% of In in the ML. Thickness of the stack is a summation of the total QW and barriers thicknesses.

The absorption rate is estimated through the Beer-Lambert law Eq. 5.1. The absorption coefficient for the $In_{0.25}Ga_{0.75}N$ ML is taken equal to that of GaN not only due to the simplicity of the estimation but because of the lack of the studies of the absorption edge for $In_xGa_{1-x}N$ either with compositions, x, close to our experimental values [262] or for the used excitation experimental range (4.79 eV). Moreover, no data on the absorption coefficients valid for sub-nm-sized quantum structures can be found in literature. The absorption coefficient of GaN for

the 4.79 eV was determined via the dielectric constants measured at low temperatures close to our experimental values [263]:

$$\alpha(E) = \frac{4\pi}{\lambda}\left(\frac{\sqrt[2]{[\varepsilon_1(E)^2+\varepsilon_2(E)^2]}-\varepsilon_1(E)}{2}\right)^{1/2} = 2.1\cdot 10^5 cm^{-1} \tag{C.5}$$

where ε_1(4.79eV)=6.1 and ε_2(4.79eV)=2.2 are the real and imaginary parts of the dielectric function.

The total absorption rate was estimated by gradual calculation of the intensity exposed to each QW that is suppressed passing through each barrier. Results for both - (i) active and (ii) noncontributing barriers (excluded absorption of the barriers) are presented in Table C. The carrier population can be calculated by normalization of the number of incident photons to the absorption rates in these two cases. Note, that for the simplification, we suppose a 100% quantum efficiency, i.e. one incident photon creates one electron-hole pair. The final amount of the carriers, N_{carr}, was corrected by the reflectance of the GaN taken as 18% [248].

SL	H_{tot} [nm]	Total absorption, "active" barriers [a.u.]	N_{carr}, "active" barriers [cm^{-2}]	QW absorption, "defective" barriers [a.u.]	N_{carr}, "defective" barriers [cm^{-2}]	P_{exp}, mW
50 MLs	142.6	0.94	$3.8\cdot10^{10}$	0.016	$6.5\cdot10^{8}$	3.2
25 MLs	72.6	0.77	$3.1\cdot10^{10}$	0.028	$1.1\cdot10^{9}$	3.9
12 MLs	36.6	0.50	$2.1\cdot10^{10}$	0.038	$1.6\cdot10^{9}$	6.0
6 MLs	19.6	0.29	$1.2\cdot10^{10}$	0.045	$1.8\cdot10^{9}$	10.3

Table C.1.: Results the calculation of the non-equilibrium carrier populations for the two extreme conditions. P_{exp} represent the experimental values used for the excitation of the SLs.

As can be seen from Table C, the number of electron-hole pairs created in the thickest and the thinnest structures under laser excitation differs by 3 times in both of the cases. Likewise, 6 MLs "active" barriers create approximately 3 times less carriers than 50 MLs. Contrary, the "defective" GaN leads to 3 times larger carrier concentration of the thinnest barrier SL compared to 50 MLs due to the continuous loss of the carriers through the thick material. Therefore, two excitation powers differing by one order of magnitude should be enough to cover the both cases opposite (i) and (ii). To obtain similar excitation conditions in each SL stack we have adjusted the experimental excitation powers by the total absorption rate, i.e. $\alpha P_{exp} \sim$ 3mW (see the last column in Table C).

Bibliography

[1] S. Nakamura and G. Fasol. *The Blue Laser Diode. GaN Based Light Emitters and Lasers*. Springer-Verlag Berlin Heidelberg GmbH, 1997. 1

[2] J. Y. Tsao, M. H. Crawford, M. E. Coltrin, A.J. Fischer, D. Koleske, G.S. Subramania, G.T. Wang, J.J. Wierer, and R. F. Karlicek. *Adv Opt Mater*, pages 1–28, 2014. 1

[3] M. R. Krames, O. B. Shchekin, R. Mueller-mach, G. O. Mueller, L. Zhou, G. Harbers, and M.G. Craford. *Journal of Display Technology*, 3(2):160–175, 2007. 1

[4] https://www.nobelprize.org/prizes/physics/2014/press release/. 1

[5] S. D. Lester, F. A. Ponce, M. G. Craford, and D. A. Steigerwald. *Appl. Phys. Lett.*, 66(10):1249–1251, 1995. 1

[6] S C Jain, J. Willander, V. Narayan, and R. Van Overstraeten. *J Appl Phys*, 87(965), 2000. 1, 7, 29, 30, 35, 78, 105

[7] Y. Narukawa, M. Ichikawa, D. Sanga, and M. Sano. *J. Phys. D. Appl. Phys.*, 43(354002), 2010. 1

[8] R. Fischer, D. Neuman, H. Zabel, and H. Morkog. *Appl Phys Lett*, 48(18):1223–1225, 1986. 1

[9] D. P. Bour, D. W. Treat, R. L. Thornton, R. S. Geels, and D. Welch. *IEEE J Quantum Electron.*, 29(5):1337–1343, 1993. 1

[10] M. R. Krames, M. Ochiai-Holcomb, G. E. Hoefler, and et al. *Appl Phys Lett*, 75(2365), 1999. 1

[11] K. Streubel, N. Linder, R. Wirth, and A. Jaeger. *IEEE J Sel Top Quant*, 8(2):321–332, 2002. 1

[12] V. Yu. Davydov, A. A. Klochikhin, S. V. Ivanov V. V. Emtsev, V. V. Vekshin, F. Bechstedt, and J. Furthmueller et al. *Phys. Stat. Sol. (b)*, 230(2):R4–R6, 2002. 1

[13] J. Wu. *J Appl Phys*, 106(011101):1–12, 2009. 1, 29, 30

[14] M. Auf der Maur, A. Pecchia, G. Penazzi, W. Rodrigues, and A. Di Carlo. *Phys. Rev. Lett.*, 116(027401):1–5, 2016. 1, 40

[15] E. L . Piner, F. G. McIntosh, J. C. Roberts, M. E. Aumer, V. A. Joshkin, S. M. Bedair, and N. A. El-Masry. *MRS Internet J. Nitride Semicond. Res.*, 1(43), 1996. 1

[16] H.-C. Lin, C.-K. Shu, J. Ou, Y.-C. Pan, W. Chen, W.-H. Chen, and M.-C. Lee. *J. Cryst. Growth*, 180/190:57–60, 1998. 1

[17] S. Nakamura, S. Masayuki, I. Naruhito, and N. Shin-ichi. *Jpn. J. Appl. Phys.*, 34(7A):L797, 1995. 1, 36, 80

[18] M. Kim, M. Schubert, Q. Dai, J. K. Kim, E. F. Schubert, J. Piprek, and Y. Park. *Appl Phys Lett*, 91(183507), 2007. 1

[19] C. J. Humphreys, J. T. Griffiths, F. Tang, F. Oehler, S. D. Findlay, C. Zheng, J. Etheridge, and T. L. Martin et al. *Ultramicroscopy*, 176:93–98, 2017. 1, 40

[20] D. Watson-Parris, M. J. Godfrey, P. Dawson, R. A. Oliver, M. J. Galtrey, M. J. Kappers, and C. J. Humphreys. *Phys. Rev. B - Condens. Matter Mater. Phys.*, 83(115321):1–7, 2011. 1, 41, 100, 108, 115

[21] D. Holec, Y. Zhang, D. V. Sridhara Rao, M. J. Kappers, C. McAleese, and C. J. Humphreys. *J Appl Phys*, 104(123514), 2008. 1, 38

[22] S. Yu. Karpov. *MRS Internet J. Nitride Semicond. Res.*, 3(16), 1998. 1, 37, 38

[23] D. Doppalapudi, S. N. Basu, K. F. Ludwig, and T. D. Moustakas. *J. Appl. Phys.*, 84(3):1389–1395, 1998. 1, 37

[24] F. Wang, Z. Ji, Q. Wang, X. Wang, S. Qu, X. Xu, Y. Lv, and Z. Feng. *J Appl Phys*, 114(163525), 2013. 1

[25] B. N. Pantha, J. Li, J.Y. Lin, and H. X. Jiang. *Appl Phys Lett*, 96(232105), 2010. 1

[26] O. Brandt, L. Tapfer, r. Cingolani, K. Ploog, M. Hohenstein, and F. Phillipp. *Phys. Rev. B*, 41(18):12599–12606, 1990. 1

[27] M. V. Belousov, N. N. Ledentsov, M. V. Maximov, and P. D. Wang et al. *Phys Rev B*, 51(20), 1995. 1

[28] P. D. Wang, N. N. Ledentsov, C. M. Sotomayor, P. S. Kopev, and V. M. Ustinov. *Appl Phys Lett*, 64(1526), 1995. 1, 2

[29] N. Grandjean, B. Damilano, and J. Massies. *J. Phys. Condens. Matter*, 13:6945–6960, 2001. 2, 26

[30] C. Skierbiszewski, H. Turski, G. Muziol, M. Siekacz, and M. Sawicka. *J. Phys. D: Appl. Phys.*, 47(073001), 2014. 2, 37

[31] M. Siekacz, M. Sawicka, H. Turski, G. CywiÅski, A. Khachapuridze, and P. Perlin et al. *J. Appl. Phys.*, 110(063110), 2011. 2, 80, 82

[32] M. J. Davies, S. Hammersley, F. C.P. P Massabuau, P. Dawson, R. A. Oliver, M. J. Kappers, and C. J. Humphreys. *J. Appl. Phys.*, 119(055708), 2016. 2, 102

[33] A Yoshikawa, S B Che, W Yamaguchi, H Saito, X Q Wang, Y Ishitani, and E S Hwang. *Appl. Phys. Lett.*, 90(073101), 2007. 2, 38, 80

[34] A. Yoshikawa, S. Che, Y. Ishitani, and X. Wang. *J. Cryst. Growth*, 311:2073–2079, 2009. 2

[35] A. Yoshikawa, K. Kusakabe, N. Hashimoto, E.-S. Hwang, D. Imai, and T. Itoi. *J. Appl. Phys.*, 120(225303), 2016. 2, 56

[36] I. Gorczyca, T. Suski, P. Strak, G. Staszczak, and N. E. Christensen. *Sci. Rep.*, 7(16055), 2017. 2, 39, 40, 100, 104, 114

[37] I. Gorczyca, T. Suski, N. E. Christensen, and A. Svane. *Cryst. Growth Des.*, 12:3521–3525, 2012. 2, 100

[38] W. Sun, C.-K. Tan, and N. Tansu. *Sci. Rep.*, 7(6671):1–8, 2017. 2

[39] M. S. Miao, Q. M. Yan, and C. G. Van De Walle. *Appl. Phys. Lett.*, 102(102103), 2013. 2, 3

[40] K. Kusakabe, D. Imai, K. Wang, and A. Yoshikawa. *Phys. Status Solidi C*, 13(5-6):205–208, 2016. 2, 54

[41] L. Zhou, E. Dimakis, R. Hathwar, T. Aoki, D. J. Smith, T. D. Moustakas, S. M. Goodnick, and M. R. McCartney. *Phys. Rev. B - Condens. Matter Mater. Phys.*, 125310(88):1–5, 2013. 2, 39, 40, 100

[42] E. Dimakis, A. Yu Nikiforov, C. Thomidis, L. Zhou, D. J. Smith, J. Abell, C. K. Kao, and T. D. Moustakas. *Phys. Stat. Sol. (a)*, 205(5):1070–1073, 2008. 2, 3

[43] C. Li, Y. Maidaniuk, A. V. Kuchuk, S. Shetty, P. Ghosh, T. P. White, and et al. *J. Appl. Phys.*, 123(195302), 2018. 2, 81

[44] E.S. Hwang, S.B. Che, H. Saito, X. Wang, Y. Ishitani, and A. Yoshikawa. *J. Electron. Mater.*, 37(5):597–602, 2008. 2, 3

[45] W. Pan, E. Dimakis, G. T. Wang, T. D. Moustakas, and D. C. Tsui. *Appl. Phys. Lett.*, 21(213503), 2014. 2, 3

[46] G. Staszczak, I. Gorczyca, T. Suski, X. Q. Wang, N. E. Christensen, A. Svane, E. Dimakis, and T. D. Moustakas. *J. Appl. Phys.*, 113(123101):1–6, 2013. 2, 3

[47] Lin W., Li W., and Kang J. *Appl. Phys. Lett.*, 96(101115):1–4, 2010. 2

[48] T Suski, T Schulz, M Albrecht, X Q Wang, I Gorczyca, K Skrobas, N E Christensen, A Svane, T Suski, T Schulz, M Albrecht, X Q Wang, I Gorczyca, and K Skrobas. *Appl. Phys. Lett.*, 104(182103), 2014. 2, 3, 80, 100

[49] A. Yoshikawa, S. B. Che, N. Hashimoto, H. Saito, Y. Ishitani, and X. Q. Wang. *J Vac Sci Technol B*, 26(1551), 2008. 3

[50] Q. Yan, P. Rinke, M. Scheffler, and C. G. Van de Walle. *Appl. Phys. Lett.*, 95(121111), 2009. 6, 29, 42

[51] B. Gil. *Physics of Wurtzite Nitrides and Oxides*, volume 197. Springer Series in Materials Science, 2014. 7, 38, 39, 48, 105

[52] Von L. Vegard. Die konstitution der mischkristalle und die raumffillung der atome. 17, 1921. 7

[53] M. E. Vickers, M. J. Kappers, T. M. Smeeton, E. J. Thrush, J. S. Barnard, and C. J. Humphreys. *J. Appl. Phys.*, 94(1565), 2003. 7, 54, 80

[54] M. Schuster, P. O. Gervais, B. Jobst, W. Hoesler, R. Averbeck, H. Riechert, A. Iberl, and R. Stoemmer. *J. Phys. D: Appl. Phys.*, 92(01633), 1999. 7

[55] Y Austin Chang and W Alan Oates. *Materials Thermodynamics*. A John Wiley & Sons, Inc., publication, 2010. 8

[56] T. Nishinaga, T. Shitara, and K. Mochizuki. *Journal of Crystal Growth North-Holland*, 99:482–490, 1990. 9

[57] Mohamed Henini. Molecular Beam Epitaxy From research to mass production. *Elsevier Sci.*, 2013. 9, 36

[58] P. Frigeri, L. Seravalli, G. Trevisi, and S. Franchi. *Molecular Beam Epitaxy: An Overview*. ISBN 978-0-444-53153-7, 2011. 9, 10

[59] M. A. Herman and H. Sitter. *Molecular Beam Epitaxy, Fundamentals and Current Status*, volume 7. Springer Series in Materials Science, SpringerâVerlag, Berlin, 1989. 9, 10

[60] Von E. Bauer. Phaenomenologische scheidung. *Der Zeitschrift fuer Kristallographie*, 110:372â394, 1958. 9, 10

[61] I. N. Sranski und L. Krastanow. Zur theorie der orientierten ausscheidung von ionenkristailen aufeinander. 19:351–364, 1938. 10

[62] Y. C. Zhang, Z. G. Xing, Z. G. Ma, Y. Chen, G. J. Ding, P. Q. Xu, and et al. *Sci. China Physics, Mech. Astron.*, 53(3):465–468, 2010. 10

[63] C Skierbiszewski, Wasilewski Z. R., I Grzegory, and S Porowski. *J. Cryst. Growth*, 311:1632–1639, 2009. 10, 11, 62, 82

[64] H. Turski, M. Siekacz, Z. R. Wasilewski, M. Sawicka, S. Porowski, and C. Skierbiszewski. *J. Cryst. Growth*, 367:115–121, 2013. 11

[65] Yoshikawa, Kusakabe K., Hashimoto N., Hwang E., and Itoi T. *Appl. Phys. Lett.*, 108(022108):1–35, 2016. 11, 64, 81

[66] C. Cheze, M. Siekacz, I. Fabio, B. Jenichen, F. Feix, T. Schulz, M. Albrecht, C. Skierbiszewski, and R. Calarco. *J. Appl. Phys.*, 120(125307), 2016. 11, 55, 56, 64

[67] C. S. Gallinat, G. Koblmueller, J. S. Brown, and J. S. Speck. *J. Appl. Phys.*, 102(064907), 2007. 11, 35, 36

[68] D. B. Williams and C. B. Carter. *Transmission Electron Microscopy. A Textbook for Materials Science*. New York: Springer US, 2nd ed., 2008. 11, 17, 21

[69] L. Reimer. *Transmission Electron Microscopy. Physics of Image Formation and Microanalysis*, volume 36. Springer series in Optical Sciences, 1997. 14

[70] A. Howie and M. J. Whelan. *Proc. R. Soc. Lond. A*, 263:217–237, 1961. 14

[71] Q. Shen. *Dynamical Diffraction in Methods in Materials Research*. John Wiley & Sons, 2000. 14

[72] M. Lentzen. *Microsc. Microanal.*, 14:16–26, 2008. 16

[73] O. Scherzer. *J. Appl. Phys.*, 20(20), 1949. 17

[74] L Cervera Gontard, R. E. Dunin-Borkowski, M. J. Hyetch, and D. Ozkaya. *Journal of Physics: Conference Series*, 26:292–295, 2006. EMAGâNANO 05: Imaging, Analysis and Fabrication on the Nanoscale. 18

[75] H. Lichte. *Ultrmicroscopy North-holland*, 38:13–22, 1991. 18

[76] H Rose. *Ultramicroscopy*, 56:11–25, 1994. 18

[77] M. Lentzen, B. Jahnen, C. L. Jia, A. Thust, K. Tillmann, and K. Urban. *Ultramicroscopy*, 92:233–242, 2002. 18, 19

[78] C. L. Jia, M. Lentzen, and K. Urban. Atomic-resolution imaging of oxygen in perovskite ceramics. *SCIENCE*, 299:2–6, 2003. 19

[79] C.-L. Jia, M. Lentzen, and K. Urban. *Microsc. Microanal.*, 10:174–184, 2004. 19

[80] P. A. Stadelmann. Ultramicrsocopy north-holland. 21:131–146, 1987. 19, 44

[81] T. Schulz, T. Remmele, T. Markurt, M. Korytov, and M. Albrecht. *J. Appl. Phys*, 112(033106), 2012. 20, 46, 47, 49

[82] C. Kisielowski, B. Freitag, M. Bischoff, H. van Lin, S. Lazar, G. Knippels, and et al. *Microsc. Microanal. 14,*, 14:469–477, 2008. 21

[83] Howie. *Journal of Microscopy*, 117(Pt 1):11–23, 1979. 21

[84] C. R. Hall and P. B. Hirsch. *Proc. R. Soc. Lond. A*, 286:158–177, 1965. 21

[85] P. M. Voyles, J. L. Grazul, and D. A. Muller. *Ultramicroscopy 96*, 96:251–273, 2003. 22

[86] C. B. Boothroyd, R. E. Dunin-Borkowski, and T. Walther. In *Mat. Res. Soc. Symp. Proc.*, volume 466, pages 113–118. Materials Research Society, 1997. 22

[87] V. Grillo and E. Carlino. *Phys Rev. B*, 77(054103), 2008. 22, 53, 54

[88] E. Carlino, S. Modesti, D. Furlanetto, M. Piccin, S. Rubini, and A. Franciosi. *Appl. Phys. Lett.*, 83(4):662–664, 2003. 22, 67

[89] V. Grillo, K. Mueller, K. Volz, F. Glas, T. Grieb, and A. Rosenauer. In *17th International Conference on Microscopy of Semiconducting Materials*, volume 326 of *Journal of Physics: Conference Series*, 2011. 22

[90] L. Kourkoutis, M. K. Parker, V. Vaithyanathan, D. G. Schlom, and D. A. Muller. *Phys. Rev. B*, 84(075485), 2011. 22

[91] H.-F Deng and J. W. Steeds. *Semicond. Sci. Technol.*, 7:125–134, 1992. 24

[92] G. Schmidt, M. Müller, P. Veit, F. Bertram, J. Christen, M. Glauser, J. Carlin, and et al. *Appl. Phys. Lett.*, 105(032101), 2014. 24

[93] A. Urban, M. Müller, C. Karbaum, G. Schmidt, P. Veit, J. Malindretos, F. Bertram, J. Christen, and A. Rizz. *Nano Lett.*, 15(8):5105–5109, 2015. 24

[94] K. Hestroffer, C. Lund, O. Koksaldi, H. Li, G. Schmidt, M. Trippel, P. Veit, and et al. *J. Cryst. Growth*, 465:55–59, 2017. 24

[95] A. Ichimiya and P.I. Cohen. *Reflection high-energy electron diffraction*. Cambridge University Press, 2004. 25

[96] https://www.svta.com/rheed-mbe equipment.html. 25

[97] S. Hasegawa. *Characterization of Materials*, chapter Reflection High-energy Electron Diffraction, pages 1925–1938. John Wiley & Sons, Inc., 2012. 25

[98] M. Dabrowska-Szata. Analysis of RHEED pattern from semiconductor surfaces. *Mater. Chem. Phys.*, 81:257–259, 2003. 26

[99] J. Jo, Y. Tchoe, G-C. Yi, and M. Kim. *Sci. Rep.*, 8(1694):1–10, 2018. 26

[100] A R Smith, V. Ramachandran, R. M. Feenstra, D. W. Greve, J. Neugebauer, and et al. *Mat. Res. Soc. Symp. Proc. Vol.*, 482:363–368, 1998. 26

[101] J. Wang, R. So, Y. Liu, H. Wu, M. H. Xie, and S. Y. Tong. *Surf. Sci. Lett.*, 600(14):169–174, 2006. 26

[102] A. R. Smith, R. M. Feenstra, D. W. Greve J., Neugebauer, and J. E. Northrup. *Phys. Rev. Lett.*, 79(20):3934–3937, 1997. 26

[103] K. Iwata, H. Asahi, S. J. Yu, K. Asami, H. Fujita, M. Fushida, and S. Gonda. *Jpn. J. Appl. Phys.*, 35(3A):289–292, 1996. 26

[104] D. Sedin and K. Rowlen. *Appl. Surf. Sci*, 182(40):40–48, 2001. 28

[105] Veeco Metrology Group Digital Insturments. *Scanning Probe Microscopy Training Notebook*. Santa Barbara, CA, 2000. 28

[106] E. F. Schubert. *Light-Emitting Diodes*. Cambridge Univ. Press, 2nd edition edition, 2006. 28

[107] H. Kalt and M. Hetterich. *Optics of Semiconductors and Their Nanostructures*. Springer-Verlag Berlin Heidelberg, 2004. 28

[108] C. E. Dreyer, A. Janotti, and C. G. Van de Walle. *Appl. Phys. Lett.*, 102(142105), 2013. 29

[109] C. Persson, A. Ferreira Da Silva, R. Ahuja, and B. Johansson. *J. Cryst. Growth*, 231(3):397–406, 2001. 29

[110] S-H. Park, D. Ahn, and S-L. Chuang. *IEEE J. Quantum Electron.*, 43(12):1175–1182, 2007. 29

[111] S-H. Park. *J. Appl. Phys.*, 91(12):9904–9908, 2002. 29

[112] M.P.C.M. Krijn. Heterojunction band offsets and effective masses in Ill-V quaternary alloys. *Semicond. Sci. Technol.*, 6(27):27–31, 1991. 29

[113] J. F. Muth, J. H. Lee, I. K. Shmagin, R. M. Kolbas, H. C. Casey, B. P. Keller, U. K. Mishra, and S. P. DenBaars. *Appl. Phys. Lett.*, 87(192117):2572–2574, 1997. 30

[114] C Merz, M Kunzer, U Kaufmann und I Akasaki, and H Amano. *Semicond. Sci. Technol.*, 11(5):712–716, 1996. 30, 115

[115] B. K. Meyer. *Mat. Res. Soc. Symp. Proc.*, 449:497–507, 1997. 30, 115

[116] S. Chichibu, T. Azuhata, T. Sota, and S. Nakamura. Spontaneous emission of localized excitons in InGaN single and multiquantum well structures. *Appl. Phys. Lett.*, 69(27):4188–4190, 1996. 30, 115

[117] K. Huang and A. Rhys. *Proceedings of the Royal Society, Proc. Roy. Soc. Lond.*, A204:406–423, 1950. 30

[118] M. Smith, J. Y. Lin, H. X. Jiang, A. Khan, Q. Chen, A. Salvador, A. Botchkarev, W. Kim, and H. Morkoc. *Appl. Phys. Lett.*, 70(21):2882–2884, 1997. 30

[119] H. Morkoc. *Handbook of Nitride Semiconductors and Devices*, volume 1, chapter General Properties of Nitrides, pages 1–61. WILEY-VCH Verlag GmbH & Co. KGaA, 2008. 30

[120] X. B. Zhang, T. Taliercio, S. Kolliakos, and P. Lefebvre. *J. Phys. Condens. Matter*, 13(32):7053–7074, 2001. 31

[121] S. Biernacki, U. Scherz, and B. K. Meyer. *Phys. Rev. B*, 49(7):4501–4510, 1994. 31

[122] R. Pässler. *Phys. Status Solidi Basic Res.*, 200(1):155–172, 1997. 31

[123] Y P Varshni. *Physica*, 34:149–154, 1967. 31, 106

[124] L Vina, S. Logothetidis, and M. Cardona. *Phys. Rev. B*, 30(4):1979–1991, 1984. 31

[125] K. P. O Donnell, J. F. W. Mosselmans, R. W. Martin, S. Pereira, and M. E. White. *J. Phys.: Condens. Matter*, 13:6977–6991, 2001. 31, 106

[126] R. Pässler. *Phys. Rev. B - Condens. Matter Mater. Phys.*, 66(8):1–18, 2002. 31

[127] B. G. Yacobi and D. B. Holt. *Cathodoluminescence Microscopy of Inorganic Solids*. Springer Series + Business Media New York, 1990. 32

[128] http://www.gel.usherbrooke.ca/casino/What.html. 32

[129] A. Gustafsson. Cathodoluminescence studies of nanostructured semiconductors. *J. Microsc.*, 224(1):72–78, 2006. 32

[130] http://www.princetoninstruments.com/userfiles/files/assetLibrary/Datasheets.pdf. 33

[131] https://www.hamamatsu.com/eu/en/product/cameras/index.html. 34

[132] http://www.cappa.ie/advanced research/techniques/timeresolvedphotoluminescence.pdf. 34

[133] A. G. Bhuiyan, A. Hashimoto, and A. Yamamoto. *J, Appl. Phys.*, 94(2779), 2003. 35

[134] S. J. Pearton, J. C. Zolper, R. J. Shul, and F. Ren. *J. Appl. Phys.*, 86(1), 1999. 35

[135] N. Newman. *J. Cryst. Growth*, 178:102–112, 1997. 35

[136] A. I. Duff, L. Lymperakis, and J. Neugebauer. *Phys. Status Solidi Basic Res.*, 252(5):855–865, 2015. 35

[137] https://www.mbe-komponenten.de/selection-guide/vapor pressure.php. 35

[138] N. Grandjean, J. Massies, F. Semond, S. Yu. Karpov, and R. A. Talalaev. *Appl. Phys. Lett.*, 74(13):1854–1856, 1999. 35, 36

[139] H. Riechert, R. Averbeck, A. Graber, M. Schienle, U. Straub, and H. Tews. *Mat. Res. Soc. Symp. Proc.*, 449:149–159, 1997. 35

[140] G. Bruno, M. Losurdo, T. Kim, and A. Brown. *Phys, Rev. B*, 82(075326):1–7, 2010. 35

[141] S. Yu. Karpov, R. A. Talalaev, Yu. N. Makarov, N. Grandjean, J. Massies, and B. Damilano. *Surf. Sci.*, 450(3):191–203, 2000. 35

[142] X. Wang and A. Yoshikawa. *Prog. Cryst. Growth Charact. Mater.*, 48-49(1-3 SPEC. ISS.):42–103, 2004. 35

[143] R. C. Schoonmaker, A. Buhl, and J. Lemley. *Phys. Chem.*, 69(3455):3455–3460, 1965. 36

[144] R. D. Jones and K. rose. *J. Phys. Chem. Solids*, 48(6):587–590, 1987. 36

[145] Hanada T. *Oxide and Nitride Semiconductors*, chapter Basic Properties of ZnO, GaN, and Related Materials, pages pp 1–19. Springer, Berlin, Heidelberg, 2009. 36

[146] A. Zoroddu, F. Bernardini, P. Ruggerone, and V. Fiorentinii¿œ. *Phys. Rev. B*, 64(045208):1–6, 2001. 36, 80

[147] H. Turski, M. Siekacz, M. Sawicka, G. Cywinski, M. Krysko, S. Grzanka, J. Smalc-Koziorowska, and et al. *J. Vac. Sci. Technol. B*, 29(03C136):03C136, 2011. 36, 80

[148] R. Averbeck and H. Riechert. *Phys. Status Solidi Appl. Res.*, 301(1):301–306, 1999. 36

[149] I. Ho and G. B. Stringfellow. *Appl. Phys. Lett.*, 69(2701), 1996. 37

[150] G. B. Stringfellow. *J. Cryst. Growth*, 312(6):735–749, 2010. 37

[151] C. K. Gan, Y. P. Feng, and D. J Srolovitz. *Phys. Rev. B - Condens. Matter Mater. Phys.*, 74(115319):1–8, 2006. 37

[152] J. A. Chan, J. Z. Liu, and A. Zunger. *Phys. Rev. B*, 82(045112):1–11, 2010. 37, 98

[153] M. Rao, D. Kim, and S. Mahajan. *Appl. Phys. Lett*, 85(1961):10–13, 2004. 38

[154] R. Singh and T. D. Moustakas. *Mat. Res. Soc. Symp. Proc.*, 395:163–168, 1995. 38

[155] A. Yoshikawa, N. Hashimoto, N. Kikukawa, S. B. Che, and Y. Ishitani. *Appl. Phys. Lett.*, 86(153115):9–11, 2005. 38

[156] Markus Pristovsek. *Appl. Phys. Lett.*, 102(24):1–4, 2013. 38

[157] E. T. Yu, X. Z. Dang, P. M. Asbeck, S. S. Lau, and G. J. Sullivan. *J. Vac. Sci. Technol. B Microelectron. Nanom. Struct.*, 17(4):1742–1749, 1999. 39

[158] R. B. Schwarz, K. Khachaturyan, and E. R. Weber. *Appl. Phys. Lett.*, 70(9):1122–1124, 1997. 39

[159] A. F. Wright. *J. Appl. Phys.*, 82(2833):2833–2839, 1997. 39, 48

[160] T. Takeuchi, S. Sota, M. Katsuragawa, M. Komori, H. Takeuchi, H. Amano, and I. Akasak. *Jpn. J. App. Phys.*, 36(Part 2, No. 4A):L382–L385, 1997. 40, 85

[161] S. Chichibu, T. Sota, K. Wada, and S. Nakamura. *J. Vac. Sci. Technol. B*, 16(2204):2204, 1998. 40

[162] I. Gorczyca, K. Skrobas, T. Suski, N. E. Christensen, and A. Svane. *J. Appl. Phys.*, 118(7), 2015. 40, 100

[163] H. Gotoh, T. Tawara, Y. Kobayashi, N. Kobayashi, and T. Saitoh. *Appl. Phys. Lett.*, 83(4791):341, 2003. 40, 101

[164] Y.-L. Li, Y.-R. Huang, and Y.-H. Lai. *Appl. Phys. Lett.*, 91(181113), 2007. 40

[165] S. F. Chichibu, A. C. Abare, M. S. Minsky, S. Keller, S. B. Fleischer, J. E. Bowers, E. Hu, and et al. *Appl. Phys. Lett.*, 73(14):2006–2008, 1998. 40

[166] M. J. Galtrey, R. A. Oliver, M. J. Kappers, C. J. Humphreys, D. J. Stokes, P. H. Clifton, and A. Cerezo. *Appl. Phys. Lett.*, 90(6):10–13, 2007. 40

[167] J. R. Jinschek, R. Erni, N. F. Gardner, A. Y. Kim, and C. Kisielowsk. *Solid State Commun.*, 137(230):230–234, 2006. 40

[168] V. B. Ozdol, C. T. Koch, and P. A. van Aken. *J Appl. Plys.*, 108(056103):1–4, 2010. 40, 46, 80

[169] M. R. McCartney, F. A. Ponce, J. Cai, and D. P. Bour. *Appl. Phys. Lett.*, 76(3055), 2009. 40

[170] C. M. Jones, C. H. Teng, Q. Yan, P. C. Ku, and E. Kioupakis. *Appl. Phys. Lett.*, 111(11):1–6, 2017. 40

[171] L. Bellaiche, T. Mattila, L. W. Wang, S. H. Wei, and A. Zunger. *Appl. Phys. Lett.*, 74(1842):1842–1844, 1999. 40, 101, 102

[172] P. R C Kent and A. Zunger. *Appl. Phys. Lett.*, 79(1977):1977–1979, 2001. 40

[173] C. K. Li, M. Piccardo, L. S. Lu, S. Mayboroda, L. Martinelli, J. Peretti, and et al. *Phys. Rev. B*, 95(144206), 2017. 40, 102, 109

[174] M. Piccardo, C. K. Li, Y. R. Wu, J. S. Speck, B. Bonef, R. M. Farrell, and et al. *Phys. Rev. B*, 95(144205):1–12, 2017. 40, 102

[175] P. Dawson, S. Schulz, R. A. Oliver, M. J. Kappers, and C. J. Humphrey. *J. Appl. Phys.*, 119(181505), 2016. 41, 100, 101

[176] S. Schulz, M. A. Caro, C. Coughlan, and E. P O Reill. *Phys. Rev. B*, 91(035439):1–12, 2015. 41

[177] Y.-H. Cho, G. H. Gainer, A. J. Fischer, J. J. Song, S. Keller, U. K. Mishra, and S. P. DenBaars. *Appl. Phys. Lett.*, 73(1370):1370–1372, 1998. 41, 106

[178] V. K. Dixit, S. Porwal, S. D. Singh, T. K. Sharma, S. Ghosh, and S. M. Oak. *J. Phys. D. Appl. Phys.*, 47(065103), 2014. 41, 105

[179] J. Bai, T. Wang, and S. Sakai. *J. Appl. Phys.*, 88(4729):4729–4733, 2000. 41, 106

[180] P. G. Eliseev, P. Perlin, J. Lee, and M. Osinski. *Appl. Phys. Lett.*, 71(5):569–571, 1997. 41, 106

[181] K. Kazlauskas, G. Tamulaitis, A. Zukauskas, M. A. Khan, J. W. Yang, J. Zhang, and et al. *Appl. Phys. Lett.*, 83(3722):3722–3724, 2003. 41, 106

[182] S. Kalliakos, P. Lefebvre, X. B. Zhang, T. Taliercio, B. Gil, N. Grandjean, B. Damilano, and J. Massie. *Phys. Status Solidi (a)*, 190(1):149–154, 2002. 41

[183] R. Pecharromán-Gallego, P. R. Edwards, R. W. Martin, and I. M. Watson. *Mater. Sci. Eng. B*, 93(1-3):94–97, 2002. 41, 88

[184] A. Morel, P. Lefebvre, S. Kalliakos, T. Taliercio, T. Bretagnon, and B. Gil. *Phys. Rev. B*, 68(045331):1–6, 2003. 41, 102

[185] Y. B. Band and Y. Avishai. *Quantum Mechanics with Applications to Nanotechnology and Information Science*. Academic Press. Elsever, 1st edition edition, 2013. 41

[186] J. Heyd, G. E. Scuseria, and M. Ernzerhof. *J. Chem. Phys.*, 118(18):8207–8215, 2003. 42

[187] S. L. Chuang and C. S. Chan. *Phys. Rev. B*, 54(4):2491–2504, 1996. 42

[188] M. Povolotskyi, M. Auf Der Maur, and A. Di Carlo. *Phys. Status Solidi C Conf.*, 2(11):3891–3894, 2005. 42

[189] O. Marquardt, D. Mourad, S. Schulz, T. Hickel, G. Czycholl, and J. Neugebaue. *Phys. Rev. B*, 78(235302):33–36, 2008. 42

[190] J. M. Cowley and A. F. Moodie. *Acta Cryst.*, 10(609), 1957. 44

[191] P. Goodman and A. F. Moodie. *Acta Cryst.*, A30(280):280–290, 1974. 44

[192] E. J. Kirkland. *Image Simulation in Transmission Electron Microscopy*. Applied and Engineering Physics Cornell University, Ithaca, N.Y. 14853, 2006. 45

[193] R. Bierwolf, M. Hohenstein, F. Phillipp, O. Brandt, G. E. Crook, and K. Ploog. *Ultramicroscopy*, 49:273–285, 1993. 46

[194] T. P. Bartel and C. Kisielowski. *Ultramicroscopy*, 108:1420–1426, 2008. 46, 47

[195] D. Gerthsen, E. Hahn, B. Neubauer, V. Potin, A. Rosenauer, and M. Schowalter. *Phys. Stat. Sol (c)*, 0(6):1668–1683, 2003. 46

[196] E. C. Do, Y. H. Shin, and B. J. Lee. *J. Phys. Condens. Matter*, 21(325801), 2009. 47

[197] T. Schulz, A. Duff, T. Remmele, M. Korytov, T. Markurt, M. Albrecht, L. Lymperakis, and et al. *J. Appl. Phys.*, 115(033113):0–9, 2014. 47, 109

[198] A. Rosenauer, T. Mehrtens, K. Mueller, K. Gries, M. Schowalter, P. V. Satyam, and S. Bley. *Ultramicroscopy*, 111:1316–1327, 2011. 47, 53, 54, 80

[199] T. M. Smeeton, C. J. Humphreys, J. S. Barnard, and M. J. Kappers. *J. Mater. Sci.*, 41:2729–2737, 2006. 49

[200] T. M. Smeeton, M. J. Kappers, J. S. Barnard, M. E. Vickers, and C. J. Humphreys. *Appl. Phys. Lett.*, 83(5419):5419–5421, 2003. 49

[201] Y. Cui, S. Lee, C. Freysoldt, and J. Neugebauer. *Phys. Rev. B*, 92(085204):1–6, 2015. 50

[202] Earl J. Kirkland, R. F. Loane, and J. Silcox. *Ultramicroscopy*, 23:77–96, 1987. 52

[203] A. Rosenauer, K. Gries, K. Mueller, A. Pretorius, M. Schowalter, and et al. *Ultramicroscopy*, 109:1171–1182, 2009. 54

[204] G. P. Dimitrakopulos, I. G. Vasileiadis, C. Bazioti, J. Smalc-Koziorowska, S. Kret, E. Dimakis, and et al. *J. Appl. Phys.*, 123(024304), 2018. 54, 80, 81

[205] C. Wouters, T. Markurt, E. Rotunno, V. Grillo, and M. Albrecht. The influence of 2s bloch wave state excitations on quantitative haadf stem imaging [awaiting publication]. 54

[206] K. Kusakabe, N. Hashimoto, T. Itoi, K. Wang, D. Imai, and A. Yoshikawa. *Appl. Phys. Lett.*, 108(152107):20–25, 2016. 56

[207] O. Dehaese, X. Wallart, and F. Mollot. *Appl. Phys. Lett.*, 66(52):52, 1995. 58

[208] C. A. Schneider, W. S. Rasband, and K. W. Eliceiri. *Nat. Methods*, 9(7):671–675, 2012. 58

[209] J. Neugebauer, T. K. Zywietz, M. Scheffler, J. E. Northrup, H. Chen, and R. M. Feenstra. *Phys. Rev. B*, 90(5):1–8, 2003. 62, 82

[210] C. Chèze, F. Feix, M. Anikeeva, T. Schulz, M. Albrecht, H. Riechert, O. Brandt, and R. Calarco. *Appl. Phys. Lett.*, 110(072104):0–4, 2017. 64, 74, 81, 82, 86, 123

[211] H. Chen, R. M. Feenstra, J. E. Northrup, T. Zywietz, J. Neugebauer, and D. W. Greve. *J. Vac. Sci. Technol. B*, 18(2284), 2000. 71, 74, 82

[212] C. Friedrich, A. Biermann, V. Hoffmann, M. Kneissl, N. Esser, and P. Vogt. *J. Appl. Phys.*, 112(033509), 2012. 74, 81

[213] M. Himmerlich, A. Eisenhardt, J. A. Schaefer, and S. Krischok. *Phys. Status Solidi B*, 246(6):1173–1176, 2009. 74

[214] K. Wang and A. R. Smith. *Comput. Phys. Commun.*, 182:2208–2212, 2011. 75

[215] J. E. Northrup, J. Neugebauer, R. M. Feenstra, and A. R. Smith. *Phys. Rev. B*, 61(15):9932–9935, 2000. 76, 82, 117

[216] L. Lymperakis, T. Schulz, C. Freysoldt, M. Anikeeva, Z. Chen, X. Zheng, and et al. *Phys. Rev. Mater.*, 2(011601 (R)), 2018. 79

[217] A. I. Duff, L. Lymperakis, and J. Neugebauer. *Phys. Rev. B*, 89(085307):43–46, 2014. 80, 82, 118

[218] C. Chèze and R. Calarco. *Nanosci. Nanotechnol. Lett.*, 9(7):1118–1122, 2017. 82

[219] S. Lee, C. Freysoldt, and J. Neugebauer. *Phys. Rev. B*, 90(24):1–10, 2014. 82

[220] M. Feneberg, S. Osterburg, K. Lange, C. Lidig, B. Garke, R. Goldhahn, and E. Richter. *Phys. Rev. B*, 90(075203):1–10, 2014. 85

[221] S. Das Sarma, R. Jalabert, and S.-R. Eric Yang. *Phys. Rev. B*, 41(12):8288–8294, 1990. 85

[222] J.-H. Ryou, P. D. Yoder, J. Liu, Z. Lochne, and et al. *IEEE J Sel Top Quant*, 15(4):1080–1091, 2009. 85

[223] S. L. Rumyantsev, M. S. Shur, and M. E. Levinshtein. Materials Properties of Nitrides: Summary. *Int. J. High Speed Electron. Syst.*, 14(01):1–19, 2011. 88

[224] D. M. Graham, A. Soltani-Vala, P. Dawson, M. J. Godfrey, T. M. Smeeton, J. S. Barnard, and et al. *J. Appl. Phys.*, 97(103508), 2005. 88, 101

[225] A. J. Fischer, W. Shan, J. J. Song, Y. C. Chang, R. Horning, and B. Goldenberg. *Appl. Phys. Lett.*, 71(1981), 1997. 89

[226] S. Sawada, N. Hamada, and N. Ookubo. Mechanisms of visible photoluminescence in porous silicon. *Phys. Rev. B*, 49(8):5236–5245, 1994. 91

[227] F. Mahler, J. W. Tomm, K. Reimann, M. Woerner, T. Elsaesser, C. Flytzanis, and V. Hoffmann. *Phys. Rev. B*, 97(16):1–5, 2018. 91

[228] F. Feix, T. Flissikowski, C. ChÃšze, R. Calarco, H. T. Grahn, and O. Brandt. *Appl. Phys. Lett.*, 109(042104), 2016. 92, 101, 103

[229] R. Pecharroman-Gallego, R. W. Martin, and I. M. Watson. *J. Phys. D. Appl. Phys.*, 37(2954), 2004. 93

[230] T. Egawa, T. Jimbo, and M. Umen. *J. Appl. Phys.*, 82(5816), 1997. 95

[231] C. Hums, T. Finger, T. Hempel, J. Christen, A. Dadgar, A. Hoffmann, and A. Krost. *J. Appl. Phys.*, 101(033113), 2007. 95

[232] S. Schulz, D. P. Tanner, E. P. O'Reilly, M. A. Caro, T. L. Martin, P. A. J. Bagot, M. P. Moody, and et al. *Phys. Rev. B*, 92(235419):1–12, 2015. 100, 107

[233] D. Chen, Y. Luo, L. Wang, H. Li, G. Xi, Y. Jiang, Z. Hao, C. Sun, and Y. Han. *J. Appl. Phys.*, 101(053712), 2007. 101

[234] K. Kusakabe and A. Yoshikawa. *Semiconductors and Semimetals*, 96:305–340, 2016. 101, 105

[235] M. Pophristic, F. H. Long, C. Tran, I. T. Ferguson, and R. F. Karlicek. *J. Appl. Phys.*, 86(1114), 1999. 101

[236] A. Kaminska, D. Jankowski, P. Strak, K. P. Korona, M. Beeler, K. Sakowski, E. Grzanka, and et al. *J. Appl. Phys.*, 120(095705), 2016. 101

[237] R. A. Mair, J. Y. Lin, H. X. Jiang, E. D. Jones, A. A. Allerman, and S. R. Kurtz. *Appl. Phys. Lett.*, 76(188), 2000. 102

[238] C. Gourdon and P. Lavallard. *Phys. stat. sol. (b)*, 153:641–652, 1989. 102

[239] A. Kaschner, T. Luettgert, H. Born, A. Hoffmann, A. Yu Egorov, and H. Riechert. *Appl. Phys. Lett.*, 78(10):1391–1393, 2001. 102

[240] L. Pavesi. *J. Appl. Phys.*, 80(1):216–225, 1996. 102

[241] S. F. Chichibu, H. Marchand, M. S. Minsky, S. Keller, P. T. Fini, J. P. Ibbetson, S. B. Fleischer, and et al. *Appl. Phys. Lett.*, 74(10):1460–1462, 1999. 102

[242] T. Langer, H. G. Pietscher, F. A. Ketzer, H. JÃ¶nen, H. Bremers, and et al. *Phys. Rev. B - Condens. Matter Mater. Phys.*, 90(205302):1–9, 2014. 102, 107

[243] M. Oueslati, C. Benoit, and M. Zouaghi. *Phys. Rev. B*, 37(6):3037–3041, 1988. 102

[244] E. Cohen and M. D. Sturge. *Phys. Rev. B*, 25(6):3828–3840, 1982. 102

[245] T. Bartel, M. Dworzak, M. Strassburg, A. Hoffmann, A. Strittmatter, and D. Bimberg. *Appl. Phys. Lett.*, 85(11):1946–1948, 2004. 102

[246] G. A. Garrett, C. J. Collins, A. V. Sampath, H. Shen, M. Wraback, S. F. LeBoeuf, J. Flynn, and G. Brandes. *Phys. Status Solidi (c)*, 2(7):2332–2336, 2005. 104

[247] E. J. Shin, J. Li, J. Y. Lin, and H. X. Jiang. *Appl. Phys. Lett.*, 77(1170), 2000. 105

[248] K. Torii, T. Deguchi, T. Sota, K. Suzuki, S. Chichibu, and S. Nakamura. *Phys. Rev. B*, 60(7):4723–4730, 1999. 107, 125

[249] S. Keller, B. P. Keller, D. Kapolnek, A. C. Abare, H. Masui, L. A. Coldren, U. K. Mishra, and S. P. Den Baars. *Appl. Phys. Lett.*, 68(22):3147–3149, 1996. 108

[250] J. H. Rice, J. W. Robinson, R. A. Taylor, R. A. Oliver, G. Andrew, D. Briggs, and et al. *Appl. Phys. Lett.*, 84(20):4110–4112, 2004. 113, 115

[251] S. Deshpande, T. Frost, L. Yan, S. Jahangir, A. Hazari, X. Liu, and et al. *Nano Lett.*, 15:1647–1653, 2015. 113, 115

[252] M. Winkelnkemper, A. Schliwa, and D. Bimberg. *Phys. Rev. B*, 74(155322), 2006. 113

[253] S. Chichibu, T. Azuhata, T. Sota, and S. Nakamura. *Appl. Phys. Lett.*, 70(2822), 1997. 115

[254] H. Schömig, S. Halm, A. Forchel, G. Bacher, J. Off, and F. Scholz. *Phys. Rev. Lett.*, 92(10):10–13, 2004. 115

[255] O. Moriwaki, T. Someya, K. Tachibana, S. Ishida, and Y. Arakawa. *Appl. Phys. Lett.*, 76(17):2361–2363, 2000. 115

[256] J. H. Kim, Y-H. Ko, S-H. Gong, S-K. Ko, and Y. H. Cho. *Sci. Rep.*, 3(2150):1–7, 2013. 115

[257] R. A. Oliver, G. A. D. Briggs, M. J. Kappers, C. J. Humphreys, S. Yasin, and et al. *Appl. Phys. Lett.*, 83(4):755–757, 2003. 115

[258] R. A. Arif, Y. K. Ee, and N. Tansu. *Appl. Phys. Lett.*, 91(091110), 2007. 115

[259] A. Even, G. Laval, O. Ledoux, P. Ferret, D. Sotta, E. Guiot, and et al. *Appl. Phys. Lett.*, 262103(26), 2017. 118

[260] Marcin Siekacz, Torsten Ernst, Ewa Grzanka, Grzegorz Staszczak, Tadeusz Suski, Anna Feduniewicz Zmuda, Marta Sawicka, Joanna Moneta, Mariia Anikeeva, Tobias Schulz, and Martin Albrecht. Superlattices and Microstructures Impact of the substrate lattice constant on the emission properties of InGaN / GaN short-period superlattices grown by plasma assisted MBE. 133(May), 2019. 118

[261] T. Schulz, M. Anikeeva, M. Siekacz, P. Wolny, T. Markurt, M. Albrecht, and L. Lymperakis. Influence of strain on the indium incorporation in (0001) gan [awaiting publication]. 118

[262] D. D Schenk, M. Leroux, and P. De Mierry. *J. Appl. Phys.*, 88(3):1525–1534, 2000. 124

[263] C. Cobet, R. Goldhahn, W. Richter, and N. Esser. *Phys. Status Solidi Basic Res.*, 246(7):1440–1449, 2009. 125

Acknowledgments

Life is not just a box of chocolates, especially if there is some physics involved...

I am very proud and grateful that I was involved in the former international project "SPRInG" organized by the European Union's Horizon 2020 research and innovation program (grant agreement No. 642574). Being a part of Marie Skłodowska-Curie Actions gave me a lot of working experience and opportunities. I deeply appreciate my scientific supervisor Dr. Martin Albrecht from IKZ who made this possible and supported my studies on all this way. I have learned and lot from him and have to say that have never met a person that has so much passion for physics. I want to acknowledge the MBE growers Dr. Caroline Cheze (PDI) and Dr. Raffaella Calacrco (PDI). I appreciate the organizational structure of the SPRInG project, that we were able to meet regularly, make fruitful discussions and plan our work.

I am personally thankful to Dr. Tobias Schulz (IKZ), for his some of his brilliant research ideas and who may have suffered from my multiple questions at the beginning of my PhD but was always there to answer. It was a great pleasure to work in such welcoming, supportive and friendly environment of the microscopy characterization group of IKZ: Thilo Remmele, Dr. Tony Markurt, Leonardo Cancellara, Charlotte Wouters, Martina Zupancic, Valeria Bonito-Oliva and my joyful office neighbor Dr. Robert Schewski. I will never forget my former colleagues who made my first times in Berlin more pleasant: Stefan Mohn and Dr. Natalia Stolyarchuk.

I was happy to have a secondment experience during my PhD to Unipress in Warsaw, Poland. I am so much thankful that I could work together with a TEM specialist Dr. Julita Smalc-Koziorowska, as well as Grzegorz Staszczak under command of Prof. Tadeusz Suski, great experts in optical and high pressure experiments. It was very helpful to get the insights about the MBE growth during my stay in Unipress and ToPGaN provided by Dr. Marcin Siekacz and Pavel Wolny. I also appreciate a great enthusiasm of the other MBE growth specialist of ToPGaN, Dr. Marta Sawicka. It was a pleasure to make friends with Joanna Moneta from Unipress, a student of SPRInG project.

A big part of this work came into life through collaborations with the theoreticians, i.e. Dr. Liverios Lymperakis and Prof. Jörg Neugebauer from Max-Planck-Institut für Eisenforschung, Düsseldorf, who were open for long discussions. I am deeply grateful to the coauthors of our paper. With the help in time-resolved experiments, an idea that had been developing for 3 years was finally published: Dr. Jens Tomm and Felix Mahler from Max-Born Institute, Berlin.

I appreciate the support from the IKZ administration, who assisted with the paper work and some legal questions, i.e. Birgit Ruthenberg. And I am deeply thankful to Prof. Thomas Schröder, head of IKZ, for understanding and financial support that made a long and challenging task of compiling my investigations into a written thesis as less troublesome as possible.

At the end, I want to thank my close ones. My parents, though, would never understand these words in English either the details of my work, but gave me the essential thing for doing my PhD dissertation - a feeling that I can do it whatever and that there are no limits for your

goals. I will always remember a person who stimulated me to come to Berlin and to do my research. Finally, I am cordially thankful to my boyfriend who was going this way nearby with me, inspired me and was just there...

Publications and contributions

Publications (ordered by date of publication):

- C. Chèze, F. Feix, *M. Anikeeva*, T. Schulz, M. Albrecht, H. Riechert, O. Brandt, and R. Calarco, "In/GaN(0001)-(√3×√3)R30 adsorbate structure as a template for embedded (In,Ga)N/ GaN monolayers and short-period superlattices", Appl. Phys. Lett. **110**, 072104 (2017);

- L. Lymperakis, T. Schulz, C. Freysoldt, *M. Anikeeva*, Z. Chen, X. Zheng, B. Shen, C. Chèze, M. Siekacz, X. Q. Wang, M. Albrecht, and J. Neugebauer, "Elastically frustrated rehybridization: Origin of chemical order and compositional limits in InGaN quantum wells", Phys. Rev. Mat. **2**, 011601(R) (2018);

- ***M. Anikeeva***[1], P. Wolny, M. Sawicka, T. Schulz, T. Markurt, M. Albrecht, M. Siekacz, and C. Skierbiszewski, "Dependence of indium content in monolayer-thick InGaN quantum wells on growth temperature in $In_xGa_{1-x}N/In_{0.02}Ga_{0.98}N$ superlattices", J. Appl. Phys. **124**, 065701 (2018);

- ***M. Anikeeva***, M. Albrecht, F. Mahler, J. W. Tomm, L. Lymperakis, C. Chèze, R. Calarco, J. Neugebauer and T. Schulz, "Role of hole confinement in the recombination properties of InGaN quantum structures", Sci. Rep. **9** 9047 (2019);

- M. Siekacz, P. Wolny, T. Ernst, E. Grzanka, G. Staszczak, T. Suski, A. Feduniewicz-Żmuda, M. Sawicka, J. Moneta, *M. Anikeeva*, T. Schulz, M. Albrecht, C. Skierbiszewski, "Impact of the substrate lattice constant on the emission properties of InGaN/GaN short-period superlattices grown by plasma assisted MBE", Superlattices and Microstructures **133** 106209 (2019).

Conference contributions (ordered by date of publication):

- M. Anikeeva, T. Schulz, I. Gorczyca, C. Cheze, F. Feix and M. Albrecht, "Optical properties and recombination processes of (In,Ga)N/GaN short period superlattices", 24th International Symposium "Nanostructures: Physics and Technology", Saint-Petersburg Russia, 2016 [oral presentation]

- M. Anikeeva, T. Schulz, P. Stark, I. Gorczyca, C. Cheze, F. Feix, R. Calarco and M. Albrecht "Recombination processes and influence of carrier localization on their optical properties in (In,Ga)N/GaN short period superlattices", International Workshop on Nitride Semiconductors (IWN), Orlando USA, 2016 [oral presentation]

- M. Anikeeva, T. Schulz, T. Markurt, M. Sawicka, C. Cheze, R. Calarco and M. Albrecht "In incorporation into (In,Ga)N/GaN short period superlattices studied by transmission

[1] Equal contribution with P. Wolny

electron microscopy", International Workshop on Nitride Semiconductors (IWN), Orlando USA, 2016 [poster]

- M. Anikeeva, T. Schulz, T. Markurt, C. Cheze, H. Riechert, M. Siekacz, P. Wolny, L. Lymperakis and M. Albrecht "Composition limitation in nominal InN layers coherent on GaN", XX Microscopy of Semi Conducting Materials, Oxford Great Britain, 2017 [oral talk]
- M. Anikeeva, T. Schulz, C. Cheze, R. Calarco, U. Jahn, P. Wolny, M. Sawicka, M. Siekacz, G. Schmidt, F. Bertram, J. Christen and M. Albrecht "Cathodoluminescence investigations of the uniformity of ML-thick (In,Ga)N quantum wells", PDI Topical Workshop on Cathodoluminescence of Semiconductor Nanostructures, Berlin Germany, 2018 [invited talk]
- M. Anikeeva, T. Schulz, C. Cheze, R. Calarco, J. W. Tomm, F. Mahler L. Lymperakis and M. Albrecht "Carrier localization and interwell coupling of ML-thick (In,Ga)N quantum wells in the (In,Ga)N/GaN superlattices", 34th International Conference on the physics of semiconductors, Montpellier France, 2018 [oral presentation]
- M. Anikeeva, T. Schulz, C. Cheze, R. Calarco, U. Jahn, P. Wolny, M. Sawicka, M. Siekacz, G. Schmidt, F. Bertram, J. Christen and M. Albrecht "Cathodoluminescence investigations of the uniformity of ML-thick (In,Ga)N quantum wells", 34th International Conference on the physics of semiconductors, Montpellier France, 2018 [poster]

Selbständigkeitserklärung

Hiermit erkläre ich, dass ich die vorliegende Arbeit selbständig ohne fremde Hilfe und nur unter Verwendung der angegebenen Literatur und Hilfsmittel angefertigt habe.

Des Weiteren bestätige ich hiermit, dass ich mich an keiner anderen Universität um einen Doktorgrad beworben habe und keinen entsprechenden Doktorgrad besitze. Ich habe Kenntnis über die dem Verfahren zugrunde liegende Promotionsordnung der Mathematisch-Naturwissenschaftlichen Fakultät der Humboldt-Universität zu Berlin.

Berlin, den 30 September 2019

Mariia Anikeeva